Alma Mater Studiorum – Università di Bologna

DOTTORATO DI RICERCA IN

CHIMICA

Ciclo XXVIII

Settore Concorsuale di afferenza: 03 / B1

Settore Scientifico disciplinare: CHIM / 03

STIMULI-RESPONSIVE NANOPARTICLES
FOR BIO-APPLICATIONS

Presentata da: **Giulia Battistelli**

Coordinatore Dottorato   **Relatore**

Prof. Aldo Roda   **Prof. Marco Montalti**

Esame finale anno 2016

Index

1.Nanoparticles in nanomedicine

1.1 Nanotechnology and Nanoparticles: overview

"*The biological examples of writing information on a small scale has inspired me to think of something that should be possible. Biology is not simply writing information; it is doing something about it. A biological system can be exceedingly small. Many of the cells are very tiny, but they are very active, they manufacture various substances; they walk around; they wiggle: and they do all kinds of marvelous things all on a very small scale. Also, they store information. Consider the possibility that we too can make a thing very small, which does what we want that we can manufacture an object that maneuvers at that level!*"[1]

In this celebre passage, a transcription of a talk given in the 1959 by the physicist Richard Feynman, firstly took shape the idea of nanotechnology, as the production and manipulation of objects in the nanometric scale. Since then, the enormous potentiality hide behind this "small" world started to be recognised, and nanotechnology earned increasing attention. Not only it become central in scientific research, but it also found applications in the everyday life, in fields such as electronics and optoelectronics,[2] biomedicine,[3] pharmacy,[4] cosmetics,[5] catalysis[6] and material science.[7]

The nanomaterials dimensions, at least one of them ranging between 1 and 100 nm, implies totally new physical properties respect to the ones displayed by the same constituting material in bulk. Becoming characterized by an high surface/volume ratio, thermodynamic, electronic, spectroscopic, electromagnetic and structural features are sensitive to size and shape. Moreover, thanks to the enhanced chemical reactivity, these properties turned to be modulable by surfaces chemical modifications. In this prospective, the possibility of efficiently tailoring nanomaterials with adequate functional groups, and their intrinsic capability of self-assemble and self-organize, allows their use as building blocks for more complex architectures. It is not surprising, hence, that nanostructure are in constant development, shaped as nanosurfaces, cylindrical nanotubes, nanosphere and thousands of other morphologies.

In this oceanic mole of systems, designs and applications, great interest is address to the particulates with at least one dimension falling within 1-100 nm[8] which, regardless to their shape or structure, are referred to nanoparticles. Despite they

are finding numerous applications in the most varied areas, from energy production, to food packaging or environmental decontamination,[9] they are having a revolutionary impact on one of the most addressed field: medicine. In some clinical applications, indeed, they not only proved to be extremely useful, but they are actually able to perform some activities which could not be obtained otherwise.

1.2 Multifunctional nanoparticles in nanomedicine

The importance of nanoparticles in medicine, proved by the birth of the term "nanomedicine", relies under the outstanding possibility offered by these systems of developing multifunctional nanosystems, capable of either accomplishing multiple goals or incorporating multiple functional units to perform a single function.[10] Nanoparticles, in fact, allow the integration of drug monitoring, targeted delivering and controlled drug releasing, within multimodal imaging, offering better images at multiple length scales or treatment stages. The combination of these two important areas of diagnosis and treatment into a single platform, opens the way to the innovative and powerful *theranostic approach*, offering the unique possibility of solving challenging medical problems, such as the necessity of personalizing disease treatments in cancer therapy.[11]

The great improvement made in this new field go beyond Feynman's imagination and the advances in the nanofabrication techniques and in the synthetic abilities, allow, nowadays, the production of nanoparticles with controlled shapes, dimensions and compositions.[12,13] Although, it cannot be ignored that important steps forward were made in the nano-characterization techniques, making possible a proper determination of these new materials chemical and physical properties. As a result, a number of nanoparticle-based products for diagnostics and therapeutics have been approved for clinical applications, some of them are under clinical trials[14-17] and the horizon of nanomedicine is still pushed through rapid expansion.[10]

It is not the purpose of this thesis to go deeply into the details of the medical techniques, but it is worthy to give a brief overview of the ones where nanoparticles have found their main applications: medical imaging and drug delivery.

1.2.1 Optical imaging

Medical imaging is the process of creating visual representation of tissues, cells or whole organisms. Obviously, it plays an important role in disease detection,

prognosis and treatment planning. Among the different and complementary types of medical imaging techniques, some of them are more prone to be improved by the nanoparticles contribution. However, they can be easily functionalized or they can incorporate small molecules into a nanometric matrix, becoming potentially useful in nearly all the imaging modalities. From our point of view, particular interest is earned by optical imaging. It includes a various imaging techniques, based on the illumination with light ranging in the ultraviolet, visible and infrared regions of the electromagnetic spectrum, characterized by an excellent spatial resolution and detection sensitivity. Furthermore,the lack of ionizing radiations and the multiplex detection capabilities, makes the technique widely applicable even *in vivo* modality. Unfortunately, the applicability is strongly limited by tissue autofluorescence, which causes a significant decreasing of the signal to noise ratio, and by the limited light penetration through the superficial layer of tissues. As a consequence, at the state of the art, optical imaging is limited to the almost exclusively use of near infrared (NIR) light, not absorbed by tissues, and it is mainly used to examine shallow lesions and superficial objects.[10] Recognising the potentiality of optical imaging with different fluorophores, even in the UV range, anyway, studies have been pushed through by the design and synthesis of new nanoparticles with improved photostability, hydrosolubility, quantum yield and signal specificity.

1.2.2 Drug delivery

During medical treatment, therapeutic compounds often need to be delivered into specific cells to exert their effects. Usually, especially in cancer treatment, the molecules are systemically administered and they are distributed into the whole body through blood circulation. In this condition, their activity is limited by hydrolysis, enzymatic degradation and rapid excretion through the urinary system. Moreover, the lack of a specific targeting, causes a suboptimal drug accumulation in the desired tissue. In this sense, the use of nanoparticles in delivery is revolutionary, thanks to the possibility of improving biodistribution and accumulation of drug molecules by targeting the carrier, protecting them from the microenvironment and, hence, increasing circulation half-life. Not only it can result in an outstanding improvement of the drug efficiency, but it can also reduce the side effects in the body. As it is easy to understand, the developing of this new field is as much interesting as challenging, since nanoparticles, to display their functions, have to overcome the immune systems, reach and recognise the target tissue, accumulate by the time necessary to release the drug and then be released by the

organism without damaging the organism itself. For this reason, an impressive number of different materials and combination of them has been studied to achieve the goal. Trying to give a brief overview of the state of the art in this complex and interdisciplinary field, the simplest classification would follow the nanoparticles composition distinguishing the inorganic and organic based ones.

1.3 Inorganic and organic based nanoparticles

The first evidence of inorganic nanoparticles use in the history date back to the 4th-century, when colloidal gold has been used for decorative and curative purposes. It stimulated a lot of alchemic interest since the 1850s, when Faraday first prepared a pure sample of colloidal gold.[18] From that moment, the interest for this powerful material and the systematic research to understand its outstanding properties begun to rise, reaching the exploit in the last decades. Nowadays, thanks to the progresses in nanocrystal synthesis, it is possible to generate nanoparticles with a great control over size, shape, and composition and[19,20] inorganic nanoparticles of various materials are now commercially available in various forms. *Gold nanoparticles* are interesting for their optical properties, due to the localized surface plasmon resonance (LSPR). When light incises on the nanoparticle surface at a specific frequency,[21] it induces the coherent oscillation of the electrons in the gold valence band. As a result, part of the light is scattered and part is absorbed and dissipated by non-radiative path. The absorption spectrum can be tuned through the nanoparticles geometry[22] and the peak energy can be modulated in order to fall in the optical window of the human tissue penetrable by light, ranging between 650 and 1300 nm. This is extremely interesting for *in vivo* imaging applications, since the strong emissive signal, typical of the resonance plasmon[23,24] can be obtained even in deep tissues. Besides that, it is possible to take advantage of gold nanoparticles photothermal properties using them as a probe for photothermal therapy.

Magnetic nanoparticles are mainly composed by iron oxides and, in less quantity by elementary iron and other magnetic elements.[25,26] Interesting properties, in this case, rise from the fact that if the nanoparticle is smaller than the magnetic domain wall width, all the unpaired electrons are coupled in one direction[27] resulting in only a single magnetic domain. As a consequence of thermal fluctuations, the coupled magnetic moment flips among crystals axes. Reducing the nanoparticle size, the fluctuation became faster until a limit size, where no net magnetization is observed. In this situation, in the absence of external magnetic field applied, the

nanoparticles are not influenced by the inter-particles interactions, while when an external magnetic field is applied, the magnetic moments of the nanoparticles align with the magnetic field, saturating at a relatively low field strength. Thanks to this properties, they has been recognised as an excellent contrast agent probes for MRI and magnetic targeting.[28,29] Moreover, under an oscillating magnetic field, they can generate heat, which is particularly interesting for applications in hyperthermia in deep tissues.[30,31]

Quantum Dots. QDs are fluorescence-emitting semiconductor nanoparticles[32] in which the optical properties are the result of quantum confinement of valence electrons at nanometric scale.[33] As additional effects the presence of dangling orbitals at the surface of the NP, or any defect states in the bulk, provides traps for the excited electrons, and holes prior to recombination. Therefore, an electron excited to the conduction band, or a valence band hole, can transfer itself non-radiatively to one of these surface or defect states, before undergoing a radiative transition to a lower energy state. The net result is that either band edge luminescence is quenched or the emission is shifted to much lower energies, compared to those of band edge recombination (red-shifted emission of NP). Respect to organic fluorophores, QDs have a narrow emission peak, modulable by size, and the absorption spectra ranges from UV to visible light. This means that multicolour emission can be obtain by excitation in the UV range QDs with a different emission wavelengths. It is straightforward to understand the great effort put to solve the problems connected with metal toxicity, in order to apply this structures in *in-vivo* imaging.[34]

Since the inorganic nanoparticle application it is mainly limited by the intrinsic toxicity of the materials (containing e.g. Cadmium and Lead), great effort to overcome the problem was put on the developing of organic nanoparticles. In fact, varying materials, shape, composition and functions, it is possible to address a wide variety of biological mechanisms and targets, overcoming toxicity limits. Some examples of the most common studied and applied materials are reported to give a brief overview of the state of the art.[35]

Liposomes. Lipid vesicles derived from self-assembled enclosed lipid bilayers, are one of the most researched drug delivery carriers. They can be loaded with a wide range of drugs and modified on their surfaces, but the most important features is the strong biocompatibility, which allowed to some of them to enter the clinical practice.[36] Although, self-assembled structures are characterized by a relative quick release of drugs and by poor storage stability.[37] To overcome this aspects, *solid lipid*

nanoparticles (SLN) and *nanostructured lipid carriers* (NLC), have been studied. Characterized by high surface area, favourable zeta potential, prolonged release profile of encapsulated drugs, rapid uptake kinetic by cells and relatively simple production methods,[38] they have found applications in cosmetic and dermatology.[39] To better overcome problems connected with toxicity, it was also improved the fabrication of intrinsically non toxic polysaccharides and protein-based nanoparticles,[40,41] and the use of chemically inert materials with surfaces prone to functionalization. A member of this last group are the *carbon-based nanomaterials*, such as single and multiwall nanotubes and C_{60} fullenerenes, carbon dots and graphene derivatives which can be functionalized with nucleic acids, peptides and proteins.[42,43] The use of this biological molecules resulted particularly interesting, since they are specifically designed by the organism to display complex functions in an extremely specific way. Unfortunately, they tend to easily be denaturated, losing the useful information, if not accurately protected by the environment. At the same time, they are not capable of displaying their biological activity if the inclusion in a protective matrix is too rigid. The balance of this two aspect is still a great challenge.

Another class of organic nanoparticles are *hydrogels*. With their 3D architecture, they are capable of imbibing high amounts of water or biological fluids and exhibit unique physic, chemical and biological characteristics.[35]

1.4 Conclusion and prospective

The classes of nanoparticles reported before are just a scant index of the most common structures attracting the attention of the scientific community. What it can be underline, is that different types of materials exhibit different bio-distribution, biocompatibility, degradation and circulation properties and that no single parameter can be denoted as the most important prerequisite for effective disease therapies. At the same time, the integration of different functionalities in the same platform, combining material, features and functions in almost infinite ways, can offer the possibility of solving complex and challenging problems in nanomedicine. Advantages and disadvantages of the different classes have been listed, even if not in detail, and it emerges that a lot of the scientific interest is pointed towards the obtaining of morphologically and chemical stable nanoparticles. This kind of structures, in fact, are easier to study in long interval of time and it is definitely easier the determination of the toxicity in biologic environment. Also, especially in organic nanoparticles, the active components are often integrated in a not active

matrix working as a platform, which guarantees their protection from the environment.

On the other hand, this limits the nanoparticles ability of releasing drugs by the desired timescales, or their capability of include contrast agents in the desired quantities. Furthermore, the optimization of the accumulation time versus the capability of the organism of cleavage remains a difficult challenge.

For these reasons, we tried to investigate new soft material nanoparticles, where external stimuli trigger specific responses by the modification of the structural components itself, letting them display proper functions. In particular, we focused the attention on nanosystems for bio-imaging, where light conducts a crucial role, both as a stimulus and response.

Bibliography

1   Feynman, R. P. There's plenty of room at the bottom. *Engineering and science* **23**, 22-36 (1960).

2   Shipway, A. N., Katz, E. & Willner, I. Nanoparticle arrays on surfaces for electronic, optical, and sensor applications. *ChemPhysChem* **1**, 18-52 (2000).

3   Choi, S., Tripathi, A. & Singh, D. Smart nanomaterials for biomedics. *Journal of biomedical nanotechnology* **10**, 3162-3188 (2014).

4   Galindo-Rodriguez, S., Allémann, E., Fessi, H. & Doelker, E. Physicochemical parameters associated with nanoparticle formation in the salting-out, emulsification-diffusion, and nanoprecipitation methods. *Pharmaceutical research* **21**, 1428-1439 (2004).

5   Wissing, S. A. & Müller, R. H. Cosmetic applications for solid lipid nanoparticles (SLN). *International Journal of Pharmaceutics* **254**, 65-68 (2003).

6   Daniel, M.-C. & Astruc, D. Gold nanoparticles: assembly, supramolecular chemistry, quantum-size-related properties, and applications toward biology, catalysis, and nanotechnology. *Chemical reviews* **104**, 293-346 (2004).

7   Niemeyer, C. M. Nanoparticles, proteins, and nucleic acids: biotechnology meets materials science. *Angewandte Chemie International Edition* **40**, 4128-4158 (2001).

8   Franklin, R. B. & Costello, L. C. Zinc as an anti-tumor agent in prostate cancer and in other cancers. *Archives of biochemistry and biophysics* **463**, 211-217 (2007).

9   Gao, W. & Wang, J. The Environmental Impact of Micro/Nanomachines: A Review. *ACS Nano* **8**, 3170-3180, doi:10.1021/nn500077a (2014).

10   Bao, G., Mitragotri, S. & Tong, S. Multifunctional Nanoparticles for Drug Delivery and Molecular Imaging. *Annual Review of Biomedical Engineering* **15**, 253-282, doi:doi:10.1146/annurev-bioeng-071812-152409 (2013).

11   Cleary, K. & Peters, T. M. Image-guided interventions: technology review and clinical applications. *Annual review of biomedical engineering* **12**, 119-142 (2010).

12   Gratton, S. E. *et al.* The pursuit of a scalable nanofabrication platform for use in material and life science applications. *Accounts of chemical research* **41**, 1685-1695 (2008).

13   Roh, K.-H., Martin, D. C. & Lahann, J. Biphasic Janus particles with nanoscale anisotropy. *Nature materials* **4**, 759-763 (2005).

14   Hrkach, J. *et al.* Preclinical development and clinical translation of a PSMA-targeted docetaxel nanoparticle with a differentiated pharmacological profile. *Science translational medicine* **4**, 128ra139-128ra139 (2012).

15   Kim, B. Y., Rutka, J. T. & Chan, W. C. Nanomedicine. *New England Journal of Medicine* **363**, 2434-2443 (2010).

16   Peer, D. *et al.* Nanocarriers as an emerging platform for cancer therapy. *Nature nanotechnology* **2**, 751-760 (2007).

17   Davis, M. E. & Shin, D. M. Nanoparticle therapeutics: an emerging treatment modality for cancer. *Nature reviews Drug discovery* **7**, 771-782 (2008).

18   Heiligtag, F. J. & Niederberger, M. The fascinating world of nanoparticle research.   *Materials   Today   **16**,   262-271, doi:http://dx.doi.org/10.1016/j.mattod.2013.07.004 (2013).

19   Euliss, L. E., DuPont, J. A., Gratton, S. & DeSimone, J. Imparting size, shape, and composition control of materials for nanomedicine. *Chemical Society Reviews* **35**, 1095-1104 (2006).

20   Champion, J. A., Katare, Y. K. & Mitragotri, S. Particle shape: a new design parameter for micro-and nanoscale drug delivery carriers. *Journal of Controlled Release* **121**, 3-9 (2007).

21   Boyer, D., Tamarat, P., Maali, A., Lounis, B. & Orrit, M. Photothermal imaging of nanometer-sized metal particles among scatterers. *Science* **297**, 1160-1163 (2002).

22   Prodan, E., Radloff, C., Halas, N. J. & Nordlander, P. A hybridization model for the plasmon response of complex nanostructures. *Science* **302**, 419-422 (2003).

23   Zharov, V. P., Galitovskaya, E. N., Johnson, C. & Kelly, T. Synergistic enhancement of selective nanophotothermolysis with gold nanoclusters: potential for cancer therapy. *Lasers in surgery and medicine* **37**, 219-226 (2005).

24   Jain, P. K., Huang, X., El-Sayed, I. H. & El-Sayed, M. A. Noble metals on the nanoscale: optical and photothermal properties and some applications in imaging, sensing, biology, and medicine. *Accounts of Chemical Research* **41**, 1578-1586 (2008).

25   Jana, N. R., Chen, Y. & Peng, X. Size- and Shape-Controlled Magnetic (Cr, Mn, Fe, Co, Ni) Oxide Nanocrystals via a Simple and General Approach.

Chemistry of Materials **16**, 3931-3935, doi:10.1021/cm049221k (2004).

26   Sun, S. *et al.* Monodisperse MFe2O4 (M= Fe, Co, Mn) nanoparticles. *Journal of the American Chemical Society* **126**, 273-279 (2004).

27   Krishnan, K. M. *et al.* Nanomagnetism and spin electronics: materials, microstructure and novel properties. *Journal of materials science* **41**, 793-815 (2006).

28   Dames, P. *et al.* Targeted delivery of magnetic aerosol droplets to the lung. *Nature nanotechnology* **2**, 495-499 (2007).

29   Namiki, Y. *et al.* A novel magnetic crystal–lipid nanostructure for magnetically guided in vivo gene delivery. *Nature nanotechnology* **4**, 598-606 (2009).

30   Rosensweig, R. E. Heating magnetic fluid with alternating magnetic field. *Journal of magnetism and magnetic materials* **252**, 370-374 (2002).

31   Lee, J.-H. *et al.* Exchange-coupled magnetic nanoparticles for efficient heat induction. *Nature nanotechnology* **6**, 418-422 (2011).

32   Alivisatos, A. P., Gu, W. & Larabell, C. Quantum dots as cellular probes. *Annu. Rev. Biomed. Eng.* **7**, 55-76 (2005).

33   Alivisatos, P. The use of nanocrystals in biological detection. *Nature biotechnology* **22**, 47-52 (2004).

34   Hong, G. *et al.* In Vivo Fluorescence Imaging with Ag2S Quantum Dots in the Second Near-Infrared Region. *Angewandte Chemie* **124**, 9956-9959 (2012).

35   Doshi, N. & Mitragotri, S. Designer biomaterials for nanomedicine. *Advanced functional materials* **19**, 3843-3854 (2009).

36   Torchilin, V. P. Recent advances with liposomes as pharmaceutical carriers. *Nature reviews Drug discovery* **4**, 145-160 (2005).

37   Sharma, A. & Sharma, U. S. Liposomes in drug delivery: progress and limitations. *International journal of pharmaceutics* **154**, 123-140 (1997).

38   Oh, K. S. *et al.* Formation of core/shell nanoparticles with a lipid core and their application as a drug delivery system. *Biomacromolecules* **6**, 1062-1067 (2005).

39   Gasco, M. R. Lipid nanoparticles: perspectives and challenges. *Advanced drug delivery reviews* **59**, 377-378 (2007).

40   Janes, K., Calvo, P. & Alonso, M. Polysaccharide colloidal particles as delivery systems for macromolecules. *Advanced drug delivery reviews* **47**, 83-97 (2001).

41   Wang, G. & Uludag, H. Recent developments in nanoparticle-based drug

delivery and targeting systems with emphasis on protein-based nanoparticles. (2008).

42   Krueger, A. New carbon materials: biological applications of functionalized nanodiamond materials. *Chemistry-a European Journal* **14**, 1382-1390 (2008).

43   Lacerda, L., Bianco, A., Prato, M. & Kostarelos, K. Carbon nanotubes as nanomedicines: from toxicology to pharmacology. *Advanced drug delivery reviews* **58**, 1460-1470 (2006).

2 Polymeric Nanoparticles

One of the main goal in nanomedicine is the development of multifunctional nanoparticles integrating different functions into a single platform and able to efficiently perform the desired functions, without damaging the treated biological system. In this prospective, polymeric components, over other types of materials, are great candidates, mainly thanks to their synthetic and morphological flexibility. Recent advances in polymerization techniques and in the application of reactive, efficient and orthogonal chemical modifications,[1] in fact, allow the production of versatile materials of various composition, morphologies, sizes and chemical properties. Accordingly, polymers are becoming central in therapeutic as biologically active polymeric drugs, polymeric-drugs conjugates, polymer-protein conjugates and polymeric-micelles to which a drug is covalently bond. Furthermore, polymeric synthesis allows the incorporation into the backbone of different functionalities, capable of either modulate the responsiveness to a specific stimuli, through the use of remote activation, or to allow their delivery beyond certain biological organelles. All these properties enabled the engineering of multifunctional polymeric nanoparticles with different shapes, sizes, internal morphologies, external surface charge and functionalization, without losing precise control over the architecture of the individual components.[2]
Polymeric nanoparticles are hence particularly useful in optical imaging, both allowing the increasing of the local contrast, thanks to the capability of directing the biodistribution of high concentration of packaged small-molecule contrast agents to a target site, and improving multimodal imaging, since multiple types of contrast agents can be carried at the same time. Moreover, they can help to solve some of the main challenges encountered in theranostic, especially correlated to the poor aqueous solubility of several organic dyes, which limits their diffusion in the biological environment and dramatically affect their brightness. Another important aspect, is the possibility of functionalize the constituting macromolecules with almost all the desired moieties with precise rationalization of the polymer/probe ratio, their spatial organization respect to the nanoparticles structure and, hence, to the external environment. Last but not least, the possibility of infinite variation of the building-blocks, may solves the biocompatibility and toxicity problems.

2.1 Structural aspects

It should be clear that designing nanoparticles able to display complex functions

requires a systematic approach, to carefully select and locate all the components. To achieve this goal, a good strategy is to adopt a core-shell morphology,[1] where the nature of the core-polymer dictates the type of therapeutics/diagnostics agents that can be incorporated, while the shell is primary responsible to the interaction with the environment. Since nanoparticles circulate in aqueous medium, the shell is usually composed by hydrophilic polymers, carefully selected to mask the internal, hydrophobic domains of the nanoparticles, to control their interaction with extracellular matrices and with the immune system components. poly(ethylene glycol) (PEG), is one of the most commonly used polymer to coat various types of nanomaterials and to impart stealth properties. This material can also be functionalize with specific moieties, such as targeting or fluorescent agents, or it can be used as template for the nanoparticles synthesis, taking advantage from its intrinsic tendency to self-organize in micelles in polar solvent, as it will better describe in the next paragraph.[3]

The control over the shell is the first important aspect for predicting the nanoparticles behaviour in the *in vitro* and *in vivo* systems, but it is extremely important to understand that safety, biocompatibility, and performance of nanomaterials depend on the overall nanoparticle shape and composition. For example, the premature disassembly of nanoparticles into the polymer constituents and/or breakdown into degradation products, results in premature release of the loaded cargoes and in spreading free polymeric chains in the organism, which may induce cyto/immunotoxicity. For this reason, controlling the stability of the nanomaterial is still an important challenge. Different strategies has been proposed, such as stereo-complexation, non-covalent interactions, and cross-linking.[4-6] Cross-linking, in the case of micelles template synthesis, can be performed within either the core or the corona of preformed micelles, it can be used to strongly incorporate functional units, such as emissive probes, or to introduce labile linkers responsive to specific external stimuli. Despite covalent linking guarantees a good stability, it can limit the versatility of the whole structures. For this reason, unimolecular hyperbranched structures or non covalent polymers that are not prone to dissociate upon dilution can be used to modulate the rigidity of the nanoparticles.

In conclusion, since, chemical composition, cross-linking of different block copolymers and the relative copolymer blocks length, affect the core/shell dimensions, the loading and release kinetics, the pH, light and thermo-responsiveness, almost infinite combinations of materials and features can be obtained, but a strong control over the synthesis and the final product

characteristics have to be achieved. Considering the complexity of this field, the accurate study of a known, efficient and successful example of multifunctional nanoparticles, the dye doped silica nanoparticles, was necessary to inspire us on the design, of new "smart" systems. I strongly believe that an overview on their advantages and limits, offers the opportunity of better orient oneself and, most of all, understand the aim of this work.

2.2 Inorganic Polymer: dye doped silica nanoparticles

Being dye doped silica nanoparticles (DDSNs) biocompatible and targetable agents,[7-11] they offer all the required features to obtain very effective tools for theranostic applications (Fig. 2.1),[7-9] and they are extensively studied as drug delivery platforms, due to their drug loading potential and their flexibility in combination with one or more imaging modes.[12-14]
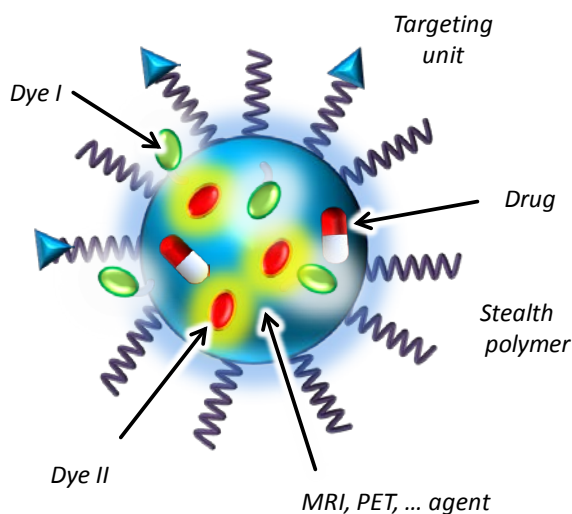
Figure 2.1: Schematic representation of a doped silica nanoparticle. Silica matrix protects different dyes, drug or contrast agents from the environment, allowing the cargo to be delivered in the proper tissue thanks to the surfaces targeting units. The PEG shell hide the cargo from the immune systems and enhance the nanoparticle colloidal stability.[15]

Since silica isphotophysically inert (transparent to visible light and not involved in energy and electron transfer processes), the photophysical properties of the final nanomaterial are conferred by the doping species and/or by the capping agents. In the silica environment, emission properties are not necessarily the same as the integrated dyes, but their cross-interactions can strongly influence the behaviour of

the whole nanoparticle, opening the way to a wide range of applications and analytical techniques. Steady-state and time-resolved fluorescence and fluorescence anisotropy, for example, can provide information on the rotational mobility of photoactive dyes, on their distance and communication to each other, or on the effect of signal amplification. Moreover the silica matrix protects the segregated species from undesired reactions, preventing the photophysical degradation and a constant chemical environment,[15] and makes possible the use of hydrophobic dyes and molecules, without affecting their desired properties. Last but not least, silica does not show internal toxicity and it does not undergo microbial attack.

2.2.1 DDSNs synthesis

Silica nanoparticles are characterised by simple, low cost and versatile synthetic strategies, which allow a great control over the architecture.
Starting from a solution of monomeric tetraethoxysilane (TEOS), which undergoes a sol-gel process,[16] the formation of different final matrix morphologies depends on catalytic conditions, particles nucleation, growth and confinement. The most common synthetic approaches actually utilized are the ones developed by Stöber[17] and successively implemented by Van Blaaderen to obtain fluorescent NPs.[18] TEOS hydrolysis is promoted by ammonia and water, ethanol is used as a co-solvent and the NPs size (potentially ranging from 10 to several hundred of nanometres) is controlled by components concentration and ratio. By using trialkoxysilane dyes-derivatized, instead of TEOS as silica precursor, photoactive units can be covalently integrated in the system, to prevent their leaching from the nanoparticles (Fig. 2.2).[19,20] In this case, the main problem associated with the DDSNs is the number of molecular dyes that can be integrate, limited by their solubility in the reaction milieu, by the synthetic accessibility of the TEOS derivatives and by the electrostatic interaction between the dye and the negatively charged matrix. The colloidal suspension is stabilized by electrostatic repulsion of the deprotonated Si–OH groups on the NPs surface stabilizes, but their functionalization may leads to aggregation or incomplete surface passivation.
In order to improve the colloidal stability, several protocols have been proposed to confine the silica formation process into nano-containers. In this prospective, the reverse microemulsion methods are usually convenient to include positively charged water soluble dyes,[21-23] easily incorporable into the hydrophilic cores and retained within the silica matrix by electrostatic interactions. Hydrophobic dyes

can be introduced confining the sol-gel process in direct micelles, taking advantage from the lipophilic nature of silica precursors. With big surfactant this leads to core-shell structure.[21,24,25] In most cases, the condensation processes are promoted in acidic environment (using acids as HCl[24] or HOAc[26]) and the hydrolysis has faster kinetics than the condensation (Fig. 2.3).[27] The formation of Si–O–Si chains occurs in the early stages of polymerization,[28] while the cross-linking at the last,[29] hence silica reacts exclusively in the micellar environment forming the NP core, trapping or/and absorbing the surfactants which forms the shell.[30]
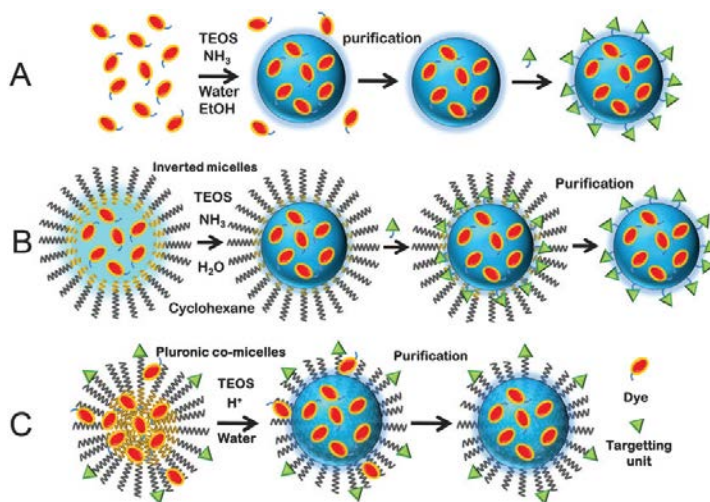
Figure 2.2: Schematic representation of different synthetic strategies to obtain dye-doped silica nanoparticles: Stöber method (A), reverse microemulsion method (B) and direct micelle assisted method (C). Adapted from ref.[7]

$$Si(OEt)_4 \ + \ 4H_2O \ \xrightarrow{\ H^+\ } \ Si(OH)_4 \ + \ 4EtOH \qquad (1)$$

$$Si(OH)_4 \ \xrightarrow{\ H^+\ } \ SiO_2 \ + \ 4H_2O \qquad (2)$$
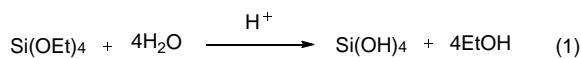
Figure 2.3: Silica nanoparticles formation results from a nucleation-growth process which involves hydrolysis (eq 1) of the TEOS precursor in ethanol followed by condensation (eq 2).[27]

The use of the big surfactant Pluronic F-127 is particularly diffused. This tri-block copolymer, with a poly(ethylene glycol)–poly(propylene glycol)–poly(ethylene glycol) (PEG_x-PPG_y-PEG_x) structure, tends to form stable micelles in water environment with a relatively polar PPO inner core,[31] allowing the formation of

micelles of 22-25 nm diameter,[31] enabling the use of TEOS as silica precursor instead of more lipophilic organoalkoxy silanes. It also contributes to the formation of a more stable and dense silica network, where many alkoxysilane derivatized dyes, in a wild range of hydrophilicity, can be used as doping units. Furthermore, when NPs enters the physiological environment, they get covered by a protein shell, known as "protein corona", which is responsible for the NPs recognition and clearance from the phagocyte system. Coating nanoparticles with PEG (PEGylation), create a hydrophilic surface which results in a significant inhibition of proteins absorption on the NP surfaces and, consequently, as a less recognition by macrophages.

2.2.2 DDSNs for optical imaging

Since DDSN may contain many fluorophores, their molar absorption coefficient (ε) can easily overcomes 10^6 mol^{-1}cm^{-1}. Moreover, silica matrix protection of the segregated dyes can increase their (photo)stability and, in many cases, their luminescence quantum yield Φ. For these reasons, DDSNs generally show high brightness B (B = $\varepsilon \times \Phi$).[32] These aspect and their outstanding colloidal stability, the internal non-toxicity and the well-defined morphological properties make DDSNs particularly suitable materials for developing bright fluorescent labels.[33-35] According to this potentiality, significant efforts have still to be done to overcome some structural problems, in order to optimize their properties and to improve the applicability.

In particular, from the photophysical point of view, nanoparticles properties are strongly influenced by the mutual distributions of fluorophores in the structure. Their uniform distribution, though, is an unrealistic situation, especially for the DDSNs obtained by the Stöber method. Their proximity in highly doped architectures, may induce process of homo- and hetero- energy transfers if they are energetically allowed, and it is usually correlated with a significant decrease of the expected quantum yield.[36] A really powerful feature of the silica nanoparticles, is that they can be engineered to present a large Stokes shift, which facilitates the development of suitable species for bar-coding and multiplexing analysis by a substantial suppression of scattering and Raman effects. This goal can be achieved either by inclusion of commercial fluorophores with intrinsic large Stokes shift, but the options are limited to the number of dyes with this specific feature,[37] or exploiting efficient energy transfer processes between two or more fluorogenic species.[38,39] By the last option, it is possible to obtain a set of nanoparticles

presenting emission of different colours by efficient excitation at the same wavelength[40,41] but either ways, the emission is still broad if compared with the QDs one, and the applicability of this technology is limited.[34] Another important aspect is the absolute number of fluorophores which can be included in the matrix, strongly limited by the reaction conditions. Recent studies proved that this is limited to few units per nanoparticle, which makes really challenging their applications as contrast agents for bioimaging with wide field techniques.

2.2.3 DDSNs functionalization

A really interesting properties of DDSNs is the possibility of functionalize the nanoparticles surface with appropriate functional groups and biomolecules.

This goal can be achieved by non-covalent or covalent interactions. The first approach generally includes physical adsorption or electrostatic interactions and it is generally applied to large molecules such as polymers or proteins (taking advantage from their amphiphatic nature and their tendency to interact non-specifically with the NP surfaces). The link between the NPs and the selected molecules is weaker respect to the one achieved by covalent coupling, which results in more robust conjugates and it is less influenced by external conditions. Silica nanoparticles stand out for the suitability to direct introduction of chemical functionality such as amines,[42] carboxylates,[43] epoxydes[44] and thiols[45] groups, through a large library of commercially available chlorosilane and alkoxysilane. Their versatility in this sense is that significant, that silica has been used as a coating layer for other material NPs more difficult to functionalize.[46]

Core–shell silica NPs functionalization can be also obtained using Pluronic F127 previously functionalized on the hydroxylic tips with –COOH and –NH$_2$ functionalities. This strategy leads to the formation of synthesized NPs with a PEG shell and the desired functional groups usable to obtain NP–oligopeptide conjugates,[47] to achieve efficient cell internalization [48] or to accurately tune the NPs ζ-potential for sentinel lymph node mapping.[49] Any need of post functionalization processes was eliminating and the control over the total number of chemical functionalities per particle was improved.

2.2.4 DDSNs : advantages and disadvantages

All these considerations, played an important role in the design of new systems suitable for bioimaging.

We particularly focused on the variety and simplicity of possible synthetic approaches, the achievable control over the size and shape, the possibility of

functionalize and load the matrix in different positions, such as the shell or the core, with a large number of organic, inorganic and biological moieties. Furthermore, silica nanoparticles precursors and reaction wastes are intrinsically non toxic, the synthesis is simple and the reagents commercially available and cheap, which is a good advantage respect to quantum dots or other expensive inorganic nanoparticles. These was summarized in the synthesis achievable in water environment, using micelles self-assembled by big and stable poloxamer (Pluronic F-127) as nano-containers for the reaction of hydrophobic components.

We also pointed out some limits intrinsic to the system, which cannot be easily overcome without completely changing some significant structural aspects. Silica matrix rigidity strongly limits the number or functionalities that can be introduced, it does not allows a good control over the spatial distribution of these moieties and the controlled degradation of the glassy matrix. These aspects inspired us to move forward, and looking for other structural materials.

2.3 Organic polymeric NPs: amphiphilic copolymer nanoparticles

In the previous paragraph, it was mentioned the use of Pluronic F-127 as self-assembly unit to achieve micellar templated synthesis. Although, this is not the only possible application of amphiphilic block copolymers (BCP)s, which, in recent decades, has attracted significant attention. As it happens with small amphiphile molecules, amphiphilic BCPs self-assemble into a variety of structures in solution[50] but, respect to the former, they typically, show a much lower or non-observable critical micelle concentrations (CMC)s,[51] a greatly improved kinetic stability,[52,53] and demonstrate ease of structure modification or functionalization.[1,54,55] These favourable attributes, along with significant progress in controlled polymerisation techniques,[56-59] have led to amphiphilic BCPs being extensively studied for applications including drug and gene delivery systems,[60] nanoreactors,[61] and nanoelectronics.[62]

In order to direct the polymer synthesis, or to predict the final morphology of the self-assembled structure, an important parameter to take into account is the packing parameter (p). p is related to the volume of the hydrophobic chains (υ), the optimal area of the head group (a_o) and the length of the hydrophobic tail (l_c) by the equation $p = \upsilon/a_o l_c$. It was observed that there is a correlation between the p value and the most common morphology adopted by a block copolymer upon aggregation: if $p \leq \frac{1}{3}$ spherical micelles are favoured, $\frac{1}{3} \leq p \geq \frac{1}{2}$ produces cylinders and $\frac{1}{2} \leq p \leq 1$ results in polymersomes (vesicles), (Fig. 2.3).

$$p = \frac{\upsilon}{a_0 l_c}$$

$< \frac{1}{3}$	$\frac{1}{3} - \frac{1}{2}$	$\frac{1}{2} - 1$	~ 1	> 1
Spherical micelles	Non-spherical micelles	Vesicles or bilayers	Bicontinous plane	Inverted structure
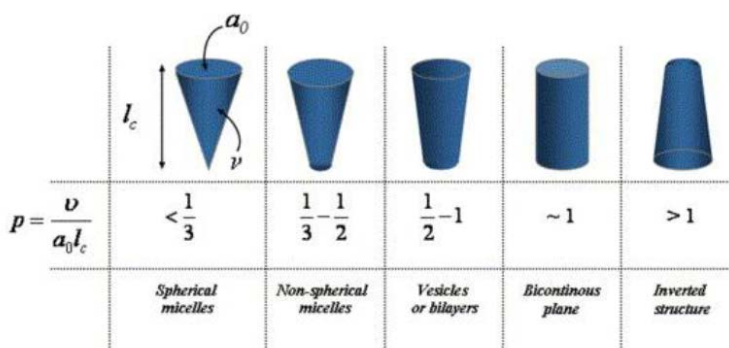
Figure 2.3: Schematic depicting BCP with different packing parameters (p) and their expected morphology upon self-assembly.[63]

It is although important to mention that, if this can serve as a useful guide for predicting the predominant structure that one block copolymer should form, multiple structures can take place depending on different preparation conditions. A systematic study to better understand this phenomena was carried out by Eisenberg on PS410-*b*-PAA polymer.[53] He has shown that the same macromolecule with packing parameter indicative of polymersome formation, is capable of forming spheres, polymersomes and multilamellar structures (called large compound vesicles, LCV), by adding different amounts of hydrochloric acid to the solution during self- assembly,[64] and it can be altered by the exact nature of the solvent mixture, polymer concentration, and other additives (e.g. homopolymer or surfactants).[65]

The reason for this complexity is that a number of thermodynamic and kinetic factors affects the morphology of the polymer assemblies, including the degree of stretching in the core block, the interfacial tension between the micelle core and the solvent outside the core, and repulsive forces between the corona chains.[66] Furthermore, as many polymeric micelles can be considered 'frozen' (i.e. no exchange of unimers over an appreciable time scale) it is therefore possible to kinetically trap various structures depending on the preparation method (Fig. 2.4).[66,67]

Typically, BCP assemblies are performed by the solvent switch method, which consists in the dissolution of the copolymer in a good solvent for both blocks, followed by addition of a selective solvent (typically water) in order to induce self-assembly. Eisenberg also showed that for PS310-*b*-PAA[68] either spheres, cylinders, or vesicles could be reversibly obtained at different concentrations of water. This

indicates that, in the formation of vesicles by this method, spheres and cylinders are formed as intermediate structures.[65]

Adams and co-workers studied the self-assembly mechanism of a pH responsive block copolymer in a polymerosome. They found that forming the polymerosomes by a pH switch method resulted in a different formation mechanism (through some disordered aggregates), which precluded the encapsulation of a hydrophilic guest.[69] These results indicate not only that the final morphology can be difficult to predict, but that the mechanism of the self-assembly can impact both the final structure and its performance in the desired application.

From these studies it can be deducted that, even when the BCP are formed, they cannot simply be considered frozen and this has to be take into account in the applicative prospective.[67] It has to be underlined that no exchange will occur if the polymer core is glassy (i.e. the temperature is below the polymer Tg), but if the polymer core is above its Tg, a number of factors will affect whether or not exchange can occur. This includes the interfacial tension between the core block and the solvent, the temperature, the core block length and the core block architecture. Even if this discussion of dynamics raises an important point on nomenclature (a polymer aggregate should only be called a 'micelle' if dynamic equilibrium has been reached, whereas 'nanoparticle' is more appropriate for a kinetically trapped system) investigating dynamics is not always simple and for many systems it is unknown whether unimers exchange or not.
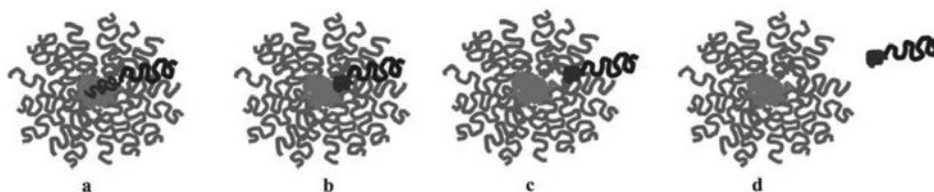
Figure 2.4: Schematic representation of the escape of a unimer from a polymeric micelle. The sovophobic block, which is somewhat stretched within the core (a) first has to disentangle from the core and form a condensed blob at the core-corona interface (b). Then the polymer has to diffuse through the corona (c) in order to completely liberate itself from the micelle (d).[67]

Despite spheres, cylinders and polymersomes are actually dominating the literature for di-block copolymers, it is important to mention that the formation of other morphologies are possible, especially when the complexity of the polymeric units increases[70-73] or when a variety of groups such as metal complexes,[74,75] enzymes,[76] or drugs[1] are included or encapsulated in polymers.

All these aspects turned to be particularly important in our work, most of all considering that the purpose of developing not rigid nanoparticles, where external parameters can control the stability of the whole structure. This means that the design of the polymer, the control over the monodispersity of the molecular composition and the understanding of the phenomena which may affect the organization of the nanoparticles in different condition, are crucial to achieve our goal.

2.4 Synthetic approaches

All the previous considerations directly lead to the conclusion that synthetic approaches, able to obtain homogeneous polymeric materials under controlled chemical conditions, have to be investigated and carefully chosen. Among the possibility, two known strategies described below were chosen to obtain different materials. The former one, the ring-opening metathesis, proved to be a great candidate for the synthesis of block copolymers with highly controlled composition, able to self-assembly in defined morphologies. The latter, the epoxy resins synthesis, was adopted to modify the direct micellar templated synthesis of nanoparticles, and to take advantages of the aggregation and disaggregation of shorter polymers.

2.4.1 Synthesis of amphiphilic copolymer: ROMP

Ring-opening metathesis polymerization (ROMP),[77,78] is a chain growth polymerization process, where a mixture of cyclic olefins is converted into a polymeric material[79] by a unique metal-mediated carbon–carbon double bond exchange process.[80] In this mechanism, any unsaturation associated with the monomer is conserved in the polymer, distinguishing ROMP from typical olefin addition polymerizations.

In general, ROMP initiation begins with the coordination of a transition metal alkylidene complex to a cyclic olefin. A subsequent [2+2]-cycloaddition affords a four-membered metallacyclobutane intermediate, which effectively forms the beginning of a growing polymer chain. This intermediate undergoes a cycloreversion reaction, to afford a new metal alkylidene with an increased size, caused by the incorporated monomer, but with the same reactivity toward cyclic olefins respect to the initiator. These steps are repeated during the propagation stage until polymerization ceases (i.e. all monomer is consumed, a reaction equilibrium is reached, or the reaction is terminated), (Fig. 2.5).
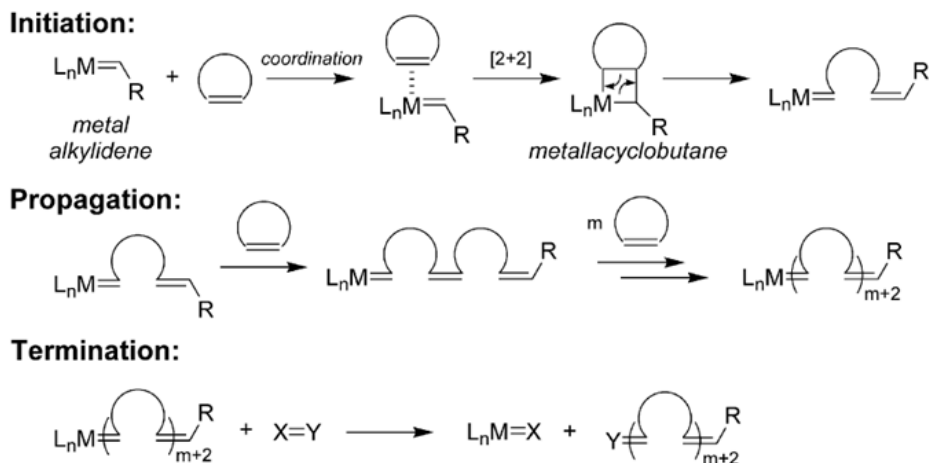
Figure 2.5: Schematic representation of a general mechanism of a typical ROMP reaction.[77]

To properly perform the reaction, some aspects are worthy to be mentioned:

- the propagating metal centres on the growing polymer chains may exist in either the metallacyclobutane or metal alkylidene form, the difference depends on the catalyst and on the reaction conditions;

- they are generally reversible, like most olefin metathesis reactions;

- they are equilibrium-controlled and the position of the equilibrium (monomer vs. polymer) can be predicted by considering the thermodynamics of the polymerization.

The reaction driving force is the release of strain associated with the cyclic olefin, balanced by entropic penalties. For this reason, the most common monomers used in ROMP are cyclic olefins, with considerable degree of strain (45 kcal/mol) such as cyclobutene, cyclopentene, cis-cyclooctene and norbornene.[81] Accordingly, the temperature and concentration at which the ROMP reaction is conducted has strong influences over the outcome of the reaction. In general, the most favourable condition for a successful ROMP reaction is the highest monomer concentration at the lowest temperature possible. In addition, to the general ROMP mechanism, equilibria can be established via other pathways, including intermolecular or intramolecular chain-transfer reactions, and propensity to form cyclic oligomers,[82] which collectively are responsible for the broadening of the molecular weight distribution (or polydispersity) of the system. Even if these side reactions may be advantageous in some cases, they challenge the realization of monodispersed and controlled polymer. For this reason, it was studied the 'living ring-opening

metathesis polymerization', where the polymerization proceeds without chain transfer or termination.[83,84]

In living polymerization the molecular weight during the reaction is directly proportional to the monomer conversion, since all chains ends grow at essentially the same rate, differently from condensation or kinetically-controlled polymerizations, where high molecular weight is achieved only at very high conversion rate and relatively early stages respectively. As a result, Gold et al. demonstrated that even when the rate of propagation is orders of magnitude greater than the rate of initiation, a living polymerization can lead to polymers with low polydispersities.[85] However, in systems where the rate of initiation is faster or similar to the rate of propagation, control over the polymerization is obtained at an earlier stage. Under these conditions, access to well defined, monodispersed materials of low molecular weight is possible. According with that, a ROMP reaction can be considered 'living controlled' if it is characterized by a fast and complete initiation (1), exhibits a linear relationship between the degree of polymerization (typically measured as the number-average molecular weight of the polymer, Mn) and monomer consumption (2), and PDIs < 1.5 (3).[86]

Considering the metal-mediated and equilibrium nature of most ROMP reactions, it becomes apparent that very special metathesis catalysts are needed to satisfy the requirements. The catalyst should, in fact, converts to growing polymer chains quantitatively and rapidly (i.e. exhibit fast initiation kinetics), mediates the polymerization without an appreciable amount of intramolecular or intermolecular chain-transfers or premature terminations, and reacts with accessible terminating agents to facilitate selective end-functionalization. For practical reasons, it is advantageous if the catalyst displays a good solubility in common organic solvents, or in aqueous media, and shows high stability toward moisture, air, and common organic functional groups. Among the numerous complexes based on titanium, tantalum, tungsten and molybdenum studied as catalysts, the most versatile turned out to be the ruthenium based ones, and, in particular, the Grubbs second generation ones, (IMesH2)(C5H5N)2(Cl)2Ru=CHPh. (Fig. 2.6)
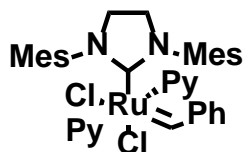
Figure 2.6: structure of Ru alkylidene(IMesH2)(C5H5N)2(Cl)2Ru=CHPh.[87]

A great capability of ROMP is to allow the direct incorporation of functional groups in the polymer backbone during the polymerization itself, preventing the need for subsequent low yielding and difficult to characterize *graft-to* reactions on macromolecules or at particle surfaces. By living ROMP polymerization, functionalities can be introduced into polymers either by the use of an initiator containing functional alkilidene, the use of strained olefin-based monomers containing various functionalities or the use of functionalized termination (or chain transfer) agents.[87]

The easiest deployed method for preparing functional polymers is through the use of monomers that contain the desired functionality or allow for its incorporation via a post-polymerization modification. In addition, the use of functionalized termination agents that allow end-labelling of polymers has garnered increasing attention.[88,89] By contrast, specially functionalized initiators are underutilized,[90-92] most likely because changes to the initiator structure can result in changes to the initiation and propagation rates and hence overall polymer quality and predictability in synthesis. Herein, each of these approaches are assessed and utilized for the preparation of micellar nanoparticles assembled from fluorescently labelled amphiphilic block copolymers.

In order to developer monomers that contain the required moiety, it is possible to use a molecule which contains a polymerizable unit and which can easily react with a variety of functional groups. To this end, polymerizable norbornene moieties derived from commercially available *cis*-5-norbornene-*exo*-2,3-dicarboxylic anhydride or 5-norbornene-2-carboxylic acid (Fig. 2.7), are widely used by Gianneschi et al.[87] This strategy allows to synthesize a vast variety of different monomers and to introduce into the polymer backbone almost every kind of functional group.

Figure 2.7: Molecular structures of cis-5-norbornene-exo-2,3-dicarboxylic anhydride (left) or 5-norbornene-2-carboxylic acid (right), commonly used as starting material for the preparation of polymerizable moieties variously functionalized. This strategy allows to efficiently introduce a variety of different functional group into the polymer backbone.

ROMP polymerization, in conclusion, proved to be a powerful tool to the synthesis of polymers and block copolymers with a great molecular weight monodispersity. Moreover it makes smartly possible the inclusion of different moieties, with various reactivity and functionalities. It allows great control over the ratio of the different blocks, making possible the production of almost any kind of self-assembled structures, by varying the starting material composition and the aggregation conditions. However, this variability has to be accurately control, since it can turn to be a limit to the system reproducibility.

2.4.2 Epoxy resins

If the ring-opening metathesis is widely utilized in nanomedicine, thanks to the outstanding properties of the achievable materials, epoxy-resins reactions have been . utilized for numerous application, without actually exploring their potentiality in theranostic.

Epoxy resins are a class of reactive pre-polymers and polymers containing epoxy group,

which may be cross-linked to obtain materials characterized by high specific stiffness, high specific strength, electrical insulating properties, corrosion resistance, chemical compatibility with reinforcing fibers, and relative ease-of-manufacture. This thermosetting polymers are hence widely used in adhesives, paints, coatings, medical implants, electrical devices and as a matrix material in fibrous composites for the aerospace and wind turbine industries.[93] Nevertheless, it is not particularly surprising that, except for few examples, they have not found application in nanoparticles production. The most common precursor of these resins, the Bisphenol A diglycidyl ether, in fact, was proved to be neuro- and cyto-toxic and the uncontrolled diffusion into the biological environment can cause damage even in low dosage and time exposure. This intrinsic limit, anyway, can be overcome by controlling the polymerization conversion grade and avoiding the leaking from the formed material into the environment. Furthermore, this should not limit its use in *in-vitro* imaging or as a model material for new proof of concept systems.

In this prospective, nanoparticles based on epoxy resins materials have been developed and studied, controlling their behaviour and avoiding the toxic effect.

2.4.3 Bisphenol A diglycidyl ether reactivity

Bisphenol A diglycidyl ether (DGEBA) is the most popular epoxy monomers and it is derived from the reaction of bis-(4-hydroxy phenylene)-2,2 propane

(Bisphenol A) with 1-chloroprene 2-oxide (epichlorohydrin) in the presence of sodium hydroxide. The resin structure and its condensed forms, depends on the stoichiometry of the reactants and resins are marketed with an 'n' value (percentage of epoxy functionalities) lying in the range 0.03-10. At room temperature, these materials are usually crystalline solids for n close to zero, liquids for n up to 0.5 and amorphous solids (glass transition temperature, (Tg) ranging between ~40–90°C) for higher n values.

Epoxy monomers are usually used for the synthesis of linear and cross linked polymer, achievable by their reaction whit co-monomers and/or initiators, either by chain or step growth polymerization mechanism. Depending on the conditions, the polymerization may occur through a combination of both mechanisms. Interestingly from our point of view, epoxy groups can react with amines, phenols, mercaptans, isocyanates or acids, where amines are the most commonly used curing agents/hardeners for epoxides. In this case, reaction is mainly described by the step-growth polymerizations, which follows the SN2-type II mechanism (thus the reaction rate obeys second-order kinetics), as reported in figure 2.8. It may involve both primary and secondary amines both as hydrogen-bonding catalysts, since it shows a considerable effect on the activation barrier of the curing reaction and promoters. Primary amines react twice with an epoxy molecule to form tertiary amines and their reactivity increase with their nucleophilic character.
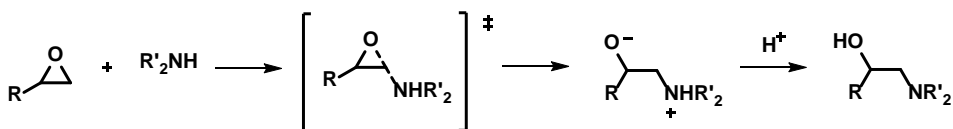
Figure 2.8: General mechanism for epoxy-amine curing. The first step is assumed to be the rate determining step, and the proton transfer is fast compared to the nucleophilic attack.

Despite the simplicity of the reactants, a number of several possible pathways may occur during the curing process. The reaction, in fact, is known to be catalyzed by hydroxyl groups, trough the formation of a tri-molecular complex which facilitates the attack of the amino group, or by other impurities. Moreover, a secondary alcohol is continuously generated and epoxy-amine reaction is autocatalysed.

Epoxy can react with primary or secondary amino groups, as showed in figure 2.9 (top and middle respectively). Usually when the concentration of epoxy groups is equal to or lower than the concentration of NH groups, side reactions do not take place. When there is an excess of epoxy groups or when the secondary amino

groups have a low reactivity, a third reaction can compete with the two previous ones (Fig. 2.9, bottom).Epoxy–hydroxy reaction (etherification) modifies the initial stoichiometric ratio based on epoxy to amino hydrogen groups.

This reaction allow to actually introduce, into the polymeric resins, different functionalities, such as fluorogenic or stimuli responsive units, with amine, phenols, mercaptans, isocyanates or acids terminations, prone to react with the epoxy rings. Furthermore, respect to the silica matrix, by playing with different parameters it is possible to modulate the n value, and control the grade of polymerization.

From this considerations, came out the idea of implementing this reaction into the micellar core of the Pluronic F-127, to obtain core shell nanoparticles with a epoxy resins core and a PEG shell.
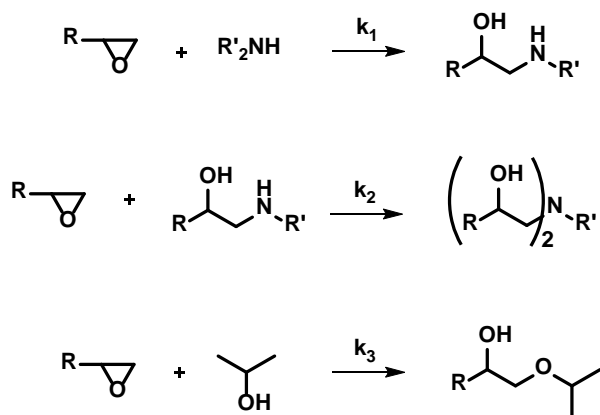
Figure 2.9: Schematic reaction mechanism of the epoxy rings with the primary (top) and secondary (middle) amino groups, kinetically described by the constant k_1 and k_2 respectively. When the second amine has a low reactivity, the etherification may compete with the resin formation and modify the initial stoichiometric ratio.

2.5 Conclusion and prospective

Nanoparticles able to self-assemble under specific condition, or either to be cross-linked with different controlled efficiency, promise to be suitable not only as multifunctional, but also as stimuli-responsive nano-systems. The response either to environmental or external solicitations can be, in fact, achieved by exploiting the same inter-components interactions that drives their assembly, meaning that self-assembled systems are, at least potentially, intrinsically responsive. For this reason, self-assembly of molecular and nanostructured building blocks, is undoubtedly one of the most versatile, straightforward and powerful strategy to achieve stimuli-responsive materials.[94-101]

Considered the nature of the interactions involved in supramolecular[102-105] and hetero-supramolecular[106-111] assembly (hydrogen bond, electrostatic attraction, hydrophobic effect, π-π stacking, electronic charge-transfer, etc.),[112,113] an interesting variety of elemental processes, including protonation-deprotonation, oxidation-reduction and polarity changes, can be easily exploited to trigger system aggregation and disaggregation.[114-116] Moreover, self-assembled aggregates can be destabilized by temperature fluctuations or upon selective irradiation of light or microwave, when absorbing components are included in the architectures.[117-123] This means that the functionality of stimuli-responsive materials can be extended, by designing systems sensitive to different kinds of solicitations, multi-responsive nano-materials.

Bibliography

1   Elsabahy, M. & Wooley, K. L. Design of polymeric nanoparticles for biomedical delivery applications. *Chemical Society Reviews* **41**, 2545-2561, doi:10.1039/C2CS15327K (2012).

2   Elsabahy, M., Heo, G. S., Lim, S.-M., Sun, G. & Wooley, K. L. Polymeric Nanostructures for Imaging and Therapy. *Chemical Reviews* **115**, 10967-11011, doi:10.1021/acs.chemrev.5b00135 (2015).

3   Rampazzo, E. *et al.* Energy Transfer from Silica Core– Surfactant Shell Nanoparticles to Hosted Molecular Fluorophores†. *The Journal of Physical Chemistry B* **114**, 14605-14613 (2010).

4   Kang, N. *et al.* Stereocomplex block copolymer micelles: core-shell nanostructures with enhanced stability. *Nano letters* **5**, 315-319 (2005).

5   Cui, H., Chen, Z., Zhong, S., Wooley, K. L. & Pochan, D. J. Block copolymer assembly via kinetic control. *Science* **317**, 647-650 (2007).

6   Yang, C. *et al.* Supramolecular nanostructures designed for high cargo loading capacity and kinetic stability. *Nano Today* **5**, 515-523 (2010).

7   Bonacchi, S. *et al.* Luminescent silica nanoparticles: extending the frontiers of brightness. *Angewandte Chemie International Edition* **50**, 4056-4066 (2011).

8   Genovese, D. *et al.* Prevention of Self-Quenching in Fluorescent Silica Nanoparticles by Efficient Energy Transfer. *Angewandte Chemie International Edition* **52**, 5965-5968 (2013).

9   Arap, W. *et al.* Luminescent silica nanoparticles for cancer diagnosis. *Current medicinal chemistry* **20**, 2195 (2013).

10   Piao, Y., Burns, A., Kim, J., Wiesner, U. & Hyeon, T. Designed Fabrication of Silica-Based Nanostructured Particle Systems for Nanomedicine Applications. *Advanced Functional Materials* **18**, 3745-3758 (2008).

11   Montalti, M., Rampazzo, E., Zaccheroni, N. & Prodi, L. Luminescent chemosensors based on silica nanoparticles for the detection of ionic species. *New Journal of Chemistry* **37**, 28-34 (2013).

12   Bardhan, R., Lal, S., Joshi, A. & Halas, N. J. Theranostic nanoshells: from probe design to imaging and treatment of cancer. *Accounts of chemical research* **44**, 936-946 (2011).

13   Chen, Y., Chen, H. & Shi, J. In Vivo Bio-Safety Evaluations and Diagnostic/Therapeutic Applications of Chemically Designed Mesoporous Silica Nanoparticles. *Advanced Materials* **25**, 3144-3176 (2013).

14   Lee, J. E., Lee, N., Kim, T., Kim, J. & Hyeon, T. Multifunctional mesoporous silica nanocomposite nanoparticles for theranostic applications. *Accounts of chemical research* **44**, 893-902 (2011).

15   Montalti, M., Prodi, L., Rampazzo, E. & Zaccheroni, N. Dye-doped silica nanoparticles as luminescent organized systems for nanomedicine. *Chemical Society Reviews* **43**, 4243-4268, doi:10.1039/C3CS60433K (2014).

16   Hench, L. L. & West, J. K. The sol-gel process. *Chemical Reviews* **90**, 33-72 (1990).

17   Stöber, W., Fink, A. & Bohn, E. Controlled growth of monodisperse silica spheres in the micron size range. *Journal of colloid and interface science* **26**, 62-69 (1968).

18   Van Blaaderen, A. & Vrij, A. Synthesis and characterization of colloidal dispersions of fluorescent, monodisperse silica spheres. *Langmuir* **8**, 2921-2931 (1992).

19   Van Blaaderen, A., Imhof, A., Hage, W. & Vrij, A. Three-dimensional imaging of submicrometer colloidal particles in concentrated suspensions using confocal scanning laser microscopy. *Langmuir* **8**, 1514-1517 (1992).

20   Verhaegh, N. A. & Blaaderen, A. v. Dispersions of rhodamine-labeled silica spheres: synthesis, characterization, and fluorescence confocal scanning laser microscopy. *Langmuir* **10**, 1427-1438 (1994).

21   Zanarini, S. *et al.* Iridium Doped Silica–PEG Nanoparticles: Enabling Electrochemiluminescence of Neutral Complexes in Aqueous Media. *Journal of the American Chemical Society* **131**, 14208-14209, doi:10.1021/ja906666e (2009).

22   Wang, L., Lofton, C., Popp, M. & Tan, W. Using luminescent nanoparticles as staining probes for Affymetrix GeneChips. *Bioconjugate chemistry* **18**, 610-613 (2007).

23   Wang, L., Zhao, W., O'Donoghu, M. B. & Tan, W. Fluorescent nanoparticles for multiplexed bacteria monitoring. *Bioconjugate chemistry* **18**, 297-301 (2007).

24   Huo, Q. *et al.* A new class of silica cross-linked micellar core-shell nanoparticles. *Journal of the American Chemical Society* **128**, 6447-6453 (2006).

25   Chi, F., Guan, B., Yang, B., Liu, Y. & Huo, Q. Terminating Effects of Organosilane in the Formation of Silica Cross-Linked Micellar Core– Shell

Nanoparticles. *Langmuir* **26**, 11421-11426 (2010).

26   Rampazzo, E. *et al.* Multicolor core/shell silica nanoparticles for in vivo and ex vivo imaging. *Nanoscale* **4**, 824-830 (2012).

27   Rampazzo, E., Bonacchi, S., Montalti, M., Prodi, L. & Zaccheroni, N. Self-organizing core-shell nanostructures: spontaneous accumulation of dye in the core of doped silica nanoparticles. *Journal of the American Chemical Society* **129**, 14251-14256 (2007).

28   Cushing, B. L., Kolesnichenko, V. L. & O'Connor, C. J. Recent advances in the liquid-phase syntheses of inorganic nanoparticles. *Chemical reviews* **104**, 3893-3946 (2004).

29   Gallagher, D. & Ring, T. Sol--Gel Processing of Ceramic Films. *Chimia* **43**, 298-304 (1989).

30   Chi, F., Guo, Y.-N., Liu, J., Liu, Y. & Huo, Q. Size-Tunable and Functional Core– Shell Structured Silica Nanoparticles for Drug Release. *The Journal of Physical Chemistry C* **114**, 2519-2523 (2010).

31   Desai, P., Jain, N., Sharma, R. & Bahadur, P. Effect of additives on the micellization of PEO/PPO/PEO block copolymer F127 in aqueous solution. *Colloids and Surfaces A: Physicochemical and Engineering Aspects* **178**, 57-69 (2001).

32   Prodi, L. Luminescent chemosensors: from molecules to nanoparticles. *New journal of chemistry* **29**, 20-31 (2005).

33   Burns, A., Ow, H. & Wiesner, U. Fluorescent core–shell silica nanoparticles: towards "Lab on a Particle" architectures for nanobiotechnology. *Chemical Society Reviews* **35**, 1028-1042 (2006).

34   Wang, L. *et al.* Watching silica nanoparticles glow in the biological world. *Analytical Chemistry* **78**, 646-654 (2006).

35   Estévez, M.-C., O'Donoghue, M. B., Chen, X. & Tan, W. Highly fluorescent dye-doped silica nanoparticles increase flow cytometry sensitivity for cancer cell monitoring. *Nano Research* **2**, 448-461 (2009).

36   Montalti, M. *et al.* Energy transfer in fluorescent silica nanoparticles. *Langmuir* **20**, 2989-2991 (2004).

37   Herz, E., Burns, A., Bonner, D. & Wiesner, U. Large Stokes-Shift Fluorescent Silica Nanoparticles with Enhanced Emission Over Free Dye for Single Excitation Multiplexing. *Macromolecular rapid communications* **30**, 1907-1910 (2009).

38   Wu, C. *et al.* Fluorescent core-shell silica nanoparticles as tunable

precursors: towards encoding and multifunctional nano-probes. *Chemical Communications*, 750-752 (2008).

39   Fedorenko, S. V. *et al.* Dual visible and near-infrared luminescent silica nanoparticles. Synthesis and aggregation stability. *The Journal of Physical Chemistry C* **114**, 6350-6355 (2010).

40   Wang, L. & Tan, W. Multicolor FRET Silica Nanoparticles by Single Wavelength Excitation. *Nano Letters* **6**, 84-88, doi:10.1021/nl052105b (2006).

41   Chen, X. *et al.* Using aptamer-conjugated fluorescence resonance energy transfer nanoparticles for multiplexed cancer cell monitoring. *Analytical chemistry* **81**, 7009-7014 (2009).

42   Kumar, R. *et al.* Covalently dye-linked, surface-controlled, and bioconjugated organically modified silica nanoparticles as targeted probes for optical imaging. *Acs Nano* **2**, 449-456 (2008).

43   Chen, Z.-Z., Cai, L., Dong, X.-M., Tang, H.-W. & Pang, D.-W. Covalent conjugation of avidin with dye-doped silica nanopaticles and preparation of high density avidin nanoparticles as photostable bioprobes. *Biosensors and Bioelectronics* **37**, 75-81 (2012).

44   Wu, Y., Chen, C. & Liu, S. Enzyme-functionalized silica nanoparticles as sensitive labels in biosensing. *Analytical chemistry* **81**, 1600-1607 (2009).

45   Kobler, J., Möller, K. & Bein, T. Colloidal suspensions of functionalized mesoporous silica nanoparticles. *Acs Nano* **2**, 791-799 (2008).

46   Smith, J. E., Wang, L. & Tan, W. Bioconjugated silica-coated nanoparticles for bioseparation and bioanalysis. *Trac Trends in Analytical Chemistry* **25**, 848-855 (2006).

47   Soster, M. *et al.* Targeted dual-color silica nanoparticles provide univocal identification of micrometastases in preclinical models of colorectal cancer. *International journal of nanomedicine* **7**, 4797 (2012).

48   Rampazzo, E. *et al.* Proper design of silica nanoparticles combines high brightness, lack of cytotoxicity and efficient cell endocytosis. *Nanoscale* **5**, 7897-7905 (2013).

49   Helle, M. *et al.* Surface chemistry architecture of silica nanoparticles determine the efficiency of in vivo fluorescence lymph node mapping. *ACS nano* **7**, 8645-8657 (2013).

50   Holmberg, K., Jönsson, B., Kronberg, B. & Lindman, B. *Surfactants and polymers in aqueous solution*. (Wiley, 2003).

51   Johnson, B. K. & Prud'homme, R. K. Mechanism for rapid self-assembly of block copolymer nanoparticles. *Physical review letters* **91**, 118302 (2003).

52   Zana, R., Marques, C. & Johner, A. Dynamics of micelles of the triblock copolymers poly (ethylene oxide)–poly (propylene oxide)–poly (ethylene oxide) in aqueous solution. *Advances in colloid and interface science* **123**, 345-351 (2006).

53   Bermudez, H., Brannan, A. K., Hammer, D. A., Bates, F. S. & Discher, D. E. Molecular weight dependence of polymersome membrane structure, elasticity, and stability. *Macromolecules* **35**, 8203-8208 (2002).

54   O'Reilly, R. K., Hawker, C. J. & Wooley, K. L. Cross-linked block copolymer micelles: functional nanostructures of great potential and versatility. *Chemical Society Reviews* **35**, 1068-1083 (2006).

55   O'Reilly, R. K., Joralemon, M. J., Wooley, K. L. & Hawker, C. J. Functionalization of micelles and shell cross-linked nanoparticles using click chemistry. *Chemistry of materials* **17**, 5976-5988 (2005).

56   Benoit, D., Chaplinski, V., Braslau, R. & Hawker, C. J. Development of a universal alkoxyamine for "living" free radical polymerizations. *Journal of the American Chemical Society* **121**, 3904-3920 (1999).

57   Kamigaito, M., Ando, T. & Sawamoto, M. Metal-catalyzed living radical polymerization: discovery and developments. *The Chemical Record* **4**, 159-175 (2004).

58   Lee, C.-U., Smart, T. P., Guo, L., Epps III, T. H. & Zhang, D. Synthesis and characterization of amphiphilic cyclic diblock copolypeptoids from n-heterocyclic carbene-mediated zwitterionic polymerization of n-substituted n-carboxyanhydride. *Macromolecules* **44**, 9574-9585 (2011).

59   Moad, G., Rizzardo, E. & Thang, S. H. Radical addition–fragmentation chemistry in polymer synthesis. *Polymer* **49**, 1079-1131 (2008).

60   Blanazs, A., Armes, S. P. & Ryan, A. J. Self-assembled block copolymer aggregates: from micelles to vesicles and their biological applications. *Macromolecular Rapid Communications* **30**, 267-277 (2009).

61   Kim, K. T., Meeuwissen, S. A., Nolte, R. J. & van Hest, J. C. Smart nanocontainers and nanoreactors. *Nanoscale* **2**, 844-858 (2010).

62   Lazzari, M., Liu, G. & Lecommandoux, S. *Block copolymers in nanoscience.* (John Wiley & Sons, 2007).

63   Rodriguez-Hernandez, J., Chécot, F., Gnanou, Y. & Lecommandoux, S. Toward 'smart'nano-objects by self-assembly of block copolymers in

solution. *Progress in Polymer Science* **30**, 691-724 (2005).

64   Zhang, L. & Eisenberg, A. Multiple Morphologies and Characteristics of "Crew-Cut" Micelle-like Aggregates of Polystyrene-b-poly(acrylic acid) Diblock Copolymers in Aqueous Solutions. *Journal of the American Chemical Society* **118**, 3168-3181, doi:10.1021/ja953709s (1996).

65   Choucair, A. & Eisenberg, A. Control of amphiphilic block copolymer morphologies using solution conditions. *The European Physical Journal E* **10**, 37-44 (2003).

66   Gale, P. A. & Haynes, C. J. *Anion Receptors Containing Heterocyclic Rings*. (Wiley Online Library, 2012).

67   Nicolai, T., Colombani, O. & Chassenieux, C. Dynamic polymeric micelles versus frozen nanoparticles formed by block copolymers. *Soft Matter* **6**, 3111-3118 (2010).

68   Cotanda, P. & O'Reilly, R. K. Molecular recognition driven catalysis using polymeric nanoreactors. *Chemical Communications* **48**, 10280-10282 (2012).

69   Adams, D. J., Adams, S., Atkins, D., Butler, M. F. & Furzeland, S. Impact of mechanism of formation on encapsulation in block copolymer vesicles. *Journal of Controlled Release* **128**, 165-170 (2008).

70   Parry, A. L., Bomans, P. H., Holder, S. J., Sommerdijk, N. A. & Biagini, S. C. Cryo Electron Tomography Reveals Confined Complex Morphologies of Tripeptide-Containing Amphiphilic Double-Comb Diblock Copolymers. *Angewandte Chemie* **120**, 8991-8994 (2008).

71   Chen, Z. *et al.* Unique toroidal morphology from composition and sequence control of triblock copolymers. *Journal of the American Chemical Society* **127**, 8592-8593 (2005).

72   Li, Z. *et al.* Disk morphology and disk-to-cylinder tunability of poly (acrylic acid)-b-poly (methyl acrylate)-b-polystyrene triblock copolymer solution-state assemblies. *Langmuir* **21**, 7533-7539 (2005).

73   Mori, H. & Müller, A. H. New polymeric architectures with (meth) acrylic acid segments. *Progress in Polymer Science* **28**, 1403-1439 (2003).

74   Moughton, A. O. & O'Reilly, R. K. Using Metallo-Supramolecular Block Copolymers for the Synthesis of Higher Order Nanostructured Assemblies. *Macromolecular rapid communications* **31**, 37-52 (2010).

75   Gohy, J.-F. Metallo-supramolecular block copolymer micelles. *Coordination Chemistry Reviews* **253**, 2214-2225 (2009).

76   van Dongen, S. F., Nallani, M., Cornelissen, J. J., Nolte, R. J. & van Hest, J. A Three-Enzyme Cascade Reaction through Positional Assembly of Enzymes in a Polymersome Nanoreactor. *Chemistry-A European Journal* **15**, 1107-1114 (2009).

77   Bielawski, C. W. & Grubbs, R. H. Living ring-opening metathesis polymerization. *Progress in Polymer Science* **32**, 1-29, doi:http://dx.doi.org/10.1016/j.progpolymsci.2006.08.006 (2007).

78   Devaraj, N. K. & Weissleder, R. Biomedical applications of tetrazine cycloadditions. *Accounts of chemical research* **44**, 816-827 (2011).

79   Wagener, K. *et al.* Kinetics of acyclic diene metathesis (ADMET) polymerization. Influence of the negative neighboring group effect. *Macromolecules* **30**, 7363-7369 (1997).

80   Calderon, N., Ofstead, E. & Judy, W. Mechanistic aspects of olefin metathesis. *Angewandte Chemie International Edition in English* **15**, 401-409 (1976).

81   Benson, S. W. *et al.* Additivity rules for the estimation of thermochemical properties. *Chemical Reviews* **69**, 279-324 (1969).

82   Jacobson, H., Beckmann, C. O. & Stockmayer, W. H. Intramolecular Reaction in Polycondensations. II. Ring-Chain Equilibrium in Polydecamethylene Adipate. *The Journal of Chemical Physics* **18**, 1607-1612 (1950).

83   SZWARC, M. 'Living'polymers. (1956).

84   Darling, T. R. *et al.* Living polymerization: Rationale for uniform terminology. *Journal of Polymer Science Part A: Polymer Chemistry* **38**, 1706-1708 (2000).

85   Gold, L. Statistics of polymer molecular size distribution for an invariant number of propagating chains. *The Journal of Chemical Physics* **28**, 91-99 (1958).

86   Webster, O. W. Living polymerization methods. *Science* **251**, 887-893 (1991).

87   Thompson, M. P. *et al.* Labelling polymers and micellar nanoparticles via initiation, propagation and termination with ROMP. *Polymer Chemistry* **5**, 1954-1964, doi:10.1039/C3PY01338C (2014).

88   Chen, B., Metera, K. & Sleiman, H. F. Biotin-terminated ruthenium bipyridine ring-opening metathesis polymerization copolymers: Synthesis and self-assembly with streptavidin. *Macromolecules* **38**, 1084-1090 (2005).

89   Rush, A. M., Thompson, M. P., Tatro, E. T. & Gianneschi, N. C. Nuclease-resistant DNA via high-density packing in polymeric micellar nanoparticle coronas. *ACS nano* **7**, 1379-1387 (2013).

90   Castle, T. C., Hutchings, L. R. & Khosravi, E. Synthesis of block copolymers by changing living anionic polymerization into living ring opening metathesis polymerization. *Macromolecules* **37**, 2035-2040 (2004).

91   Schwab, P., Grubbs, R. H. & Ziller, J. W. Synthesis and Applications of RuCl2 (CHR')(PR3) 2: The Influence of the Alkylidene Moiety on Metathesis Activity. *Journal of the American Chemical Society* **118**, 100-110 (1996).

92   Ambade, A. V., Yang, S. K. & Weck, M. Supramolecular ABC triblock copolymers. *Angewandte Chemie International Edition* **48**, 2894-2898 (2009).

93   Odegard, G. M. & Bandyopadhyay, A. Physical aging of epoxy polymers and their composites. *Journal of Polymer Science Part B: Polymer Physics* **49**, 1695-1716, doi:10.1002/polb.22384 (2011).

94   Aida, T., Meijer, E. W. & Stupp, S. I. Functional Supramolecular Polymers. *Science* **335**, 813-817, doi:10.1126/science.1205962 (2012).

95   Chen, B., Xiang, S. & Qian, G. Metal-Organic Frameworks with Functional Pores for Recognition of Small Molecules. *Accounts of Chemical Research* **43**, 1115-1124, doi:10.1021/ar100023y (2010).

96   Lehn, J. M. Perspectives in supramolecular chemistry - from molecular recognition towards molecular information-processing and self-organization. *Angewandte Chemie-International Edition in English* **29**, 1304-1319, doi:10.1002/anie.199013041 (1990).

97   Lingwood, D. & Simons, K. Lipid Rafts As a Membrane-Organizing Principle. *Science* **327**, 46-50, doi:10.1126/science.1174621 (2010).

98   Mai, Y. & Eisenberg, A. Self-assembly of block copolymers. *Chemical Society Reviews* **41**, 5969-5985, doi:10.1039/c2cs35115c (2012).

99   Whitesides, G. M., Mathias, J. P. & Seto, C. T. MOLECULAR SELF-ASSEMBLY AND NANOCHEMISTRY - A CHEMICAL STRATEGY FOR THE SYNTHESIS OF NANOSTRUCTURES. *Science* **254**, 1312-1319, doi:10.1126/science.1962191 (1991).

100   Wurthner, F. Perylene bisimide dyes as versatile building blocks for functional supramolecular architectures. *Chemical Communications*, 1564-1579, doi:10.1039/b401630k (2004).

101   Yan, X., Wang, F., Zheng, B. & Huang, F. Stimuli-responsive supramolecular

polymeric materials. *Chemical Society Reviews* **41**, 6042-6065, doi:10.1039/c2cs35091b (2012).

102   Montalti, M. & Prodi, L. A supramolecular assembly controlled by anions: threading and unthreading of a pseudorotaxane. *Chemical Communications*, 1461-1462, doi:10.1039/a802157k (1998).

103   Asakawa, M. *et al.* A chemically and electrochemically switchable 2 catenane incorporating a tetrathiafulvalene unit. *Angewandte Chemie-International Edition* **37**, 333-337, doi:10.1002/(sici)1521-3773(19980216)37:3<333::aid-anie333>3.0.co;2-p (1998).

104   Ashton, P. R. *et al.* Molecular meccano. 26. Hydrogen-bonded complexes of aromatic crown ethers with (9-anthracenyl)methylammonium derivatives. Supramolecular photochemistry and photophysics. pH-controllable supramolecular switching. *Journal of the American Chemical Society* **119**, 10641-10651, doi:10.1021/ja9715760 (1997).

105   Montalti, M., Ballardini, R., Prodi, L. & Balzani, V. Electronic energy transfer in adducts of aromatic crown ethers with protonated 9-methylaminomethylanthracene. *Chemical Communications*, 2011-2012, doi:10.1039/cc9960002011 (1996).

106   Descalzo, A. B., Martinez-Manez, R., Sancenon, R., Hoffmann, K. & Rurack, K. The supramolecular chemistry of organic-inorganic hybrid materials. *Angewandte Chemie-International Edition* **45**, 5924-5948, doi:10.1002/anie.200600734 (2006).

107   Battistini, G. *et al.* The erratic emission of pyrene on gold nanoparticles. *Acs Nano* **2**, 77-84, doi:10.1021/nn700241w (2008).

108   Montalti, M., Zaccheroni, N., Prodi, L., O'Reilly, N. & James, S. L. Enhanced sensitized NIR luminescence from gold nanoparticles via energy transfer from surface-bound fluorophores. *Journal of the American Chemical Society* **129**, 2418-+, doi:10.1021/ja068095d (2007).

109   Montalti, M., Prodi, L., Zaccheroni, N. & Battistini, G. Modulation of the photophysical properties of gold nanoparticles by accurate control of the surface coverage. *Langmuir* **20**, 7884-7886, doi:10.1021/la0491044 (2004).

110   Montalti, M. *et al.* Kinetics of place-exchange reactions of thiols on gold nanoparticles. *Langmuir* **19**, 5172-5174, doi:10.1021/la034581s (2003).

111   Mazzaro, R. *et al.* Photoinduced Processes between Pyrene-Functionalized Silicon Nanocrystals and Carbon Allotropes. *Chemistry of Materials* **27**,

4390-4397, doi:10.1021/acs.chemmater.5b01769 (2015).

112   Kay, E. R., Leigh, D. A. & Zerbetto, F. Synthetic molecular motors and mechanical machines. *Angewandte Chemie-International Edition* **46**, 72-191, doi:10.1002/anie.200504313 (2007).

113   Prins, L. J., Reinhoudt, D. N. & Timmerman, P. Noncovalent synthesis using hydrogen bonding. *Angewandte Chemie-International Edition* **40**, 2382-2426, (2001).

114   Stuart, M. A. C. *et al.* Emerging applications of stimuli-responsive polymer materials. *Nature Materials* **9**, 101-113, doi:10.1038/nmat2614 (2010).

115   Mura, S., Nicolas, J. & Couvreur, P. Stimuli-responsive nanocarriers for drug delivery. *Nature Materials* **12**, 991-1003, doi:10.1038/nmat3776 (2013).

116   Roy, D., Cambre, J. N. & Sumerlin, B. S. Future perspectives and recent advances in stimuli-responsive materials. *Progress in Polymer Science* **35**, 278-301, doi:10.1016/j.progpolymsci.2009.10.008 (2010).

117   Kawano, T., Niidome, Y., Mori, T., Katayama, Y. & Niidome, T. PNIPAM Gel-Coated Gold Nanorods, for Targeted Delivery Responding to a Near-Infrared Laser. *Bioconjugate Chemistry* **20**, 209-212, doi:10.1021/bc800480k (2009).

118   Jiang, J. Q., Tong, X., Morris, D. & Zhao, Y. Toward photocontrolled release using light-dissociable block copolymer micelles. *Macromolecules* **39**, 4633-4640, doi:10.1021/ma060142z (2006).

119   Yang, Y., Velmurugan, B., Liu, X. & Xing, B. NIR Photoresponsive Crosslinked Upconverting Nanocarriers Toward Selective Intracellular Drug Release. *Small* **9**, 2937-2944, doi:10.1002/smll.201201765 (2013).

120   Jiang, J., Qi, B., Lepage, M. & Zhao, Y. Polymer micelles stabilization on demand through reversible photo-cross-linking. *Macromolecules* **40**, 790-792, doi:10.1021/ma062493j (2007).

121   Jiang, J. Q., Tong, X. & Zhao, Y. A new design for light-breakable polymer micelles. *Journal of the American Chemical Society* **127**, 8290-8291, doi:10.1021/ja0521019 (2005).

122   He, J. & Zhao, Y. Light-responsive polymer micelles, nano- and microgels based on the reversible photodimerization of coumarin. *Dyes and Pigments* **89**, 278-283, doi:10.1016/j.dyepig.2010.03.032 (2011).

123   Katz, J. S. & Burdick, J. A. Light-Responsive Biomaterials: Development and Applications. *Macromolecular Bioscience* **10**, 339-348, doi:10.1002/mabi.200900297 (2010).

3 Analysis techniques. Microscopy and Scattering

In chapter 1it has been mentioned that an important step forward in the development of new nano-systems was made possible by the development of new identification techniques, able to furnish important information regard these materials. In fact, despite in some cases many of the standard analysis techniques available to chemists (e.g. NMR, IR, UV), can be used to infer information about nanoparticles in solution, the most common techniques used for initial analysis are based on microscopy or scattering. Typically a combination of these two techniques are required, since they provide complementary information about the particles. Scattering techniques, on one side, give good statistics (typically > 10^9 particles),[1] are not disruptive and can be conducted in solution. Unfortunately, the resulting data provide an average overview of the sample, which always requires to be fitted to a model, meaning that analysing samples containing multiple or completely unknown structures can be very problematic. On the other hand, optical, electron or scanning microscopyallow to image directly, and the differences in individual particles can be readily observed. Although, somemicroscopy techniques (e.g. transmission electron microscopy, TEM) involve removing the sample from its natural state in solution, somehow affecting its behaviour. Moreover, analysis of many particles can be time consuming and the statistic over the data is limited to hundred objects, instead of billion. This makes, in some cases, microscopy partiallysubjective, since the user has to arbitrarily select which areas of the sample are 'representative', and then image them. Since both the benefits and restrictions of analysis techniques should not be underestimated, the most common analysis techniques based on light scattering and optical microscopy will be reviewed trying to point out advantages and weakness of both of them.

3.1 Scattering techniques

The most common scattering techniques for soft materials in solution are static and dynamic light, small angle X-ray and small angle neutron scattering. As it can be seen in the simplified scheme of the general scattering experimental setup (Scheme 1), a known intensity (I_0) radiation hits the sample, than the radiation interact with the scattering centres (particles) within the sample, causing a deviation in trajectory (scattering). The intensity of the scattered radiation (I_s) is then detected at some angle (θ), which is not 180°, in order to avoid the source signal. Changing

θallows for the detection of radiation at different scattering vectors q, where $q = 4\pi \sin \theta/\lambda$, and λ is wavelength of the radiation. The scattering vector q has units of reciprocal length and can be related to the length scale over which the measured radiation has been scattered. Since larger q values correspond to smaller length scales, the lengths scales being measured can be tailored by changing both λ or θ. Scattering data can provide information about the particles size, shape and molecular weight. Generally, for strongly scattering systems (e.g. polymer micelles), the error in parameters obtained by DLS, SLS or SANS is roughly 10-20%,[2] which can be attributed to the accuracies in measuring the standards or backgrounds. However, the error is significantly smaller (5%) when comparing values from the same apparatus under the same conditions. According with the purpose of this thesis, only the Laser Light Scattering techniques (static and dynamic light scattering) are described more in detail.
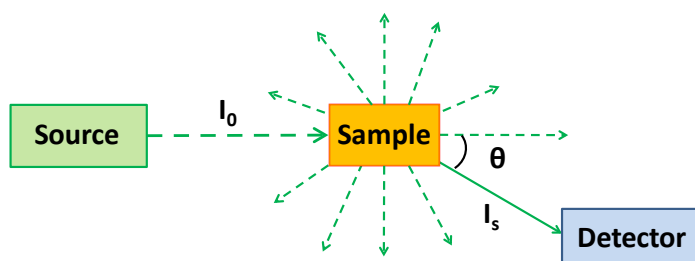
Scheme 3.1: Basic schematic for the experimental setup of scattering experiments

3.1.1 Laser Light Scattering (LLS)

This techniques[1,3,4] are based on the fact that, being light made up of oscillating electric and magnetic field components, its interaction with matter has the effect of altering the spatial charge distribution within the molecules. The magnitude of this interaction is related to how easily the charges can be shifted, referred as the polarisability, which can be determined for each sample by measuring the refractive index increment, *dn/dc*, where *n* is the refractive index of the solution and *c* is the sample concentration in mass/volume. For complex materials, such as core-shell nanoparticles of block co-polymers aggregates, should be considered the relative contribution of each component, or block, due to different*dn/dc* values, to the scattered radiation.[5] The LLS techniques allow the determination of particle molecular weight, either by measuring *dn/dc* directly or calculating it for the mixed component system,[6] but the interpretation of these values have to be taken with

care. In fact, small particles (radius, $R<\lambda/20$) obey Rayleigh scattering and emit light isotropically. For larger particles ($R > \lambda/20$), there is sufficient distance between scattering centres within individual particles, and the scattered radiation can be of a sufficiently different phase to cause interference with each other.[1]This leads to anisotropic diffusion and the scattering have to be modelled by Mie theory.Without going deeper into these theory explanations, there are some important consequences implied which deserve to be summarized. This can be explained by considering the relationship between I_s, molecular weight (MW) and size for a 3D object. From the Zimm equation,[1]$I_s$isproportional to MW, MW proportional to volume (Eq. 3.1) and volume proportional to L^3 for a 3D object, where L is some length and NA is Avogadro's number:

$$\frac{MW}{N_A} = mass = \ density \times volume \ (Eq.3.1)$$

This can be summarized with the fact that, even the very low concentration impurities, as dust or aggregates of particles, can cause a significant error in the measurement. Secondly, for particles obeying Mie scattering, the larger the particle, the more it scatters in the forward direction. This can have serious consequences when trying to measure highly disperse samples or samples that contain multiple size distributions. When scattered photons reach the detector, the number of photons per unit time is measured. If the time constant is in the range of microseconds, the solution dynamic of the particles plays a role in the evolving data set (dynamic light scattering). If the time constant is in the range of seconds, the information regard the dynamic are lost, and only the average scattered intensity is considered (static light scattering). These two experiments, dynamic light scattering (DLS) and static light scattering (SLS) form the two basic LLS techniques used for analysing assembled polymers in solution using light.

3.1.2 Dynamic light scattering (DLS)

This techniques is based on the fact that particles in temperature equilibrated solution move under Brownian motion. Accordingly, their speed can be related to the hydrodynamic size (r_H) by the Stokes-Einstein equation (Eq. 3.2).

$$r_H = \frac{k_B T}{6\pi n D}(Eq.\ 3.2)$$

where r_H is the hydrodynamic radius, k_B is the Bolzmann' constant, T is the temperature and n is the refractive index of the solvent, which must be accounted

for resulting in $q = 4\pi n \sin\theta/\lambda$. The hydrodynamic radius (r_H) reported by DLS, is the theoretical radius of a perfect hard sphere which moves with the same translational diffusion coefficient (D) as the particle being measured. In order to determine D it is necessary to determine the speed of the electric field variation, which is the electric field auto correlation $g1(q,t)$. The superposition of all the scattered electric field generated by the interaction of the incident light with the particles will have a some value E_0, hence $g1(q,t)$, can be determined by equation:

$$g1(q,t) = \frac{< E_0(q,t)E_{0+\Delta t}(q,t) >}{< E_0(q,t) >^2} \quad (Eq.\,3.3)$$

where E_0 is compared to $E_{0+\Delta t}$ and Δt is a small variation in time for many iteration of Δt. Eventually, electric field variation has to be related to the quantity measured by the DLS, the intensity of light. This can be achieved by the Siegert equation[1](Eq. 3.4) where the electric auto correlation function, $g1(q,t)$ is related to the intensity auto correlation function $g2(q,t)$:

$$g2(q,t) = 1 + g1(q,t)^2 \quad\quad (Eq.\,3.4)$$

where the intensity auto correlation function $g2(q,t)$can easily be measured by equation 3.5 which is analogous to equation 3:

$$g2(q,t) = \frac{< I_0(q,t)I_{0+\Delta t}(q,t) >}{< I_0(q,t) >^2} \quad (Eq.\,3.5)$$

For a single population of monodispersed spheres, it has been shown that (Eq. 5.6):

$$g1(q,t) = e^{-t/\tau} \quad\quad (Eq.\,3.6)$$

with τ relaxation time. Eventually, equation 6 can then be used to determine the apparent diffusion coefficient (D_{app})(Eq. 3.7):

$$\tau = D_{app} \times q^2 \quad\quad (Eq.\,3.7)$$

The most common DLS instrument is the Zetasizer range from Malvern (http://malvern.com). It is characterized by a small bench top apparatus and provides a quick assessment of particle size distributions. Typically, and it is the case of the instrument used during this thesis work, the detector is settled up at θ = 173 ° (termed 'back scatter' detectors) in order to avoid scattering due to larger impurities and to back scattering phenomena. This makes the instrument easier to

use, but it is also a limitation, since the measure cannot be collected at different angles, which would make the determination of the D_{app} more accurate (plotting the τ^{-1} versus q^2). It would also make possible to obtain the true diffusion coefficient D for systems which are not monodisperse and obey Mie scattering. Once an angular independent D_{app} is obtained, in fact, measuring this value for various concentrations will allow extrapolation of D_{app} to zero concentration. This accounts for interparticle interactions and a true diffusion coefficient D can be obtained. As previously mentioned D can then be used to determine r_H using the Stokes-Einstein equation (Eq. 3.8). Due to the scaling of scattering intensity with size, r_H values from DLS can be considered as Z-averages, $< r_H >_z$:

$$< r_H >_z = \frac{\sum n_i r_i^6}{\sum n_i r_i^5} \qquad (Eq.\,3.8)$$

where n_i is the number of particles of radius i.

3.1.3 Static Light Scattering (SLS)

Averaging the scattered light intensity measurements over time scales longer than 1 second, results in loss of solution dynamics. Consequently the information is based on particle size and shape and it can be used to determine the molecular weight of the analyzed structure, which is, in the case of polymeric aggregates, the polymer molecular weight. The Zimm equation stated in the form below (Eq. 3.9) reveals the information that can be obtained from SLS measurements performed at multiple angles (θ) and concentrations (c). The average scattered intensity of the sample (I_{sample}) is measured in relation to the average scattered intensity of the solvent ($I_{solvent}$) and a standard ($I_{standard}$). This is used to determine the Rayeigh Ratio (R_θ) for the sample, based on the known Rayleigh Ratio of the standard ($R_{\theta,standard}$), equation 9. K_c/R_θ can then be determined using equations 10 and 11 taking into account the wavelength of the laser (λ), the refractive index of the solvent ($n_{solvent}$), the dn/dc of the sample and Avogadro's number (NA). Plotting $Kc/R\theta$ vs. q^2 allows for the determination of the radius of gyration (R_g) from the slope and K_c/R_θ at zero angle (zero q) by the intercept.

$$\frac{K_c}{R_\theta} = \frac{q^2 R^2 g}{3MW} + \frac{1}{MW} + 2A_2 c \qquad (Eq.\,3.9)$$

$$R_\theta = \frac{I_{sample} - I_{solvent}}{I_{standard}} R_{\theta,standard} \qquad (Eq.\,3.10)$$

$$K = \frac{4\pi n_{solvent} \left(\frac{dn}{dc}\right)^2}{N_A \lambda^4} \qquad (Eq.\,3.11)$$

Plotting K_c/R_θ at zero angle versus concentration has the result of removing the q^2 term from the equation and it results in

$$\frac{K_c}{R_\theta} = \frac{1}{MW} + 2A_2 c \qquad (Eq.\,3.12)$$

This allows for the determination of the molecular weight (MW). As the molecular weight obtained from SLS is a weight average molecular weight, it is more appropriate to use the weight average molecular weight of the polymer (M_w).

For polymer assemblies particle MW is almost always used to determine the aggregation number of the assembly (N_{agg}), since:

$$N_{agg} = \frac{MW_{particle}}{MW_{polymer}} \qquad (Eq.\,3.13)$$

3.2 Microscopy techniques

Microscopy techniques complement scattering data as they directly image individual particles. Microscope types are numerous but can be broadly divided into two categories depending on the working modality. Wide-field microscopes use a beam of radiation (e.g. light or electrons) which is projected onto the object in order to form directly a complete image of that object. Scanning microscopes use a probe which scans each point of the object serially in order to form an image of that object. An *'image'* is not the object itself, but merely a representation of the object, and furthermore, one object can be represented by many different types of *images*.

In particular wide-field Optical microscopes that were used in this work and will be discussed in detail can be used in transmission or fluorescence modality. Moreover the wide field microscopy respect to confocal methods allows to collect a high number of frame per minutes in low power excitation conditions and, hence, to follow long processes with adequate temporal resolution without severe effect of photobleaching.

3.2.1 Wide field fluorescence microscopy

Basically, fluorescence microscope allows the irradiation of the sample with the desired wavelength and then to separate the weaker emitted light (fluorescence)

from the excitation one. Only the emission light should reach the detector, so that the fluorescent areas are contrasted against a dark background. The detection limit is largely determined by the darkness of the background, since the excitation light is typically 10^5 or 10^6 times brighter than the emitted light.

Usually, the sample is illuminated by a laser beam, which is expanded by a telescope and focused on the back focus of the microscope objective by a lens. In the path between the lens and the objective (which optical axis are perpendicular) the beam is reflected by a dichroic mirror. Since the beam converge in the back focus of the objectives, it exits from the microscope as a spot composed of rays parallel to the optical axis that irradiate the specimen in a homogeneously way within a circle that depends on the optical aperture of the excitation system. In the sample, light is absorbed and emits in all directions by the fluorescent units, with longer wavelength respect to the excitation source. A fraction of the emitted fluorescence is collected by the microscope objective and imaged onto a camera . The image of the sample placed in the focal plane of the objective is then enlarged and reconstructed on the camera by the tube lens of the microscope.In order to better understand the advantages and the limitations of this microscopic techniques, it will give an overviewon the involved optical processes.

*Principles of optics*When light incises on the interface between two media, the ray path changes abruptly: part is reflected and part is transmitted, with a changed direction of propagation (refraction). This process is described by the Snell's law (Eq. 3.14), which states that the ratio of the sines of the angles of incidence ($sin\theta_i$) and refraction ($sin\theta_R$) is equivalent to the ratio of the phase velocity in the two media (v_1 and v_2), the ratio of the light wavelengths in the two media (λ_1 and λ_2), and to the reciprocal of the ratio of the refractive index (n_1 and n_2).

$$\frac{sin\theta_i}{sin\theta_R} = \frac{v_1}{v_2} = \frac{\lambda_1}{\lambda_2} = \frac{n_2}{n_1} \qquad (Eq.\,3.14)$$

On this basic law, is based the operation principle of the optical lenses. A lens, in fact, constitute the material with different refractive index respect to the air, which transform the diverging spherical wave front, radiated by a point source, to a converging spherical wave. If the point source is the analyzed object, the converging wave is the formed image. Clearly, if the spherical waves radiated by the object extend over the full 4π radians of a sphere, the converging spherical wave is clipped by the limited size of the lens, given by its aperture. This clipping of the wavefront and the diffraction phenomena occurring at the edges of the aperture

limits the size of the image point and causes a blurring of the image of the point source. For an ideal, aberration-free lens, the size of the distribution of the image object is determined only by the light wavelength, the lens numerical aperture (NA) and the diffraction limit, where NA is related to the semi-aperture angle of focusing (α) through the refractive index (n) as NA=n ×·sin(α).The diffraction pattern of a converging spherical wave from a circular aperture, can be calculated from diffraction theory. Starting from Maxwell's equations, a number of approximations are required to obtain an analytical expression for the focal-field distribution. The first one is the Kirchhoff approximation, which assumes that the optical field within the aperture is equal to the optical field directly in front of the aperture, whereas it is zero everywhere else. The second is the Debye approximation, which neglects the diffraction from the aperture edges by considering only plane waves within the focusing cone with solid angle $\pi\alpha^2$. Finally, the paraxial approximation assumes that sin$\alpha \approx \alpha$.If the validity of the Kirchhoff approximation has been tested extensively and is found to be generally correct, the Debye approximation is correct only when the following condition is satisfied:

$$\frac{2\pi}{\lambda} \cdot f \gg \frac{\pi}{sin^2\left(\frac{\alpha}{2}\right)} \qquad (Eq.\,3.15)$$

where f is the geometrical focal length of the lens and α is the semi-aperture angle of focusing. It is generally valid only if $f \gg a \gg \lambda$ and if $a^2/\lambda f \gg 1$, where a is the aperture radius. It means that for a fixed focal position, this approximation improves as the numerical aperture becomes larger, and for a fixed numerical aperture, it becomes more accurate as the focal distance increases.On the other hand, the paraxial approximation is true only for small aperture angles ($\alpha \ll 20°$).Under ideal circumstances and with the appropriate approximations, the distribution of the image points in the focal plane is described by equation 3.16:

$$I(v) \propto \left|\frac{2J_1(v)}{v}\right|^2 \qquad (Eq.\,3.16)$$

with $v = r \times NA \times 2\pi/\lambda$. Solving the equation, the first minimum (v_0) is found at 1.22 π, becoming, in real space units (Eq. 3.17):

$$r_0 = \frac{0.61 \cdot \lambda}{NA} \qquad (Eq.\,3.17)$$

Considering λ= 200nm for UV light, the diffraction limit of light microscope is about 150nm (300 nm for λ= 400 nm) Unfortunately, this is not the only parameter that limits of the instrumental resolutionhence the smallest feature that can just be resolved by the microscope, or the smallest distance that can be determined between features. This important parameter, alsodepends onthe signal-to-noise ratio (SNR) of the imaging system, on the imaging mode, and on *a priori* knowledge of the specimen.

One of the most common applied criterion to determine the optical resolution is the Rayleigh criterion, which states that two components of equal intensity should be considered to be just resolved when the principal intensity maximum of one coincides with the first intensity minimum of the other. Accordingly, almost a 20% drop in intensity occurs between the two maxima.As mentioned, an important aspect to consider is the signal-to-noise ratio, defined as:

$$SNR = \frac{|meansignal - background|}{signalstandarddeviation}$$

In this definition, all kinds of noise (shot, thermal, read-out, photon statistical, photon-scattering, quantization) plays a role, affecting either the background level or the signal standard deviation, reducing the optical resolution and therefore limiting the quality of the image. It is worthy to stress that this parameter can, potentially, be strongly optimize, both increasing the sample emitted signal and reducing all the side phenomena responsible of the background luminescence. Although, this is still a really challenging aspect especially in bioimaging, where the tissue autofluorescence is hard to remove, unless using infra-red emitters, which significantly reduce the number of usable high fluorescent quantum yield emissive dyes. This is one of the main reason, in our prospective, which makes particularly interesting the development of new high brightness systems, able to drastically increase the marker signal and, consequently, the *SN* ratio.

Image formation and magnification. The image of an object in a microscope can be mathematically computed by expressing the object-plane field as weighted sum over impulse functions, and then expressing the image plane field as the weighted sum over the images of these impulse functions. The images of the individual object plane impulse function are called *point spread functions* (PSF), reflecting the fact that a mathematical point of light in the object plane is spread out to form a finite area in the image plane. When the object is divided into discrete point objects of varying intensity, the image is computed as a sum of the PSF of each point Image

formation in a wide-field microscope is a linear process, hence, the measured image I (X, Y, Z) of an object O (x, y, z) can be mathematically described as

$$I(X,Y,Z) = \iiint_{-\infty}^{\infty} O(x,y,z) \cdot PSF\left(x - x', y - y', z - z'\right) dx' dy' dz'$$

where X,Y,Z and x,y,z are the spatial coordinates in image and object space, respectively. Mathematical calculation of this integral is significantly simplified using Fourier theory.To visualize this mathematical dissertation, the physical behaviour of the microscope lens has to be considered. According with paraxial theory, the optical paths of the principal rays through a biconvex thin lens can be describe by the following scheme3.2:
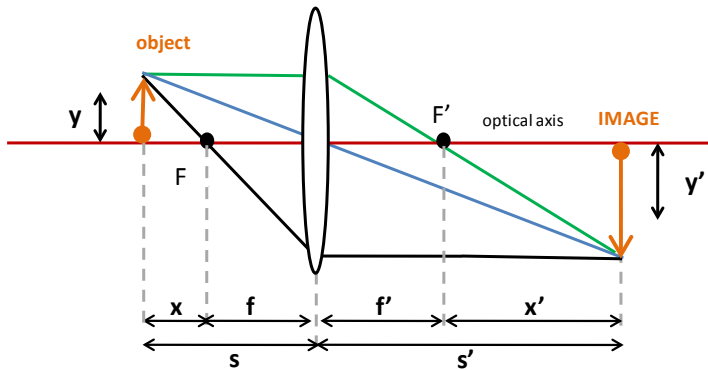
Scheme 3.2: Formation of a real magnified image by a thin positive lens.

From this description, it can be appreciate that the path of an optical ray passing through the center of a thin lens (blue line) is left unchanged; the optical ray incident parallel to the optical axis (green line) are refracted to pass through the focal point behind the lens; and the optical ray originating from the focal point in front of the lens (black line)are refracted to propagate parallel to the optical axis after the lens.Considering an ideal imaging system consisting of a single positive lens and paraxial rays (Scheme 3.2), when an object is positioned in one side of this lens and beyond its focal point **F** (also called the back focal point), a real image is formed on opposite side. Every point of the object is imaged to a single point on the image. **F** and **F'** (the image focal point) of the lens are located at a distance *f* in front of and *f'* (where *f* = *f'*) behind the lens, respectively.

The image of the object is imaged by the lens as an inverted and magnified image, located at a distance s' behind the lens. It follows, from the principle of reversibility of light rays, that object and image are interchangeable, so they are said to be conjugate. If $f = f'$, the system follows the general Gaussian law of geometrical optics for thin lenses:

$$\frac{1}{s} + \frac{1}{s'} = \frac{1}{f} \qquad (Eq.\,3.18)$$

It is straightforward to derive the lateral magnification factor

$$M_{lat} = \frac{y'}{y} = \frac{s'}{s} \qquad (Eq.\,3.19)$$

The same principles hold if the object is closer to the lens than its focal point (Scheme 3.3). In this case the optical rays in the image space diverge and thus form a virtual image in front of the lens. The closer the object moves towards the lens, the larger it seems (Scheme 3.3).
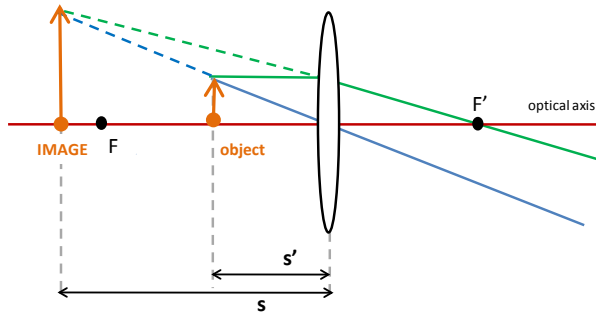
Scheme 3.3: Formation of a virtual magnified image by a thin positive lens.

This is referred as angular magnification. In the microscope, this is combined with the angular magnification due to the eyepiece (Scheme 3.4), M_{ang}, which is the ratio of the angle subtended by the image θ' to the angle subtended by the object θ:

$$M_{ang} = \frac{\theta'}{\theta} \qquad (Eq.\,3.20)$$

and this is achieved by the use of a tube lens, forming a real intermediate image serving as the object for the lateral magnification (Scheme 3.4). Eventually, the total magnification is given by:

$$M_{tot} = M_{lat} \cdot M_{ang} \qquad\qquad (Eq.\,3.21)$$
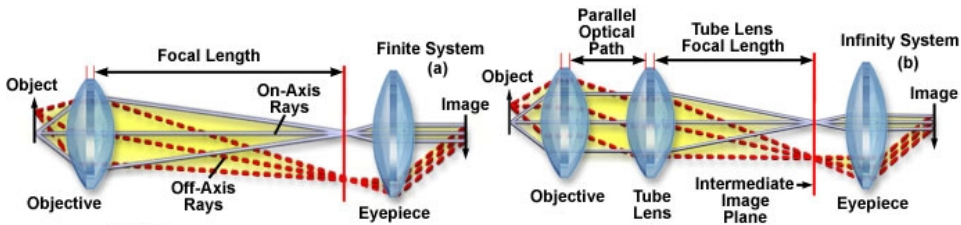
Scheme 3.2: (a) In a finite optical system of fixed tube length, light passing through the objective is directed toward the intermediate image plane (located at the front focal plane of the eyepiece) and converges at that point. (b)For infinity-corrected optical systems the objective produces a flux of parallel light wavetrains imaged at infinity (often referred to as infinity spacewhich are brought into focus at the intermediate image plane by the tube lens.(http://www.microscopyu.com/)

To be more precise, the objective is composed by more than ten separate lens elements to correct for aberrations, and additional lenses to relay the image and further correct aberrations. Every kind of aberration distorts the wave propagation through the system and causes a loss in resolution compared to this diffraction-limited optimum: if in the excitation path they lead to a spreading of the excitation PSF over a larger volume, while in the detection path give rise to a spreading of the detection PSF.For this reasons they have to be taken into account and, when possible, reduced by optical design of the microscope. Otherwise, their presence have to be recognise in theimage analysis. The capability of a wide field microscope of generating a sharp and clean image is, hence, affected by the background signal and the presence of lenses aberration. Although, other parameters have to be consider, such as limited detection efficiency, the spatial size of the optical-probe volume and the objective lens' collection efficiency. These phenomena causes loss of photons along the light path, which have direct implications in the detectable signal. For this reason, as well, the development of strong emitters, with large Stokes shifts, high photostability and brightness, is highly requested.

3.3 Conclusion and prospective

Understanding advantages and limits of both the discussed techniques, was particularly important for the developing of new materials and, afterwards, for their characterization. Accordingly, some aspects have been taken into account in the design and study of our systems. Scattering techniques requires monodispersed samples, with known structure and predictable behaviours, while nanostructures

can be observed by optical microscopy only if highly fluorescent and photophysically stable. If the former request, as already explained, has to be satisfy for any kind of nanomaterials, the latter turned to be an interesting challenge, and particular attention was spent to reach this goal.

Bibliography

1   Schärtl, W. *Light scattering from polymer solutions and nanoparticle dispersions*. (Springer Science & Business Media, 2007).
2   Colombani, O. *et al.* Structure of micelles of poly (n-butyl acrylate)-block-poly (acrylic acid) diblock copolymers in aqueous solution. *Macromolecules***40**, 4351-4362 (2007).
3   Patterson, J. P. *The synthesis, self-assembly and analysis of amphiphilic polymers: developing microscopy techniques using graphene oxide and building catalytic palladium nanostructures*, University of Warwick, (2013).
4   Santos, N. C. & Castanho, M. Teaching light scattering spectroscopy: the dimension and shape of tobacco mosaic virus. *Biophysical journal***71**, 1641 (1996).
5   Tsunashima, Y. & Kawamata, Y. Dynamics of polystyrene subchains of a styrene-methyl methacrylate diblock copolymer in solution measured by dynamic light scattering with an isorefractive index solvent. 1. Dilute solution region. *Macromolecules***26**, 4899-4909 (1993).
6   Bushuk, W. & Benoit, H. l. Light-scattering studies of copolymers: I. Effect of heterogeneity of chain composition on the molecular weight. *Canadian Journal of Chemistry***36**, 1616-1626 (1958).

4 High-bright fluorescent nanoparticles

Ultra-bright nanosized emitters can, at least in principle, be directly obtained by the incorporation of a large number of molecular fluorophores in a nanoparticle (NP). Actually, the electronic interactions arising from fluorescent precursors aggregation during the NPs growth cause fluorescence quenching by a process known as aggregation-caused quenching (ACQ).[1-3] Moreover in NPs, as well as in most multichromophoric systems, the presence of aggregated dyes becomes particularly deleterious, because it causes a severe quenching of the non aggregated dyes emission.[4-6] This phenomenon occurs through Förster resonance energy transfer (FRET) processes and even a low fraction of aggregates can behave as excitation energy traps. As it will discuss, dyes close packing in the nanostructure amplifies the fluorescence quenching even in the absence of aggregation, simply because of the close proximity between the emitters. This last mechanism involves excited state interactions rather than ground state ones as in ACQ, and it is called proximity-caused quenching (PCQ).

4.1 Amplified Quenching in NPs

Interest through the effect of dye aggregation on light emission properties in mutichromophoric systems increased together with their application for bioimaging.[7-10] Nevertheless the concept that photolumiscence (PL) quenching in the NPs is not simply caused by ACQ, but also by PCQ, is still often neglected.

The phenomena, schematized in figure 4.1, shows that in ACQ aggregation occurs at molecule ground state and, consequently, both absorption and emission spectra are affected (indicated as B in fig. 4.1, left). In PCQ, dyes in close proximity (indicated as B in fig. 4.1, right) interact only after excitation, producing quenched excimers or charge transfer states. In this case, only emission spectrum is affected. PCQ efficiency depends on dyes distribution in the NPs, a parameter which is only partially controlled by the direct ground state interactions between the chromophore, and which strongly reflects the constrains imposed by the structural matrix. Emitters may hence be 'forced' to stay in close proximity although their electronic interactions at the ground state are weak. In NPs, the effect of ACQ and PCQ is extended to the surrounding dye molecules because of FRET processes. As shown in figure 4.1, a few quenched centres can collect the excitation energy of a large number of non-aggregated dyes in the surrounding area. This causes a

phenomenon similar to the one reported by Swager in the case of conjugated polymer as amplified quenching.[11-13]
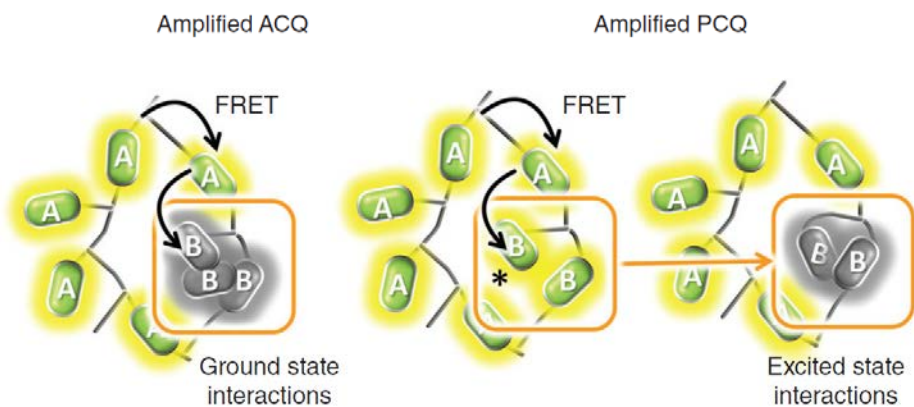
Figure 4.1: Amplification of aggregation-caused quenching (ACQ, left) and proximity-caused quenching (PCQ) in NPs. The former process involves Förster resonance energy transfer (FRET) form 'isolated' excited dyes (A molecules) to not non-luminescent aggregates already present before excitation because of the action of ground state interaction between B molecules. Amplified PCQ (right) is analogous, but takes place also in the absence of aggregates: FRET leads to excitation of molecule which are not aggregated (weak ground state interaction), but are close enough to bind after excitation to give quenched species.[14]

4.2 Brightness of molecular-based NPs

Brightness (B) allows to quantify the actual fluorescence or, more in general, PL signal generated by an emitter (e.g. a molecule or a NP) and it is the product of its molar absorption coefficient (ε) and of the PL quantum yield (φ).[15] In the low concentration regime, typical of imaging applications, the PL intensity is directly proportional to B= ε φ. Ultra-bright NPs can be, in principle, obtained by incorporation of a large number (n) of molecular emitters in a single particle. In fact, assuming that ε and φ of the dyes are not modified in the NPs, ε(NP) =n×ε and φ(NP) =φ, brightness of the NPs is B(NP) =n×ε×φ. In real NPs, dyes distribution is non-homogeneous and parameters as n, ε and φ are determined as average value <n>, <ε>, <φ> and B(NP) = <n> <ε> <φ>. As shown in figure 4.2, ACQ and PCQ affect <φ> that decreases dramatically with increasing <n>. Preparing NPs with high <n> without compromising <φ> is the real challenge in producing ultra-bright systems (Fig. 4.3).

Strategies for minimizing PL quenching in NPs are based onto two general approaches. The former one is to use only those molecular emitters which do not

undergo severe ACQ or PCQ as fluorescent doping agents (referred as non-quenching dyes). The latter general strategy consists into avoid dyes aggregation and proximity by controlling their distribution in the NPs. With respect to the former approach, this latter one implies a major effort in the synthetic design but, as an advantage, it permits to exploit almost any kind of fluorophore for NPs preparation. The use of non-quenching molecules on the contrary makes the production of the NPs less critical but the variety of possible starting emitting materials is limited.
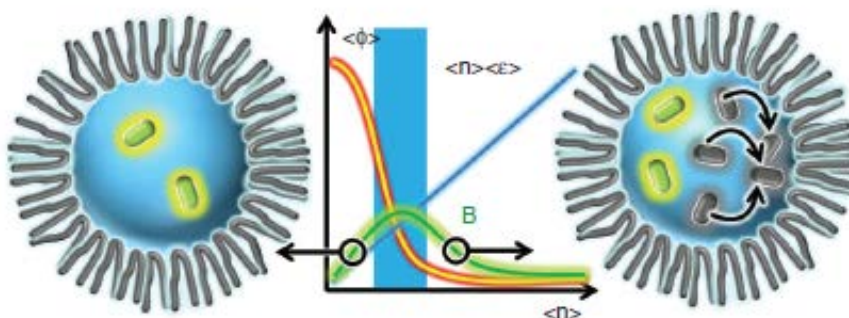
Figure 4.2: Effect of amplified aggregation-caused quenching (ACQ) and proximity caused quenching (PCQ) on the brightness of nanoparticles (NPs). At low dye doping level (left) the emitting molecules do not interact: $<\varphi>$ is maximum but $<n>$ $<\varepsilon>$ are low. At high doping level (right), ACQ and PCQ combined to Förster resonance energy transfer, cause an amplified quenching and severe decrease of $<\varphi>$. These effects prevent the preparation of ultra-bright NPs Optimal low window is shown in blue.[14]
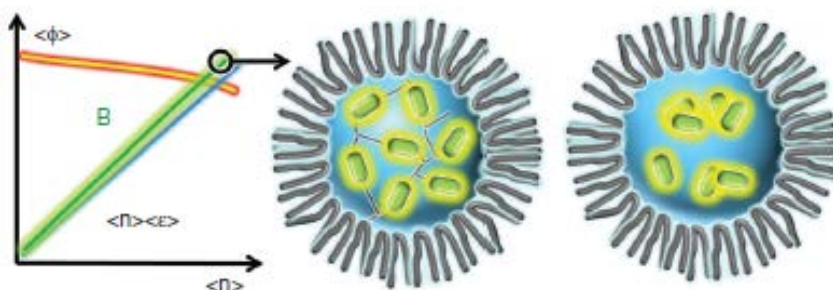
Figure 4.3: Most typical strategies to prepare ultra-bright nanoparticles (NPs). Aggregation-caused quenching (ACQ) and proximity-caused quenching (PCQ) can be prevented by controlling the dye distribution in the structure (left) or using specific dyes that do not give these kind of processes (right). $<\varphi>$ is almost independent on the doping level and brightness increase together with $<n>$ $<\varepsilon>$ leading to ultra-bright NPs.[14]

4.3 Ultra-bright NPs based on non-quenching dyes

The design based on molecular or polymeric emitters which does not suffer severe ACQ or PCQ[16,17] is discussed firstly. Although in general this strategy does not require elevated structural control, geometrical distribution and orientation of the emitters in the NPs may play a role in the final emission properties.

4.3.1 Aggregation-Induced Emission

While most organic fluorophores undergo quenching upon aggregation, examples of molecules which are not fluorescent in solution and forms strongly luminescent aggregates have been reported. This peculiar phenomenon has been defined aggregation-induced emission (AIE)[2,3,18] or crystallization-induced emission (CIE) in the case of crystal formation.[19] Mechanism of AIE has been mostly identified in restriction of intramolecular rotation (RIR),[20] although a contribution due to J-aggregate formation, twisted intramolecular charge transfer (TICT),[21] and excited-state intramolecular proton transfer (ESIPT) has not been ruled out.[22,23] Incorporation of the AIE fluorophores into NPs can derive from different strategies. A very direct one is to prepare nanocrystals simply by diluting concentrated organic solution of the AIE dyes in water, where they are poorly soluble. A more popular method to produce AIE dots suitable for bioimaging application[24] is based on the encapsulation of molecules or polymer[9,25] with AIE behaviour in polymeric NPs or micelles. Advantages of this approach are an increased control of the size and colloidal stability as well as the possibility of surface functionalization for targeted delivery. Preferred stabilizers are biocompatible polymers with versatile functional groups including poly(DL-lactide-co-glycolide) (PLGA),[26] and 1,2-distearoyl-sn-glycero-3-phosphoethanolamine-N-(polyethylene glycol) (DSPE PEG).[24,27,28] Also micelles formed by the neutral surfactant Pluronic F127 has been proposed[29,30] as well as silica NPs[31,32] and bovine serum albumin (BSA).[24] In a different approach polymers with AIE behaviour, obtained by polymerization of AIE chromophores, have been covalently cross linked to yield covalent NPs.[33-35] A further strategy is the AIE dyes self-assembly after their modification with suitable functional groups[36,37] also exploiting a supramolecular approach.[38] A drawback of AIE as a tool for the design of ultra-bright luminescent NPs is that it becomes poorly efficient if the hosting matrix of the NPs favours dyes disaggregation.

4.3.2 Excimer-based NPs

Although formation of quenched excimers yields to PCQ, some molecules form

emitting excimers.[39] That is the case of pyrene that has been used by Prodi's group[40] to prepare bright silica-doped NPs. A combination of dynamic light scattering and photophysical measurements allowed the investigation of the dye molecules organization in the final NPs. The results demonstrated that pyrene, bound inside the silica matrix by copolymerization, was incorporated mostly in the initial stage of NPs growth, forming a high dye density nucleus in a spontaneously generated core-shell structure. Depending on the doping level, the resulting core showed the typical emission of the pyrene monomer (light doping) or excimers (heavy doping). Interesting, the results demonstrated that distribution of dye molecules in dye-doped silica NPs is far from being homogeneous. Moreover, it was observed that the bare silica shell, formed in the final stage of NPs growth, reduced the diffusion rate of atmospheric oxygen toward the emitting core increasing its brightness and photostability.

4.3.2 Conjugated polymers-based NPs

The effect of aggregation on the PL properties of conjugated polymers is strongly dependent on chain conformation and aggregate morphology[10] and examples of bright NPs have been reported. The actual loading level of these conjugated polymer dots (Pdots), as well as their brightness, strongly depend on the synthetic approach. Using re-precipitation method have been prepared Pdots with a volume fraction or weight concentration of conjugated polymers higher than 50% and up to 100%.[10] Pdots can be directly synthesized from low-molecular weight monomers (direct polymerization), but their preparation from, already synthesized, high-molecular-weight polymers (post-polymerization) is more versatile and convenient. Typical methods of the post-polymerization approach include miniemulsion and re-precipitation techniques. For example, NPs with sizes ranging from few to 13 nm of a Poly(p-phenylene vinylene) PPV derivative were prepared by miniemulsion technique starting from a dichloromethane solution containing PEG as a stabilizer.[41,42] PLGA particles loaded with semiconducting polymer were also obtained by the miniemulsion technique (semiconducting polymer/PLGA ca. 1%, w/w).[43] Despite it, miniemulsion method is not fully reproducible and it is not suitable to produce heavily doped materials with a loading of active polymer higher than 1% (w/w) with respect to the stabilizing matrix. An exception is represented by the encapsulated in phospholipidic matrixes, which yielded functionalized NPs with a fluorophores loading concentration of approximately 8.5% (w/w).[44] Re-precipitation method, on the

other hand, produces Pdots of pure conjugated polymer with diameters of about 5–30 nm, being the particle size varied by adjusting the polymer concentration in the precursor solution.[45] The brightness of these NPs is roughly three orders of magnitude greater than that of typical organic fluorescent dyes.[46]

4.3.3 Luminescent metal complexes-based NPs

Many luminescent metal complexes show solid-state luminescence and they are suitable to prepare bright and heavily doped NPs. Hydrophilic complexes, such as $[Ru(bpy)_3]^{2+}$, were incorporated into silica NPs by exploiting electrostatic interactions and physical trapping. Dye loading was increased by growing the silica NP in reverse microemulsion,[47] but ultra-doped NPs could be prepared only after covalent functionalization of the metal complex precursor. As already mentioned, water insoluble complexes can be directly incorporated in silica NPs, thanks to their hydrophobicity. This approach allows to obtain bright NPs suitable for electrochemical excitation and to use luminescent metal complexes with poor water solubility in biological environment.[48,49]

4.3.4 J-Aggregates-Based NPs

Nano-aggregates of J type have been proposed for the design of bright luminescent NPs.[50] Nevertheless, these aggregates show a PL which depends significantly on the actual molecular organization.
This phenomenon has been investigated in detail by Würthner and co-workers who reported that the emission quantum yield of aggregates of the same perylene diimide (PDI) molecules increase relevantly, going from nanorods to nanoribbons structures.[30] Moreover, the study of individual nanoclusters of similar molecules with super-resolution microscopy, demonstrated the presence of local environmental perturbations in the structure. This was reported to create localized excited states that act as excitation energy traps and show a peculiar red shifted emission.[25] On the other hand, strong emission from H-type aggregates has also been reported in apparent contrast with the excitonic coupling theory.[51]

4.3.5 Energy transfer-based NPs

FRET is a powerful tool to control the properties of molecular-based NPs and, in particular, to tune the excitation and emission features.[52,53] Combination of different dyes, with a selected energy levels cascade, has been used to produce homogenous sets of probes for single excitation and multicolor detection.[53]

Recently, it was demonstrated that FRET can also be used to prevent ACQ and PCQ in silica NPs.[54] The approach schematized in figure 4.4 is based on the incorporation of a low fraction of energy acceptor dye (BODIPY) in NPs heavily doped with an excitation energy donor (coumarin). Fluorescence spectra revealed that, in the absence of BODIPY, formation of coumarin excimers, which mostly deactivate via a non-radiative pathway, caused NPs quenching. On the contrary the BODIPY, when present as an energy acceptor, collected the energy absorbed by the donor units originating strong PL. A relevant advantage of this approach is that high brightness is achieved in conditions where excitation and detection are performed in completely separated spectral region (high pseudo Stoke's shift). This allows, in principle, to maximize the signal-to-noise ratio in imaging applications. Finally, thanks to this strategy, the emission colour can be easily tuned by changing the energy acceptor moiety or exploiting a FRET cascade.[53]
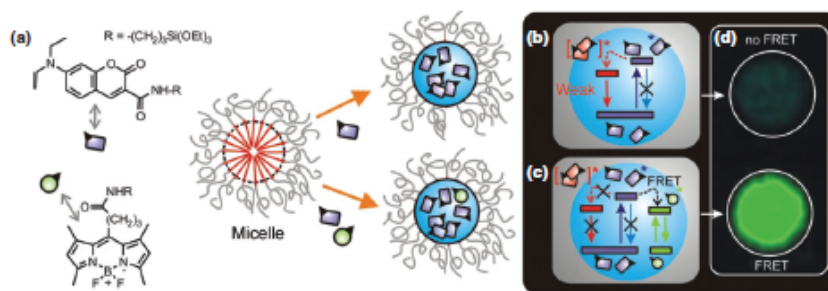
Figure 4.4: (a) Scheme of the preparation of silica nanoparticles using Pluronic F-127 micelles as templates (b) Heavily coumarin-doped NPs are poorly fluorescent because of the formation of weak emitting excimers and aggregates. (c) Co-encapsulation of BODIPY as an excitation energy acceptor at low doping level activate a very efficient FRET process that becomes the dominant channel of deactivation of coumarins and leads to ultra-bright NPs. (d) Fluorescent images of equimolar suspension of the two kinds of NPs.[54]

4.4 Ultra-Bright NPs based on dyes organization

The interaction between chromophores can be tuned by controlling their organization in the volume of the NPs. Some relevant examples of this kind of approach applied to the design of ultra-bright NPs are discussed in this section.

4.4.1 Bulky counterions as spacers

A convenient approach to avoid ACQ by partial organization of dyes has been proposed by Klymchenko and co-workers in the case of organic NPs obtained by

nano-emulsification. These NPs consist in oily nano-droplets with liquid-core stabilized by neutral surfactants. Incorporation of charged molecules such as cyanines in these structures is poorly efficient because of the apolar nature of the matrix. The use of bulky lipophilic counterions was hence proposed as an effective method to achieve heavy loading of the NPs and, simultaneously, to minimize ACQ. NPs could be loaded at up to 8%(w/w) concentration into nanodroplets of controlled size in the range from 30 to 90 nm giving systems that contained >10,000 cyanine molecules per particle. These NPs were >100-fold righter than quantum dots and, despite their liquid nature, they demonstrated to be stable enough for in vivo imaging and single-particle tracking in the blood flow of live zebrafish embryo (as demonstrated in figure 4.5), showing minimal cytotoxicity.[55]

In a similar approach, liquid-like salts of a cationic dye (octadecyl rhodamine B) with a bulky hydrophobic counterion (fluorinated tetraphenylborate) were used to prepare 40-nm PLGA NPs containing up to 500 dyes and brighter than quantum dots. Moreover, these NPs exhibited photo-induced reversible on/off fluorescence switching suitable for super-resolution imaging due to the collective switching of hundreds of dyes resulting from ultrafast FRET. These NPs were spontaneously endocytosed by living cells, showing high signal-to-noise ratio and absence of toxicity.[56]
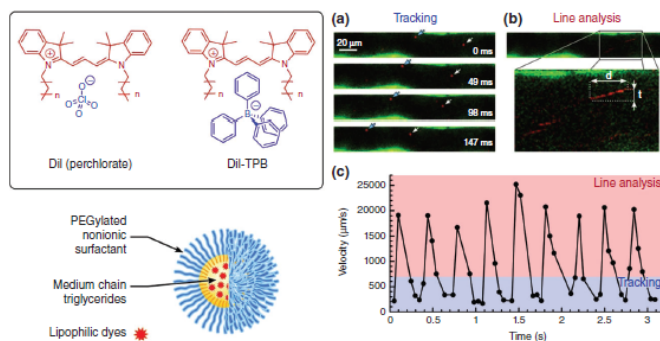
Figure 4.5: (Left) Chemical structures of DII perchlorate and DII-TPB and schematic presentation of nanotroplet encapsulating them. (Right) Single-particle tracking of DII-TPB nanodroplets in zebrafish vessels. During the diastole single particles were followed in consecutive frames (a). During the systole the velocity was calculated from the shape of the line, which is a result of the movement of the particles during the line scanning (b). (c) Reconstruction of the blood profile.[55]

4.4.2 Bulky Substituents

Aggregation of the dyes can be prevented by introducing bulky substituent in

their structures. Application of this strategy to NPs was recently demonstrated in the case of PDIs[57] encapsulated into biodegradable PLGA NPs. Two different kinds of PDIs were tested, one bearing bulky hydrophobic groups at the imides, while the other was substituted in both imide and bay regions (Lumogen Red, Fig. 4.6). In contrast to the former dye, Lumogen Red showed nearly no aggregation inside the polymer NPs and maintained high quantum yield and photostability. PLGA NPs loaded with 1% (w/w) Lumogen Red were >10-fold brighter than quantum dots (QD-585), were stable in biological media and, as shown in figure 4.6, entered spontaneously into HeLa cells by endocytosis showing no sign of cytotoxicity.

4.4.3 Mesoporous Matrix

Sokolov and coworkers proposed the use of mesoporous silica NPs as hosting materials to control intermolecular interactions.[58] According to this strategy, dye molecules are physically entrapped in the cylindrical nano-channels created through a templated sol-gel synthesis. These authors showed that the lack of aggregation, and consequently of the fluorescence quenching, can be extended to a level of dye concentrations which are up to four orders of magnitude higher than for the free dye in water.
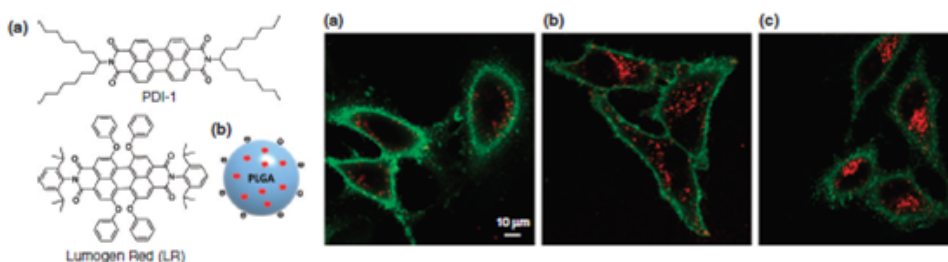
Figure 4.6: Left: chemical structure of PDI-1 and LR dyes (a) and schematic presentation of dye-doped poly(DL-lactide-co-glycolide) (PLGA) nanoparticles (b). Right: confocal fluorescence imaging of HeLa cells cultured for 1 (a), 2 (b) and 6 (c) h in the presence of 1wt% LR NPs and for 10 minutes in the presence of wheat germ agglutinin-Alexa488 for labelling cell membranes.[57]

4.5 Stimuli responsive probes

ACQ and PCQ and their amplification are severe drawbacks of multichromophoric systems in their use as environmental insensitive nanoprobes, but they can become powerful tool to develop stimuli-responsive NPs.
Stimuli-induced disaggregation of the moieties quenched by ACQ and PCQ, in fact,

produces a real blast of the PL signal allowing ultrasensitive detection. Surprisingly, although ACQ has been reported far before AIE, application of the related DIE process to the design of light-up nanosystems has not been systematically considered yet. On the contrary, a substantial number of review articles discussing AIE have recently appeared.[2,3,18] Here, they will be discussed some relevant examples of DIE-based fluorogenic NPs. Haag and co-workers synthesized and characterized a new water-soluble membrane marker based on an amphiphilic dendritic polyglycerol perylene imido dialkylester which forms quenched aggregates in water. These NPs become highly green fluorescent when incorporated into a lipophilic environment, such as biological membranes.[59] These fluorogenic NPs were used as fluid phase marker for disordered domains in artificial membranes and they were efficiently taken up into living cells following endocytic pathways. Zheng and co-workers proposed the use of nanovesicles generated by porphyrin bilayers (porphysomes) as multimodal contrast agents.[60] These NPs showed tunable extinction coefficients and structure-dependent fluorescence self-quenching. Quenched porphysomes enabled the sensitive visualization of lymphatic systems using photoacoustic tomography. On the other hand, NIR fluorescence could be turned on by inducing dyes dissociation via enzymatic linkers degradation allowing low-background fluorescence imaging. Finally, the authors demonstrated the applicability of porphysomes as photo-therapeutic agents: upon systemic administration, porphysomes accumulated in tumours allowing laser irradiation-induced photothermal tumour ablation.
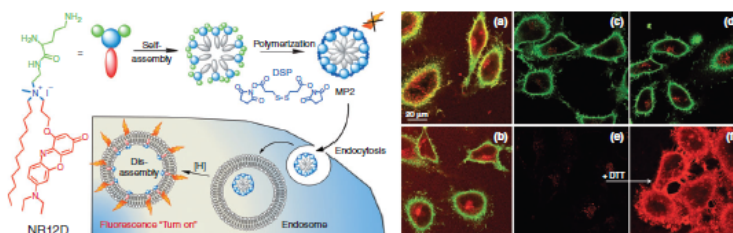
Figure 4.7: (Left) Scheme of the disassembly driven fluorescence turn-on in micellar nanoparticles by intracellular reductive stimuli. (Right) Fluorescent turn-on of polymerized micelles in living HeLa cells under reductive stimuli. Fluorescence confocal images of HeLa cells incubated with NR12D (a, b) and MP2 (c, d) for 10 min (a, c) and 1 h (b, d). (e, f) Images of HeLa cells after 1 h incubation with MP2 before (e) and after (f) addition of 10 μM reducing agent (dithiothreitol, DTT). Concentration of NR12D and MP2 (expressed in amphiphile molecules) was 0.5 μM. The green fluorescence corresponds to the membrane marker wheat germ agglutinin-Alexa Fluor 488, while the red fluorescence corresponds to the Nile Red-based dyes.[61]

Klymchenko and coworkers prepared redox responsive fluorogenic 20nm NPs, which disassemble in living cells into highly fluorescent molecular units, by polymerizing fluorescent amphiphiles with a redox-cleavable cross-linker.[61] The fluorescent precursor NR12D (Fig. 4.7) is a membrane probe which bears the hydrophobic fluorophore Nile Red and that self-assembly into self-quenched micellar structures. The two hydrophilic amine groups of the ornithine residue were polymerized with an amine-reactive agent bearing a redox-cleavable disulfide bond. The response of the fluorogenic probe to a reductive stimulus in HeLa cells is shown in figure 4.7. According to the authors, their results pave the way to new stimuli-responsive NPs that combine background-free imaging and drug delivery.

4.6 Conclusion and prospective

High brightness is not a trivial feature of heavily dye-doped nanomaterials. Processes as ACQ and PCQ lead to a severe quenching of the PL of NPs because of collective events involving FRET. Access to ultra-bright NPs requires hence a dedicated synthetic design that, at the same time, needs to be conveniently simple, considered that the most intriguing advantage of NPs with respect to macromolecular systems with a well-defined structure and composition, is their easiness of preparation. Although ACQ and PCQ can be prevented with a minimal synthetic effort through a specific choice of the luminescent precursor, this approach reduces the variety of building block available. On the contrary, a control of the dye distribution in the NPs aimed to avoid proximity and aggregation, consents the use of a large library of precursors, but it requires smart and convenient strategies to control at least in part their mutual interactions. Although both approaches are in principle efficient, we believe that a complete control of the photophysical properties of dye bases nanosystems is still challenging especially because of the complexity of these structures and of the poor knowledge of the actual organization and mobility of the emitters in their interior.

Nevertheless, these NPs showed unique performances in the amplification and easy detection of biological relevant events if properly designed to respond to internal or environmental signals. Focusing on this aspects, we tried to develop stimuli responsive nanoparticles, based on dye with a strong tendency to aggregate and quench in aqueous environment, but able to generate strongly fluorescent species in different conditions, such as concentration or polarity, as a consequence of DIE. Considering that a detailed photophysical characterization of the existing materials, combined with an appropriate modelling of their properties, would give a decisive input to the design of better performing NPs, we based our research on perylene

diimide derivatives, since, as it will further show, they are well studied and their properties perfectly matched with the desired ones.

Bibliography

1   Montalti, M., Battistelli, G., Cantelli, A. & Genovese, D. Photo-tunable multicolour fluorescence imaging based on self-assembled fluorogenic nanoparticles. *Chemical Communications* **50**, 5326-5329, doi:10.1039/C3CC48464E (2014).

2   Hong, Y., Lam, J. W. Y. & Tang, B. Z. Aggregation-induced emission. *Chemical Society Reviews* **40**, 5361-5388, doi:10.1039/C1CS15113D (2011).

3   Hong, Y., Lam, J. W. & Tang, B. Z. Aggregation-induced emission: phenomenon, mechanism and applications. *Chemical communications*, 4332-4353 (2009).

4   Montalti, M. *et al.* Energy transfer from a fluorescent hydrogel to a hosted fluorophore. *Langmuir* **22**, 2299-2303 (2006).

5   Montalti, M., Zaccheroni, N., Prodi, L., O'Reilly, N. & James, S. L. Enhanced sensitized NIR luminescence from gold nanoparticles via energy transfer from surface-bound fluorophores. *Journal of the American Chemical Society* **129**, 2418-2419 (2007).

6   Rampazzo, E. *et al.* Energy Transfer from Silica Core– Surfactant Shell Nanoparticles to Hosted Molecular Fluorophores†. *The Journal of Physical Chemistry B* **114**, 14605-14613 (2010).

7   Montalti, M., Prodi, L., Rampazzo, E. & Zaccheroni, N. Dye-doped silica nanoparticles as luminescent organized systems for nanomedicine. *Chemical Society Reviews* **43**, 4243-4268, doi:10.1039/C3CS60433K (2014).

8   Caltagirone, C., Bettoschi, A., Garau, A. & Montis, R. Silica-based nanoparticles: a versatile tool for the development of efficient imaging agents. *Chemical Society Reviews* (2015).

9   Hu, R., Leung, N. L. & Tang, B. Z. AIE macromolecules: syntheses, structures and functionalities. *Chemical Society Reviews* **43**, 4494-4562 (2014).

10   Wu, C. & Chiu, D. T. Highly fluorescent semiconducting polymer dots for biology and medicine. *Angewandte Chemie International Edition* **52**, 3086-3109 (2013).

11   Bonacchi, S. *et al.* Amplified fluorescence response of chemosensors grafted onto silica nanoparticles. *Langmuir* **24**, 8387-8392 (2008).

12   Fan, C. *et al.* Beyond superquenching: hyper-efficient energy transfer from conjugated polymers to gold nanoparticles. *Proceedings of the National Academy of Sciences* **100**, 6297-6301 (2003).

13   Montalti, M., Prodi, L. & Zaccheroni, N. Fluorescence quenching amplification in silica nanosensors for metal ions. *Journal of Materials Chemistry* **15**, 2810-2814 (2005).

14   Battistelli, G., Cantelli, A., Guidetti, G., Manzi, J. & Montalti, M. Ultra-bright and stimuli-responsive fluorescent nanoparticles for bioimaging. *Wiley Interdisciplinary Reviews: Nanomedicine and Nanobiotechnology*, n/a-n/a, doi:10.1002/wnan.1351 (2015).

15   Stennett, E. M., Ciuba, M. A. & Levitus, M. Photophysical processes in single molecule organic fluorescent probes. *Chemical Society Reviews* **43**, 1057-1075 (2014).

16   Anthony, S. P. Organic Solid-State Fluorescence: Strategies for Generating Switchable and Tunable Fluorescent Materials. *ChemPlusChem* **77**, 518-531 (2012).

17   Fery-Forgues, S. Fluorescent organic nanocrystals and non-doped nanoparticles for biological applications. *Nanoscale* **5**, 8428-8442 (2013).

18   Ciardelli, F., Ruggeri, G. & Pucci, A. Dye-containing polymers: methods for preparation of mechanochromic materials. *Chemical Society Reviews* **42**, 857-870 (2013).

19   Lin, Y. *et al.* Diethylamino functionalized tetraphenylethenes: structural and electronic modulation of photophysical properties, implication for the CIE mechanism and application to cell imaging. *Journal of Materials Chemistry C* **3**, 112-120 (2015).

20   Chen, J. *et al.* Synthesis, light emission, nanoaggregation, and restricted intramolecular rotation of 1, 1-substituted 2, 3, 4, 5-tetraphenylsiloles. *Chemistry of materials* **15**, 1535-1546 (2003).

21   Butler, T., Morris, W. A., Samonina-Kosicka, J. & Fraser, C. L. Mechanochromic luminescence and aggregation induced emission for a metal-free β-diketone. *Chemical Communications* **51**, 3359-3362 (2015).

22   Chi, Z. *et al.* Recent advances in organic mechanofluorochromic materials. *Chemical Society Reviews* **41**, 3878-3896 (2012).

23   Mei, J. *et al.* Aggregation-Induced Emission: The Whole Is More Brilliant than the Parts. *Advanced Materials* **26**, 5429-5479 (2014).

24   Ding, D., Li, K., Liu, B. & Tang, B. Z. Bioprobes based on AIE fluorogens. *Accounts of chemical research* **46**, 2441-2453 (2013).

25   Merdasa, A. *et al.* Single Lévy states–disorder induced energy funnels in molecular aggregates. *Nano letters* **14**, 6774-6781 (2014).

26   Geng, J. *et al.* Eccentric Loading of Fluorogen with Aggregation-Induced Emission in PLGA Matrix Increases Nanoparticle Fluorescence Quantum Yield for Targeted Cellular Imaging. *Small* **9**, 2012-2019 (2013).

27   Li, K. *et al.* Organic dots with aggregation-induced emission (AIE dots) characteristics for dual-color cell tracing. *Chemistry of Materials* **25**, 4181-4187 (2013).

28   Zhang, X. *et al.* A novel method for preparing AIE dye based cross-linked fluorescent polymeric nanoparticles for cell imaging. *Polymer Chemistry* **5**, 683-688 (2014).

29   Zhang, X. *et al.* Surfactant modification of aggregation-induced emission material as biocompatible nanoparticles: Facile preparation and cell imaging. *Nanoscale* **5**, 147-150 (2013).

30   Liu, M. *et al.* Ultrabright and biocompatible AIE dye based zwitterionic polymeric nanoparticles for biological imaging. *RSC Advances* **4**, 35137-35143 (2014).

31   Kim, S., Pudavar, H. E., Bonoiu, A. & Prasad, P. N. Aggregation-Enhanced Fluorescence in Organically Modified Silica Nanoparticles: A Novel Approach toward High-Signal-Output Nanoprobes for Two-Photon Fluorescence Bioimaging. *Advanced Materials* **19**, 3791-3795 (2007).

32   Wang, Z. *et al.* Folic acid-functionalized mesoporous silica nanospheres hybridized with AIE luminogens for targeted cancer cell imaging. *Nanoscale* **5**, 2065-2072 (2013).

33   Zhang, X. *et al.* Novel biocompatible cross-linked fluorescent polymeric nanoparticles based on an AIE monomer. *Journal of Materials Chemistry C* **2**, 816-820 (2014).

34   Yu, J. *et al.* Water-Dispersible, pH-Stable and Highly-Luminescent Organic Dye Nanoparticles with Amplified Emissions for In Vitro and In Vivo Bioimaging. *Small* **10**, 1125-1132 (2014).

35   Zhang, X. *et al.* Aggregation induced emission-based fluorescent nanoparticles: fabrication methodologies and biomedical applications. *Journal of Materials Chemistry B* **2**, 4398-4414 (2014).

36   Xia, Y. *et al.* Water-soluble nano-fluorogens fabricated by self-assembly of bolaamphiphiles bearing AIE moieties: towards application in cell imaging. *Journal of Materials Chemistry B* **3**, 491-497 (2015).

37   Yu, Y. *et al.* Cytophilic Fluorescent Bioprobes for Long-Term Cell Tracking. *Advanced Materials* **23**, 3298-3302 (2011).

38   Zhang, X. *et al.* Fabrication of aggregation induced emission dye-based fluorescent organic nanoparticles via emulsion polymerization and their cell imaging applications. *Polymer Chemistry* **5**, 399-404 (2014).

39   Pedone, A. *et al.* Understanding the photophysical properties of coumarin-based Pluronic–silica (PluS) nanoparticles by means of time-resolved emission spectroscopy and accurate TDDFT/stochastic calculations. *Physical Chemistry Chemical Physics* **15**, 12360-12372 (2013).

40   Rampazzo, E., Bonacchi, S., Montalti, M., Prodi, L. & Zaccheroni, N. Self-organizing core-shell nanostructures: spontaneous accumulation of dye in the core of doped silica nanoparticles. *Journal of the American Chemical Society* **129**, 14251-14256 (2007).

41   Howes, P., Thorogate, R., Green, M., Jickells, S. & Daniel, B. Synthesis, characterisation and intracellular imaging of PEG capped BEHP-PPV nanospheres. *Chem. Commun.*, 2490-2492 (2009).

42   Hashim, Z., Howes, P. & Green, M. Luminescent quantum-dot-sized conjugated polymer nanoparticles—nanoparticle formation in a miniemulsion system. *Journal of Materials Chemistry* **21**, 1797-1803 (2011).

43   Li, K. *et al.* Polyhedral Oligomeric Silsesquioxanes-Containing Conjugated Polymer Loaded PLGA Nanoparticles with Trastuzumab (Herceptin) Functionalization for HER2-Positive Cancer Cell Detection. *Advanced Functional Materials* **21**, 287-294 (2011).

44   Howes, P., Green, M., Levitt, J., Suhling, K. & Hughes, M. Phospholipid encapsulated semiconducting polymer nanoparticles: their use in cell imaging and protein attachment. *Journal of the American Chemical Society* **132**, 3989-3996 (2010).

45   Wu, C., Bull, B., Szymanski, C., Christensen, K. & McNeill, J. Multicolor conjugated polymer dots for biological fluorescence imaging. *Acs Nano* **2**, 2415-2423 (2008).

46   Wu, C. *et al.* Design of highly emissive polymer dot bioconjugates for in vivo tumor targeting. *Angewandte Chemie International Edition* **50**, 3430-3434 (2011).

47   Wang, L., Yang, C. & Tan, W. Dual-luminophore-doped silica nanoparticles for multiplexed signaling. *Nano letters* **5**, 37-43 (2005).

48   Rampazzo, E. *et al.* Nanoparticles in metal complexes-based electrogenerated chemiluminescence for highly sensitive applications.

Coordination Chemistry Reviews **256**, 1664-1681 (2012).

49 Zanarini, S. *et al.* Iridium Doped Silica–PEG Nanoparticles: Enabling Electrochemiluminescence of Neutral Complexes in Aqueous Media. *Journal of the American Chemical Society* **131**, 14208-14209, doi:10.1021/ja906666e (2009).

50 Xu, Z. *et al.* Water-miscible organic J-aggregate nanoparticles as efficient two-photon fluorescent nano-probes for bio-imaging. *Journal of Materials Chemistry* **22**, 17737-17743 (2012).

51 Wang, L. *et al.* Novel highly emissive H-aggregates with aggregate fluorescence change in a phenylbenzoxazole-based system. *Chemical Communications* **50**, 8723-8726 (2014).

52 Genovese, D. *et al.* Energy transfer processes in dye-doped nanostructures yield cooperative and versatile fluorescent probes. *Nanoscale* **6**, 3022-3036 (2014).

53 Rampazzo, E. *et al.* Pluronic-silica (plus) nanoparticles doped with multiple dyes featuring complete energy transfer. *The Journal of Physical Chemistry C* **118**, 9261-9267 (2014).

54 Genovese, D. *et al.* Prevention of Self-Quenching in Fluorescent Silica Nanoparticles by Efficient Energy Transfer. *Angewandte Chemie International Edition* **52**, 5965-5968 (2013).

55 Kilin, V. N. *et al.* Counterion-enhanced cyanine dye loading into lipid nano-droplets for single-particle tracking in zebrafish. *Biomaterials* **35**, 4950-4957 (2014).

56 Reisch, A. *et al.* Collective fluorescence switching of counterion-assembled dyes in polymer nanoparticles. *Nature communications* **5** (2014).

57 Trofymchuk, K., Reisch, A., Shulov, I., Mély, Y. & Klymchenko, A. S. Tuning the color and photostability of perylene diimides inside polymer nanoparticles: towards biodegradable substitutes of quantum dots. *Nanoscale* **6**, 12934-12942 (2014).

58 Cho, E. B., Volkov, D. O. & Sokolov, I. Ultrabright fluorescent silica mesoporous silica nanoparticles: control of particle size and dye loading. *Advanced Functional Materials* **21**, 3129-3135 (2011).

59 Heek, T. *et al.* An Amphiphilic Perylene Imido Diester for Selective Cellular Imaging. *Bioconjugate Chemistry* **24**, 153-158, doi:10.1021/bc3005655 (2013).

60 Lovell, J. F. *et al.* Porphysome nanovesicles generated by porphyrin bilayers

for use as multimodal biophotonic contrast agents. *Nature materials* **10**, 324-332 (2011).

61   Niko, Y., Arntz, Y., Mely, Y., Konishi, G. i. & Klymchenko, A. S. Disassembly-Driven Fluorescence Turn-on of Polymerized Micelles by Reductive Stimuli in Living Cells. *Chemistry-A European Journal* **20**, 16473-16477 (2014).

5. Perylene diimide derivatives

The first perylene-3,4,9,10-tetracarboxylic acid diimide (PDI) appeared as a colorant in1913[1] known as Pigment Red 179. Derived from the Perylene-3,4,9,10-tetracarboxylic dianhydride (PTCDA), it was the forefather of a class of industrial pigments with red to violet and even black shades, differently functionalized to obtain variations on molecular packing in the solid state.[2] The fortune of this group of compounds was due to the excellent chemical, thermal, photo and weather stability, but also to the good migration stability on plastic coating and the easy applicability as over-coating of other painted surfaces.[1-4] Since the early '50s PDIs were widely applied in industry both as dyes and pigments and they found, nowadays, uses in fibers and high-grade industrial paints, thanks to the high quality and durability of the colours.[1-4]

Perylene diimide derivatives applications, anyway, are not limited to pigment industries. They attracted attention also for the near unity fluorescent quantum yield and the strong electron-accepting character. These features, combined with the strong photostability, made PDIs and the related mono-imide derivatives, attractive for electronic and optical applications, as organic field-effect transistor (OFETs),[5-8] fluorescent solar collectors,[9] electro-photographic devices,[10] dye lasers [11] and organic photovoltaic cells (OPVs).[6,12,13] Moreover PDIs have proved to be great candidates for single molecules spectroscopy, [14] to be suitable for sensors at single molecule level[15] and to be archetype building blocks for self assembled functional supramolecular materials.[16] Briefly, they show an outstanding combination of favourable properties for fundamental studies, for a broad variety of industrial applications and, last but not least, simplicity to be tailored for their self assembly into supramolecular architectures.[16]

5.1 PDIs characteristic overview

The suitability of perylene diimide derivatives in such a large range of applications, can be spotted in the molecular structure. The rigid polycyclic aromatic unit, the perylene, is substituted with two dicarboxylic acid imide groups at the *3,4-* and *9,10-peri*-position, forming an acceptor-donor-acceptor scaffold between the electron-rich perylene core and the strongly conjugated electron-withdrawing amino groups. That causes the absorption band of perylene shifting from ~440 to ~525 nm without changing the characteristic vibronic progression of

the aromatic portion.[16] Moreover, since the scaffold is rigid and planar and the triplet level is very low, the unfavourable $S_1 \rightarrow T_1$ intersystem crossing[11] makes the fluorescence spectrum mirroring the absorption and an almost unitary fluorescent quantum yield can be observed either in aliphatic, aromatic, chlorinated and dipolar solvents, when the aggregation is avoided. If the almost unitary fluorescence quantum yield is a common property to a large class of fluorophores, it is the combination with the characteristic thermal, chemical and photochemical stability which makes PDIs unique, and opens the door to the multitude of the applications listed above. Thanks to the poorness of the π-conjugated scaffold, in fact, the structure is very resistive to oxidative degradation and other decomposition pathways, while the inaccessibility of the triplet state reduces the probability of a photochemical reaction.

5.2 Preparation of PDI derivatives

In the industrial field of colorants, insoluble symmetrical PDIs with high melting point are easily obtained reacting the PTCDA with the respective aliphatic amines or anilines.[17] Typically reactions occur in high yields, such as in the case of the common Pigment Red 179, Pigment Red 178, and Pigment Red 149 (1A-C, scheme 5.1), where yields of over 90% from PTCDA are afforded. This strategy, anyway, cannot satisfy the new applicative fields, where PDIs with a reasonable solubility in common solvents are required.[4,18,19] In this prospective, two successful synthesis strategies from PTCDA have been developed: the imidization and the substitution in bay position.

5.2.1.Imidization.

Firstly developed by Langhals and co-workers in the 1990s, it is the most commonly employed approach[20] and consists of the introduction of the solubilizing groups at the imide nitrogen position (**1d, 1e** of scheme 5.3)[21] It was proved that branched long alkyl chain attached at the imide nitrogen atom through their central position ("swallowtail substituents")[22] and ortho-substituted *N*-aryl groups,[23] are forced out of the plane of the PDI chromophore, limiting the face-to-face π-π stacking of the PDI molecules.[4,22,23] Interestingly, photophysical properties are not influenced, because the coupling between the perylene diimide units and the imide substituents is reduced to a minimum by the presence of nodes in the HOMO and LUMO at the imide nitrogen.[21]

According with this synthetic method, symmetrically *N,N'*-substituted PDIs are

obtained by the condensation reaction of PTCDA with anilines and aliphatic primary amines (A, scheme 5.1). Because PTCDA is strongly insoluble in almost all the most common organic solvents, the reaction is carried out in molten imidazole or quinoline at temperatures higher than 160°C and with zinc acetate anhydrous (typically 10-30 mol %) as a catalyst. The product can be easily purified and the isolated yields usually approach 95%.[4,20,24] Isolated yields over 90% are alternatively obtained by treatment of PTCDA (or analogues with dibromo or tetrachloro substitution of the "bay" positions) with primary amines in hot alcohols (e.g. *n*-butanol), carboxylic acids (e.g. acetic and propionic acid), or alcohol/water mixtures (e.g. 1:1 *n*-butanol/water) (B, scheme 5.1).[24] Reacting PTCDA with *o*-phenylenediamine derivatives (C, scheme 5.1),benzoimidazole derivatives in good isolated yields can be obtained, even if the mixture of the two regioisomers is not easy to separate, either by column chromatography or re-crystallization.[19,24,25]
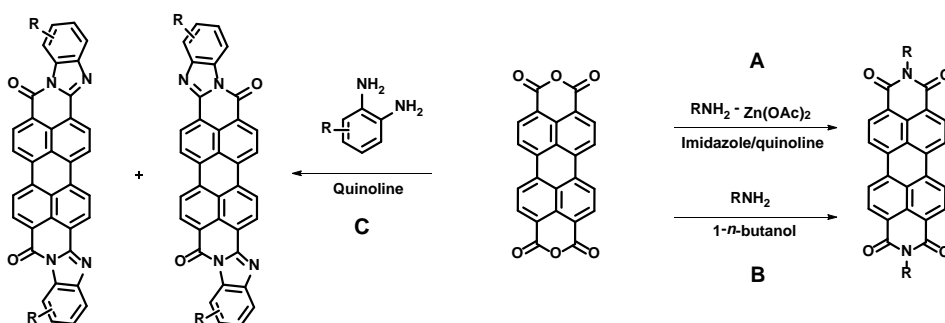
Scheme 5.1: (A and B) conversion of PTCDA to dialkyl and diaryl PDIs. (C) Conversion of PTCDA in perylene benzoimidazole derivatives.

Synthetic effort was even performed to obtain PDIs with different substituents on each imide position (asymmetric derivatives). Either simultaneous or sequential addition of two different amines to PTCDA, anyway, came out to be unsuccessful, because of the amines different reactivity with PTCDA which typically results in the formation of the symmetrical PDIs derivatives and only traces of the desired product.[24] Accordingly, multistep methods where developed.[24]

The most common one (Method I, scheme 5.2) is the partial hydrolysis of symmetrical PDIs to perylene monoimide monoanhydride compounds and their imidization with the second amine or aniline. Imide-benzoimidazole has also been prepared from a mixed imide-anhydride with an *o*-phenylenediamine derivative.[26] It should be noted that it is typically challenging to direct synthesize perylene

monoanhydride monoimide compounds by imidization of PTCDA. Even when a strong defect of primary amine is used, diimides are the predominant products, probably because the first imidization causes a significant increasing of the intermediate mixed imide-anhydride solubility respect to that of PTCDA.

Another method to achieve asymmetrical PDI synthesis, described by Tam-Chan and co-workers in the late 1990s (Method II, scheme 5.2),[27]is based on partial hydrolysis of PTCDA to a mixed anhydride-dicarboxylate salt, followed by successive imidization reactions. However, the possibility of obtaining the desired material in higher yield and by usually easy purification, makes method I the most widely utilized.[26,28-31]
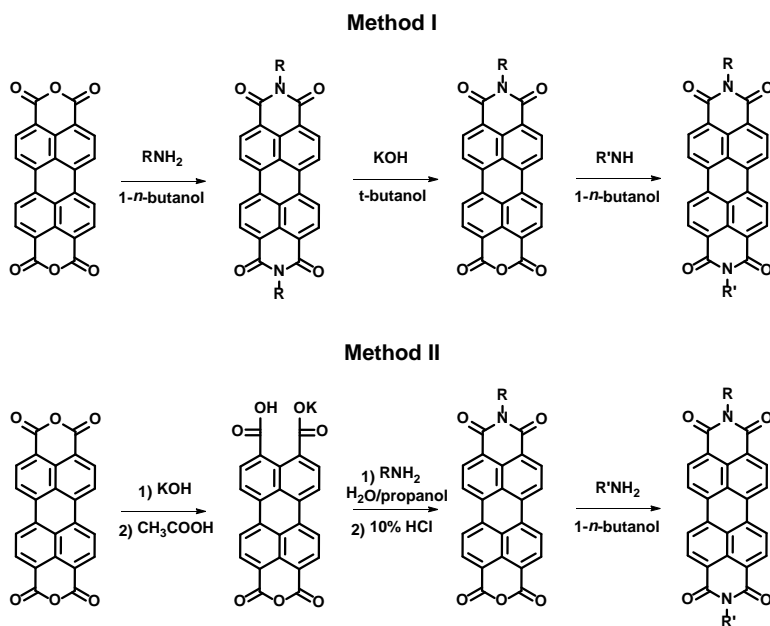
Method I

Method II

Scheme 5.2: Methods for the preparation of asymmetrical PDIs with different substituents on the imide positions.(Top) Method I: partial hydrolysis of symmetrical PDIs to perylene monoimide monoanhydride compounds and their imidization with the second amine or aniline. (Bottom) Method II: partial hydrolysis of PTCDA to a mixed anhydrid-dicarboxylate salt, followed by successive imidization reactions.

5.2.2 Substitution in bay position

Substitution in bay position consists in the carbocyclic scaffold functionalization in the so-called "bay-area". As in the case of imidization, the substituents are forced out of the molecule plane, reducing the steric interactions. Moreover, they induce

the twist of the naphtalene half units in PDIs, amplifying this effect. By this strategy, the effect on the solubility is reasonable for small substituents, such as bromo, and it can be increased by several orders of magnitude by the incorporation of bulky groups.[32] This strategy can be used to significantly modify the molecular-level electronic and optical properties of PDIs. Substitution in bay position was firstly developed at BASF in the 1980s by Seybold and co-workers, who incorporated four phenoxy groups in high yield by nucleophilic displacement of chlorine substituents (**9a,** scheme 5.3) heating the corresponding tetrachloro species with phenol and potassium carbonate in *N*-methylpyrrolidone.[33] Unfortunately, the introduction of other nucleophiles was proved to be difficult and a single reaction product with reasonable yield was rarely afforded.[16] Although the procedure for fourfold chlorination of perylene bisanhydride **2** (scheme 5.3) was already known for a while,[34,35] only very recently it was discovered that bromination of perylene bisanhydride **2** affords di-substituted derivatives **4**.[36] However, the product mixture obtained by bromination is even worse than in the case of chlorination, because threefold bromination products are formed. Moreover a significant amount of a second dibromo regioisomers, which cannot be easily removed from the product mixture[37,38] and which is only detectable by high field (>400 MHz)^{1}H NMR spectroscopy, is formed.[32,39] Gratifyingly, exchange of the bromine substituents of **4** is straightforward; thus, carbon[36], cyano,[5] oxygen[36] and nitrogen[40,41] nucleophiles could be coupled to the perylene core leading to novel perylene diimide dyes **5-8** with interesting optical and redox features. Starting from the acetylenic derivative **8a** even corenene diimides **10** can be obtained in isomeric mixture, which could not be separated.[37,38]
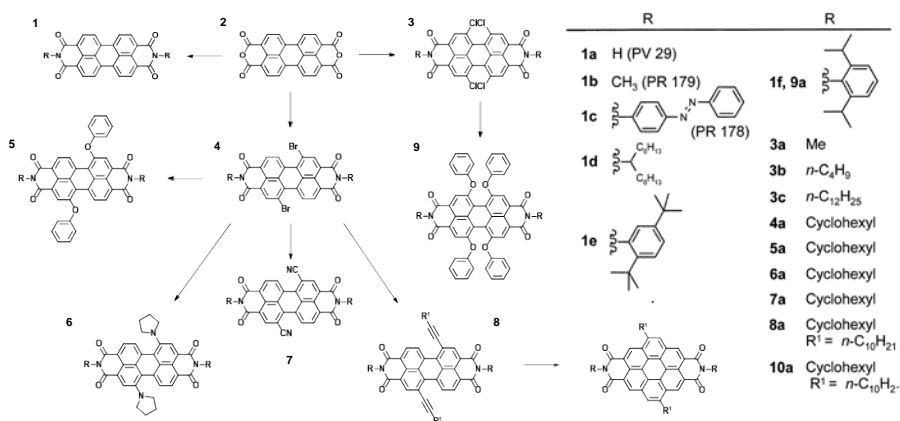
Scheme 5.3:Preparation of PDIs with various substituents in the bay position.[4]

5.3 Optical properties

Typical *N,N'*-dialkyl or diaryl PDIs can be regarded as a closed chromophoric system with an $S_0 \rightarrow S_1$ transition polarized along the long molecular axis and described, by computational calculations, as a HOMO-LUMO excitation.[2,35] In the absence of aggregation effects and of substituents on the "bay" area, it consists in strong vibronically structured absorptions located between 524 and 527 nm (in dichloromethane),[42] with maxima at ca. 525 nm and peak absorption coefficients approaching 10^5 $M^{-1}cm^{-1}$. The corresponding fluorescence spectrum typically exhibits a small Stokes shift and mirrors the absorption spectrum in solvents such as toluene and chloroform.[4] In many cases, the fluorescence quantum yields are higher than 0.9, and the singlet excited-state lifetimes are approximately 4 ns in common organic solvents, as it can be appreciated in table 5.1.[4,11,24,43,44] Moreover, photophysical properties are modestly influenced by the solvent and the maximum absorption changes from 517 nm in aliphatic solvents to 530 nm in chloroform for alkyl substituted PDIs.[42] This effect can be attributed to the excited state polarization by the solvent molecules which polarity is related to the refractive index. The symmetries of the orbitals also implies that the nitrogen atoms are located on nodal planes of both HOMO and LUMO (Fig. 5.1) and, accordingly, the effects of imide substitution on the frontier orbital energies are inductive in nature and similar for both the frontier orbitals. This leads to little changes in the optical properties for absorption and emission maxima, which generally, shift by ca. < 5 nm with variation of *N,N'* aryl or alkyl substituents.[24] By Molecular Orbitals calculations has been explained, as well, the bathochromical shift of benzoimidazole-annulated derivatives spectra respect to those of simple PDIs, consistent with a more extensive delocalization of the HOMO into the terminal arylene group.[45,46]
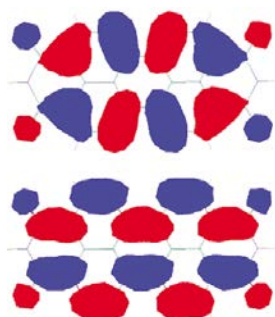
Figure 5.1: (top) HOMO and (bottom) LUMO of perylene diimides. Both the frontiers orbitals exhibit nodes at the imide nitrogens.[4]

Even if it does not influence the energetic level of the molecules, the presence of imide substituents plays an important role in the fluorescence behaviour. Simple phenyl group can induce the vibronic motion ('loose bolt effect')[23] reducing the quantum yield of 30%[35] while more electron-rich aromatic groups, such as alkylated and alkoxylated phenyl groups[47,48] can reduce the quantum yield to values < 5%[23,49] in solvents from intermediate to high polarity, as a consequence of the photo-induced electron transfer that occurs from the substituent to the electron-poor perylene scaffold.

Differently respect to the imidization, the core substitution can affect the PDIs redox and photophysical properties, because there are significant HOMO and LUMO coefficients on the positions *1*, *6, 7* and *12*. According with theory, the functionalization in the "bay" area always leads to bathochromic shifts of the spectra since π-donor substituents destabilize the highest occupied orbital and π-acceptors stabilized the lowest unoccupied orbital.[50] It is also true that steric hindrance of the substituents can induce a PDIs cores twisting, which causes an hypsochromic shift, but this effect is usually negligible respect to the former one.[4]

Absorption maximum compared to that of the unsubstituted dyes **1** shifts by about 20 nm when two phenoxy groups are linked in positions *1* and *7*[4,49] and by almost 50 nm with four phenoxy groups. The respectively fluorescence colour changes to orange in **5** and to red in **9**. Interestingly, in both cases are maintained the high fluorescence quantum yield, the small solvent effects on the optical properties, the high photostability and the vibronic structure.

When two electro-donating groups are connected, such as in molecule **6**, where the substituents are pyrrolidino groups,[40] bathochromic shift is more pronounced, molecules turn green in colour and emission shifts in the infrared region. Because the effect is due to the photo-induced electron transfer, solvatochromism is stronger in this case and fluorescence is significantly decreased.[4,8,40]

The bathochromic effect of fluoro, chloro and bromo is of only few nanometres and, because their weak π-donor character, no significant charge-transfer is detected.[4,5,32,51] If electro-withdrawing substituents are attached, as in the case of dyes **3**, **4** and **7** little variations respect to the cases mentioned before are reported. In coronene diimide (**10**) the π-conjugated system orthogonal to the N-N axis results expanded and the observed significant changes in the absorption spectra are not typical for PDIs dyes.[32]

All the photophysical values referred to the mentioned compounds are reported below, in table 5.1.[4]

	λ_{abs}/nm	ε/M^{-1} cm^{-1}	λ_{em}/nm	Φ_f	τ_f/ns
1d	526	88 000	533	1.00	4.0
1e	526	95 000	537	1.00	3.7
3b	524	42 300	551	0.92	
4a	526	57 300	547		
5a	549	55 000	578	ca. 1	4.5
6a	686	46 000	721	0.35	4.5
7a	530	47 000	545	1.00	
8a	552	45 000	571		
9a	573	45 300	608	>0.96	7.4
10a	511	19 700	517		

Table 5.1: Optical properties of PDIs reported in scheme 5.3 in chloroform.[4]

As already mentioned, PDIs propensity to π-stacking induces dyes self-assembly, leading to a loss of the vibronic structure and to a change in the ratio between the vibronic resolved bands both for the absorption and fluorescence spectra. In particular the absorption bands of PDIs assemblies, respect to the monomeric ones, can be bathochromically (longer wavelengths) shifted with band sharpening and increasing of absorption coefficient, or hypsochromically (shorter wavelengths) shifted with band broadening and intensity decreasing (Fig. 5.2). Since the 1960s, self-assembled structures displaying bathochromic shifted absorption bands are called J aggregates, from Jelley[52] the name of the inventor of these aggregates made of cyanine dyes.[53] Self-assemblies with hypsochromic shifts of absorption bands, on the other hand, are commonly termed as H-aggregates. In both cases, assemblies display a lower fluorescence quantum yield respect to the relative monomers (Fig. 5.2).

While Kasha's exciton coupling theory[54-56] (i.e. coupling of transition dipole moments of the constituent dyes molecules with respect to their geometrical arrangements upon photoexcitation) well explain this behaviour in H-aggregates, it predicts a strong emission for the J-aggregates. In this latter spatial organization, other phenomena like quenching by trap sites[57,58] and singlet fission[59] are to take into account.

Kasha's exciton coupling model was discussed by Würthner and co-workers[16] in order to explain the spectral changes observed for both H and J-type PDIs self-assemblies. The model, schematized for PDIs molecules in figure 5.3, predicts that vertical excitation from S_0 to S_1 can lead to different higher electronic states, depending on the spatial arrangements of the dye unit constituting the assembly. For this reason, it was firstly took into account the easiest monomer configuration

for the dimer formation, which involves PDIs oriented with coplanar, parallel and equidistant transition moments. For the formed dimer, the gain achieved by Van der Waals forces, reduces both the energies of the ground state and of the excited state respect to that of the monomers. The effect is stronger for excited state, because here molecules are more polarizable and Van der Waals interactions are increased (ΔE_{VdW}). The excited state of such dimer splits in two excitonic state (called Frenkel excitons) as a consequence of excitonic coupling and the magnitude of this splitting ($\Delta\varepsilon$) depends on the magnitude of the dyes transition dipole moments (μ_{eg}), the distance and the mutual arrangement between the chromophores.

In the study[16] only the two borderline cases were described, in which the transition moments are in-line (with a slip angle of $\theta = 0°$, J-aggregate) or stacked on top of each other ($\theta = 90°$, H-aggregate). In between of these two limit conformations, there is a point, where sigmoidal curves have an intersection point and the alignment, has no energetic splitting. This occurs when the angle between the PDIs molecules is $\theta = 54,7°$ and the spectra of this aggregates are not distinguished from those of their monomers. Then, because the energy levels on the solid sigmoidal curve are allowed (high oscillator strengths), while the ones on the dashed lines are strictly forbidden (no oscillator strength), for PDI-PDI arrangements with θ values smaller than 54.7° the transition is energetically decreased with respect to the monomers transition (absorption maxima bathochromically shifted), whereas larger θ values result in an energy increase (absorption maxima hypsochromically shifted).

Upon photoexcitation of an ensemble of coupled chromophore, several additional relaxation processes, become feasible respect to the single dye, leading to new non radiative and/or radiative deactivation paths, as schematized in figure 5.4. According to Kasha's rule, when a single chromophore undergoes photoexcitation, the first occurring process is the very fast deactivation from the higher energy levels (S_n, $n \geq 1$) to the first excited state (S_1).[60] Possible deactivation path of such an electronic state in the case of PDI aggregate are schematized in figure 5.4.

It has been already mentioned that the fluorescence quantum yield for PDIs is generally very high and this is because the dominant process in this molecule is the allowed radiative deactivation to the ground state (S_0). On the contrary, non radiative path is poorly efficient because of the rigid structure of the perylene core, while intersystem crossing (ISC) is not competitive because the significant energetic difference between the singlet (S_1) and the triplet (T_1) involved state. On

the other hand, in the case of interacting PDIs molecules, selective excitation of an individual chromophore can lead to the formation of an excimer ^{1}(PDI-PDI)*, which has a lifetime enhanced up to 20 ns and which shows a red-shifted fluorescence and a reduced quantum yield. As an alternative, in the case of the formation of a PDI-PDI dimer at the ground state, the system could be directly excited at the first ^{1}(PDI-PDI)* state and then undergoes ISC to the triplet state, forming the triplet-singlet state ^{3}(PDI-PDI). This path is made more favourable in the dimer with respect to the monomer, because it may occur through intermediate charge transfer (PDI$^+$-PDI$^-$)[61] or excimer state. Although the endoergonic spin-allowed singlet (exciton) fission is also possible as a deactivation pathway, this process has only been observed in solid materials,[59] where it becomes favoured by entropy. It has to me mentioned, as well, that if charge separation take place (PDI$^+$-PDI$^-$), the radiationless charge recombination become strongly competitive.[61,62]
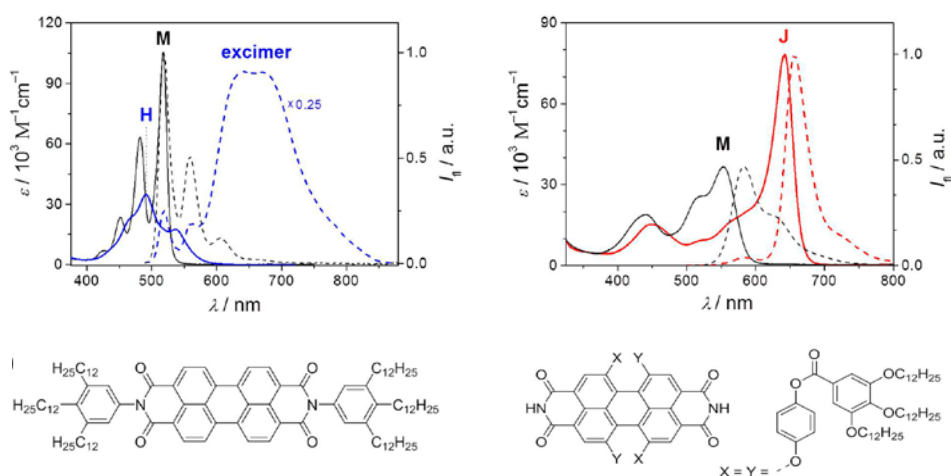
Figure 5.2: UV/Vis absorption (solid lines) and fluorescence spectra (dashed lines) of (left) an H-aggregating PDI and (right) a J-aggregating PDI in methylcyclohexane. (left) Monomer absorption (black, solid line; denoted with M) and emission spectra (black, dashed line) of the PDI at a low concentration of 2 × 10^{-7} M and hypsochromically shifted absorption (blue, solid line; denoted with H) and bathochromically shifted, broad excimer emission spectra (blue, dashed line) upon aggregation at a higher concentration of 1 × 10^{-3}M at 25 °C. (right) Monomer absorption (black, solid line; at 90 °C; denoted with M) and emission spectra (black, dashed line; at 50 °C) of the PDI, and bathochromically shifted J-aggregate absorption (red, solid line; denoted as J) and emission spectra (red, dashed line) at 15 °C. For the H-aggregating PDI the concentrations of the absorption measurements are 6 × 10^{-7} M and of the fluorescence experiments 2 × 10^{-7} M.[16]
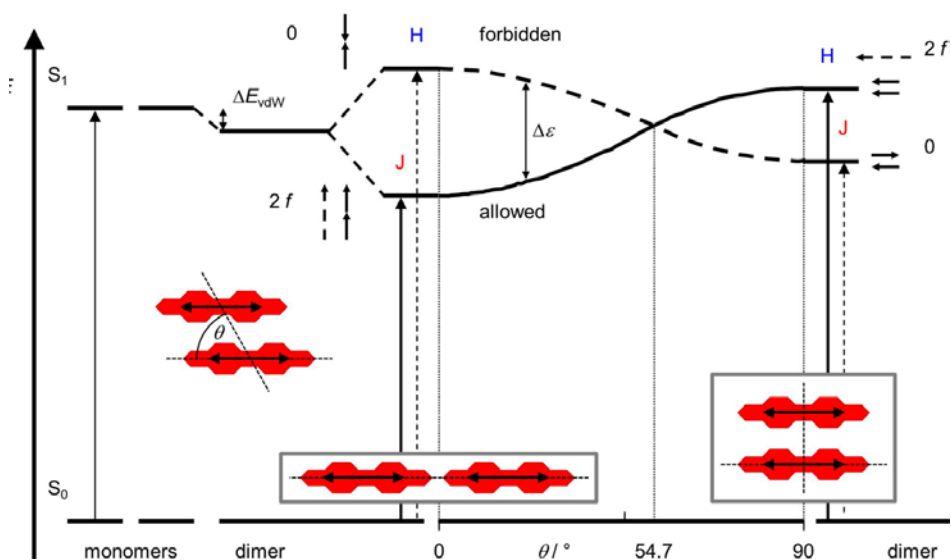
Figure 5.3: Schematic energy level diagram for the excitonic coupling of PDI dimers with coplanar transition dipole moments (μ_{eg}, depicted as double arrows) tilted toward the interconnecting axis by the slip angle θ. The two borderline cases, i.e., in-line (θ= 0°) and sandwich-like arrangement (θ= 90°), are shown in the gray boxes on the left and right side of the diagram. Additionally, for these two alignments, the resulting overall oscillator strengths (small dashed arrows) as well as the oscillator strengths (f, small solid arrows) of the two individual PDI units are indicated.[16]
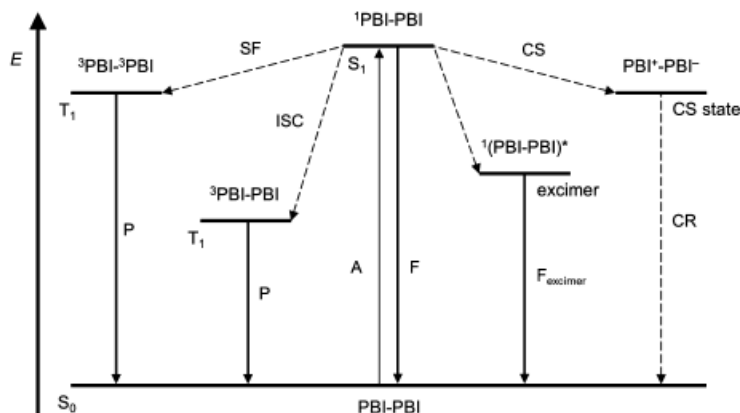
Figure 5.4: Simplified schematic energy level diagram for different excited states of a hypothetical PDI dimer (PDI–PDI) with possible radiative (solid arrows) or radiationless (dashed arrows) relaxation and excitation processes (A, absorption; F, fluorescence; SF, singlet fission; ISC, intersystem crossing; P, phosphorescence; CS, charge separation; CR, charge recombination). The respective higher vibrational levels of each state are not shown for clarity.[16]

Although a satisfactory description of the different properties of PDI monomer and dimers (considered as simple aggregate species), can be achieved simply considering the longitudinal shift along the dyes transition dipole moments, transversal displacement or rotational twist effects should also be taken into account. It is known by quantum dynamical calculations implemented by Engel and co-workers[63-65] that these parameters and as well the presence of larger oligomers, also influence the excitonic coupling and the resulting spectral behaviour.[66]

5.3.1 Aggregation stability models

As far as the aggregates stability is concerned, according to a first model, referred as monomer-dimer model,[67] the system is considered as an equilibrium between monomer and dimer as a single aggregated species. When the aggregated species become larger than dimer, though, this model does not fit anymore and other mathematical models has to be used to describe the aggregation process of PDIs in solution,[68] such as the isodesmic[69] and the modified isodesmic model.[70]
In the isodesmic model the PDIs ensemble grows as a chain with a binding constant (K) equal for every monomer addition.[67,69] To describe the situation in a more realistic way, the constant of the initial binding step (nucleation) can be considered different from that of the rest of the chain elongation. In this way it is possible to differentiate two situations, the cooperative mechanism, where the nucleation is less favourable than the chain elongation step[69], and the anti-cooperative, when the opposite situation is verified.[69] These common mathematical models revealed to be useful to explore the mechanisms of self-assembly process either from concentration- or temperature-dependent studies. It allows to analyze the process by simple fitting of the UV/Vis spectroscopic changes upon aggregation, thanks to their intense and characteristic absorption bands.

5.4 Effect of the solvent on the aggregation

The π-π stacking of aromatic molecules attracted considerable attention in the past decades, because is one of the most important non-covalent interaction for self-assembly. Most of the factors that contribute to π-π interactions such as electrostatic dispersion, and charge transfer interactions have been shown to be highly solvent dependent.[71] This is reasonable because the solvent molecules compete with the solute molecules to provide energetically favourable contact with the lowest overall free energy. Moreover, in PDI derivatives other parameters (such as the different solubilizing chains at the imide positions) control the π-π stacking

forces. Despite the importance of the understanding of this phenomena, a systematic study of the influence of different contributes that influences the π-π stacking forces between PDI imide substituted molecules was firstly carried out only in 2012 by Chen and co-workers.[42]

A series of PDIs derivatives with different hydrophilicity–hydrophobicity substituents (Fig. 5.5) has been chosen in order to achieve sufficient solubility for aggregation studies in a broad polarity range from *n*-exane to water.
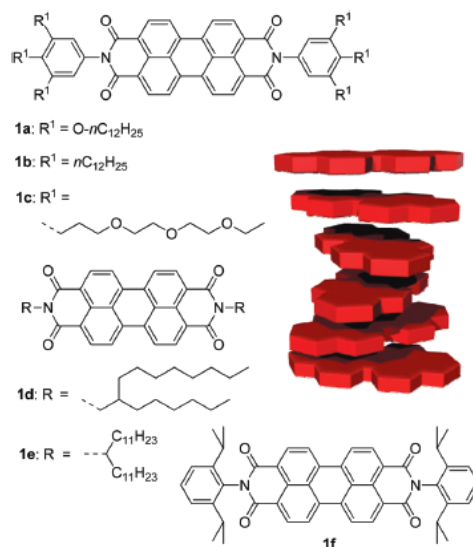
Figure 5.5: Chemical structures of the PDIs dyes 1 a-f sketch for the assumed arrangement of 1a-e in a column aggregate according to experimental and quantum chemical investigations.[42]

It was observed that, despite the different substituents at the imide nitrogen, shape and position of the absorption and emission bands of compounds *1a–f* are almost identical in their non-aggregated state, and well-resolved vibronic structures can be observed in the S_0–S_1 band with an energy progression of about 1400 cm^{-1}. If dye *1b–f* are strongly fluorescent and the spectra are mirror images of the corresponding absorption bands (accompanied by well-resolved fine structures), *1a* emission is quenched by the photo-induced electron transfer from the electron-rich trialkylphenoxy substituents to the electron poor PDI core.[47,49] Notably, quantum yield values for dyes *1 b,c* are lower than those of *1d–f* (N-diisopropyl and N-alkyl-substituted PDIs) indicating that a certain degree of electron transfer is present for the trialkylphenyl groups (*1b*).

By this preliminary measurements, it was proved that, accordingly with the lack of a dipole moment which characterize this molecules,[72] the solvatochromism is weak. The aggregation constant values (K) for each dyes was eventually obtained by UV/Vis, fitting the spectral data according with the isodesmic model. The substituent effect was studied in the solvent where all dyes exhibit reasonable to very high solubility, allowing to study the equilibrium between monomeric and aggregated species over a sufficient concentration range by UV/Vis spectroscopy: tetrachloromethane (CCl_4). It was observed that K for derivatives *1b-d*, which bear aromatic or aliphatic imide substituents without significant steric demand, is in the range of 10^2–10^3 M^{-1}. *1a* is made more prone to aggregate by charge transfer interactions between the PDI imide units and the 3,4,5-trialkoxyphenyl units of neighbouring units in the π-stack, while 1f does not aggregate at all in the investigated range, thanks to the very effective sterical shielding. This means that swallow-tail substituents are less suitable for columnar self-assembly in solution than trialkoxyphenyl and trialkylphenyl substituents. In the second part of the study, where solvent effect on the aggregation was investigated, concentration-dependent UV/Vis spectra were recorded for dyes *1a-c* in 17 different solvent with different polarity, polarizability and hydrogen bond donor and acceptor capabilities. Upon increasing the concentration, in all solvents is observed a broadening of the absorption band with a concomitant decreases of the absorption coefficients as a clear evidence that PDIs undergo aggregation and there is a strong electronic interaction between aggregated chromophore. It emerged that the magnitude of K (which can varies up to six order of magnitude) and of the corresponding Gibbs free energy changes $\Delta G° = -RTlnK$ of the aggregation process, is significantly modulated by the solvent and a biphasic behaviour was observed respect to the common empirical solvent polarity scales. In particular, the increase of polarity of aliphatic and dipolar aprotic solvents up to solvent of intermediate polarity (THF, toluene) results into a decreasing of the aggregation constant, while the opposite effect was observed increasing the polarity for strongly dipolar and protic solvents. Interestingly, intermediate polarity and high polarizable solvents (CH_2Cl_2 and $CHCl_3$), stabilize the dyes in the monomeric form. This results are not surprising taking into account that the impact of electrostatic, dispersion and solvophobic forces involved in the aggregation to a different extent, respect to the nature of the respective solvent. In protic solvent, solvophobic interaction may be helped by the presence of hydrogen bonding interaction between the solvent molecules and the carbonyl oxygens of the PDIs, in apolar solvents the quadrupole

interaction added to the electrostatic interactions typical organic molecules, may play a role in the increasing of the K. When PDIs molecules are dispersed in intermediate polarity and high polarizable solvents, the dispersion interaction become more important respect to common organic molecules thanks to the electric quadrupole that makes the molecule more prone to interact with the solvent. It has to be underlined that the K calculated in water is incredibly high.

This behaviour was elucidated by Görl and co-worker[73] by computational calculations implemented to determine the aggregation constants by UV/Vis data fitting. A trialkyl chains substituents and a trioligoethylene glycol chains as been used as a proof of concept, since the two special effect arising from the chains does not appear to exist and identical values were obtained in several solvents. It was even pointed out the interesting aspect that PDIs with hydrophilic substituents (oligoethylene chains) form in water or methanol the same kind of aggregate that the same dyes with hydrophobic substituents (alkyl chains) form in organic solvent. The common tendency is to pack in a columnar stack with rotationally displacement of about 30° to each other[4,74] with a long-lived and strongly red shifted emission, typical of H-type aggregates.[73] From the study it can be generalized that a really strong hydrophobic contribution has to be taken into account for perylene derivatives in water and different substituents features can be used to reduce the aggregation constant. As already mentioned, sterical hindered substituents at the imide position (such as three or four generation dendrons)[75,76] can completely avoid the aggregation. Moreover, the aggregation can be modulated by pH, introducing ionic chains as substituents such in the case of spermine-functionalized PDIs.[77] Charge repulsion has the predictable effect of reducing the aggregation constant, but the opposite effect may occur when concentration increase and protons of the side chains in the aggregate are transferred to the surrounding water to minimize the electrostatic repulsion. Hydrogen bonds may as well take place between the charged and the neutral eteroatoms, facilitating the π-stacking. Aggregation process is differently affected by the substituents at the bay area respect to the ones at the imide positions. When the core is functionalized, the steric constraint induces the distortion of the PDI core and the aggregation constants result 2–3 orders of magnitude lower than those of core-unsubstituted ones.[74] Moreover, substituents at bay positions are directed toward the same side of the PDI plane, generating a difference in the two π-surface hinders, that inhibiting the aggregation on one side of the molecule. The other side of the π-surface, which is more accessible, will tend to stack with another dye forming a

stable dimer. It is not difficult to imagine that the twisting angle also influences the supramolecular arrangements and the self assemblies of their electronic, as well as liquid-crystalline properties. [16]

5.5 PDI as a sensor

Although the effect of parameters controlling the π-π stacking of PDI derivatives was elucidated to a large extent, prediction of supramolecular architectures created by a given PDI molecule is still challenging. This problem becomes harder to solve in the case of assemblies formed by amphiphilic building blocks in water, where the hydrophobic effect exerts a decisive influence. Formation of different kinds of aggregate structures and their sizes are dependent on many factors, such as temperature,[78] concentration,[79] solvent composition,[80] molecular structure and form of building blocks,[81] steric interactions between molecular units, presence of particular additives,[82] and relative ratio of hydrophobic and hydrophilic units within the molecules.[83] In the case of block copolymers, polymer molecular weight might also influence the size of the resulting supramolecular structures.[84]

As mentioned before, substituents exercise a crucial influence on the ability of PDIs to aggregate in water, which is an interesting tool in the prospective of the development supramolecular self-assemblies able to display specific functions. A significant number of groups, indeed, worked in order to take advantages of the PDIs derivatives versatility for different applications such as membranes,[85] VAT dyes[86] or liquid crystals preparation.[87] Particularly interesting is the involvement of these derivatives in sensing. Würthner and co-workers, for examples, synthesized two asymmetrical PDIs derivatives with the same triethylene glycol chain on one said and a trialkyl chain and a exylester on the other[81]. Mixing the two molecules in different ratios, they were able to form structure from micelles (3-4 nm of diameter) to bilayers vesicles with the hydrophilic part of the molecule oriented through the solvent and the hydrophilic through the centre of the structure. Loading the structures with an amino ionic derivative of pyrene, in the right range of pH upon photoexcitation, they observed Förster resonance energy transfer (FRET) from the pyrene-excimer (donor) to the perylene derivative (acceptor),[88] thanks to the overlap between the emission spectrum of the pyrene and the absorption spectrum of the perylene. The position and the band shape of the PDI emitted from the membrane are in accordance with the structural relaxation of excited PDIs with population of the excimer-type excited state and, interestingly, the spectral overlap from the donor to the acceptor results in a pH-dependent

fluorescence passing even through the white light. This system is particularly interesting for diagnostic purposes. In another interesting work of Liu and co-workers[89] prepared an amphiphilic cyclodextrin-PDI conjugate and they studied the aggregation in vesicles which embed in polyvinylidene fluoride (PVDF) membrane were used for the detection of organic amines in the gas phase by fluorescence quenching. The analytes, in fact, can be bound to the cyclodextrin and induces electron transfer to the electron poor perylene core. According with authors, the inclusion of the analytes has the second effect of disturb the well-defined aggregate structures, reducing the excitonic migration in the aggregate.

5.6 Conclusion and prospective

Perylene diimide derivatives is a class of versatile compounds, which can be employ in a vast area of applications. This is extremely interesting, since the development of new nanoparticles based on this material can turn to be useful even in fields different with respect to the ones it was design for. Moreover, a lot of parameters can be modulated to make the PDIs chemical and photophysical properties fit to the designed systems.

Thanks to the acquired knowledge, new perylene diimide derivatives have been synthesised by innovative procedure, and they have been used both as probes and constituent materials of stimuli-responsive nanoparticles. In particular, we took advantage of concentration, being a very important parameter that affects the stability of self-assembled structures, controlling they disaggregation upon dilution.[90-93] On the other hand, light is a very versatile, easily controllable and tuneable stimulus, that allows to activate, specifically and locally, photo-responsive materials. [89,94-100] We thought that the coupling of these environmental and external stimuli can increase control and specificity of the whole system response.

Bibliography

1   Kardos, M. (1913).
2   Kazmaier, P. M. & Hoffmann, R. A Theoretical Study of Crystallochromy. Quantum Interference Effects in the Spectra of Perylene Pigments. *Journal of the American Chemical Society* **116**, 9684-9691, doi:10.1021/ja00100a038 (1994).
3   Kardos, M. (1913).
4   Wurthner, F. Perylene bisimide dyes as versatile building blocks for functional supramolecular architectures. *Chemical Communications*, 1564-1579, doi:10.1039/B401630K (2004).
5   Ahrens, M. J., Fuller, M. J. & Wasielewski, M. R. Cyanated Perylene-3,4-dicarboximides and Perylene-3,4:9,10-bis(dicarboximide): Facile Chromophoric Oxidants for Organic Photonics and Electronics. *Chemistry of Materials* **15**, 2684-2686, doi:10.1021/cm034140u (2003).
6   Zhan, X. *et al.* A High-Mobility Electron-Transport Polymer with Broad Absorption and Its Use in Field-Effect Transistors and All-Polymer Solar Cells. *Journal of the American Chemical Society* **129**, 7246-7247, doi:10.1021/ja071760d (2007).
7   Jones, B. A. *et al.* High-Mobility Air-Stable n-Type Semiconductors with Processing Versatility: Dicyanoperylene-3,4:9,10-bis(dicarboximides). *Angewandte Chemie International Edition* **43**, 6363-6366, doi:10.1002/anie.200461324 (2004).
8   Jiménez, Á. J. *et al.* A Tightly Coupled Bis(zinc(II) phthalocyanine)–Perylenediimide Ensemble To Yield Long-Lived Radical Ion Pair States†. *Organic Letters* **9**, 2481-2484, doi:10.1021/ol0707968 (2007).
9   Gvishi, R., Reisfeld, R. & Burshtein, Z. Spectroscopy and laser action of the "red perylimide dye" in various solvents. *Chemical Physics Letters* **213**, 338-344, doi:http://dx.doi.org/10.1016/0009-2614(93)85142-B (1993).
10   Law, K. Y. Organic photoconductive materials: recent trends and developments. *Chemical Reviews* **93**, 449-486, doi:10.1021/cr00017a020 (1993).
11   Ford, W. E. & Kamat, P. V. Photochemistry of 3,4,9,10-perylenetetracarboxylic dianhydride dyes. 3. Singlet and triplet excited-state properties of the bis(2,5-di-tert-butylphenyl)imide derivative. *The Journal of Physical Chemistry* **91**, 6373-6380, doi:10.1021/j100309a012 (1987).
12   Zhan, X. *et al.* Rylene and Related Diimides for Organic Electronics. *Advanced Materials* **23**, 268-284, doi:10.1002/adma.201001402 (2011).
13   Schmidt-Mende, L. *et al.* Self-Organized Discotic Liquid Crystals for High-Efficiency Organic Photovoltaics. *Science* **293**, 1119-1122, doi:10.1126/science.293.5532.1119 (2001).
14   Weil, T., Vosch, T., Hofkens, J., Peneva, K. & Müllen, K. The Rylene Colorant Family—Tailored Nanoemitters for Photonics Research and Applications.

Angewandte Chemie International Edition **49**, 9068-9093, doi:10.1002/anie.200902532 (2010).

15   Zang, L., Liu, R., Holman, M. W., Nguyen, K. T. & Adams, D. M. A Single-Molecule Probe Based on Intramolecular Electron Transfer. *Journal of the American Chemical Society* **124**, 10640-10641, doi:10.1021/ja0268074 (2002).

16   Würthner, F. *et al.* Perylene Bisimide Dye Assemblies as Archetype Functional Supramolecular Materials. *Chemical Reviews*, doi:10.1021/acs.chemrev.5b00188 (2015).

17   Hunger, K. *Industrial organic pigments: production, properties, applications*. (Wiley-VCH, 1997).

18   Maki, T. & Hashimoto, H. *Kogyo Kagaku Zasshi* **54**, 544-546, doi:10.1246/nikkashi1898.54.544 (1951).

19   Maki, T. & Hashimoto, H. Vat Dyes of Acenaphthene Series. IV. Condensation of Perylenetetracarboxylic Acid Anhydride with <I>o</I>-Phenylenediamine. *Bulletin of the Chemical Society of Japan* **25**, 411-413, doi:10.1246/bcsj.25.411 (1952).

20   Langhals, H. Cyclic carboxylic imide structures as structure elements of high stability. Novel developments in perylene dye chemistry. *Heterocycles* **1**, 477-500 (1995).

21   Langhals, H., Demmig, S. & Huber, H. Rotational barriers in perylene fluorescent dyes. *Spectrochimica Acta Part A: Molecular Spectroscopy* **44**, 1189-1193, doi:http://dx.doi.org/10.1016/0584-8539(88)80091-6 (1988).

22   Wescott, L. D. & Mattern, D. L. Donor–σ–Acceptor Molecules Incorporating a Nonadecyl-Swallowtailed Perylenediimide Acceptor. *The Journal of Organic Chemistry* **68**, 10058-10066, doi:10.1021/jo035409w (2003).

23   Rademacher, A., Märkle, S. & Langhals, H. Lösliche Perylen-Fluoreszenzfarbstoffe mit hoher Photostabilität. *Chemische Berichte* **115**, 2927-2934, doi:10.1002/cber.19821150823 (1982).

24   Nagao, Y. Synthesis and properties of perylene pigments. *Progress in organic coatings* **31**, 43-49 (1997).

25   Maki, T. & Hashimoto, H. Vat Dyes of Acenaphthene Series. VI. Derivatives of Acenaphthene Violet. *Bulletin of the Chemical Society of Japan* **27**, 602-605 (1954).

26   Sommer, M., Lindner, S. M. & Thelakkat, M. Microphase-Separated Donor–Acceptor Diblock Copolymers: Influence of HOMO Energy Levels and Morphology on Polymer Solar Cells. *Advanced Functional Materials* **17**, 1493-1500, doi:10.1002/adfm.200600634 (2007).

27   Iverson, I. K. & Tam-Chang, S.-W. Cascade of molecular order by sequential self-organization, induced orientation, and order transfer processes. *Journal of the American Chemical Society* **121**, 5801-5802 (1999).

28   Lindner, S. M., Kaufmann, N. & Thelakkat, M. Nanostructured semiconductor block copolymers: π–π Stacking, optical and electrochemical properties. *Organic electronics* **8**, 69-75 (2007).

29   Sommer, M., Lang, A. S. & Thelakkat, M. Crystalline–crystalline donor–acceptor block copolymers. *Angewandte Chemie International Edition* **47**, 7901-7904 (2008).

30   Lindner, S. M., Hüttner, S., Chiche, A., Thelakkat, M. & Krausch, G. Charge Separation at Self-Assembled Nanostructured Bulk Interface in Block Copolymers. *Angewandte Chemie International Edition* **45**, 3364-3368 (2006).

31   Hüttner, S., Sommer, M. & Thelakkat, M. n-Type organic field effect transistors from perylene bisimide block copolymers and homopolymers. *Applied Physics Letters* **92**, 093302 (2008).

32   Würthner, F. *et al.* Preparation and Characterization of Regioisomerically Pure 1,7-Disubstituted Perylene Bisimide Dyes. *The Journal of Organic Chemistry* **69**, 7933-7939, doi:10.1021/jo048880d (2004).

33   Seybold, G. & Wagenblast, G. New perylene and violanthrone dyestuffs for fluorescent collectors. *Dyes and Pigments* **11**, 303-317 (1989).

34   Iden, R. D. & Seybold, G. D.   (Google Patents, 1985).

35   Sadrai, M. *et al.* Lasing action in a family of perylene derivatives: singlet absorption and emission spectra, triplet absorption and oxygen quenching constants, and molecular mechanics and semiempirical molecular orbital calculations. *The Journal of Physical Chemistry* **96**, 7988-7996, doi:10.1021/j100199a032 (1992).

36   Böhm, A., Arms, H., Henning, G. & Blaschka, P. in *Chem. Abstr.* 96569g.

37   Rohr, U. *et al.* Liquid Crystalline Coronene Derivatives with Extraordinary Fluorescence Properties. *Angewandte Chemie International Edition* **37**, 1434-1437, doi:10.1002/(SICI)1521-3773(19980605)37:10<1434::AID-ANIE1434>3.0.CO;2-P (1998).

38   Rohr, U., Kohl, C., Mullen, K., van de Craats, A. & Warman, J. Liquid crystalline coronene derivatives. *Journal of Materials Chemistry* **11**, 1789-1799, doi:10.1039/B009708J (2001).

39   Lee, S. K. *et al.* Electrochemistry, spectroscopy and electrogenerated chemiluminescence of perylene, terrylene, and quaterrylene diimides in aprotic solution. *Journal of the American Chemical Society* **121**, 3513-3520 (1999).

40   Zhao, Y. & Wasielewski, M. R. 3, 4: 9, 10-Perylenebis (dicarboximide) chromophores that function as both electron donors and acceptors. *Tetrahedron letters* **40**, 7047-7050 (1999).

41   Lukas, A. S., Zhao, Y., Miller, S. E. & Wasielewski, M. R. Biomimetic Electron Transfer Using Low Energy Excited States: A Green Perylene-Based Analogue of Chlorophyll a. *The Journal of Physical Chemistry B* **106**, 1299-1306, doi:10.1021/jp014073w (2002).

42   Chen, Z., Fimmel, B. & Wurthner, F. Solvent and substituent effects on aggregation constants of perylene bisimide [small pi]-stacks - a linear free energy relationship analysis. *Organic & Biomolecular Chemistry* **10**, 5845-5855, doi:10.1039/C2OB07131B (2012).

43   Hongyu, W., Bo, P. & Wei, W. Solar cells based on perylene bisimide

derivatives. *Progress in Chemistry* **20**, 1751-1760 (2008).

44   Langhals, H., Karolin, J. & Johansson, L. B.-Å. Spectroscopic properties of new and convenient standards for measuring fluorescence quantum yields. *Journal of the Chemical Society, Faraday Transactions* **94**, 2919-2922 (1998).

45   Correˆa, D. S. *et al.* Investigation of the two-photon absorption cross-section in perylene tetracarboxylic derivatives: nonlinear spectra and molecular structure. *The Journal of Physical Chemistry A* **110**, 6433-6438 (2006).

46   Oliveira, S. L. *et al.* Perylene Derivatives with Large Two-Photon-Absorption Cross-Sections for Application in Optical Limiting and Upconversion Lasing. *Advanced Materials* **17**, 1890-1893 (2005).

47   Beckers, E. H. *et al.* Charge separation and recombination in photoexcited oligo (p-phenylene vinylene): Perylene bisimide arrays close to the marcus inverted region. *The Journal of Physical Chemistry A* **108**, 6933-6937 (2004).

48   Hippius, C., van Stokkum, I. H., Zangrando, E., Williams, R. M. & Würthner, F. Excited state interactions in calix [4] arene-perylene bisimide dye conjugates: Global and target analysis of supramolecular building blocks. *The Journal of Physical Chemistry C* **111**, 13988-13996 (2007).

49   Würthner, F., Thalacker, C., Diele, S. & Tschierske, C. Fluorescent J-type Aggregates and Thermotropic Columnar Mesophases of Perylene Bisimide Dyes. *Chemistry-a European Journal* **7**, 2245-2253 (2001).

50   Huang, C., Barlow, S. & Marder, S. R. Perylene-3,4,9,10-tetracarboxylic Acid Diimides: Synthesis, Physical Properties, and Use in Organic Electronics. *The Journal of Organic Chemistry* **76**, 2386-2407, doi:10.1021/jo2001963 (2011).

51   Schmidt, R. *et al.* Core-Fluorinated Perylene Bisimide Dyes: Air Stable n-Channel Organic Semiconductors for Thin Film Transistors with Exceptionally High On-to-Off Current Ratios. *Advanced Materials* **19**, 3692-3695 (2007).

52   Jelley, E. E. Spectral absorption and fluorescence of dyes in the molecular state. *Nature* **138**, 1009-1010 (1936).

53   Würthner, F., Kaiser, T. E. & Saha-Möller, C. R. J-Aggregates: From Serendipitous Discovery to Supramolecular Engineering of Functional Dye Materials. *Angewandte Chemie International Edition* **50**, 3376-3410 (2011).

54   McRae, E. G. & Kasha, M. Enhancement of Phosphorescence Ability upon Aggregation of Dye Molecules. *The Journal of Chemical Physics* **28**, 721-722, doi:doi:http://dx.doi.org/10.1063/1.1744225 (1958).

55   Kasha, M. Energy transfer mechanisms and the molecular exciton model for molecular aggregates. *Radiation research* **20**, 55-70 (1963).

56   Kasha, M., Rawls, H. & Ashraf El-Bayoumi, M. The exciton model in molecular spectroscopy. *Pure and Applied Chemistry* **11**, 371-392 (1965).

57   Tian, Y., Stepanenko, V., Kaiser, T. E., Würthner, F. & Scheblykin, I. G. Reorganization of perylene bisimide J-aggregates: from delocalized

collective to localized individual excitations. *Nanoscale* **4**, 218-223 (2012).

58   Merdasa, A. *et al.* Single Lévy states–disorder induced energy funnels in molecular aggregates. *Nano letters* **14**, 6774-6781 (2014).

59   Eaton, S. W. *et al.* Singlet exciton fission in polycrystalline thin films of a slip-stacked perylenediimide. *Journal of the American Chemical Society* **135**, 14701-14712 (2013).

60   Kasha, M. Characterization of electronic transitions in complex molecules. *Discussions of the Faraday society* **9**, 14-19 (1950).

61   Veldman, D. *et al.* Triplet formation involving a polar transition state in a well-defined intramolecular perylenediimide dimeric aggregate. *The Journal of Physical Chemistry A* **112**, 5846-5857 (2008).

62   Giaimo, J. M., Gusev, A. V. & Wasielewski, M. R. Excited-state symmetry breaking in cofacial and linear dimers of a green perylenediimide chlorophyll analogue leading to ultrafast charge separation. *Journal of the American Chemical Society* **124**, 8530-8531 (2002).

63   Seibt, J. *et al.* On the geometry dependence of molecular dimer spectra with an application to aggregates of perylene bisimide. *Chemical physics* **328**, 354-362 (2006).

64   Seibt, J., Dehm, V., Würthner, F. & Engel, V. Absorption spectroscopy of molecular trimers. *The Journal of chemical physics* **126**, 164308 (2007).

65   Seibt, J. *et al.* Vibronic transitions and quantum dynamics in molecular oligomers: a theoretical analysis with an application to aggregates of perylene bisimides. *The Journal of Physical Chemistry A* **113**, 13475-13482 (2009).

66   Hartnett, P. E. *et al.* Slip-stacked perylenediimides as an alternative strategy for high efficiency nonfullerene acceptors in organic photovoltaics. *Journal of the American Chemical Society* **136**, 16345-16356 (2014).

67   Chen, Z., Lohr, A., Saha-Möller, C. R. & Würthner, F. Self-assembled π-stacks of functional dyes in solution: structural and thermodynamic features. *Chemical Society Reviews* **38**, 564-584 (2009).

68   Martin, R. B. Comparisons of indefinite self-association models. *Chemical reviews* **96**, 3043-3064 (1996).

69   De Greef, T. F. *et al.* Supramolecular polymerization. *Chemical Reviews* **109**, 5687-5754 (2009).

70   Zhao, D. & Moore, J. S. Nucleation–elongation: a mechanism for cooperative supramolecular polymerization. *Organic & biomolecular chemistry* **1**, 3471-3491 (2003).

71   Adams, H. *et al.* Quantitative determination of intermolecular interactions with fluorinated aromatic rings. *Chemistry-a European Journal* **7**, 3494-3503 (2001).

72   Reichardt, C. & Welton, T. *Solvents and solvent effects in organic chemistry*. (John Wiley & Sons, 2011).

73   Görl, D., Zhang, X. & Würthner, F. Molecular Assemblies of Perylene Bisimide Dyes in Water. *Angewandte Chemie International Edition* **51**, 6328-6348, doi:10.1002/anie.201108690 (2012).

74   Chen, Z. *et al.* Photoluminescence and Conductivity of Self-Assembled π–π Stacks of Perylene Bisimide Dyes. *Chemistry-a European Journal* **13**, 436-449 (2007).

75   Mordasini Denti, T. Z., van Gunsteren, W. F. & Diederich, F. Computer simulations of the solvent dependence of apolar association strength: Gibbs free energy calculations on a cyclophane-pyrene complex in water and chloroform. *Journal of the American Chemical Society* **118**, 6044-6051 (1996).

76   Smithrud, D. B. & Diederich, F. Strength of molecular complexation of apolar solutes in water and in organic solvents is predictable by linear free energy relationships: A general model for solvation effects on apolar binding. *Journal of the American Chemical Society* **112**, 339-343 (1990).

77   Rehm, S., Stepanenko, V., Zhang, X., Rehm, T. H. & Würthner, F. Spermine-Functionalized Perylene Bisimide Dyes—Highly Fluorescent Bola-Amphiphiles in Water. *Chemistry – A European Journal* **16**, 3372-3382, doi:10.1002/chem.200902839 (2010).

78   Yin, H., Zhou, Z., Huang, J., Zheng, R. & Zhang, Y. Temperature-induced micelle to vesicle transition in the sodium dodecylsulfate/dodecyltriethylammonium bromide system. *Angewandte Chemie* **115**, 2238-2241 (2003).

79   Leng, J., Egelhaaf, S. U. & Cates, M. E. Kinetics of the micelle-to-vesicle transition: aqueous lecithin-bile salt mixtures. *Biophysical journal* **85**, 1624-1646 (2003).

80   Zhang, L. & Eisenberg, A. Multiple Morphologies and Characteristics of "Crew-Cut" Micelle-like Aggregates of Polystyrene-b-poly(acrylic acid) Diblock Copolymers in Aqueous Solutions. *Journal of the American Chemical Society* **118**, 3168-3181, doi:10.1021/ja953709s (1996).

81   Zhang, X., Chen, Z. & Würthner, F. Morphology Control of Fluorescent Nanoaggregates by Co-Self-Assembly of Wedge- and Dumbbell-Shaped Amphiphilic Perylene Bisimides. *Journal of the American Chemical Society* **129**, 4886-4887, doi:10.1021/ja070994u (2007).

82   Kim, H.-J., Kim, T. & Lee, M. Responsive Nanostructures from Aqueous Assembly of Rigid– Flexible Block Molecules. *Accounts of chemical research* **44**, 72-82 (2010).

83   Shimizu, T., Masuda, M. & Minamikawa, H. Supramolecular nanotube architectures based on amphiphilic molecules. *Chemical reviews* **105**, 1401-1444 (2005).

84   Uzun, O., Sanyal, A., Nakade, H., Thibault, R. J. & Rotello, V. M. Recognition-induced transformation of microspheres into vesicles: Morphology and size control. *Journal of the American Chemical Society* **126**, 14773-14777 (2004).

85   Krieg, E., Weissman, H., Shirman, E., Shimoni, E. & Rybtchinski, B. A recyclable supramolecular membrane for size-selective separation of nanoparticles. *Nature nanotechnology* **6**, 141-146 (2011).

86   Herbst, W. & Hunger, K. *Industrial organic pigments: production, properties,*

applications. (John Wiley & Sons, 2006).

87   Tam-Chang, S.-W., Helbley, J. & Iverson, I. K. A study of the structural effects on the liquid-crystalline properties of ionic perylenebis (dicarboximide) s using UV-vis spectroscopy, polarized light microscopy, and NMR spectroscopy. *Langmuir* **24**, 2133-2139 (2008).

88   Zhang, X., Rehm, S., Safont-Sempere, M. M. & Würthner, F. Vesicular perylene dye nanocapsules as supramolecular fluorescent pH sensor systems. *Nature chemistry* **1**, 623-629 (2009).

89   Jiang, B.-P., Guo, D.-S. & Liu, Y. Self-Assembly of Amphiphilic Perylene–Cyclodextrin Conjugate and Vapor Sensing for Organic Amines. *The Journal of organic chemistry* **75**, 7258-7264 (2010).

90   Fernandez, G., Stolte, M., Stepanenko, V. & Wuerthner, F. Cooperative Supramolecular Polymerization: Comparison of Different Models Applied on the Self-Assembly of Bis(merocyanine) Dyes. *Chemistry-a European Journal* **19**, 206-217, doi:10.1002/chem.201202679 (2013).

91   Mayerhoeffer, U. & Wuerthner, F. Cooperative self-assembly of squaraine dyes. *Chemical Science* **3**, 1215-1220, doi:10.1039/c2sc00996j (2012).

92   Wuerthner, F., Kaiser, T. E. & Saha-Moeller, C. R. J-Aggregates: From Serendipitous Discovery to Supramolecular Engineering of Functional Dye Materials. *Angewandte Chemie-International Edition* **50**, 3376-3410, doi:10.1002/anie.201002307 (2011).

93   Chen, Z., Lohr, A., Saha-Moeller, C. R. & Wuerthner, F. Self-assembled pi-stacks of functional dyes in solution: structural and thermodynamic features. *Chemical Society Reviews* **38**, 564-584, doi:10.1039/b809359h (2009).

94   Kawano, T., Niidome, Y., Mori, T., Katayama, Y. & Niidome, T. PNIPAM Gel-Coated Gold Nanorods, for Targeted Delivery Responding to a Near-Infrared Laser. *Bioconjugate Chemistry* **20**, 209-212, doi:10.1021/bc800480k (2009).

95   Jiang, J. Q., Tong, X., Morris, D. & Zhao, Y. Toward photocontrolled release using light-dissociable block copolymer micelles. *Macromolecules* **39**, 4633-4640, doi:10.1021/ma060142z (2006).

96   Yang, Y., Velmurugan, B., Liu, X. & Xing, B. NIR Photoresponsive Crosslinked Upconverting Nanocarriers Toward Selective Intracellular Drug Release. *Small* **9**, 2937-2944, doi:10.1002/smll.201201765 (2013).

97   Jiang, J., Qi, B., Lepage, M. & Zhao, Y. Polymer micelles stabilization on demand through reversible photo-cross-linking. *Macromolecules* **40**, 790-792, doi:10.1021/ma062493j (2007).

98   Jiang, J. Q., Tong, X. & Zhao, Y. A new design for light-breakable polymer micelles. *Journal of the American Chemical Society* **127**, 8290-8291, doi:10.1021/ja0521019 (2005).

99   He, J. & Zhao, Y. Light-responsive polymer micelles, nano- and microgels based on the reversible photodimerization of coumarin. *Dyes and Pigments* **89**, 278-283, doi:10.1016/j.dyepig.2010.03.032 (2011).

100   Katz, J. S. & Burdick, J. A. Light-Responsive Biomaterials: Development and

Applications. *Macromolecular Bioscience* **10**, 339-348, doi:10.1002/mabi.200900297 (2010).

6 Aim of the work

A huge number of new nanosystems are being developed and some of them are already of common use, nanostructures able to display different functions are designed and implemented, nano-machines capable of achieve work are studied in our laboratories.[1] In this fervent period, stimuli-responsive nanomaterials are finding increasing importance in fields of high social and economic impact, that include drug delivery, diagnostics, tissue engineering and 'smart' optical systems, as well as microelectronics, biosensors, micro-electromechanical systems, coatings and textiles.[2-4] The reason is not difficult to understand: would you rather have an incredible machine able to do whatever you want, or have an incredible machine able to do whatever you want *when and how you desire it to do it*? Despite the strong scientific effort put in this field, anyway, we are still far from reaching the goal, and the work presented in this thesis is, hopefully, a step forward along this difficult path.

Among the possible applications of these structures, we primarily focused on bio-imaging, combining fluorescence sensibility and nanoparticles versatility to obtain new photo-active nano-probes, able to respond to external or environmental stimuli with a luminescent signal as strong as possible and specific.

According to the bio-application prospective, the work focused on self-assembly, and self-organization, in water environment. This process typically arises from electronic coupling of the aromatic systems and, if suitably exploited, yields aggregates with emerging new functionalities, absent in the individual molecular components.[24,34-37] Aggregation causes fluorescence quenching of most common organic dyes, opening the way to the disaggregation induce emission process, can be exploited to design high-brightness nanoparticles. A strong difference in the quantum yield of the components before and after the assembly is an extremely powerful tool to dramatically improve the signal to noise ratio in optical imaging. To obtain a strong responsive signal, it was crucial to choose a dye characterised by radical changes in the electronic and optical properties of the assembled molecule, with respect to the isolated components.[5-7] As already pointed out, a great candidates is the family of perylene diimide derivatives (PDIs). These well studied molecules are, also, highly chemical and photo-stable and their photophysical properties can be modulated by chemical functionalization in the region of the aromatic core. Moreover, shape and stability of the aggregated species are dependent on the interactions between the substituents on the imide position.

System prepared and characterized in my thesis are briefly summarized in the next three subsections.

6.1 Self-assembled fluorogenic nanostructure

Synthesis of PDIs typically starts from perylene-3,4,9,10-tetracarboxylic dianhydride (PTCDA) and requires quite high temperatures, long reaction times and the use of specific solvents. Since particularly important, for our point of view, was the preparation of our materials by straightforward, reproducible and mild procedures, we primarily concentrated our effort in the synthesis of a new perylene diimide derivative **(P)** by short-time microwave (MW) heating, using glycols as solvents. It was achieved convenient and efficient conversion of PTCDA into a PDI, where the core (green square, Fig. 6.1) was substituted on the imide position with a branched polypropylene oxide oligomer (yellow square, Fig. 6.1), containing amines as pH sensitive and reactive groups (blue circles, Fig. 6.1).
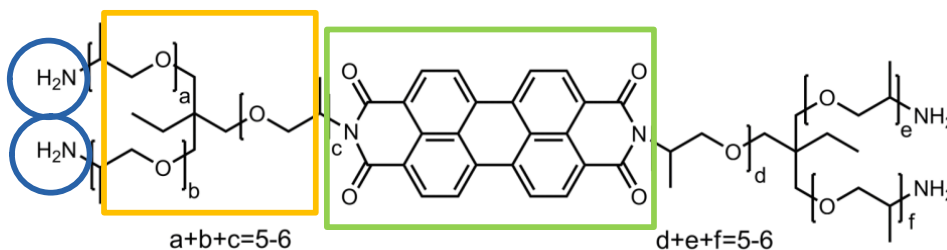
*Figure 6.1: Chemical structure of the molecular PDI derivative **P** functionalized in the imide position. It can be distinguished the PDI core (green square), the polypropylene oxide braches (yellow square) and the amine terminations (blue circles).*

The tendency of this molecule to self-assemble in polar environment, controlled both by aromatic core π-π stacking and inter-substituent interactions (Fig. 6.2), drove the formation of quenched nanoparticles with potential application as fluorogenic and photo-tuneable agents for multicolour cellular labelling. It is worthy to underline that dyes molecules are not only the fluorogenic components, but they display structural roles.
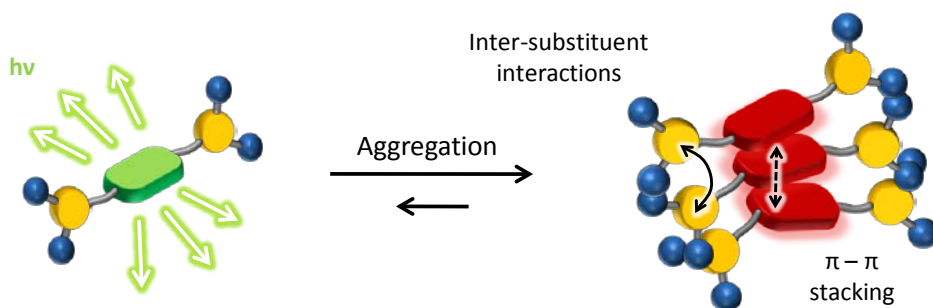
Figure 6.2: Schematic representation of the monomeric emissive specie, which undergoes aggregation and fluorescence quenching. The stability of the aggregate is dependent on the π-π stacking interactions of the aromatic core, and on the inter-substituents interactions.

6.2 Cross-linked photo-responsive nanoparticles

The stability of the nanoparticles cannot be underestimated, since uncontrolled dissociation of the components can lead to leaking of toxic component in the biological environment, or to the ubiquitous spreading of high emissive component all over the sample. Accordingly, once proved the applicability of **P** as self-assembly building block for optical imaging, it was covalently reacted with diglycidyl ether Bisphenol A to obtain oligomers partially cross-linked into the poloxamer direct micelles core, used as reactors. The hydrophobic part of the poloxamer get trapped into the assembled matrix and formed the nanoparticles (**PNPs**) core (Fig. 6.3).
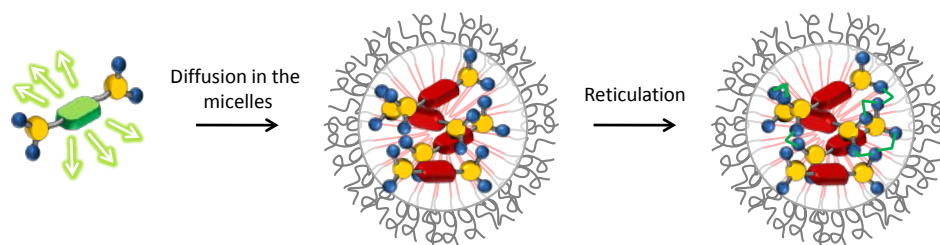
*Figure 6.3:Schematic representation of the templated cross-linking reaction of the fluorescent monomer **P** into the quenched core-shell nanoparticles.*

As in the previous case, perylene diimide derivative **P** is a structural component of the nanoparticles core but, in this case, a partial control over the dyes organization can potentially be achieved by the spacers and the reticulation grade. It is expected, in fact, that **P** oligomers cannot only self-organize in the thermodynamically stabilised structures, but it can get trapped into kinetic conformations at higher

energy. Moreover, size, shape and functional groups of the spacers can be potentially modified, forcing the aggregates in different morphologies. The photophysical behaviour of **PNP**s within their applicability in imaging will be described.

6.3 Fluorescent pH-responsive polymeric nanoparticles

The tendency to self-assemble is not specific of small molecules, indeed it is pronounced for macromolecules, such as amphiphilic co-block polymers Accordingly, a perylene diimide derivative, was covalently linked to a block copolymer (Fig. 6.4) prone to self-assembly in spherical micelles. Dye unit was incorporated in order to investigate the luminescence triggering by pH variations, ranging from 7.4 to 5, in water environment
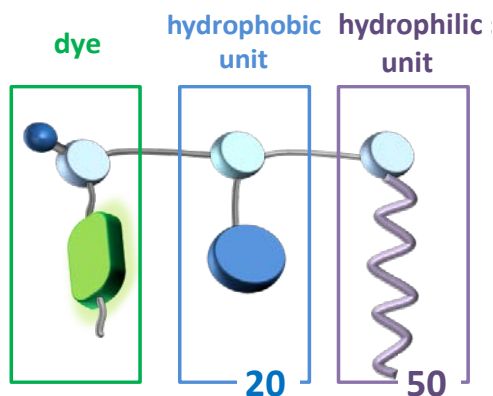
Figure 6.4: Schematic representation of the amphiphilic block-copolymer. Fluorescent unit is linked to the hydrophobic block, while the hydrophilic one terminates the chain (composed by 20 and 50 monomers each respectively)

The importance of this work can be find in the developing a new 'smart' nano-system with high biological specificity to differentiate tumours from normal tissues,[8] being 7.4 and 5, the typical pH of circulating blood and acidic extracellular tumour milieu respectively.

In the four next chapters results will be presented and discussed.

Bibliography

1   Ragazzon, G., Baroncini, M., Silvi, S., Venturi, M. & Credi, A. Light-powered autonomous and directional molecular motion of a dissipative self-assembling system. *Nature nanotechnology* **10**, 70-75 (2015).

2   Stuart, M. A. C. *et al.* Emerging applications of stimuli-responsive polymer materials. *Nature Materials* **9**, 101-113, doi:10.1038/nmat2614 (2010).

3   Mura, S., Nicolas, J. & Couvreur, P. Stimuli-responsive nanocarriers for drug delivery. *Nature Materials* **12**, 991-1003, doi:10.1038/nmat3776 (2013).

4   Roy, D., Cambre, J. N. & Sumerlin, B. S. Future perspectives and recent advances in stimuli-responsive materials. *Progress in Polymer Science* **35**, 278-301, doi:10.1016/j.progpolymsci.2009.10.008 (2010).

5   Genovese, D. *et al.* Energy transfer processes in dye-doped nanostructures yield cooperative and versatile fluorescent probes. *Nanoscale* **6**, 3022-3036 (2014).

6   Genovese, D. *et al.* Prevention of Self-Quenching in Fluorescent Silica Nanoparticles by Efficient Energy Transfer. *Angewandte Chemie-International Edition* **52**, 5965-5968, doi:10.1002/anie.201301155 (2013).

7   Rampazzo, E. *et al.* Multicolor core/shell silica nanoparticles for in vivo and ex vivo imaging. *Nanoscale* **4**, 824-830, doi:10.1039/c1nr11401h (2012).

8   Wang, Y. *et al.* A nanoparticle-based strategy for the imaging of a broad range of tumours by nonlinear amplification of microenvironment signals. *Nat Mater* **13**, 204-212, doi:10.1038/nmat3819

http://www.nature.com/nmat/journal/v13/n2/abs/nmat3819.html#supplementary-information (2014).

7 Materials and methods

In this chapter the reader can find an overview of materials and techniques used in most works presented in this thesis. All the chemicals were used as received without any further purification except where differently stated.

7.1 Materials

All reagents and solvents were used as received without further purification: non ionic surfactant Pluronic® F-127, 4,4'-isopropylidenediphenol diglycidyl ether (Bisphenol A), Fluorescein isothiocyanate (FITC, 95%), sodium hydroxide (NaOH, 98 %), Perylene-3,4,9,10-tetracarboxylic dianhydride (PTCDA), N,N′-Bis (2,5-ditert-butylphenyl)-3,4,9,10-perylenedicarboximide, were purchased from Sigma Aldrich. Boric Acid (99.8 %) was purchased from Merck. The polyethertiamine Jeffamine T-403 was a gift by Hunstmann Corporation.
A Milli-Q Millipore system was used for the purification of water (resistivity 18 MΩ).

7.2 Methods

7.2.1 Dialysis experiments:

Dialysis was performed versus water at room temperature under gentle stirring with regenerated cellulose dialysis tubing (Sigma Aldrich, molecular weight cut-off > 12 000 Da, average diameter 33 mm).

7.2.2 Photophysical experiments

Thanks to the reduced dimensions of the nanoparticles, the light scattering in the UV-Vis range of light is negligible. Moreover, DLS measurements show no aggregation of the NPs, even after several months. This properties allows to treat the system, from the photophysical point of view, as any solution of molecular species.

UV-Vis absorption spectra were recorded at 25 °C by means of Perkin-Elmer Lambda 45 spectrophotometer. Quartz cuvettes with optical path length of 1 cm were used.

Steady State Fluorescence Detection. Emission and excitation spectra in the 200–900 nm range were recorded on a Perkin Elmer LS50 spectrofluorometer and on a Edinburgh FLS920 both equipped with a Hamamatsu R928P photomultiplier.

Fluorescence intensity is quantitatively dependent on the same parameters as absorbance as well as on the fluorescence quantum yield of the dye, the excitation source intensity and fluorescence collection efficiency of the instrument. In dilute solutions, fluorescence intensity is linearly proportional to these parameters. However, when sample absorbance exceeds about 0.1 in a 1 cm path length, the relationship becomes non-linear and measurements may be distorted by artefacts such as self-absorption and the inner-filter effect. Because fluorescence quantisation is dependent on the instrument, fluorescent reference standards are essential for calibrating measurements made at different times or using different instrument configurations.[1] Luminescence spectra recorded in 200–900 nm region were corrected for the non linear response of the photomultiplier towards photons of different wavelength using a previously obtained calibration curve.

Luminescence quantum yields (uncertainty ± 15%) were determined using N,N′-Bis (2,5-ditert-butylphenyl)-3,4,9,10-perylenedicarboximide in $CHCl_3$ solution (Φ = 0.99) for experiment in Chapter 8 and 10 and Fluorescein isothiocyanate in a 0.1 M NaOH water solution (Φ = 1.0) in experiment in Chapter 9 and 10 at room temperature using the relative method reported in Montalti et al. *Handbook of Photochemistry.*[1]

Fluorescence Anisotropy. All fluorescence anisotropy measurements were performed on an Edinburgh FLS920 equipped with Glan-Thompson polarisers. Anisotropy measurements were collected using an L-format configuration, and all data were corrected for polarization bias using the G-factor. Four different spectra were acquired for each sample combining different orientation of the excitation and emission polarisers: IVV, IVH, IHH, IHV (where V stands for vertical and H for horizontal; the first subscript refers to the excitation and the second subscript refers to the emission). The spectra were used to calculate the G-factor and the anisotropy r: G (IHV/ IHH, r) (IVV - GIVH)/IVV + 2GIVH. For all of the samples, r was mediated in the 700-750 nm spectral range.[2]

Time-Resolved Fluorescence Detection. Fluorescence lifetimes, τ_F (mean deviation of three independent experiments, ca. 5%) were measured with a Edinburgh FLS920 equipped with a Hamamatsu R928P photomultiplier connected to a PCS900 PC card for the time-correlated single-photon counting (TCSPC) experiments.

Spectrophotometric and spectrofluorimetric titrations. Spectrophotometric and spectrofluorimetric titrations were used to determine the effect of concentration

variation on the spectral shapes. A know volume of solution (2, 2.5 or 3 ml) containing one of the two partners was placed in a quartz cuvette and titrated with a concentrated solution of the other partner. The titrating species was added with high–precision micropipettes in amounts of 2 to 100 μl. The absorption and/or emission spectra were recorded at each addition; excitation for the emission spectra was at a wavelength where corrections due to spectral overlap were minimal.

7.2.3 Microscopy and Scattering

Wild field fluorescence microscopy measurements For experiments described in chapter 8, sample in PBS was dropped on a 0.13 mm thick cover slide. For experiment described in chapter 9 sample was prepared dissolving 5 μL of **PNP**s water solution in 500 mg of glycerol under fast stirring. The suspension were directly dropped on the top of a 0.1 mm thick glass covered with a 0.13 mm cover slide separated by two known thickness (0.11 ± 0.01 mm) tape slices.
In both cases, samples was observed using an Olympus IX 71 inverted microscope equipped with a Xenon lamp (450 W) for fluorescence excitation and a Basler Scout scA640-70gc CCD camera for images acquisition. Lamp was attenuated with an absorptive filter Thorlabs NE30B and coupled to a fluorescence cube mounting the filters set Chroma 11001v2 blue. Images with 10X magnification were taken using the objective Olympus UPLFLN10X2 while the objective UPLFLN10X2 was used for 100X magnification.

Transmission Electron Microscopy Experiments. A Philips CM 100 TEM operating at 80 kV was used. For TEM investigations, a Formvar foil supported on conventional copper microgrids was dried up under vacuum after deposition of a drop of NPs solution diluted with water (1:50). We obtained the size distribution by analyzing images with a block of several hundred NPs.

Dynamic Light Scattering: Determination of the **PNP**s hydrodynamic diameter distributions was carried out through DLS measurements employing a Malvern Nano ZS instrument with a 633 nm laser diode. Samples were housed in disposable polystyrene cuvettes of 1 cm optical path length using water as solvent. Width of DLS hydrodynamic diameter distribution is indicated by PdI (polydispersion index). In the case of a monomodal distribution (Gaussian) calculated by means of cumulant analysis, PdI = $(\sigma/Z_{avg})^2$, where σ is the width of the distribution and Z_{avg} is average diameter of the particles population respectively.

ζ-Potential measurement. ζ-Potential values were determined using a Malvern Nano ZS instrument. Samples were housed in disposable polycarbonate folded capillary cell (750 μL, 4 mm optical path length). Electrophoretic determination of ζ-potential was made under Smoluchowski approximation in acqueous media at moderate electrolyte concentration.

7.2.4 Spectrometry measurements

NMR measurement Unless otherwise specified, NMR measurements were recorded at 25 °C, in CDCl$_3$, on a Varian Mercury Plus 200, 300 and 400 MHz spectrometer. Chemical shifts are reported in δ from CDCl$_3$ (δ = 7.27 ppm for [1]H-Nmr or δ = 77.0 ppm for ^{13}C-NMR). Multiplicities are reported using the following abbreviations: s (singlet); d (doublet); t (triplet); q (quartet), m (multiplet); br (broad), or a suitable combination. All coupling constants J are expressed in Hz.

Size exclusion chromatography Measurement of polymer molecular weight (MN) and dispersity (MW/MN) was performed using size exclusion chromatography with multiangle light scattering (SEC-MALS). The columns were Phenomenex Phenogel 5u 10, 1K–75K, 300 × 7.80 mm in series with a Phenomex Phenogel 5u 10, 10K–1000K, 300 × 7.80 mm (0.05 M LiBr in DMF), and the pump was a Shimadzu LC-AT-VP. The light scattering setup included a multiangle light scattering detector (DAWN-HELIOS: Wyatt Technology), a refractive index detector (Wyatt Optilab T-rEX), and a UV–vis detector (Shimadzu SPD- 10AVP). The system was calibrated with a polystyrene (PS) and poly(methyl methacrylate) (PMMA) standards. The *dn/dc* values for (PEG)$_4$ in DMF were measured and are 0.100 ml/g, respectively Size exclusion chromatography (SEC) measurement were performed on with HPLC grade dimethylformamide (DMF) (Fisher) with 1.06 g/L of LiCl at 40°C at a flow rate of 1 ml/min.

7.2.5 Cells studies

MCF10A cells (ATCC: crl-10317) were cultured in (1:1) Dulbecco's Modified Eagle's Medium (DMEM)/Nutrient Mixture F-12Ham (Gibco-Life Technolo- gies Corporation) supplemented with 5% horse serum, 20 ng/ml epidermal growth factor (EGF), 50 ng/ml cholera toxin, 500 ng/ml hydrocortisone and 0.01 mg/ml insulin (Gibco-Life Technologies Corporation). Cells were passed upon trypsin digestion and kept in incubation at 5% of CO2 and 37°C.

Bibliography

1   Montalti, M., Credi, A., Prodi, L. & Gandolfi, M. T. Handbook of Photochemistry. *CRC Press: Boca Raton, FL,* (2006).

2   Lakowicz, J. R. Principles of Fluorescence Spectroscopy. *Kluwer Academic/Plenum Publishers: New York* (1999).

3   Zanarini, S. *et al.* Iridium Doped Silica–PEG Nanoparticles: Enabling Electrochemiluminescence of Neutral Complexes in Aqueous Media. *Journal of the American Chemical Society* **131**, 14208-14209, doi:10.1021/ja906666e (2009).

8 Photo-tunable multicolour self-assembled NPs

8.1 Synthesis of perylene diimide derivative (P)

Perylene diimide derivative **P** (Fig. 8.1) was prepared by microwave assisted reaction of PTCDA with Jeffamine T-403, a polyetheramine with three polypropylene oxide branches, terminated with three primary amines (Fig. 8.2). This substituent was chosen because it was expected to strongly improve the solubility of the molecule both in organic and in water solvent, and to introduce a reactive pH sensitive terminal groups for future works.
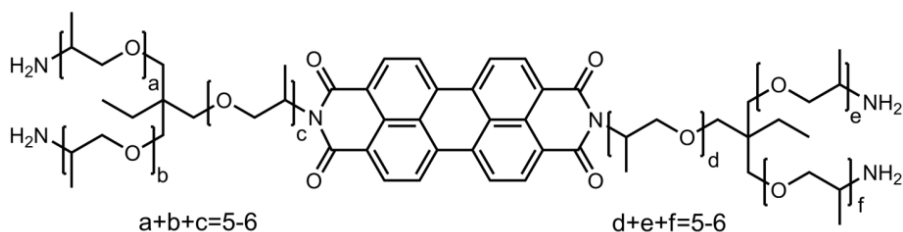
Figure 8.1: Chemical formula of the PDI derivative P
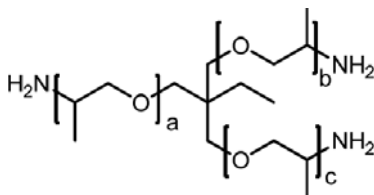
Figure 8.2: Chemical formula of Jeffamine T-405 (J)

100 mg (MW = 392.32 g/mol, 0.25 mmol) of PTCDA and 2500 mg (5.4 mmol) of Jeffamine (**J**) were sonicated for 1 minute in 15 ml of ethylene glycol in a 250 ml Erlenmeyer flask, in order to increase the dispersion of the reactant in the reaction mixture. The Jeffamine perfectly dissolved in the solvent, while the PTCDA was only suspended after the sonication, accordingly with the proved poor solubility of this compound, forming a strongly red dispersion. The flask was heated one minute in a commercial microwave oven at 900 W for five times, manually stirring the reaction mixture each time. After heating, the solution turned deep purple and perfectly clear, probably as a consequence of the opening of the anhydride ring. The red

product **P** was then isolated as a sticky solid on the surface of the flask by adding 150 ml of water to the reaction mixture and by stirring and heating at 80°C for 10 minutes. In this way, one of the **J** terminal amine reacts with the opened ring of the reaction intermediate and the formation of the PDI occurs. The calculated yield of **P** is > 95%.

8.2 Spectroscopic characterization of P

In order to characterize the product **P**, it was necessary a preliminary characterization of the Jeffamine T-405, not purchased by Hunstmann Corporation. Unfortunately, it was not possible to follow the same procedure for PTCDA, since it was too insoluble to allow the study by ESI-mass and NMR, but all the necessary data are, anyway, already reported in literature.

The polyethertriamine **J** mass distribution was investigated by ESI-mass (1mg/1ml in MeOH). The resulting mass spectrum, shown in figure 8.3, presents three groups of peaks in different colours, corresponding to the mono-, di-, and tri-protonated **J**, respectively indicated as **JH$^+$** (red) , **JH$_2$$^{2+}$** (green) and **JH$_3$$^{3+}$** (cyan). The different constitutional isomers are labelled by n, being n=a+b+c. The ESI-mass spectrum clearly shows that isomers with n=5 and =6 are the predominant species, being the sum of their molar fraction about 0.60. The sum of the molar fraction of the two isomer n=4 and n=7 is about 0.30. Lastly the sum of the molar fraction of the isomers n=3 and n=8 is about 0.05 and the molar fraction of isomers with n<3 or n>8 is less than 0.05. The molar mass calculated from the mass distribution data was 460 g/mol with a polydispersity index (PdI) of 1.02.
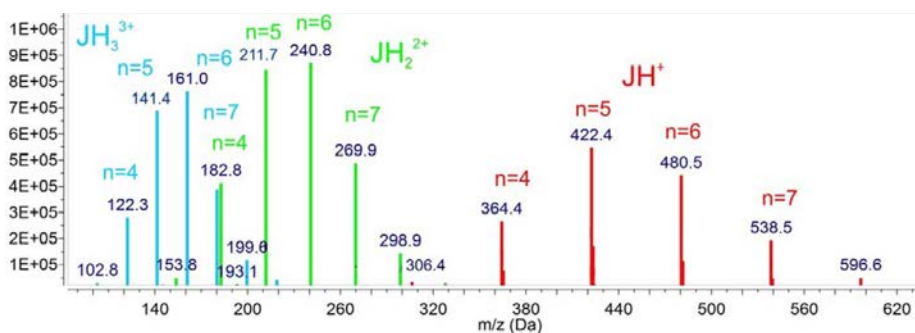
Figure 8.3: ESI mass spectrum of J

^{1}H NMR proton NMR was collected for the Jeffamine **J** in deuterated chloroform at a 400 MHz instrument. The resultant chemical shift are: δ (ppm) 3.60 (m, 3H,

CH$_2$CH(CH$_3$)O; 3.10-3.50 (m, 18H, OCH$_2$); 3.06-2.92 (m, 3H, CH(CH$_3$)NH$_2$); 1.40 (s, 2H, CH$_3$CH$_2$); 1.11 (d, 9H,CH(CH$_3$)O, J=6.2 Hz); 1.02 (d, 9H, CH(CH$_3$)N J=6.5 Hz); 0.81-0.89 (m, 3H, CH2CH$_3$).

Then mass distribution of **P** was investigated by ESI-mass (1mg/1ml in MeOH). The resulting mass spectrum, shown in figure 8.4, presents four groups of peaks in different colours corresponding to the mono-, di-, tri- and tetra-protonated **P** labeled as **PH$^+$** (black), **PH$_2{}^{2+}$** (red) and **PH$_3{}^{3+}$** (green) and **PH$_4{}^{4+}$** (cyan) respectively. The different constitutional isomers are labelled by n, being n=a+b+c+d+e+f. The ESI-mass spectrum clearly show that isomers with n=9, 10 and 11 are the predominant species, being the sum of their molar fraction about 0.75. The sum of the molar fraction of the two isomer n=8 and n=12 is about 0.20. Lastly the sum of the molar fraction of the isomers with n<8 or n>12 is less than 0.05. This is perfectly in accord with the result obtained for the ESI-mass spectrum for **J**. The molar mass calculated from the mass distribution data was 1190 g/mol with a polydispersity index PdI=1.01.
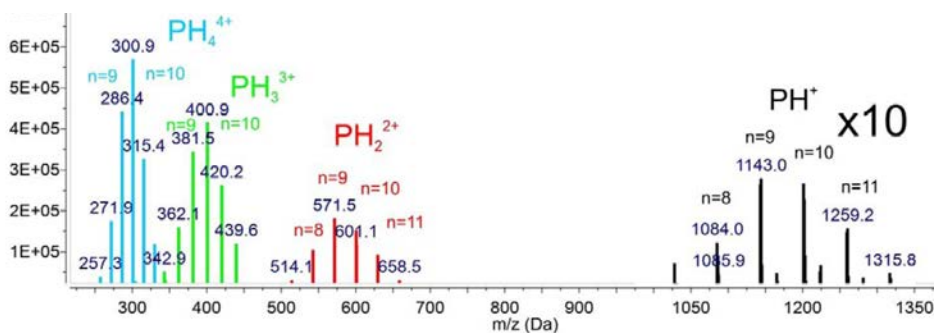
Figure 8.4: ESI mass spectrum of P. The signal of PH$^+$ have been multiplied by 10.

^{1}H NMR proton NMR was collected for **P** in deuterated chloroform at a 400 MHz instrument. The resultant chemical shift are δ (ppm) 8.71-8.61 (m, 8H, arom C**H**); 4.40-4.33 (m, 2H,NCHCH$_3$); 3.65-2.95 (m, 46H, CH$_2$CH(CH$_3$)O+OCH$_2$+CH(CH$_3$)NH$_2$); 1.59 (d, 6H, NCH(CH$_3$), J=6.7 Hz); 1.40 (s, 4H, CH3CH$_2$); 1.2-0.85 (m, 36H, C(CH$_3$)HO+C(CH$_3$)HNH$_2$+CH$_2$CH$_3$).

8.3 Photophysical characterization of P

Absorption and fluorescence spectra of the purified product **P** in chloroform solution, with fluorescence intensities corrected for inner filter effects according to standard methods,[1] are shown as filled orange curves in figure 8.5 and 8.6

respectively. The absorption spectrum presents the typical structured band of the PDI chromophore with a maximum at λ_{max} = 525nm (ε_{max} = 8 × 10^4 M^{-1}cm^{-1}) in good accordance with the ones measured for similar PDIs. Similarly, the fluorescence of **P** in CHCl$_3$ (λ_{exc} = 488 nm) shows, as reported for analogous PDI fluorophores, a typical vibrational spectral structure (λ_{max} = 534) and a fluorescence quantum yield (Φ) of 0.9 ± 15% (determined using N,N′-Bis(2,5-ditert-butylphenyl)-3,4,9,10-perylenedicarboximide in CHCl$_3$ solution, Φ=0.99). It also display a mono-exponential decay of the excited state with τ = 3.7 ns.[2]

By photophysical measurements, it was also possible to determine the degree of conversion of PTCDA into **P** after microwaves irradiation. To this end 0.010 ml of such homogeneous mixture has been diluted in 10 ml of ethanol and the absorption spectrum has been recorded. The resulting spectrum shows the typical structured band of PDI with a maximum at λ=526 nm where the absorbance is 1.33. Being the molar absorption coefficient of **P** at that wavelength 8×10^{-4} M^{-1}cm^{-1}, it was calculated the concentration of **P** (c=0.017 M) to be compatible with a complete conversion of PDATC in PDI.

With the aim of apply this molecule in molecular imaging, an important aspect to consider was the of the solubility and aggregation properties of **P** in water under physiological conditions. It was hence prepared a set of PBS dispersions of the dye at concentrations of **P** ranging from 1×10^{-6} M to 1.2×10^{-4} M. The molar absorption coefficient spectra of these dispersions, shown as continuous lines in figure 8.5, are largely perturbed when compared to the absorption spectrum recorded in CHCl$_3$ (orange filled in Fig. 8.5). In particular, the absorption band is broader and the vibrational structure is much less defined in PBS than in the organic solvent. Moreover, it can be noticed that these changes are more marked at higher concentrations of **P**. Analogous changes have been reported in literature for other PDI derivatives as resulting from π–π stacking interactions that, especially in polar solvents, lead to the formation of aggregates.[3-5]

The presence of a quite mono-disperse population of NPs, resulting from self-assembly of **P,** was indeed confirmed by dynamic light scattering (DLS, average diameter d = 109 nm, PdI = 0.19) as shown in the inset of figure 8.5. The morphology of the aggregated species was investigated by TEM, depositing and drying under vacuum a drop of nanoparticles suspension on a standard 3.05 mm copper grid (400 mesh) covered by a Formvar support film (Fig. 8.7).

As far as fluorescence is concerned, the corrected spectra[1] of the PBS dispersions, plotted as continuous lines in figure 8.6, show that NPs formation in PBS leads to a

strong decrease of the fluorescence intensity, without changing significantly the spectral profile of the emission. The spectral structure is, in fact, similar to the one observed in CHCl$_3$ and independent on the concentration of **P**; only a 10 nm red-shift of the maximum in PBS is observed, which is compatible with the different solvent polarity.[2] More in detail, the fluorescence quantum yield in PBS is in any case much lower (less than 10% in the investigated concentration range) than the one measured in chloroform, and it progressively decreases upon increasing the concentration (Fig. 8.6, top).

In order to investigate the origin of these residual emissions, we acquired the fluorescence excitation spectra and excited state decays of the PBS dispersion. As for the emission, the profile of the fluorescence excitation spectrum (λ_{em} = 590nm, not shown) is concentration independent and it presents the typical vibrational structure of the non-aggregated PDI. Similarly, the decay of the excited state in PBS is mono-exponential and the excited state lifetime does not change with the concentration, being comparable with the one measured in chloroform (Fig. 5.6, top).

All these observations allowed us to conclude that aggregation leads to the formation of completely quenched **NP**s and that the residual weak fluorescence observed in PBS is due to a small fraction of non-aggregated **P** molecules.
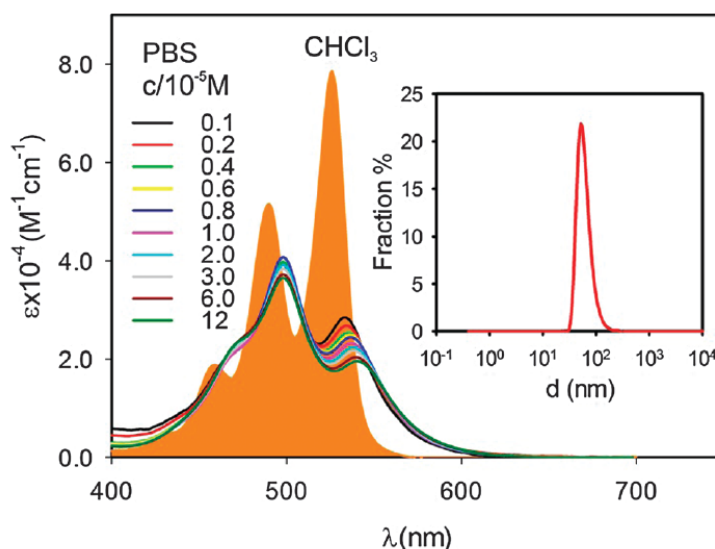
Figure 8.5: Molar absorption coefficient of P in CHCl3 (filled orange curve) and in PBS at concentrations ranging from 1 x 10^{-6} M to 1.2 x 10^{-4} M. Inset: size distribution of the P NPs in PBS measured by DLS
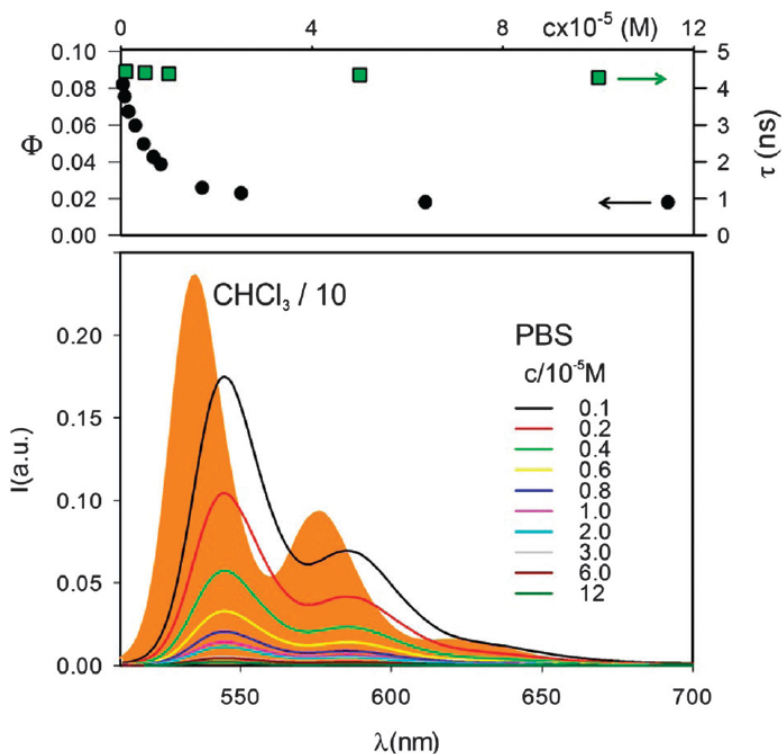
Figure 8.6: (bottom) Corrected fluorescence spectra of P in CHCl₃ (filled orange curve) and in PBS at concentrations ranging from 1 x 10⁻⁶ M to 1.2 x 10⁻⁴ M (λₑₓc = 488 nm). (top) Fluorescence quantum yield and the excited state lifetime of P as a function of its concentration in PBS.
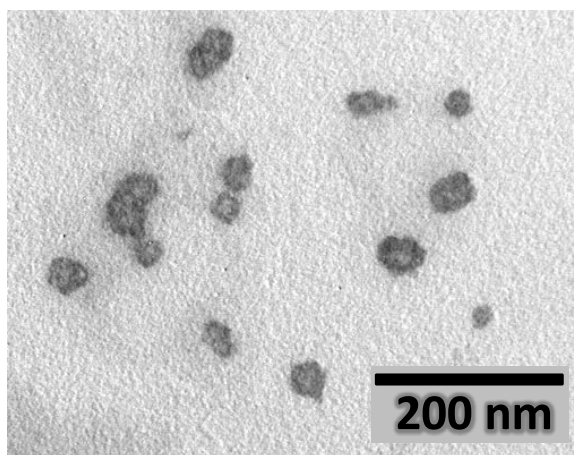
Figure 8.7: TEM grid image of the P aggregates in PBS.

8.4 Cells studies

Being very poorly fluorescent, NPs of **P** resulted very good candidates as potential fluorogenic nanoprobes for cell labelling based on disaggregation induced emission. In order to confirm this hypothesis, such an application of the **P** NPs was studied in the case of *Saccharomyces cerevisiae* yeast cells, organisms that have been reported to be relevant models in cancer research.[6] They are even easier to manipulate and less sensitive to contamination and environmental factors.

First, it was studied the cellular uptake of the NPs by incubating the yeast (2.5×10^6 cells per ml) in PBS with NPs obtained at different concentrations of **P**. In order to determine the actual molar fraction of **P** adsorbed by the yeast, a suspension of cells was prepared by vortex stirring 100 mg of yeast in 10 ml of PBS solution. 0.25 ml of the resulting suspension were added to 2.25 ml of the PBS dispersions of **P**, having a concentration of the dye ranging from 1×10^{-6} to 1.2×10^{-4} M. The resulting suspensions were vortex stirred for one minute in Eppendorf test tubes and then incubated at room temperature for 30 minutes. Lastly, the incubated suspensions were centrifuged for 5 minutes at 1000 rpm and the surnatant has been transferred to spectrophotometric cuvettes in order to measure the absorbtion spectrum. The fraction adsorbed at the different concentrations (χ) was determined by comparing the final absorbance at 498nm (A) to the one measured before the yeast addition (A_0) according to the equation (S1). The adsorption of the NPs is almost complete for concentrations up to 1×10^{-5} M (Fig. 8.8, a).

$$\chi = \frac{A_0 - \dfrac{A}{0.9}}{A_0} \qquad (Eq. S1)$$

Then, the fluorescent spectra of two yeast dispersions in PBS after incubation with the NPs (concentration of **P** 1×10^{-6} M and 1×10^{-5} M) were recorded before centrifugation (Fig. 8.8,b). Interestingly, these spectra are clearly different and a red emission centred at about 630 nm can be detected in the sample with the highest concentration of **P**. This particular behaviour was attributed to local effect of **P** on the yeast cells.

In order to better understand the phenomena, fluorescence microscopy measurements were carried out. The sample was prepared incubating the yeast cells with the NPs dispersion as reported before but, in this case, the cells were not centrifuged and 0.1 ml of the suspension were directly dropped on the top of a 0.13 mm thick cover slide (without any washing or post-treatment). The microscope,

was equipped with a Xenon lamp (450 W) for fluorescence excitation and a CCD camera for images acquisition, the lamp was attenuated with an absorptive filter and coupled to a fluorescence cube mounting the filters set Chroma 11001v2 blue. Collecting the images at 10X magnification, it was confirmed the difference in the emission colour observed for the solutions at different concentrations, since either only green emitting (concentration of **P** 1 × 10^{-6} M, Fig. 8.9, left) or red emitting yeast cells (concentration of **P** 1 × 10^{-5} M, Fig. 8.9, right) can be observed.

Increasing the magnification at 100X, (Fig. 8.10), it was still possible to observe the concentration dependent colour and appreciate that the distribution of the fluorescence is not homogeneous, but it depends on the local accumulation is cells compartments. This is particularly interesting form the applicative point of view, since it can provide information about the anatomy of the cells. The measurements conditions also allow to confirm that the nanoparticles are not deposited on the cell surface, but they penetrated the cytosol. In fact, since the objective used has high NA and a nominal depth of field lower than 100 nm, it is possible to observe thin slides of cells. As already mentioned in the introduction, one of the main problems which are still limiting the fluorescence imaging applications is the strong noise signal. In this case, it is worthy to stress that background fluorescence is almost negligible and only specific emission from the cells is observed, although the images of both the green and red emitting samples were taken without any washing of the yeast cells.[7,8]
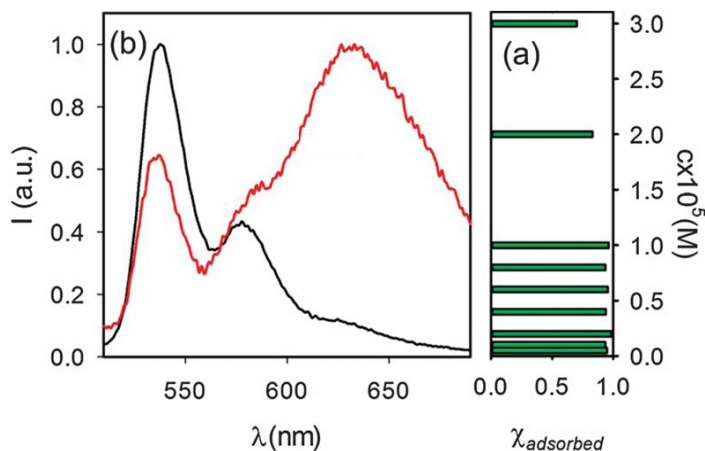
Figure 8.8: Molar fraction of P adsorbed by yeast cells (2.5× 10^6 cells ml^{-1}) as a function of P concentration in PBS. (b) Fluorescence spectra (λ_{exc} = 488nm) of the yeast suspensions for concentration of P 1 × 10^{-6} M (black curve) and 1 × 10^{-5}M (red curve).
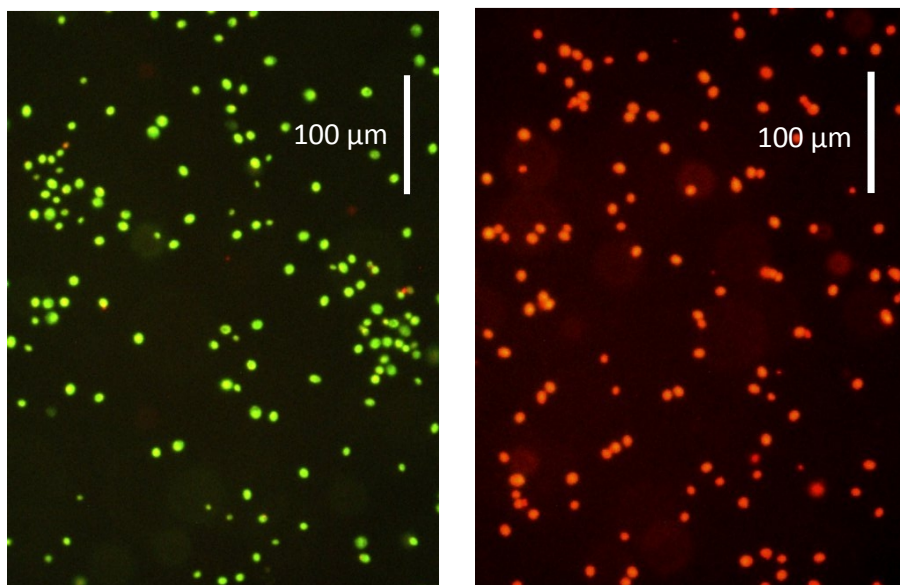
Figure 8.9: Fluorescence image (10X magnification) of living cells after incubation with PBI nano-aggregates at low (1 µM, left) or high (10µM, right) dosage. Both sample were image directly without any cells washing.
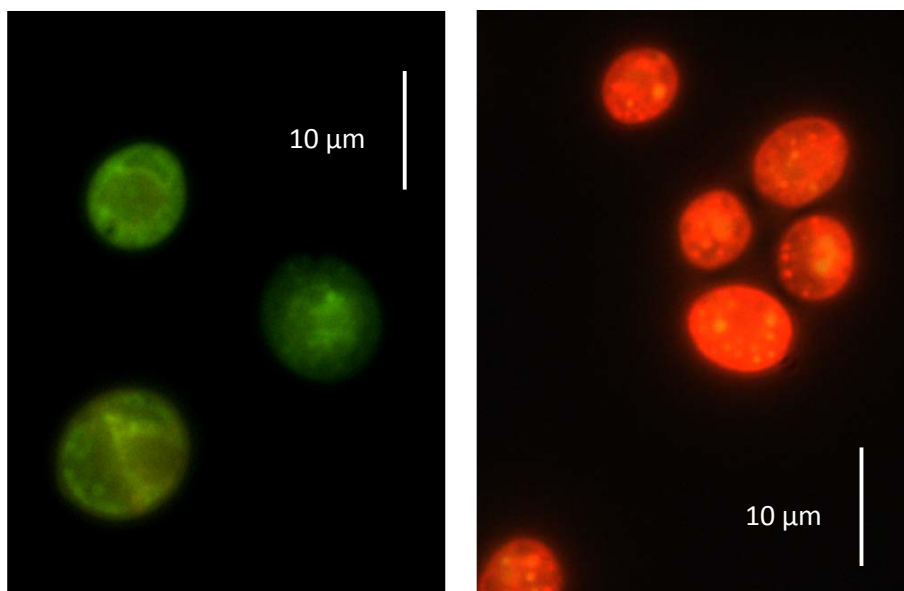
Figure 8.10: Fluorescence image (100X magnification) of living cells after incubation with PBI nano-aggregates at low (1 µM, left) or high (10µM, right) dosage.

The overall observed behaviour was interpreted as resulting from the adsorption of **P** by the target cells, followed by its redistribution and reorganization in the different cellular compartments (Scheme 8.1). In this prospective, the green emission is due to individual **P** molecules (case A), while the red fluorescence is due to some aggregates formed into the yeast cell, with an intensities largely dependent on the nature of the aggregates themselves, on their size and on the external environment.[4,9] In accordance with such a reported variability our results demonstrated that, when **P** assembles in PBS forming the NPs, it undergoes complete quenching. In the cellular environment, on the other hand, **P** aggregates generate strongly red emissive species. Unfortunately, the actual quantum yield of the red emission in the yeast cell, which would provide important information about the nature of the aggregates, can hardly be measured, because of the strong scattering effect generated by the sample and the instrumental setting. Anyway, from the fluorescence images, it is clear that the intensity of the red emitting yeast is stronger than the one of the green emitting cells and that it is suitable for imaging purposes. Summarizing, NPs made of **P** not only behave as fluorogenic nano-probes suitable for cell labelling, but the disaggregation can be complete (case A) or partial (case B) and the resulting DIE being green or red, respectively. This means that dosage dependent specific coloration can be achieved.
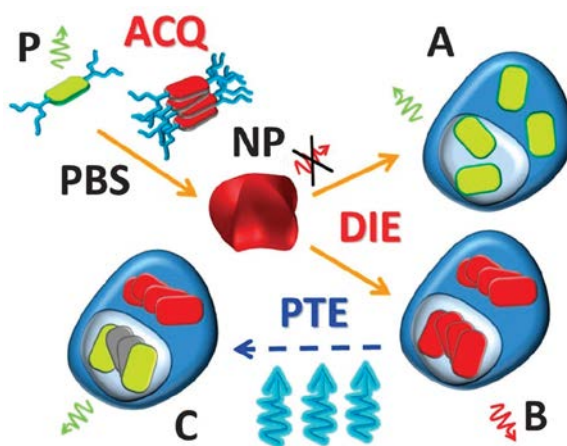
Scheme 8.1: The fluorescent polyetheramine P aggregates in PBS and forms NPs that are not fluorescent due to ACQ. Adsorption by cells leads to disaggregation of the NPs and to fluorescence recovery (DIE). The cells become green fluorescent (case A) or red fluorescent (case B), respectively, at low and high NPs dosage. Exposure to strong visible light allows the phototuning of the emission (PTE) of specific cellular compartments (C).

As mentioned, fluorescence distribution in the cells, as observed in figure 8.8, b allows us, to some extent, to visualize the different cellular compartments. Nevertheless the level of contrast achieved in these almost monochromatic images is quite poor.

Surprisingly, we observed a very peculiar development of the fluorescence images in the case of the red staining (case B) during irradiation of the sample with strong blue light, that allows a substantial improvement of the contrast. We would like to stress that such a change occurs only when the excitation intensity in the microscope is increased by three orders of magnitude with respect to the one used for the acquisition of images shown in figure 8.9 and 8.10. In this case, in fact, no relevant changes in the fluorescence images were observed in the minutes time scale in the case of low power excitation. To increase the irradiation power, the same experimental setup was adopted, but the sample was first focused attenuating the excitation with an absorptive filter (Thorlabs NE30B), then the filter was removed and the acquisition immediately started.

More in particular, as shown in figure 8.11, the photo-tuning (PT) process allowed to turn the fluorescence of some specific cellular compartments from red to yellow and then to green. Figure 8.11 clearly shows that the various compartments respond in a different way to the PT, giving coloured photo-tuned emission (PTE). Since local pH and redox potential are expected to play a role in the colour change, we investigated their effect on the fluorescence properties of **P** in solution.
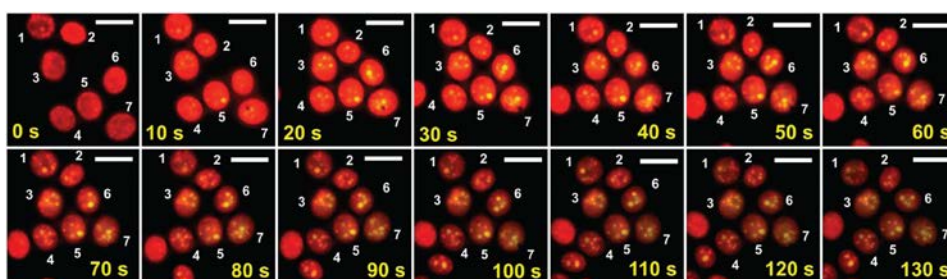
Figure 8.11: Fluorescence images (magnification 100X) of a suspension of yeast cells (2.5 × 10⁶ ml⁻¹) after incubation with P 1 × 10⁻⁵ M in PBS taken at different delay times during excitation with intense blue light. The cells were numbered to allow their identification. The scale bar is 10 μm.

8.5 Study of pH and redox effects

It is known that a lot of different environment are present in the cells, and in particular pH and redox potential can vary in different compartment. In order to

exclude the contribution of this parameters on the tuned emission, their effects were investigated on the absorption and fluorescence spectra of **P.**

Photophysical properties were investigated in the typical cellular pH range (4.0-8.5 pH) in the case of a PBS solution $1x10^{-5}$ M of **P**. The pH of the solution was decreased to 4.0 by adding CH_3COOH 1 M and then increased gradually by adding NaOH 0.1 M. No significant changes were observed either in the absorption (Fig. 8.12) or fluorescence (Fig. 8.13) spectra in the typical cellular pH range.

In order to ruled out any direct redox effect, electrochemical experiments were carried out in argon purged water solution at 298 K. The cyclic voltammetry (CV) was collected using glassy carbon electrode (0.08 cm^2) as working electrode and a Pt spiral as counter electrode. It was studied a solution at a concentration of **P** of the order of $5x10^{-4}$ M, where $LiClO_4$ 0.1 M was added as supporting electrolyte. Cyclic voltammograms were obtained with scan rates in the range 0.05–20 V s-1. In the range of potential potential for **P** $E_{1/2}$ = -0.54 V (**P/P**$^-$), no oxidation of **P** was observed in the -1.00-0.00 V interval.
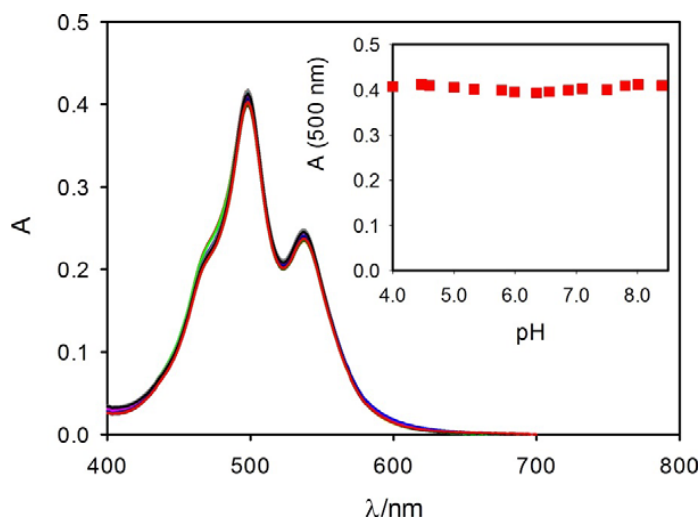
Figure 8.12:Absorption spectrum of P $1x10^{-5}$ M at different pH. Inset: absorption at 500 nm of the $1x10^{-5}$ M solution of P as a function of pH

Considering the effect of aggregation on the fluorescence of **P**, the colour change was interpreted as a consequence of a local decrease of **P** concentration, due to a partial photo-bleaching of the red emitting aggregates. That leads to the disaggregation of **P** in the form of individual green emitting. This model does not exclude an indirect effect of the pH and redox potential on the PT process since the

former parameter could influence the uptake and the distribution of the dye and the latter could affect the photo-bleaching rate. Although, the investigation of the specific response of different organelles to this photo-activation process is beyond the objective of this thesis work. What it has to be stresses is that, since the photo-activation is strongly affected by local properties, the controlled and selective irradiation can be, at least in principle, exploited to develop new protocols for specific imaging and investigation of cellular metabolic and regulatory processes.
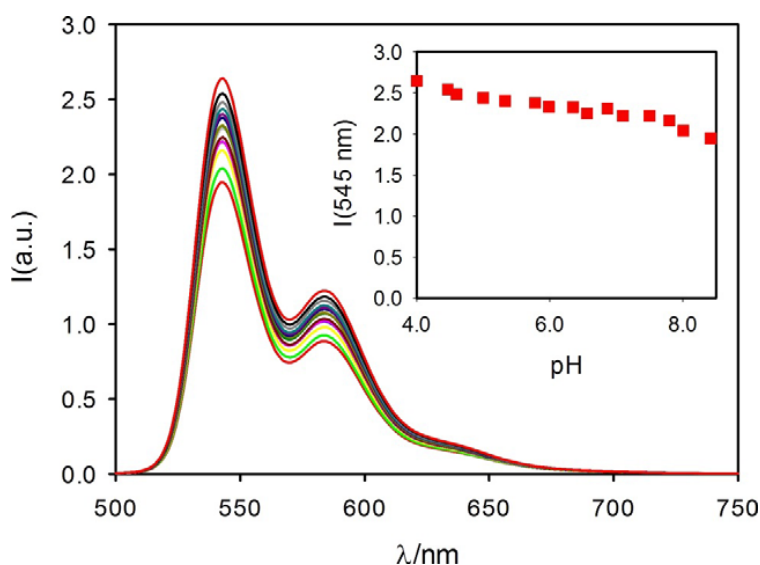
Figure 8.13: Fluorescence spectra of P 1x10^{-5} M at different pH. Inset: absorption at 500 of the 1x10-5 M solution of P as a function of pH.

8.6 Cytotoxicity studies

Eventually, it was investigated the cytotoxicity of **P** on the yeast cells. To this end *Saccharomyces Cerevisiae* (2.5x10^6 cells/ml) were suspended either in PBS (samples **PBS0**, **PBS1** and **PBS2**) or in an SD culture medium (samples **C0**, **C1** and **C2**) either in the absence of **P** (samples **PBS0** and **C0**) or in the presence of **P** (10^{-6} M in the case of **PBS1** and **C1** and 10^{-5} M in the case of **PBS2** and **C2**). All the samples were incubated at 30 °C for 4 hours and stained with Trypan blue (0.4 %) in order to investigate cells viability. The total concentration of cells and the concentration of dead cells was determined using a hemocytometer. In figure 8.14 are reported the final concentrations of the total cells (black bars) and of the dead cells (red bars) starting in all cases from an initial concentration of cells 2.5 × 10^6

cells per ml. The data in figure 8.14 show that the presence of **P** does not increase significantly the mortality and does not inhibit the growth of the cells, which is particularly interesting for further applications.
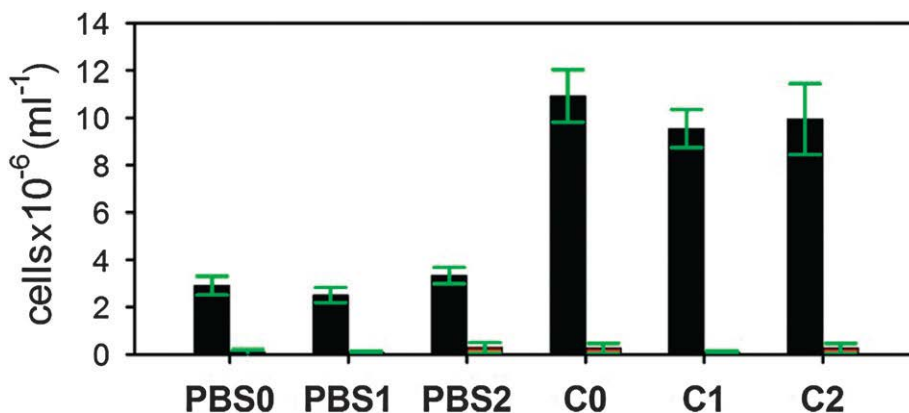
Figure 8.14: Concentration of yeast cells (total: black bars, dead: red bars) after 4 hours incubation at 30°C in PBS (PBS0) or culture medium (C0); P 10^{-6} M in PBS (PBS1) or culture medium (C1); P 10^{-5} M in PBS (PBS2) or culture medium (C2). The cell concentration before incubation was in all the cases 2.5 x 10^6 cells per ml.

8.7 Conclusions

In conclusion it was reported the efficient microwave assisted synthesis of a new strongly fluorescent perylene derivative that can be dispersed in water in the form of self-assembled non-fluorescent NPs. We demonstrated that these NPs are efficient fluorogenic imaging agents in the case of model yeast cells and that, by controlling the dosage, either green or red fluorescence can be obtained. The same NPs can be used to achieve multicolour fluorescence imaging by photo-activation of the sample. Considering these features, the lack of toxicity and the versatility of the proposed synthetic methodology, although the applicability of this NPs to other cells has to be investigated, we believe that our approach can be an inspiration for the design of new smart imaging agents for application in life sciences.

Bibliography

1 Montalti, M., Credi, A., Prodi, L. & Gandolfi, M. T. Handbook of Photochemistry. *CRC Press: Boca Raton, FL,* (2006).

2 Ford, W. E. & Kamat, P. V. Photochemistry of 3,4,9,10-perylenetetracarboxylic dianhydride dyes. 3. Singlet and triplet excited-state properties of the bis(2,5-di-tert-butylphenyl)imide derivative. *The Journal of Physical Chemistry* **91**, 6373-6380, doi:10.1021/j100309a012 (1987).

3 Görl, D., Zhang, X. & Würthner, F. Molecular Assemblies of Perylene Bisimide Dyes in Water. *Angewandte Chemie International Edition* **51**, 6328-6348, doi:10.1002/anie.201108690 (2012).

4 Chen, Z., Fimmel, B. & Wurthner, F. Solvent and substituent effects on aggregation constants of perylene bisimide [small pi]-stacks - a linear free energy relationship analysis. *Organic & Biomolecular Chemistry* **10**, 5845-5855, doi:10.1039/C2OB07131B (2012).

5 Gesquiere, A. J., Uwada, T., Asahi, T., Masuhara, H. & Barbara, P. F. Single Molecule Spectroscopy of Organic Dye Nanoparticles. *Nano Letters* **5**, 1321-1325, doi:10.1021/nl050567j (2005).

6 Hartwell, L. H., Szankasi, P., Roberts, C. J., Murray, A. W. & Friend, S. H. Integrating genetic approaches into the discovery of anticancer drugs. *Science* **278**, 1064-1068 (1997).

7 Heek, T. *et al.* Highly fluorescent water-soluble polyglycerol-dendronized perylene bisimide dyes. *Chemical Communications* **46**, 1884-1886, doi:10.1039/B923806A (2010).

8 Hori, Y. & Kikuchi, K. Protein labeling with fluorogenic probes for no-wash live-cell imaging of proteins. *Current opinion in chemical biology* **17**, 644-650 (2013).

9 Tian, Y., Stepanenko, V., Kaiser, T. E., Würthner, F. & Scheblykin, I. G. Reorganization of perylene bisimide J-aggregates: from delocalized collective to localized individual excitations. *Nanoscale* **4**, 218-223 (2012).

9 Cross-linked core-shell multi-responsive NPs

9.1 Synthesis of P nanoparticles (PNPs)
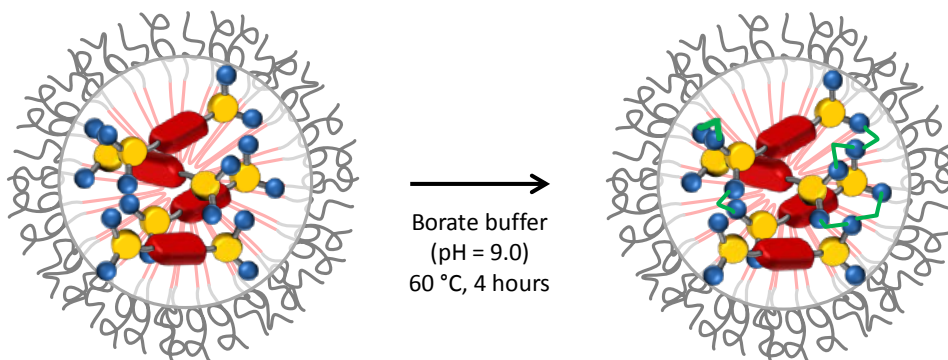
*Figure 9.1: Schematic representation of the PDI-core and PEG-shell cross-linked nanoparticles (**PNP**s), formed after P monomer reaction with diglycidyl ether (BADGE) in the Pluronic F-127 micelle core.*

Nanoparticles (**PNP**s) (Fig.9.1) were prepared dissolving 16 mg of the starting material P[1](synthesis and characterization described in chapter 8) and 8 mg of the cross-linker 4,4'-isopropylidenediphenol diglycidyl ether (BADGE) (2 equivalents of P per molar equivalent of cross-linker) in 8 ml of a borate buffer solution, in the presence of 500 mg of the block copolymer Pluronic® F-127. The poor solubility of P and BADGE in the polar environment at the pH working conditions, induced the inclusion of the precursors in the core of the Pluronic® F-127 micelles, already formed at the operative poloxamer concentration.[2] The alkaline conditions (pH = 9) were required to catalyze the epoxydic rings opening under the nucleophilic attack of P amine terminations (Fig. 9.2). Heating of the reaction mixture at 60°Cwas also needed.

P displays four amino groups, able to undergo twice attacks each, while BADGE has two epoxidic rings as termination groups. This allows the cross-linking of the two monomers to form polymers/oligomers into the micelles core. The reaction product, obtained after 4 hours under magnetic stirring, is a cross-linked matrix that traps the Pluronic® F-127 poly-(propylene oxide) hydrophobic blocks. By this procedure, nanoparticles of P (**PNP**s), constituted by a covalently linked PDI core and a poly-(ethylene glycol) chains shell, were obtained (Fig. 9.1).

Considering a complete conversion of the starting material P, it can be estimated an average number of perylene diimide units per nanoparticle ranging around 25

(P_{MW}=1388g mol^{-1}, average Pluronic F-127$_{MW}$=12600 g mol^{-1}; aggregation number of Pluronic F-127 at 60°C ~80).
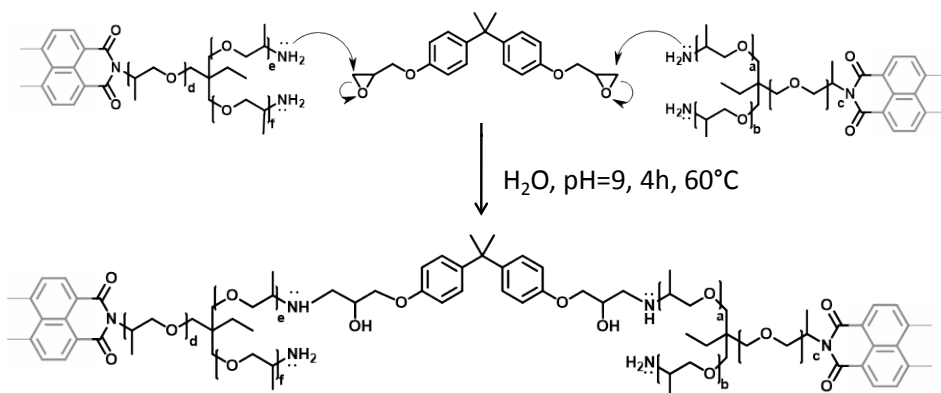
Figure 9.2: Schematic proposed reaction mechanism: nucleophilic attack of the terminal amino groups of P leads to the Bisphenol epoxy rings opening and the reactant cross-linking in the Pluronic micelle core.

9.2 Morphological and photophysical characterization of PNPs

A preliminary morphological characterization has been carried out by dynamic light scattering (DLS), after 10 times dilution of the **PNP**s in PBS 1X (pH = 7.4).[3] This particular dispersant was chosen because it is commonly used in biological tests, and because buffering the solution at neutral pH allows a better control over the whole system behaviour, being the components pH sensitive. Moreover it was expected to increase the nanoparticles colloidal stability by increasing the net charge. At this **PNP**s concentration, back-scattering phenomena are avoided and Pluronic® F-127 micelles signal can be considered negligible respect to the one due to the nanoparticles(critic micellar concentration (c.m.c.) of Pluronic F-127 at 25°C is 950-1000 ppm). Discriminate the formed nanoparticles from the surfactant micelles, in fact, is quite challenging at the reaction concentration, according with the fact that they display the same hydrodynamic volume. As a confirmation test of the nanoparticles formation, the DLS measurements has been recorded at three different temperatures, since the poloxamer micellization is strongly temperature dependent.[4,5] Although the values reported in literature vary substantially, the c.m.c clearly decrease with an increase in temperature. The average aggregation number and the micellar size, likewise, increase with temperature, although these absolute values vary between different systems and even between different batches. On the

other hand, anyway, no size changes are expected for the cross-linked nanoparticles. As reported in figure 9.3, an hydrodynamic diameter of 34 ± 9 nm was measured at 25°C for the **PNP**s, and no significant variations are observed at 10°C and 60°C (36 ± 10 and 35 ± 10nm respectively). It is worthy to mention that DLS measurements have been collected also for the reaction mixture before the reaction at the same dilution conditions. As in the case of Pluronic F-127 dispersed in PBS, scattering signal intensity is more than ten times lower than in the case of the formed nanoparticles, and it approaches the instrument limit of detection.
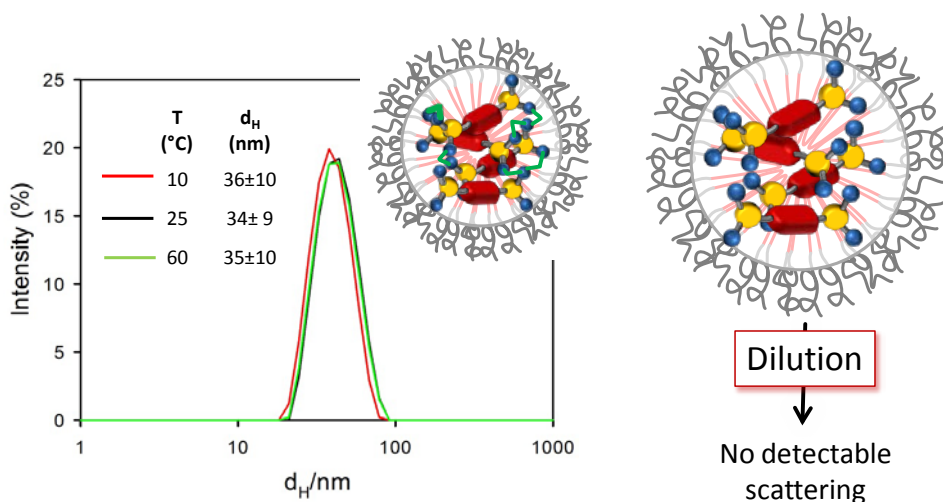
*Figure 9.3: (Left) DLS **PNP**s measurement after cross-linking. Under ten times dilution respect to the synthesis concentration, no variations are detectable for the hydrodynamic diameter value measured at 10, 25 and 60 degrees. (Right) Under the same dilution conditions, the reaction mixture before the cross-linking do not show any detectable scattering signal.*

7 days after the synthesis, confirmed the sample colloidal stability by DLS, ζ-potential value of +7mV has been measured for the **PNP**s. It is known that a colloidal system is electrostatically stabilized if the ζ-potential is higher than +30 mV or lower then -30mV. The +7 mV observed value, combined with the colloidal stability of the sample, confirms that the PEG chains of the shell sterically stabilize the nanoparticles.

The **PNP**s sample, diluted 100 times in PBS ([P] = 2.2 × 10^{-5} M), has been photophysically characterized and the spectra compared to the ones of the monomer P at the same concentration in chloroform(although soluble in water, P

tends to aggregate with stability constants that range around 10^7 M^{-1}). As it can be appreciate for the normalized spectra in figure 9.4, absorption band of the nanoparticles (red line) is broader respect to the monomer one (black line) and it shows an inversion in the intensity of the 0→0 and the 0→1 vibronic transitions. Emission spectra (normalized in Fig. 9.5) have been collected at the same conditions of solvent and dilution, exciting the sample at 480nm, where the difference in absorbance between the monomeric and the aggregated species is minimum. The maximum of the emission band of the aggregate (black curve) is 116nm red shifted respect to the monomer one (λ_{max}= 650nm and 534nm respectively), it is broader and the vibronic structures is completely lost.
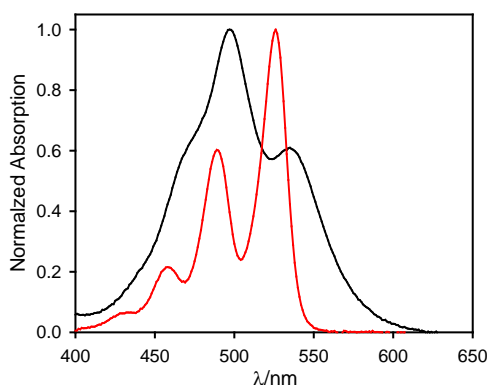
*Figure 9.4: (black curve) normalized absorption spectra of the formed **PNPs** at a P concentration 2.2 × 10^{-5} M in PBS; (red curve) normalized absorption spectra of P, concentration 2.2 × 10^{-5} M in chloroform.*
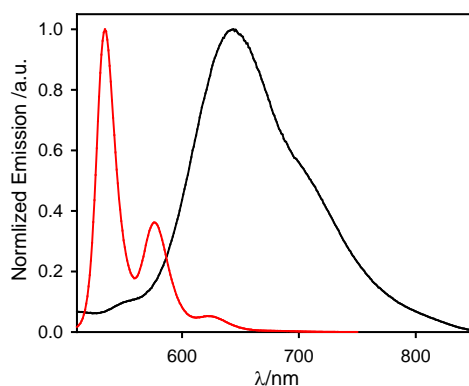
*Figure 9.5: (black curve) normalized emission spectra of the formed **PNPs** at a P concentration 2.2 × 10^{-5} M in PBS; (red curve) normalized absorption spectra of P, concentration 2.2 × 10^{-5} M in chloroform.*

Normalized excitation spectra of **PNP**s were collected at 560nm (red curve, Fig. 9.6), corresponding to the maximum of the **P** emission band, and at 660nm (blue curve), corresponding to the maximum of the aggregated emission band. They were compared to the **PNP**s absorption curve (black curve). Although they do not perfectly overlap the **PNP**s absorption curve, they significantly differ from the one of the monomer (orange curve). That proves that the contribution of monomer to the emission is not significant, even if the quantum yield difference is extremely high. The similarity of the excitation spectra collected at 560 and 660 nm confirms that the a reasonable amount of the emissive specie is the aggregated PDI, while differences between them and the absorption spectrum can be attributed to the presence of different populations of PDIs units in the nanoparticles core. These molecules, in fact, can generate different aggregated species, completely quenched, or characterized by reduced fluorescent quantum yield. Moreover they are expected to undergo energy transfer in the NPs, a process that makes possible complex excited state deactivation pathways.

Photophysical and morphological characterizations discussed above proved that perylene diimide derivative P formed aggregated species in the Pluronic F-127 micelles, and the colloidal stability of the dispersion is guaranteed by the steric hindrance of PEG chains, even at concentration lower than the polymer c.m.c.
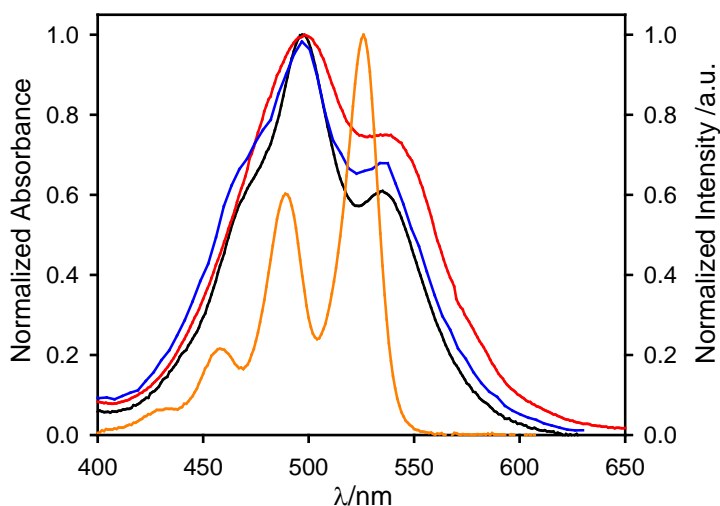
Figure 9.6: (red curve) **PNP**s *normalized excitation spectra (λ_{em} = 560 nm) in PBS; (blue curve)* **PNP**s *normalized excitation spectra (λ_{em} = 660 nm) in PBS; (black curve)* **PNP**s *normalized absorption band in PBS; (orange curve) P normalized absorption band in chloroform.*

Unfortunately, this is not a convincing proof of P covalent cross-linking into the nanoparticle core. In fact, at the measurement concentration conditions, it cannot be excluded the effect of aggregation of the monomer in the micelles core, only promoted by π-π stacking. To confirm the covalent reaction, the important effect of dye concentration on the photophysical properties turns to be useful. In a non covalent system, where only electrostatic forces affect dyes interactions, the dilution is expected to cause spectral shape variations, with the disappearance of the typical aggregated features and the recovering of the disaggregated one. On the other hand, in a covalently cross-linked system the aggregation grade does not change under dilution, causing only variation in spectral intensity. Accordingly, a titration increasing the **PNP**s concentration measuring absorption and the emission spectra has been carried out, to prove a linear dependence between the concentration and the photophysical quantities. For the absorption spectra, a **PNP**s solution obtained after synthesis was diluted ten times in PBS (pH =7.4), reaching a nominal P concentration of 1.8×10^{-4} M. Successive 5µl and eventually three 30µl-50µl-50 µl aliquots of this solution were added to a 2.5 ml PBS solution in a quartz cuvette. Absorption spectra were recorded after each addiction, exploring the nanoparticles behaviour at a concentration of P ranging from 3.8×10^{-7} to 1.4×10^{-5} M. This interval has been chosen considering 3.8×10^{-7} M as the lowest concentration detectable by the instrument and 1.4×10^{-5} M as the lowest molar concentration at which significant variation between the aggregate and the monomer could be observed. In figure 9.7, where are reported the absorption spectra corrected for the dilution, it can be observed that, while the absorbance regularly increases with the NPs quantity, there are not variations in the spectral shape. This is clearly enhanced normalizing the absorption spectra (Fig. 9.7, inset). The dependence between the absorbance collected at the maximum wavelength (470 nm) respect to the added volume is well fitted by a line, meaning that the solution dilution is affecting only the nanoparticles, and not the dye, concentration (Fig. 9.8).

In order to reach a lower concentration and to enhance the disaggregation effect, the titration was carried out measuring the **PNP**s emission spectra. Successive aliquots of **PNP**s water solution (concentration of $P=1.9 \times 10^{-5}$ M), were added to 2.5 ml of PBS in a quartz cuvette. The studied concentration range between 1.9×10^{-8} M and 1.9×10^{-7} M is critical, since P in the monomeric form typically displays a monomeric behaviour even in polar solvent. This is confirmed by the control titration, carried out with a P monomer solutions in PBS, in the same concentration

range. As shown in figure 9.9, both **PNP**s (red, gray curves) and P monomer (black, gray curves) emission profiles do not display spectral changes under dilution. In particular, no monomer contribution is detected reducing the **PNP**s concentration. This is particular important, also considering the strong difference in the quantum yields of the monomer, 0.9 respect to the aggregate species 0.005.
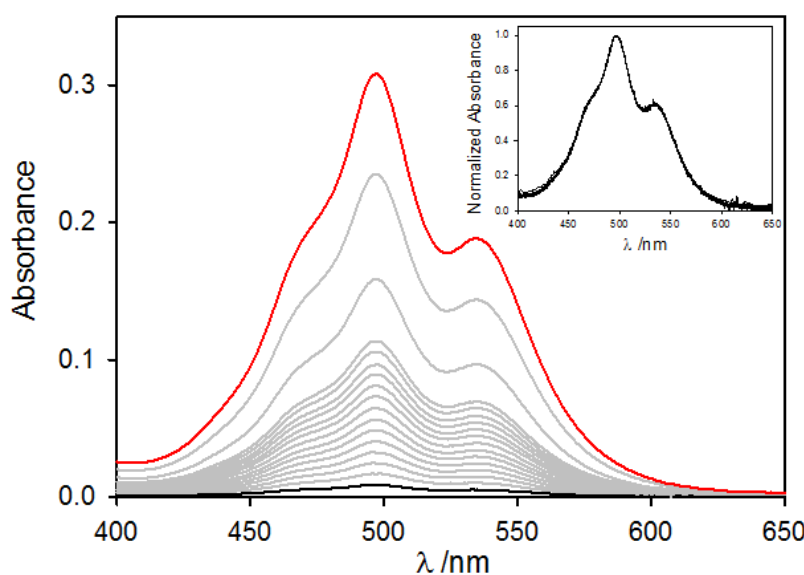
Figure 9.7: Absorption PNPs titration in PBS varying the concentration of P from 3.8 x 10^{-7}M (black curve) to 1.4 x 10^{-5} M (red curve). No spectral shape variation are detected in the interval, as enhanced by the normalized absorption spectra (inset).
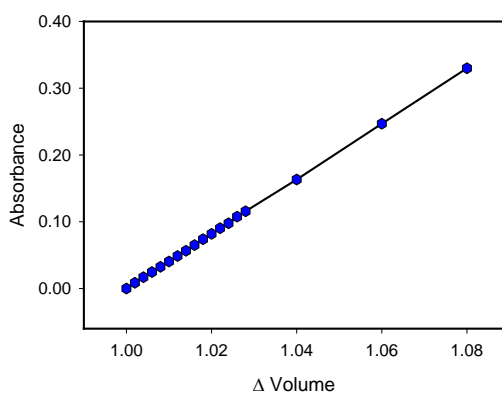
*Figure 9.8: Dependence between the absorbance of the **PNP**s collected at the maximum wavelength (470 nm) respect to the added volume. It is well fitted by a line, proving that no variations in the aggregation occurs under dilution.*
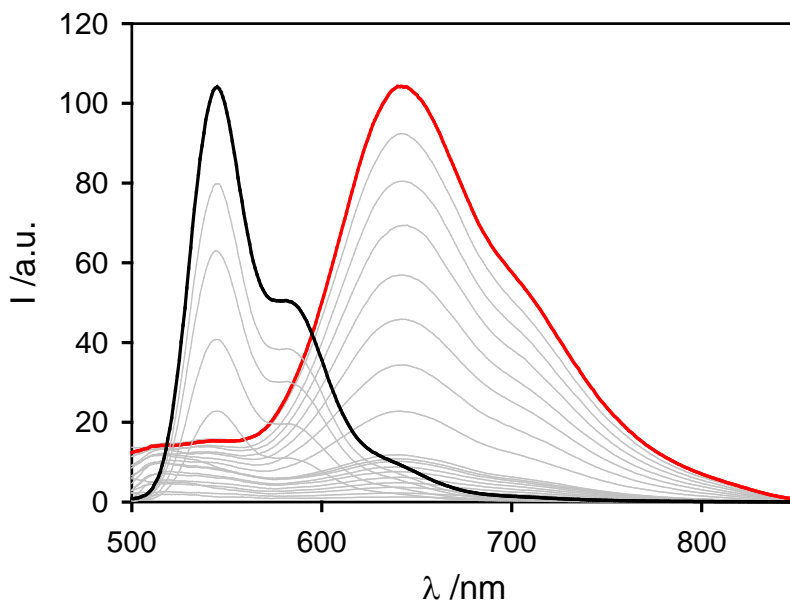
*Figure 9.9: (Red-gray curves) Emission titration of the **PNP**s at a P concentration ranging from 1.9 x 10⁻⁸ M and 1.9 x 10⁻⁷ M in PBS 1X. (Black-gray curves) Emission titration of P at a concentration ranging from 1.9 x 10⁻⁸ M and 1.9 x 10⁻⁷ M in chloroform. No spectral shape variations are observed in both cases,*

This means that P in the monomeric form is not released from the nanoparticle core into the environment. Since the aggregation constant for the monomer is not high enough to keep the dye units strongly stacked in this conditions, other forces have to be involved to trap P into the micelle core. To confirm that the P leaking is prevented by the monomer cross-linking into the nanoparticle cores, emission spectra of the reaction mixture where collected at different delay time during the **PNP**s synthesis.

The reaction mixture was prepared at the same conditions previously described, and an aliquot was collected and diluted in 2.5 ml of PBS in a quartz cuvette, reaching a concentration of P of 1.9 x 10⁻⁷ M. The procedure was repeated every 50 minutes along the 250 minutes of reaction and the emission spectra were collected for all the solutions. In figure 9.10 the profile of the intensity measured at 550 nm (maximum emission wavelength of the monomer) versus the reaction delay time is plotted. It can be appreciate that the signal is maximum at initial time and it drops to zero after 250 minutes of reaction. As reported in the inset, indeed, the emission intensity of the monomer decreases during the reaction while a weak contribution

from the aggregate form appears at 650 nm. The low intensity value measured for the aggregate is consistent with the remarkable difference in the quantum yield.
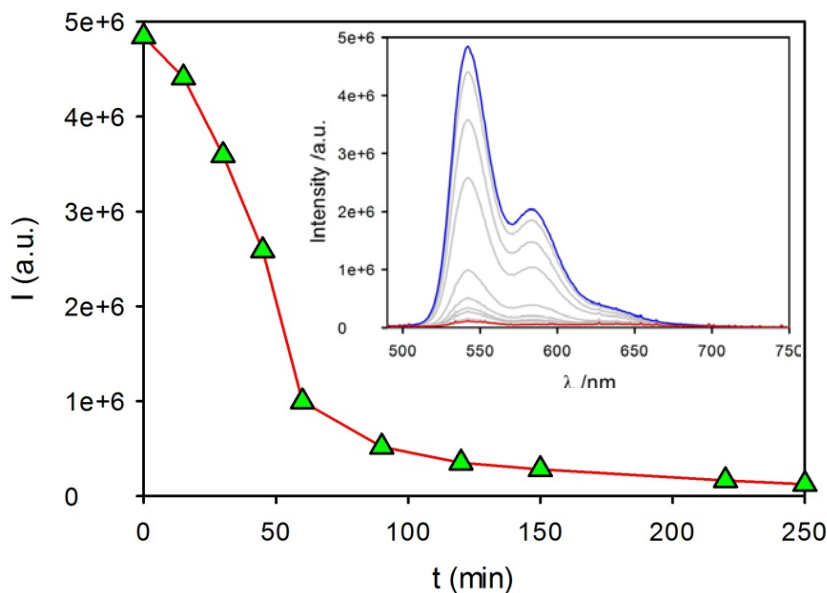
*Figure 9.10: Emission intensity at λ = 550 of the reaction mixture diluted in PBS (P concentration of 1.9 x 10^{-7} M) collected every 50 minutes during the **PNP**s synthesis plotted versus the delay time. (Inset) Respective emission spectra collected over the all emissive range (500-750 nm)*

This observation is a convincing proof that the detected emission is not due to the perylene diimide monomer aggregated in the micelles core, but to the **PNP**s where P is covalently reticulated in the core through the BADGE molecules, with the aromatic units spaced by the Jeffamine aliphatic branches. Unfortunately, the templated synthesis and the soft matter core-shell structure make very challenging the characterization of the nanoparticles by many of the standard analysis techniques available to us (e.g. NMR, IR, UV), making quite tough to define the exact chemical composition of **PNP**s. Anyway, it can be assumed that the matrix is not well defined and oligomers of different molecular weight took shape in the core, both considering the synthesis procedure and the photophysical properties displayed by the system. This is even more probable considering that the P molecule itself was not perfectly monodispersed as can be appreciated by the distribution of molecular weight calculated by the mass spectroscopy (Chapter 8). Despite the complexity of the system, further studies have been conducted to better

characterize the nanoparticles composition and to confirm that the used reactant ratio was the best one in term of nanoparticles stability.

9.3 Study of PNPs stability under different reactant ratios.

In the prospective of applying **PNP**s in bio-imaging, it is necessary to avoid the reactants release form the core into the environment. Not only PDIs may tends to interact with DNA strands, resulting toxic for cells,[6,7] but from the imaging point of view, the contrast would be strongly affected by the presence of high emissive component ubiquitous in the cell. In this prospective, it was critical the maximization of the PDI monomer conversion in the polymeric form or, at least, the reduction of its release in the environment afterwards. It was expected, in fact, that residual P monomer, not involved in the covalent bond formation, would get trapped in the micelle core by non-covalent forces (π-π stacking), being more prone to leach out of the NPs.

The epoxy-amine polymerization can mainly be described by step-growth or chain-growth mechanisms. In the former one, the hydroxyl groups forms a tri-molecular complex, catalyzing the nucleophilic attack of the amino groups. Side reactions do not take place when the epoxy groups concentration is equal or inferior respect to the concentration of NH groups. When the epoxy groups excess occurs, or the amine have low reactivity, the etherification reaction may take place, changing the initial stoichiometric ratio. In the latter case, a Lewis base catalyzes the nucleophilic attack of the amine, giving a zwitterion that contains an alkoxide anion and a quaternary (when the amine is tertiary) nitrogen atom. The ammonium salt can be considered as the initiator of the chain reaction. In most situations, although, the mechanism becomes a combination between the chain-growth and the step-growth ones. This last case probably better describe the reaction between P and the BADGE in the micelles core. In fact, it can be expected that the diffusion of the reactants into the Pluronic F-127 micelles do not occur at the same rate for the two of them, and their relative concentration changes during the polymerization itself. Since it was not possible to have a strict control over the reagents internalization into the micelles, a study of the **PNP**s formation reaction with different initial ratios of P and BADGE was carried out.

Three samples of **PNP** nanoparticles were prepared dissolving, in 3 ml of a borate buffer solution (pH=9), 7.5 mg of the starting material P and 3mg (sample *1*), 5mg (sample *2*) and 7.5mg (sample *3*) of the cross-linker 4,4'-isopropylidenediphenol diglycidyl ether (Bisphenol A), in the presence of 470mg of the block copolymer

Pluronic® F-127. In this way, 2.5, 1.5 and 1 molar equivalent of P were added respect to BADGE, respectively for **1**, **2** and **3**. Reaction at higher concentration of reactants were not investigated, since they were hardly longer soluble.

As a reference, 0.6 µl of the reaction mixture was collected before the reaction beginning and diluted in PBS reaching a P concentration of 3.8 x 10^{-7} M. The emission spectrum was collected exciting at 480nm. Then, the reaction mixtures were stirred at 60°C for 250 minutes and the nanoparticles formation was followed by fluorescence, monitoring the **P** monomer signal at different delay time along the reaction (λ = 542 nm). Hence, every 15 minutes 0.6 µl of the samples were diluted in PBS, without changing the concentration of P respect to the reference, and the emission spectra were collected at the same conditions as before.

As reported in literature,[1] at these dilution conditions the effect of π -π stacking is negligible for PDIs even in polar solvent, and non-covalent forces are not strong enough to induce the aggregation between P molecules. This is in accord with the observation, for the reference solution prepared before the reaction beginning, of an emission spectra with the typical feature of the monomeric P (Fig. 9.11, sample **3** as example, blue curve). Accordingly, it can be assumed that eventual fluorescence quenching occurring during the reaction could be only due to the formation of covalently linked species with different photophysical properties respect to the starting material P**,** responsible for a reduction of the fluorescence quantum yield. As far as fluorescence concerned, all samples corrected spectra collected during the synthesis are strongly dominated by P monomer features. The **PNP**s formation, indeed, leads to a strong decrease in the fluorescence intensity (Fig. 9.11). As expecting, knowing the **PNP**s photophysical behaviour, the disappearance of the free monomer signal is accompanied by the formation of a broader band centred at 640 nm, typical of the aggregated dye. This red-shifted band is only appreciable normalizing the emission spectra (Fig. 9.11, inset), since, in these diluted conditions, the low quantum yield makes the spectra strongly dominated by the monomer emission, even if in two hundred times lower concentration.

In order to visualize the effects of different reactants ratios in the **PNP**s formation, intensities recorded at 542 nm for samples **1** (yellow),**2** (red) and **3** (green) are plotted versus the reaction time in figure 9.12. It can be appreciate that for the three samples intensity variation is larger in the first 50 minutes of reaction, but after 250 minutes only sample **3** reaches the zero value (97% quenched respect to the initial value), **2** approaches the almost complete quenching (95% quenched respect to the initial value) and **1** shows a significant residual emission (78%

quenched respect to the initial value). This means that only in the sample with the highest BADGE/ P ratio (1:1 %w/w), the monomer got completely trapped in the core matrix, and the dilution does not causes the leaking into the solution. The release under dilution, when Pluronic micelles are no longer formed and the π-π staking does not take place, is still possible for **1** and **2** after 250 min. This can be explained considering that the polymerization grade reached for sample **3** is sufficient to stabilize the NPs, while in the other cases, reaction yield is not high enough to completely form the stabilizing oligomers/polymers. Longer reaction times results were not reported because, extending the experiment duration, the reaction conditions induced the **PNP**s aggregation and precipitation. It is interesting to notice that sample **1** and **2**,after 120 minutes, show an increasing in the emission intensity. This phenomenon can be due to the reaching of a **P** critical concentration point where the aggregation structure is not perfectly relaxed and the non-radiative deactivation route is less efficient.[8]
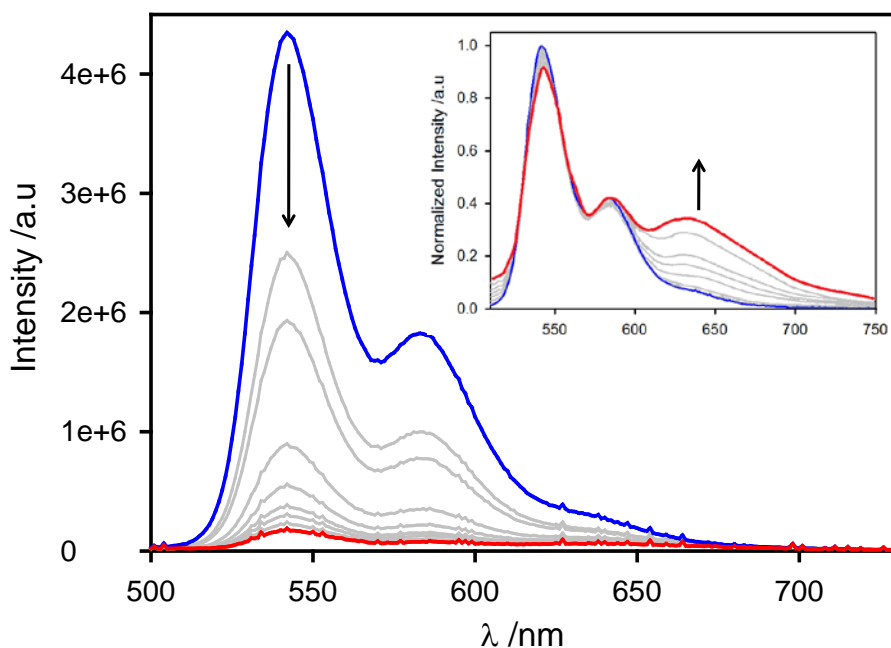
Figure 9.11: Sample 3 in PBS ([P]= 3.8 x 10⁻⁷M) emission curves exciting at 480nm. Curve collected at t=0 minutes (blue curve), along the reaction path every 15 (gray curves) through t=250min (red curve). The spectral shape is typical of the P in the monomeric form and the intensity dramatically drops as a consequence of the PNPs formation. (Inset) Normalized emission spectra, the increasing if the red-shifted band, due to the aggregated specie, become more evident.
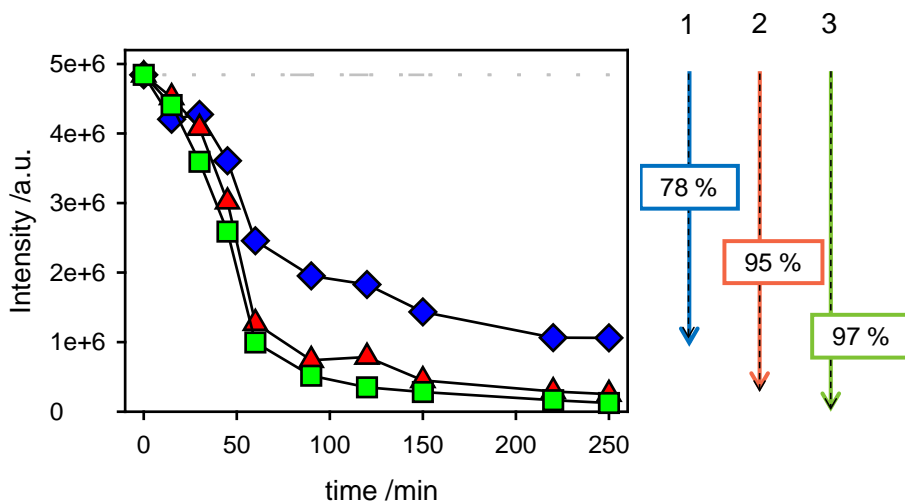
*Figure 9.12: Emission intensity collected at 542 nm versus time delay for sample **1** (blue), **2** (red) and **3** (green). The gray dotted line is the intensity of the reference, prepared before the reaction beginning, along the experiment duration.*

Emission spectra of the same diluted solutions, without preparing new samples but simply using the same cuvettes, were collected after 24 and 48 hours. In these remarkable high dilution and low temperature conditions, with respect to the ones required for the synthesis, no significant advance in the polymerization is expected to occur. Accordingly, variation in fluorescence can be induced only by the monomer leaking from the nanoparticles. This should provide information about the kinetic stability of the nanoparticles along their formation path. In figure 9.13, emissions collected during the synthesis at $\lambda = 542$ nm and after 24 (triangles) and 48 (squared) hours are reported for sample **1** (blue), **2** (red) and **3** (green).

For sample **3**, the variation is not significant for the solutions collected in the first 50 minutes of the reaction. This result was expected, since nanoparticles are still not formed and the monomer is almost completely free in solution. Once the nanoparticles start to form, the variation in intensity increases, as long as the structures into the core become stable. Eventually, after 250 minutes, P release is negligible, proving that cross-linking is complete and nanoparticles are formed. For this last solution, particularly relevant since the **PNP**s are considered formed, the sample recovers the 1% of the emission after 24 hours and the 4% after 48h.

Same trend is observable for samples **2**, which recovers the 7% of the initial emission after 24 hours and the 13% after 48 hours.

In sample **1**, the stabilization after 50 minutes which characterize the sample **2** and

3, does not properly occur, and a strong contribution of the monomeric specie dramatically affect the curve from 50 to 250 minutes. As a consequence, it results quenched only for the 30% and the 36% after 24 and 48 hours respectively, respect to the initial emission value.
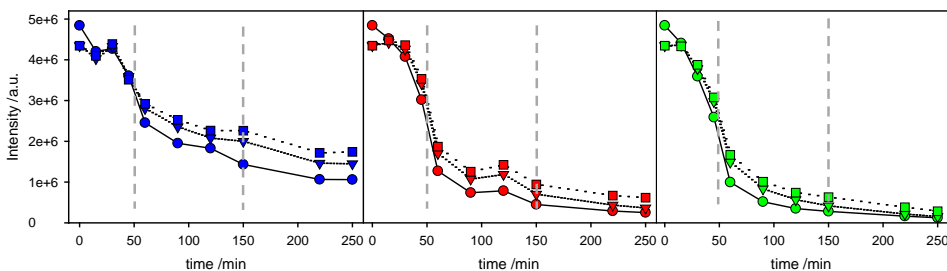
*Figure 9.13: Emissions collected during the synthesis at t=0 (circles), t=24h (triangles) and t = 48h are reported for sample **1** (blue), **2** (red) and **3** (green).*

It is interesting to notice, anyway, that absolute variation is not significantly different for the three samples, if the residual emission of P is excluded. Normalizing the intensities collected at 250 minutes for all the samples at 24 and 48 hours respect to the respective intensity at 0 hours, in fact, it can be excluded the contributions of the not reacted monomer (Fig. 9.14). In this way, it can be appreciate that the variation after 24 and 48 hours is 3% and 5% for sample**2**, and 1% and 4% for **3**. The behaviour is slightly different for **1**, where an initial 8% increasing is observed after the first 24 hours, but the emission intensity decreases to the 6% after the second 24. This can be explained considering the solution concentration, which, although it is low enough to avoid the monomer aggregation, it may be sufficiently high to reduce the kinetic of the PDI release from the nanoparticles to the solution, causing the downward trend. Anyway, this values are all into the error range, and the most important consideration is that even in sample **1**, when only the 60% of the P monomer is involved in the reaction, the emission intensity is not completely recovered after 48h.

This means that **PNP**s get formed in all the analyzed conditions, even if with different yields of P conversion. This is in accord with the emission intensities collected at 640nm, where the nanoparticles display their emission maximum and the intensity is not affected by the monomer concentration. At this wavelength, no variations in time are observed for all the samples at different time delays after the reactions.
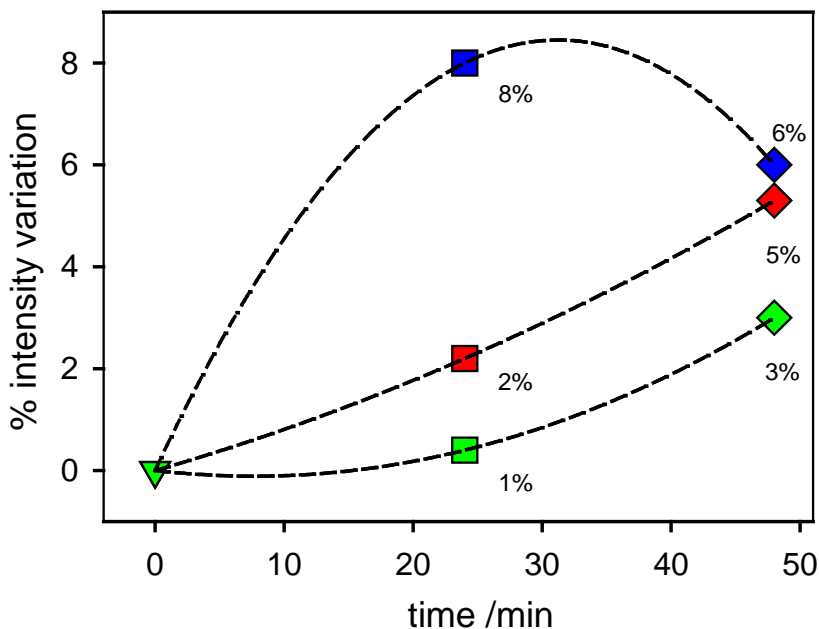
Figure 9.14: Emission intensity for sample diluted after 250 minutes from the synthesis start. In 1 (blue), 2 (red) and 3 (green) are shown the values after 0 (triangles), 24 (square) and 48 (rhombus) after the synthesis termination.

Interestingly, no significant variation are reported for the emission intensity of the same solutions after longer delay time (164 hour). That confirms that, once the polymerization occurred in the core and the residual monomer is completely released, kinetic has no longer effect on the **PNP**s stability.

Unfortunately, this experiment is not sufficient to better understand the either reaction mechanism or the nanoparticles composition. In fact, if the emission change is considered as the conversion grade in the polymeric form, the trend plotted in figure 9.12 can be assimilated to the one followed by the step-growth polymerization expected in the experimental reaction condition. Although, the curve profile could either be the representation of the inclusion process of the reactants into the micelles core and not of the cross-linking rate.

Trying to better characterize the products, DLS experiments were carried out 48 hours after the synthesis for samples **1**, **2** and **3**, ten times diluted in PBS (P concentration 7.2×10^{-4}) and any without filtration. They showed a monodispersed population, with an hydrodynamic diameters of 24 ± 4 nm, 28 ± 3 nm and 27 ± 4 nm respectively. It was observed that the correlation function at zero time for sample **1** is 0.58, lower respect to the 0.7 of **2** and **3**, while the scattering signal is

two times stronger for samples **2** (4552) and **3** (4792) respect to **1** (2394). This differences suggest slight morphological variations caused by the different reaction ratios, but they do not allow to attain any convincing conclusion about the composition itself. They can, in fact, be due to different factors, such as the variation of PNPs density (as a consequence of the reduced polymerization grade of sample **1** respect to the other) which affects the differential refractive index, or the formation of smaller or fewer nanoparticles.

Considering the complexity of the samples, no further experiments have been carried out to better understand the reaction process, even because we achieved the goal of optimize the reaction parameters to obtain **PNP**s more stable in time and with the lowest tendency to release dye in the environment. Instead, we actually focused on proving that this release is not occurring even changing the experimental conditions. Considering the importance of concentration in the photophysical properties, it was interesting to confirm the previous results for the formed and concentrate samples.

After 48 hours from the synthesis **1** ml of samples **1**, **2** and **3** at the synthesis concentration were dialyzed in a cellulose membrane (size exclusion 8kD) in bi-distilled water for 36 hours, changing the bath every 12 hours. In this way, all the not reacted monomer is expected to diffuse in the water bath. Accordingly, the samples before the treatment have been diluted 4 times in PBS, reaching the same concentration as the kinetic experiment ones. To exclude any contribution due to the volume variation caused by the purification process, the not-dialyzed nanoparticles have been diluted reaching the same nominal concentration.

Fluorescence emission have been measured exciting at 480 nm and the spectra reported in figure 9.15, 9.16 and 9.17 for **1** (top), **2** (middle) and **3** (bottom) respectively.

The strongest variation was observed in sample **1** (Fig. 9.15), where the emission is dominated by the perylene monomer contribution both before (blue line) and after the dialysis (red line), as it can be appreciate from the normalized emissions (Fig. 9.15, inset). The intensity at the maximum (λ_{em} = 542nm) although, it is 70% quenched after the dialysis. This change is perfectly in agreement with the quenching occurred during the synthesis for the same sample.

In **2** (Fig. 9.16) monomer intensity is 45% reduced, but the red-shifted band of the nanoparticles become dominant after dialysis. Considering the intensity variation along the all interval, only an 11% quenching is measured.

In sample **3** (Fig. 9.17), accordingly with the previous results, spectral shape and

intensity are not influenced by the purification process, and the quenching is the 10% if measured one the emission maximum and the 2% on the all spectral interval. In this case, all the monomer is reacted in the nanoparticle cores and it cannot diffuse into the water, as can be better appreciated normalizing on the maximum the emission spectra (Fig.17, inset).
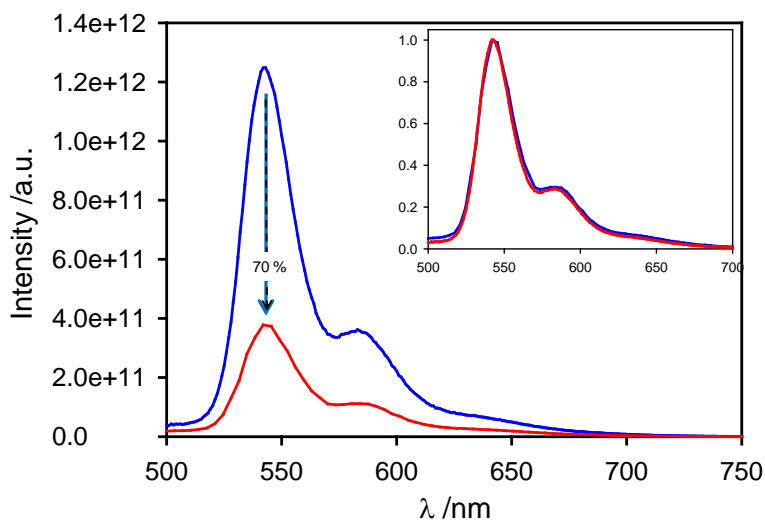
*Figure 9.15:Emission spectra sample **1** collected at the same sample dilution before (dotted curve) and after (solid curve) dialysis. Inset: normalized spectra.*
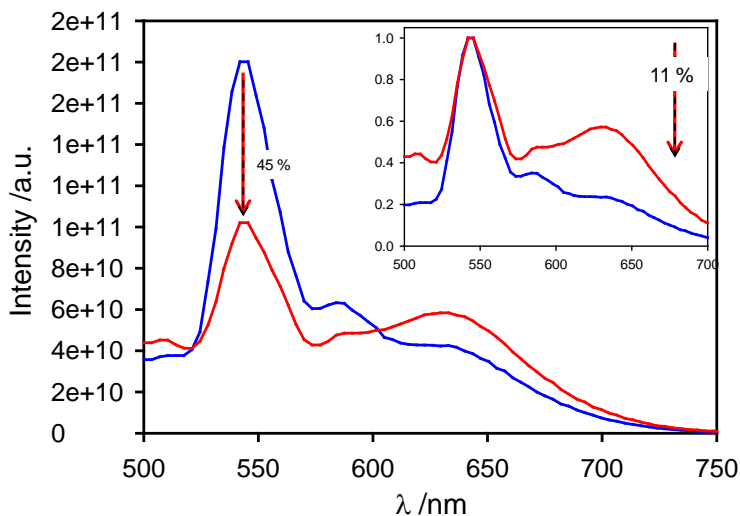
Figure 9.16: Emission spectra sample 2 collected at the same sample dilution before (dotted curve) and after (solid curve) dialysis. Inset: normalized spectra.
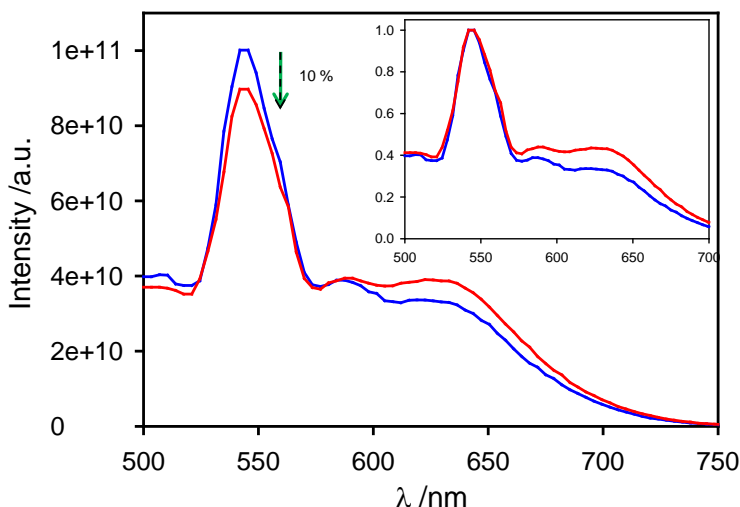
*Figure 9.17:Emission spectra sample **3** collected at the same sample dilution before (dotted curve) and after (solid curve) dialysis. Inset: normalized spectra.*

From these experiments it can be confirmed that PDI polymerize in the micelles core and the reaction reaches the maximum grade when the weight ratio is highest between Perylene and BADGE.

The trend can be easily appreciated: the higher is the w/w% Bisphenol A/P ratio, the higher is the reaction conversion grade. The longer the nanoparticles are stored in diluted solution at room temperature for the first 48, where the reaction may no longer take place, the more pronounced is the leaking of P from the nanoparticles. Furthermore, it depends on the conversion grade, being limited for **3** respect to **2**, and for **2** respect to **1**. This can be explained by the presence, into the cross-linked core, of some P not reacted, but as well trapped by non covalent forces. If the polymerization is complete, the quantity of monomeric P is reduced.

The percentage values for the released P, anyway, suggest that the nanoparticles are formed in all cases and the reaction is lightly affected by the reactants ratio. The red-shifted emission clearly demonstrate the formation of aggregated, but the complex situation in the core, where the monomers are spatially confined and forced to react in the presence of Bisphenol A, suggests that a more complex structure would describes the P organization.

9.4 Wide field microscopy measurements

According to the aim of applying the studied nanoparticles in molecular imaging, have been carried out wide field microscopy measurements.

In a 20 ml glass vial, 5 μl of the concentrated nanoparticles sample has been dispersed into 500 mg of glycerol, under vigorous stirring to avoid the aggregation of the nanoparticles in the viscous dispersant. Then10 mg of the dispersion has been drop off on a thick microscope glass and covered by a thinner one to stack the sample into a defined volume and to reduce the mobility of the sample itself. To better control these parameters a double-sided tape(thickness c.a. 0.1mm) has been interposed in between the two slides (Fig. 9.18)
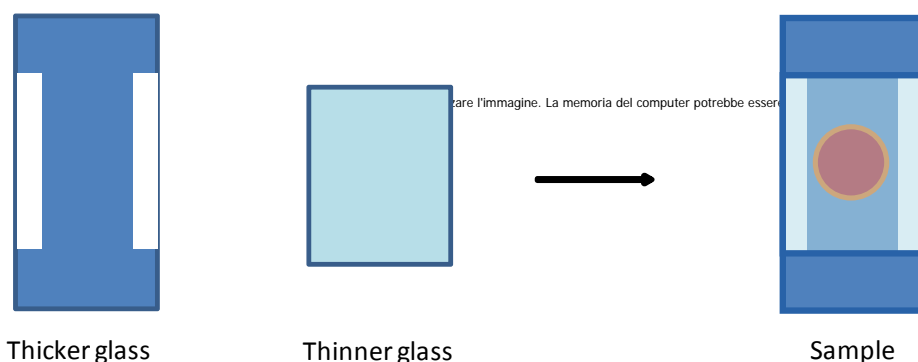
Figure 9.18: representation of the microscope sample preparation setting.

PNPs have been irradiated using a FITC filter, with an objective of 100X, for 500 seconds, acquiring 1 frame per second. At the initial time, the signal detected from the camera was close to zero, according with the measured 0.005 **PNP**s fluorescence quantum yield. Increasing the irradiation time, the light intensity emitted by the sample started to rise, with the appearance of intense spots randomly changing position. The spot intensity continues to grow along the measurement duration, reaching a plateau after 350 s with an average intensity 20 times increased, as calculated by Image J software.

Since the recorded movie cannot be reported in this contest, some of the frames in false colours are shown (Fig. 9.19, top). To better appreciate the contribute of the nanoparticles on the focal plane, the background signal has been removed (Fig. 9.19, bottom-left) for the frame at time t = 0 and t = 150 s.

To obtain quantitative data, and in particularly to determine the size of the fluorescent spots, they were tracked frame by frame (image stack). This requires some precaution, since both the spatial and the temporal aspect have to be considered. The former consists in the particle detection respect to the background and in the capability of estimate their coordinates in every frame of the image

sequence; the latter regards the connection of the detected particles frame to frame to form the track. To properly treat these aspects, and to manage the significant amount of data, it was chosen the MosaicSuite macro of the ImageJ software, validated by Nature Methods.[9]
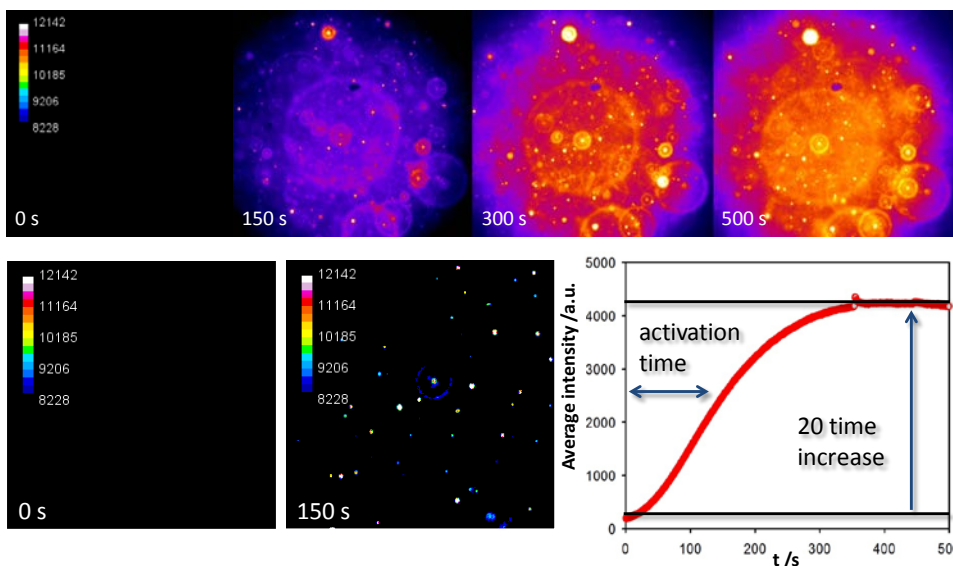
Figure 9.19: (Top) PNPs irradiated using a FITC filter, 100X magnification, 1 frame per second for 500 seconds. Frames reported in fouls colour after 0, 150, 300 and 500 of delay time. Increasing in intensity can be appreciated. (bottom-left) background signal removed for the frame at time t = 0 and t = 150 s, to enhance the contribution of the nanoparticles on the focal plane. (bottom-left) average intensity calculated using ImageJ software plotted versus the delay time from the irradiation beginning. 20 times increasing can be appreciate after 350 s.

The program first pre-processes the images to enhance the object signal respect to the nonlinear background, starting from the assumption than the object regions are small respect to the background regions. Instead of using the rolling ball algorithm, as in the standard ImageJ implementation (proposed by Steinberg in 1983), the plug-in builds local histograms and it assumes the most occurring intensity to be part of the background.[10] Then, the generated background image is convolved with a Gaussian kernel and removed by the original image. In the second step, the foreground spots have to be correlated in different frame, which consists into the definition of the nearest neighbour distance (NND). The adopted ImageJ plug-in uses an extension of the most common object-based co-localization (OBC), where the NND from one point pattern to another is plotted as an histogram and the

146

threshold is set (typically the diffraction-limit resolution). Fixing the parameters, such as the *particles radii*, the *cut-off* and the *percentile*, which allows to determine which bright spots are accepted as particles, the object displacement coordinates in the horizontal (Δx^2) and vertical (Δy^2) axes are computed.[11]

Since nanoparticles are only subjected to Brownian motion, their hydrodynamic diameter can be calculated by Stoke-Einstein equation (Eq. 9.1), where D is the diffusion constant, T is the absolute temperature, η is the dynamic viscosity and d_H is the hydrodynamic diameter.

$$D = \frac{k_B T}{3\pi\eta d_H}$$

(Eq. 9.1)

In the considered case, where $4DT = <\Delta x^2 + \Delta y^2>$, $\eta = 1.408\ Pas$, and $T = 25°C$, it was calculated a dimensional distribution of hydrodynamic values, fitted with a Gaussian distribution. The most representative value is the hydrodynamic nanoparticle diameter $(d_H) = 35 \pm 10$ nm (Fig. 9.20).
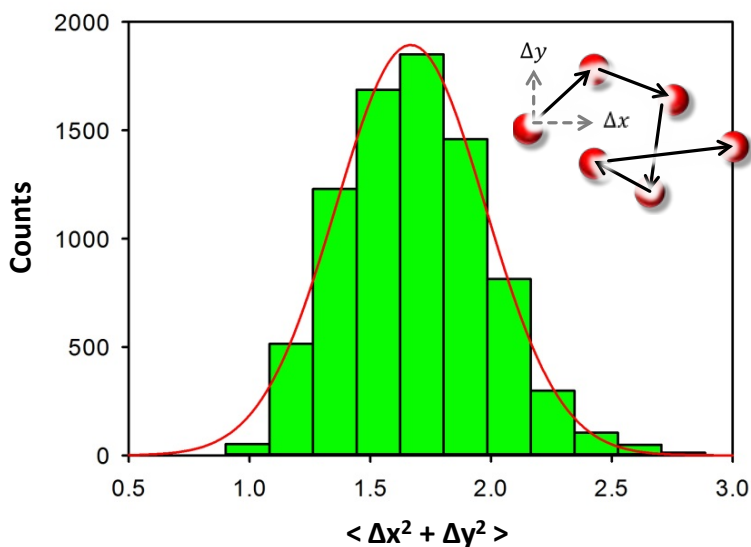
Figure 9.20: dimensional distribution of hydrodynamic values obtained by the Stokes Einstein equation, well fitted by a Gaussian distribution, with the most representative value (d_H) 35 $\pm$ 10 nm.

This result, obtained by a single particles study in glycerol, perfectly matched the hydrodynamic value obtained by the DLS at 25°C (35 ± 10 nm) in phosphate buffer. This offers a convincing proof that the nanoparticles are formed and

responsible of the emission, excluding any contribution due to different aggregated species. In the experiment, the out of plane axe (z) signal was not considered, because the displacements in the three different directions (x, y and z) are reciprocally independent. Although, the movement of the spots out of the focal plane can causes their defocusing or disappearance, sensitively reducing the number of cumulated data. In this experiment, particular relevance is earned by the use of glycerol as dispersant for the nanoparticles, since the high viscosity reduces their average speed and allows the acquisition of significant number of points.

9.5 Irradiation Studies

The strong variations on the **PNP**s emission properties detected by the microscope images is extremely interesting. The light irradiation, if fact, is capable of triggering matrix structural changes and dramatic changes in the nanoparticles photophysical properties. To better understand the phenomena and to detect spectral changes in the sample, a kinetic measurement was carried out irradiating the nanoparticles sample at the spectrofluorimeter.

A nanoparticles sample was prepared diluting the **PNP**s in PBS, reaching a P concentration of 5 x 10^{-6} M. The solution was irradiated under stirring with 480 nm light for 300 minutes, collecting the emission spectra every 12 minutes. The instrumental conditions where settled up in order to optimize the irradiation efficiency of the sample, hence they were used large slits in excitation and narrow ones in emission. It can be noticed that the emission intensity globally increases during irradiation for the first 200 minutes, when it reaches the plateau (Fig. 9.21). After the first minutes, in fact, the green structured emission typical of the monomeric P (blue curve, Fig. 9.21) starts to appear, becoming stronger upon irradiation. On the other hand, the red emission (black curve, Fig. 9.21) typical of the nanoparticles and due to the aggregates, increase for the first 60 minutes and then starts to decrease. Between 60 to 200 minutes, the monomer emission intensity increases and the one of the aggregate decreases (red curve, Fig. 9.21), while in the last 100 minutes the P intensity reaches a plateau and only the aggregate emission gradually decreases. To better appreciate the shape variation in time, a 3D plot of the same measurement was reported in figure 9.22.

These observation suggest that during the first hour of irradiation, some perylene diimide units are partially released from the nanoparticle, spreading out from the shell and dissolving into the PBS solution. At this reduced concentration, they emit in water as a monomeric species. At the same time, light furnishes the energy for

dyes reorganization into the nanoparticle cores, causing a slight increase on the emission intensity in the red region.
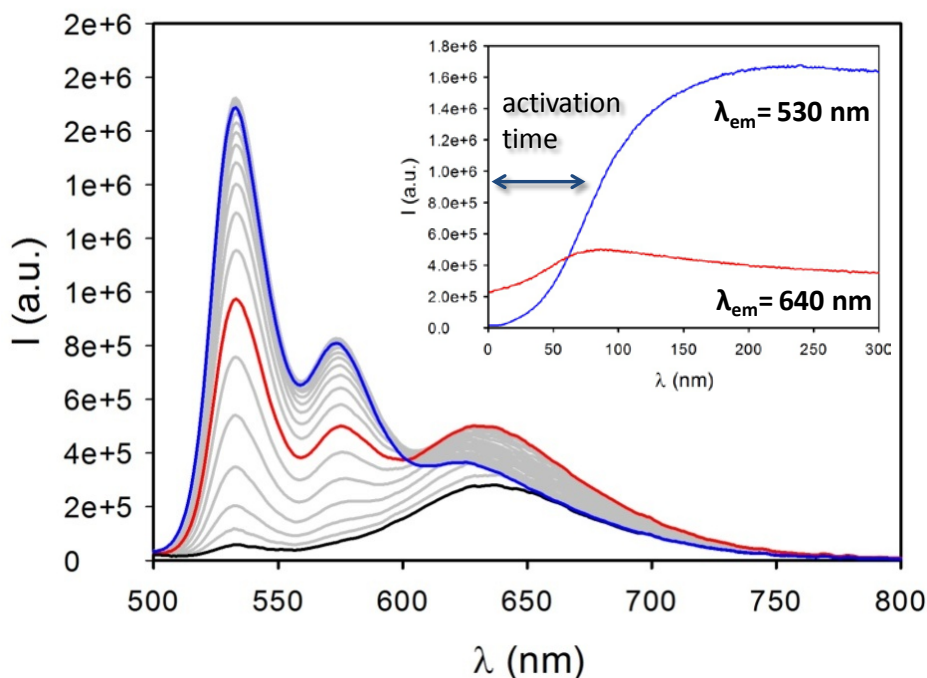
Figure 9.21: Emission spectra of PNPs in PBS (P concentration 5 x 10⁻⁶ M) collected every 12 minutes under irradiation at λ = 480 nm for 300 minutes. (black curve) t=0only the aggregate emission is detectable, after 80 minutes (red curve) both the aggregate and the monomeric specie show up, and after 300 minutes (blue curve) the emission is almost completely due to the monomeric form. Inset: the emission intensity collected under irradiation at λ_{em} = 530 nm and λ_{em} = 640 nm are plotted versus the irradiation time (blue and red curve respectively).

Once the system reaches the more stable organization, this effect become negligible, while perylene diimide continues to be released into the solution. The plateau of the monomeric emission is reached when the dye concentration in water is too high to be not aggregated, but the 640 nm signal continues to decrease as long as the core release dye into the environment. It is interesting to observe that the fluorescent intensity increases by less than 20 times, as it was previously observed for the same sample irradiated by microscope in glycerol. Although the same process occurs in both the conditions the difference in the increase is due to the different experimental concentrations. Furthermore, in both cases a similar

profile and an activation time, as the time necessary to the green emissive specie to reach the plateau, were observed. Only a temporal shift is detected, since the activation time is shorter for the sample irradiated in PBS (200 s) respect to the one irradiated in glycerol (350 s). This can be explain by the different irradiation intensity and by the different utilized dispersant were the measurements are conducted. In glycerol the dye diffusion is lower than in water and the molecules reaches an higher local concentration in the space close to the nanoparticle. This is only partially balanced by the lower aggregation constant for the PDI. An effect of the light source should be considered as well on the efficiency of the whole process.
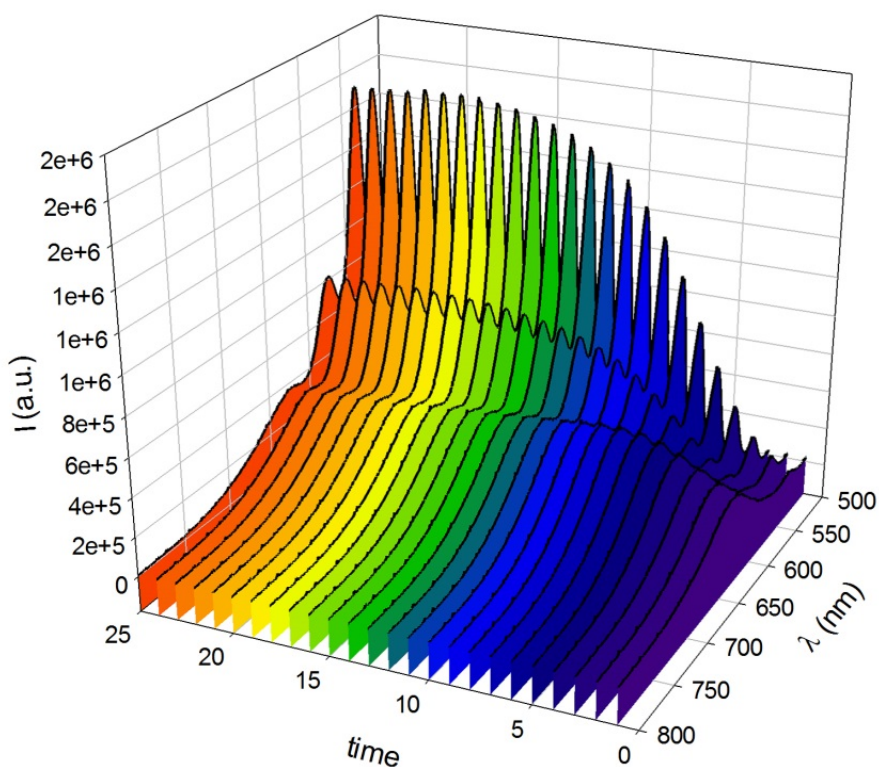
*Figure 9.22: The emission spectra of the irradiated **PNPs** are reported as a 3D graph, to better appreciate the variations in the spectral shapes and the reaching of the maximum intensity plateau.*

9.6 Extraction experiments

According with the irradiation studies, we hypothesized that the luminescence

intensity rises as a consequence of dye release into the water solution. This phenomenon does not causes the complete nanoparticles disintegration, or a significant morphological variation detectable by DLS. As well, the eventual formation of new aggregated species in solution cannot be observed by the same techniques, being the formed **PNP**s signal too strong to observe any variation in the scattered signal. According with the initial idea of the reaction mechanism, all the P units should have been cross-linked one to another through the Bisphenol A, forming a rigid core with the PPO chains strongly trapped into it. This model cannot easily be adapted to the further observation, since the release could not be caused by the disruption of the covalent bonds between the dyes units. As the BADGE is not electronically connected with the absorbing perylene core, in fact, the irradiation at 480 nm could not affect this bond and catalyse the dye release. At the same time, it was proved that the formed **PNP**s do not release P simply under dilution, as it happen for the reaction mixture before cross-linking. This indicates that same sort of stabilization occurs for the monomer in the micelles core under the reaction conditions. The suggested explanation resides into the hypothesis that the P cross-linking reaction do not lead to the formation of high molecular weight polymer, but to the formation of short polymers, such as dimers or oligomers, stabilized into the micelles core by their π -π stacking interactions. The increased size causes a stronger non-covalent stabilization respect to the single P units, and it conserves intact the nanoparticle even under dilution. To better understand the mechanism, it was necessary to characterize the **PNP**s after irradiation.

To confirm this explanation, 500 μl of **PNP**s irradiated sample, diluted 10 times respect to the synthetic mixture, were added to an equal volume of chloroform and gently stirred for 5 minutes. The same procedure was adopted for the not irradiated **PNP**s to prepare the reference sample. Since chloroform is known to be one of the best perylene diimide solvent, it was expected to extract all the emissive compound released from the nanoparticle core after irradiation. Then absorption and emission spectra were collected for the organic fractions of the irradiated and not irradiated nanoparticles. The chloroform fraction for the irradiated nanoparticles (Fig. 9.23, orange-filled curve) shows an emission signal 21,5 times more intense than the respective reference (Fig. 9.23, yellow-filled curve), and this result is confirmed by the absorption spectrum (Fig. 923, inset). This value is perfectly in accord with the intensity increasing for the same solution under irradiation both at the microscope and the fluorimeter.

These observation suggest that during the first hour of irradiation, some perylene

diimide units are partially released from the nanoparticle, spreading out from the shell and dissolving into the PBS solution. At this reduced concentration, they emit in water as a monomeric species. At the same time, light furnishes the energy for dyes reorganization into the nanoparticle cores, causing a slight increase on the emission intensity in the red region. Once the system reaches the more stable organization, this effect become negligible, while perylene diimide continues to be released into the solution. The plateau of the monomeric emission is reached when the dye concentration in water is too high to be not aggregated, but the 640 nm signal continues to decrease as long as the core release dye into the environment. It is really interesting to observe that the fluorescent intensity increases 20 times, as it was observed for the same sample irradiated by microscope in glycerol. This confirms that in these the same process occurs in both the conditions.
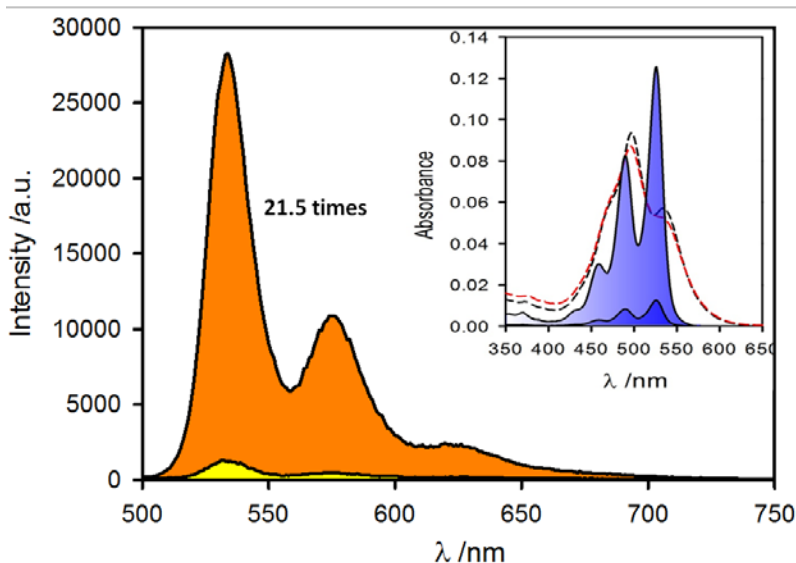
Figure 9.23: Emission plot of the organic fractions of the irradiated (orange filled) and not irradiated (yellow filled) PNPs fractions. (inset) Relative absorption spectra overlapped with the respective absorption spectra before chloroform extraction.

The organic fraction of the irradiated sample was hence photophysically studied. In figure 9.24 the normalized absorption spectra (red-curve) is overlapped with the monomer **P** one (black-curve), and it can be observed only a slight difference between them. The slight broadening of the red curve can be explained by the presence of a small quantities of aggregated species, despite the dominant contribution is due to the monomeric one. This conclusion are in accord both with

the normalized emission spectra, since they are completely overlapped, and with the normalized excitation spectra, collected at 540 nm (blue curve) and at 640 nm (red-curve), almost perfectly matching the absorption spectrum of the nanoparticles (yellow-filled curve). This is also confirmed by the fluorescent quantum yield measurements, calculated using Fluorescein in KOH 1M as a reference. The fraction extracted in chloroform quantum yield is $\Phi = 38\%$, significantly lower than the **P** one before the synthesis ($\Phi = 99\%$). Since it was proved that **P** at the solution concentration in chloroform is not aggregated, the quenching is probably due to a new non emissive specie, formed within the reaction.
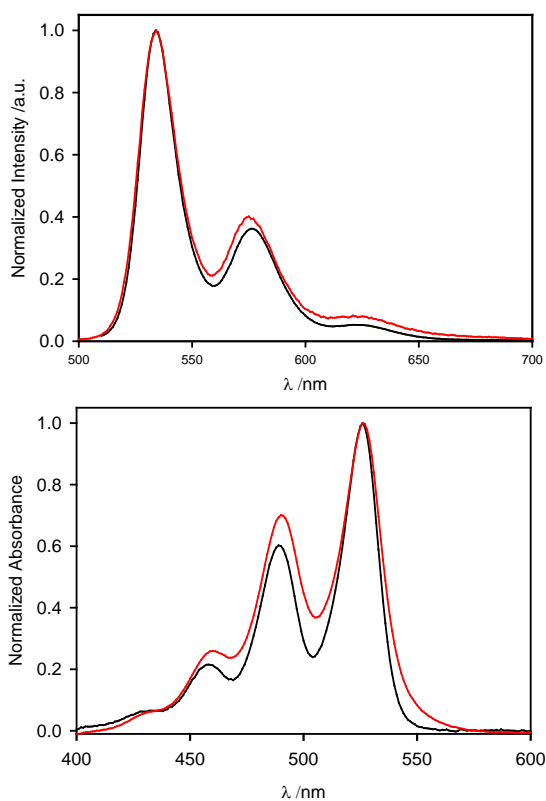
*Figure 9.24: Normalized absorption (top) and emission spectra (bottom) of the P monomer and the organic fraction of the irradiated **PNPs** in chloroform.*

According with the fact that both the absorption and the emission spectra are shaped as the ones typical of the monomers, it can be assumed the dye ε equal to

the monomer one. In this it was possible to calculate that from the irradiated solution over the 80% of the dye was extracted in chloroform, while less than 10% was released in the organic solvent from the reference.
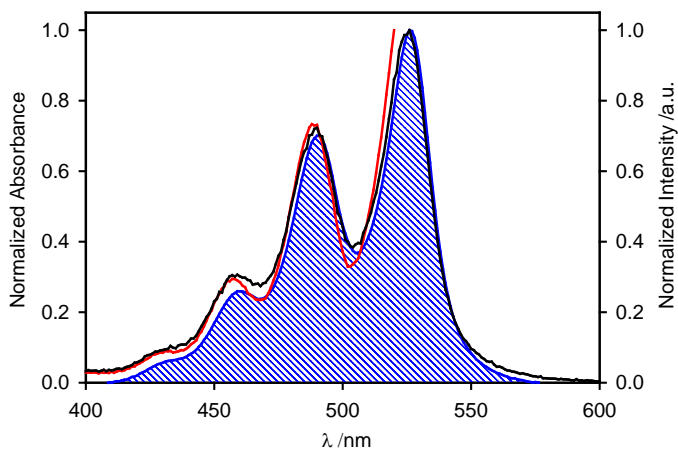
Figure 9.25: Normalized excitation spectra of the organic fraction of the irradiated PNPs collected at λ_{em} = 540 (red curve) and λ_{em} = 640 nm (black curve) compared with the normalized absorption spectra of the same sample (filled).

9.7 Proposed mechanism

Summarizing the information collected it can be proposed a mechanism for the observed process, although it still requires further studies. PNPs formation was firstly proved by the photophysical features variations displayed by the starting material P. Respect to P, formed nanoparticles are characterized by a red-shifted, broader and less resolved emission band. Furthermore, the fluorescent quantum yield in PBS is 0.5%. This is in accord with the formation of quenched aggregates into the Pluronic F-127 micelles core. The absorption and emission spectra confirm the presence of aggregates, despite the complex situation makes quite challenging to imagine a clear and ordered dyes organization. A realistic description would be a chaotic spatial distribution of the molecules, organized in a combination of J, H and distorted geometries. Since the not-aggregated photophysical features are not recovered under nanoparticles dilution, it can be assumed that covalent bond get formed between P amine terminations and BADGE epoxy rings.

Irradiating the PNPs with a strong light source, causes strong variation of their photophysical features. The fluorescence quantum yield, in fact, increases from 0.5 0 to 1.6% thanks to the recovering of the green emission. At the same time, the red-

shifted band typical of the aggregates increases and then drops approaching to zero. This can be explained considering the formation, into the micelles core, of fluorescence conjugated polymers[12], where the resonance interaction between the dyes molecules leads to delocalization of the excited states over many molecules. The excitonic coupling, which causes the bathochromic shift of the absorption band, can funnel the excitons from a large part of the aggregates to significant lower energy states acting as energy traps[13]. This results in the quenching of the red-emission, since only excitons that cannot reach the trap emit from the lowest locally accessible exciton state. Although in some cases longer wavelength-shifted emission band is observed, it is not the case of PNPs. This is not surprising, since the trap states have more emissive events in any time-interval then the other exciton states, having greater probability of getting quenched[13,14]. Because properties of the exciton states in molecular aggregates depend on the variation of transition energies of the aggregated monomers and/or variations of the resonance intermolecular interactions between monomers, it can be affected by PNPs long time irradiation. Hence, upon prolonged irradiation the low energy trap state can be photo-degraded and the 640 nm emission completely recovered. This kind of energy traps can be originated by dipole-dipole interactions with a random environment or either by the presence of specific sites in the matrix. Furthermore, it was recently proved that the exciton transport can occur over 100 nm, depending on the aggregates structures and organization[15]. The second consequence of the irradiation is the recovery of the green emission, due to the not-aggregates perylene diimide P. This was explained by the hypothesis of the formations of dimers/oligomers as a consequence of the P cross-linking (Fig. 9.26). Despite this short macromolecules are stronger packed into the nanoparticles core respect to molecular P, 480 nm high-power irradiation can causes PDI oxidation, leading to the aromatic cores disaggregation. As long as the photo degradation occurs, more macromolecules spread from the nanoparticles in the solution. To this is attributed the green emission increasing during the first 200 minutes. When the concentration of the leaked specie in solution reached the solubility limit, aggregation occurs and the 540 nm band reaches a plateau, as it is confirmed by the PNPs fluorescence quantum yield variation measured at 4.4 10^{-7}M and 7 10^{-5} M before and after irradiation. In diluted solution, Φ is increases of 3.1 times, respect to the concentrate where the variation is only 1.2 times. Meantime, intensity detected at 640 nm decrease as long as the aggregated specie in the nanoparticle core is consumed by photo degradation.
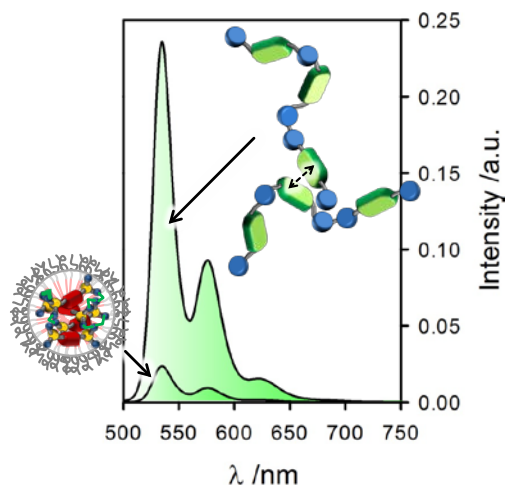
Figure 9.26: Emission bands of the nanoparticles irradiated and not irradiated after chloroform extraction. The irradiation causes a preferential disaggregation of the oligomers, inducing the perylene diimide units spreading into the environment. The emission intensity dramatically increases respect to the one due to the still formed nanoparticles, not-irradiated.

In order to confirm the hypothesis, an extraction in chloroform was carried out. As expected, not strongly stabilized irradiated nanoparticles dissolved in the organic fraction, thanks to the perylene diimide affinity for this solvent (chapter 5). The non-irradiated PNPs, on the other hand, proved to be stable, with the dye-core protected from the PEG shell, not soluble in chloroform. Furthermore, the fluorescence quantum yield of the irradiated sample extracted in chloroform (58%, measured using Fluorescein in NaOH 1M) is significantly lower respect to the one of P in the monomeric form (90%). It confirms that the specie released from the nanoparticle core is not the starting material, but some variations occurred in the molecular structure, affecting the photophysical properties.

9.8 Cells studies

The studied behaviour showed that **PNP**s are very good candidates as potential fluorogenic nanoprobes. The strong difference in fluorescence quantum yield before and after irradiation, in fact, is very interesting in the prospective of significantly increase the signal to noise ratio, which is still challenging in optical imaging. Furthermore, the structural components are extremely photostable and they are not prone to photobleaching processes. For this reason, **PNP**s have been

studied in *NIH 3T3 mouse fibroblast cells*, that have been reported to be relevant models in cancer research.

A cell culture was prepared in a 5 cm Petri dish, then the growth medium was took off and the cells carefully washed for three times with PBS, in order to remove any medium contamination and dead cells eventually present. Afterwards, 2ml of PBS solution containing 5 ul of concentrated PNPs (concentration of P=2 mM, 6.3 mg/ml) was slowly added to the dish. The addition of the nanoparticles in diluted solution proved to be extremely important not to locally increase the concentration of P. In this case, the toxicity would be locally enhanced and the sample would result inhomogeneous.The sample was immediately irradiated with wide field microscope equipped with a Xenon lamp (450 W) for fluorescence excitation, a CCD camera for images acquisition and a FITC filter for the fluorescence collection. A series of 500 frames (1 frame/s) was collected at a 100X magnification. Although the complete series is not reported in this thesis, 5 representative every 100 seconds are shown in figure 9.27. It can be appreciated that cells are almost completely not detectable at time zero, while the signal significantly increases during the irradiation, as a consequence of the nanoparticles quantum yield increasing under light irradiation. Interestingly, cells fluorescence is detectable only in the spot irradiated by the microscope, and not in the other regions where the signal is collected. This proves that the emission is actually triggered by light, and not by the simply nanoparticles internalization in lipophilic environment.

Figure 9.27: Montage of 5 images at 100s delay time of cells collected under samples irradiation. (Magnification 100X, Xenon lamp power 450 W, 500 frame in total, lateral size 82 μm).

To better appreciate difference in the variation intensity, frame at time 0 and 150 s of the same image stack were reported subtracting the mean value of the background signal, due to the emission of the out of focus cells. (Fig. 9.28) It is important to underline that this operation of subtraction is straightforward when the emission of the observed objects in high respect to the background, but it become extremely challenging when they are comparable. For this reason, the use

stimuli responsive nanoparticles based on DIE process is a successful strategy to obtain good images by fluorescence microscopy.
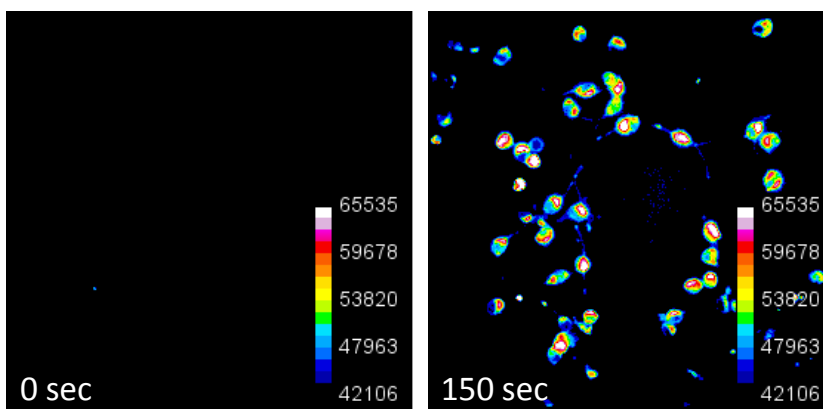
Figure 9.28: image collected at time zero and 150 of sample irradiation after the background subtraction. (Magnification 100X, Xenon lamp power 450 W, 500 frame in total, lateral size 82 µm).

9.9 Conclusions

Although further experiments are required to confirm the conclusions, it is out of doubt that the PNPs are formed under the studied conditions, and that light irradiation is necessary to trigger the nanoparticles disaggregation. Hence, the cross-linked dye can be solubilised by photo-irradiation. Nevertheless, strong effects on the photophysical properties are achievable only combining this responsiveness with variation in concentration or in environmental polarity. These makes the nanoparticles interesting multi-stimuli responsive systems, as confirmed by the preliminary cells studies previously reported. In this case, in fact, the light excitation source can trigger the disaggregation, while different local polarity causes fluorescence signal switching. Although no experiments have been carried out in this sense yet, PNPs are extremely attractive for drug-delivery applications, in particular in the prospective of photo activated the drug releasing. In this sense, multifunctional nanoparticles can be developed, allowing to perform image-guided drug delivery, addressing tissue by imaging tools. Last but not least, the synthesised perylene diimide derivative (P) chemical and photophysical properties can be easily modulated either by bay region or free amine position functionalization, which suggest the integration of the epoxy-resins in smart nanocomposites, such as epoxy-graphene.

Bibliography

1   Montalti, M., Battistelli, G., Cantelli, A. & Genovese, D. Photo-tunable multicolour fluorescence imaging based on self-assembled fluorogenic nanoparticles. *Chemical Communications***50**, 5326-5329, doi:10.1039/C3CC48464E (2014).

2   Malmsten', M. & Lindman, B. Self-Assembly in Aqueous Block Copolymer Solutions. *Macromolecules***25**, 5440-5445 (1992).

3   Rampazzo, E. *et al.* Energy Transfer from Silica Core– Surfactant Shell Nanoparticles to Hosted Molecular Fluorophores†. *The Journal of Physical Chemistry B***114**, 14605-14613 (2010).

4   Linse, P. Micellization of poly (ethylene oxide)-poly (propylene oxide) block copolymers in aqueous solution. *Macromolecules***26**, 4437-4449 (1993).

5   Linse, P. & Malmsten, M. Temperature-dependent micellization in aqueous block copolymer solutions. *Macromolecules***25**, 5434-5439 (1992).

6   Franceschin, M. G-Quadruplex DNA Structures and Organic Chemistry: More Than One Connection. *European Journal of Organic Chemistry***2009**, 2225-2238, doi:10.1002/ejoc.200801196 (2009).

7   Görl, D., Zhang, X. & Würthner, F. Molecular Assemblies of Perylene Bisimide Dyes in Water. *Angewandte Chemie International Edition***51**, 6328-6348, doi:10.1002/anie.201108690 (2012).

8   Heek, T. *et al.* Highly fluorescent water-soluble polyglycerol-dendronized perylene bisimide dyes. *Chemical Communications***46**, 1884-1886, doi:10.1039/B923806A (2010).

9   Chenouard, N. *et al.* Objective comparison of particle tracking methods. *Nat Meth***11**, 281-289, doi:10.1038/nmeth.2808
http://www.nature.com/nmeth/journal/v11/n3/abs/nmeth.2808.html#s upplementary-information (2014).

10   Pang, J.-S. Error bounds in mathematical programming. *Mathematical Programming***79**, 299-332 (1997).

11   Thomann, D., Rines, D., Sorger, P. & Danuser, G. Automatic fluorescent tag detection in 3D with super-resolution: application to the analysis of chromosome movement. *Journal of Microscopy***208**, 49-64 (2002).

12   Hide, F., DÍaz-GarcÍa, M. A., Schwartz, B. J. & Heeger, A. J. New developments in the photonic applications of conjugated polymers. *Accounts of chemical research***30**, 430-436 (1997).

13   Merdasa, A. *et al.* Single Lévy states–disorder induced energy funnels in molecular aggregates. *Nano letters***14**, 6774-6781 (2014).

14   Yu, J., Hu, D. & Barbara, P. F. Unmasking Electronic Energy Transfer of Conjugated Polymers by Suppression of O2 Quenching. *Science***289**, 1327-1330, doi:10.1126/science.289.5483.1327 (2000).

15   Lin, H. *et al.* Collective Fluorescence Blinking in Linear J-Aggregates Assisted by Long-Distance Exciton Migration. *Nano Letters***10**, 620-626, doi:10.1021/nl9036559 (2010).

10 pH-responsive fluorogenic NPs

The use of amphiphilic block co-polymer offers the advantages typical of the self assembly structures, correlated to their tendency to self-organize in aggregates with defined morphology. Although, to display this property in a controlled and reproducible way, macromolecules have to be chemically uniform, hence, monodispersed in size and in the hydrophilic/hydrophobic block ratios and length.

In the prospective of obtaining stimuli-responsive nanoparticles, polymers have to include structural moieties sensitive to a desired stimulus and able to somehow modify the whole system morphology to trigger the signal switching. Since the differentiation of tumours from normal tissue remain a big challenge in nanomedicine, nanoparticles have been designed to response to pH, which is different in these particular environments.

In the studied case, nanoparticles have been programmed to response strongly enhancing a fluorescent signal, taking advantages from its specificity and sensitivity in detection. The emissive component can potentially be integrated in the nanoparticles either by covalently and non covalently interactions. Although the latter strategy may be easier from the synthetic point of view, the former guarantees a better control over the spatial distribution and quantification of the integrated moieties, also reducing the uncontrolled leaking with undesired chemical and biological effects. The integrated fluorophore photophysical properties have to be affected by the structural nanoparticles modifications, displaying different behaviour before and after the stimulus triggering. Aggregation and disaggregation of specific fluorophores proved to be extremely useful from this point of view, since this variation can dramatically affect the fluorescent quantum yield. To this end, the use PDI is extremely suitable, since it can offer a fluorescent quantum yield variation ranging around one or two order of magnitude in the aggregated and disaggregated form. A proper design in the combination of a stimuli-responsive structural component, with the possibility of dramatically change the emissive response of the probe, allow to achieve the almost complete ON/OFF signal switching of the nanoparticles.

All the mentioned aspects have to be translated into the synthesis of amphiphilic block co-polymers by a strategy which allows high control over all the macromolecule structure, obtaining a monodispersed population of molecular weight, and capable of including several different moieties in the backbone. Great candidate to reach these goals is the ring opening metathesis polymerization

(ROMP) using variously functionalized norbornene derivatives as polymerizable unit to carry the desired pH responsive and PDI moieties.

The first part of the work, hence, concerns the synthesis and characterization of the different monomers required for the polymer formation.

10.1 Perylene diimide monomer (m1) synthesis

In order to make PDI polymerizable, a new derivative has been synthesised substituting one of the amide position with a polymerizable norbornene unit derived from the commercial available *cis*-5-Norbornene-*exo*-2,3-dicarboxylic anhydride. The dye aromatic core is spaced respect to the norbornene by a C8 aliphatic carbon chain, in order to improve the solubility of the whole molecule, which is otherwise strongly insoluble in all the common organic solvents. For the same reason, the other amidic position was functionalized with a C10 aliphatic carbon chain. The choice of this simple substituents, respect to other branched or PEGylated ones, has been made in the perspective of balancing the possibility of efficiently dissolving monomer (**m1**) in the polymer reaction milieu and of allowing the PDI strong aggregation into the micelles core.

Another important property conferred from the aliphatic chains, regards the phase (shape, size, overall morphology) of the assembled amphiphiles. Despite it is still under debate,[1,2] it seems that spherical geometries nanoparticles favourites internalization by cells. It is also out of doubt that higher symmetric structures, respect to rod or other shaped structures, makes the morphological characterization of the nanoparticles easier to achieve by traditional methods, especially by scattering techniques. This is an important advantage considering that structural variations are expected in the studied system. In order to obtain spherical micelles, as desired for our application, the amphiphilic polymer should aggregate with a proper cone angle, which depends on the magnitude of the sterical and electrostatic interactions between the blocks.[3] Since this fluorogenic unit consists in the termination of the hydrophobic block, the use of linear chains should favourite large cone angles as reported in figure 10.1, requested for the spherical micelle formation, respect to smaller, which would favourite rod geometries.

Synthesis of the fluorescent monomer (**m1**) was achieved starting from the commercial available perylene-3,4,9,10-tetracarboxylic acid dianhydride (*1a*) and adopting the method II described in chapter 5. *1a* was reacted with potassium hydroxide to open the anhydride ring and to obtain the monopotassium salt (*1b*) and then with decylamine to obtain the mono-anhydride mono-amide derivative

(*1c*). This last compound was reacted one pot whit the norbornene unit (*1e*) to achieve the monomer **m1**.
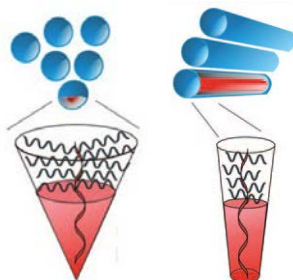
Figure 10.1: Assembly of copolymers into micelles with spherical or cylindrical morphologies. Amphiphile structures are represented as cones for each respective morphology, with the hydrophobic domain highlighted in red. Higher cone angle favourite aggregation with spherical morphology. Image modified from reference 3.

The synthesis of the *N-Decylperylene-3,4,9,10-tetracarboxylic-3,4-anhydride-9,10-imide (1c)* was obtained following the procedure reported in ref. 4 and described in Scheme 10.1.

Perylene-3,4,9,10-tetracarboxylic Acid Mono-anhydride Mono-potassium Salt (1b):
Perylene-3,4,9,10-tetracarboxylic acid dianhydride (*1a*) 1.96 g, 5 mM was dissolved in a 5% potassium hydroxide (22.4 g, 20 mM) solution at 90 °C. The resulting solution had a pH of about 10.5. A 14.0 g sample of a 10% acetic acid was added dropwise over 30 min at 90 °C, and the pH was 4.5-5.0. The suspension was stirred for another 1 h at the same temperature; the precipitated bordeaux-colored potassium salt (*1b*) was filtered at room temperature, washed with water, and dried at 130 °C. The desired product was obtained a with 95% yield (2.2 g). The MS data, collected by negative ion mode electrospray ionization mass spectrometry, were the same as reported in ref 5 with a main peak at 531 m/z and a second at 670 m/z due to the starting material (*1a*). NMR spectrum was not collected for this sample since it proved to be to insoluble at the concentration requested for the measure in all the usable solvents.

Synthesis of *N-Decylperylene-3,4,9,10-tetracarboxylic-3,4-anhydride-9,10-imide (1c).*
A mixture of perylene-3,4,9,10-tetracarboxylic acid monoanhydride monopotassium salt (*1b*) (1.25 g, 2.79 mM) and a 4.4 molar ratio of decylamine (1.93 g, 12.3 mM) and 12ml of H2O-PrOH (v/v)) 1:1 mixture as solvent, was stirred at room temperature for 4 h and heated at 90 °C for 2 h with stirring. The reaction mixture was acidified with 10% hydrochloric acid, and the resulting precipitate was

filtered and washed with water to remove residual amine. The residue was stirred into hot 10% potassium hydroxide, and to the mixture was added 8% potassium chloride to separate the precipitated potassium salt of *1c* and the symmetrically substituted diimide from the soluble, unreacted *1b*. The solid was stirred into water and the insoluble, symmetrically substituted diimide was removed. The filtrate was acidified with 20% hydrochloric acid. The precipitate was filtered, washed with water, and dried to yield *1c* in 70.4% yield. The NMR and MS data were the same as those reported in ref. 6. ESI-MS negative ion mode: m/z calculated is 531.2; observed: 531.4. The peak at 670.6 m/z is due to the residual symmetrically substituted diimide (calculated 670.4)(Fig.10.2).This was no longer removed from the mixture, since it is not reactive in further synthetic steps and it can be easily removed by purification processes adopted for compound **m1**.

NMR was not collected for this sample since it proved to be to insoluble at the concentration requested for the measure in all the usable solvent.
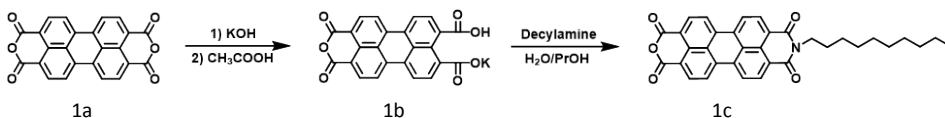
Scheme 10.1: Schemeof reaction mechanism for the synthesis of N-Decylperylene-3,4:9,10-tetracarboxylic-3,4-anhydride-9,10-imide (1c).
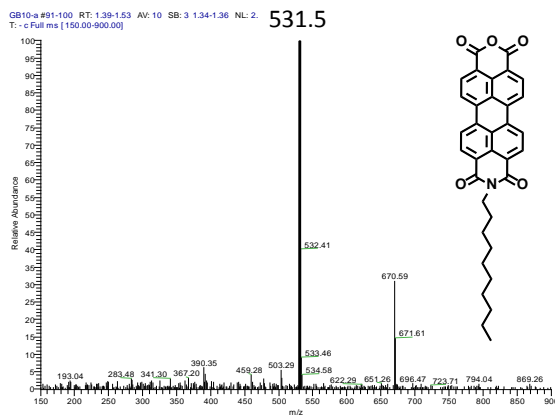
Figure 10.2: ESI-MS negative ion mode of 1c: m/z calculated is 531.2; observed: 531.4. The peak at 670.6 m/z is due to the symmetrically substituted diimide (calculated 670.4).

For the synthesis of the intermediate *N-octylamine norbornene* (*1d*), the mono Boc-

octylamine (7.9 10^{-3} mol) in 50 ml of toluene was added to the norbornene anhydride (8.69 × 10^{-3} mol, 1.1 eq) and heated with a dean stark trap in place overnight. Than the reaction was cooled at room temperature and concentrate to dryness. The product was purified by flash chromatography (3:7=hexane:ethylacetate) and obtained as a clear oil with a 75% yield. ESI-MS: m/z calculated is 290.2; observed: 291.2

The **¹H NMR** proton NMR was collected in deuterated chloroform at a 400 MHz instrument: δ (ppm) 1.25 (d, 1H, CH2), 1.30 (m, 2H, 6 x CH2) 1.50 (d, 1H, CH2,), 2.78 (s, 2H, 2 × CH), 3.14 (t, 2H, CH2), 3.21 (m, 2H, 2 × CH), 3.79 (t, 2H, CH2), 6.34 (s, 2H, HC=CH).[7]

N-Decyl,N'-Octilnornbornin-3,4,9,10, perylen-dicarboxiimide (**m1**) synthesis was achieved modifying the procedure reported in literature in ref. 8, through the condensation reaction between (*1d*) and (*1c*), scheme 10.2. The reaction mixture was stirred at 180°C for 4 hours using anhydrous zinc (II) acetate as a catalyst,[9] and purified by flash chromatography 9:1=DCM:MeOH. The product was isolated with about 75% yield. ESI-MS negative ion mode: m/z calculated is 803.4; observed: 804.5 (Fig.10.3).
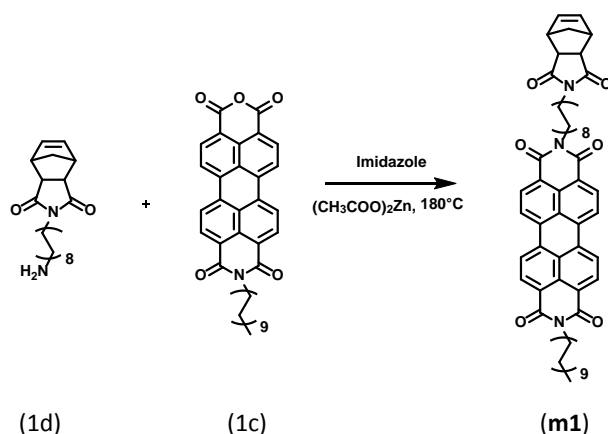
*Scheme 10.2:Schemeof reaction mechanism for the synthesis of N-Decyl,N'-octilnornbornin-3,4,9,10, perylendicarboxiimide (**m1**):*

Proton NMR of the product was collected in deuterated chloroform, the only solvent where the compound proved to dissolved in sufficient concentration. Although the collected spectrum was pure, proton integration was not possible to achieve, since the aromatic region of the PDI tends to aggregate reducing the signal contribution due to the bay region protons respect to the aliphatic chain ones.

¹H NMR proton NMR was collected in deuterated chloroform at a 400 MHz instrument. The resultant chemical shift are δ (ppm) 1.5-2.0 (broad, aliphatic), 2.78 (s, CH), 3.25 (d, PDI-amidic), 3.50 (m, CH), 4.25 (m, norb-amidic), 6.25 (s, HC=CH), 8.50 (m, arom), 8.65 (m, arom).
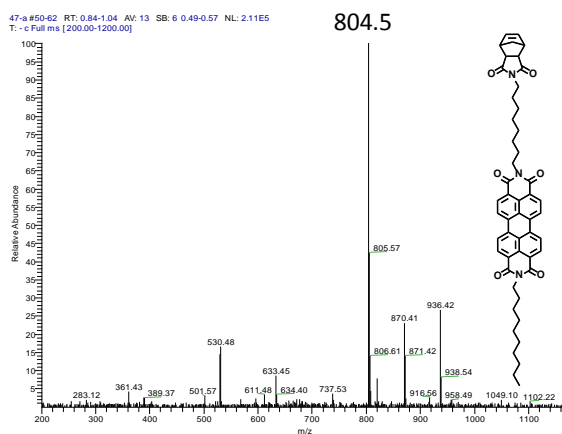
Figure 10.3: ESI-MS negative ion mode of N-Decyl,N'-Octilnornbornin-3,4,9,10, perylen dicarboximide (m1). m/z calculated is 803.4; observed: 804.5.
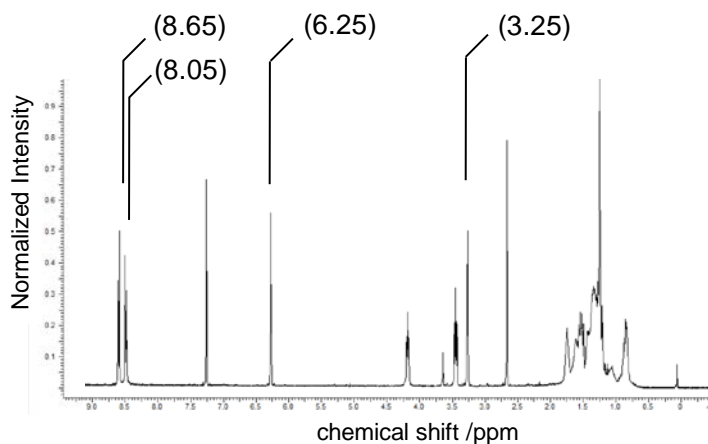
Figure 10.4: ¹H NMR proton NMR was collected in deuterated chloroform at a 400 Hz instrument. Are reported the most diagnostic peaks relative to the aromatic core (8.65-8.05 ppm), to the amidic proton (3.25 ppm) and to the olefinic protons of the norbornene (6.25). This last one is particularly important since its disappearance can be followed during the polymerization to confirm the inclusion of the monomer in the backbone.

Monomer **m1**absorption and emission spectra was recorded in chloroform. (Fig.

10.5). The absorption spectrum presents the typical structured band of the PDI chromophore with a maximum at λ_{max} = 525nm (ε_{max} = 8 × 10^4 $M^{-1}cm^{-1}$) in good accordance with the ones measured for similar PDIs. Similarly, the fluorescence of **m1** in $CHCl_3$ (λ_{exc} = 488 nm) shows, as reported for analogous PDI fluorophores, the typical vibrational spectral structure (λ_{max} = 534) mirroring the absorption band.
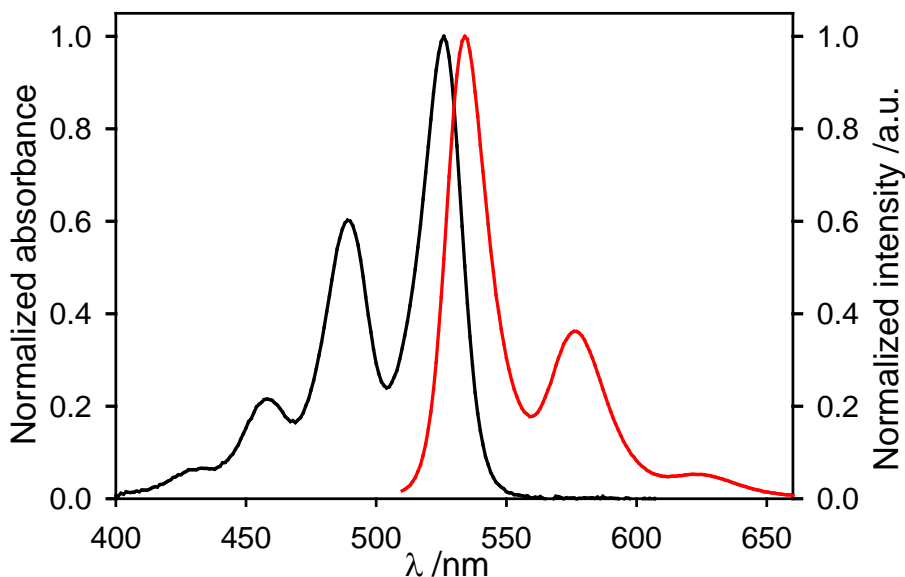
Figure 10.5: Normalized absorption (black curve) and emission (red curve) spectra of the m1 monomer in chloroform.

10.2 Hydrophobic (m2) and hydrophilic (m3) monomers synthesis and characterization

Once obtained the fluorescent monomer, polymerizable units necessary to form the hydrophobic and the hydrophilic block were synthesised.

The hydrophobic monomer (**m2**) was chosen in the prospective of forming the nanoparticles-core, prone to aggregate in polar environment. This unit was designed to be responsive to environmental pH variation, changing the molecular structure and water solubility in the pH range required for biological applications. For this reason, a tertiary amine, with a pKa = 6.9 linked to a polymerizable norbornene unit molecule was synthesised. The poor steric hindrance make the unit efficiently polymerizable, and it can also be obtained by a quite straightforward synthetic strategy further described and showed in scheme 10.3.

Synthesis for the hydrophobic monomer (**m2**),was achieved adding to a stirred solution of 2-aminoethyldiisopropylamine (648 mg, 4.5 mmol) in dry toluene (50 mL) 5-norbornene-*exo*-2,3-dicarboxylic anhydride (492 mg, 3 mmol) and triethylamine (606 mg, 6 mmol). The reaction was heated to reflux overnight. The solvent was reduced to a minimum under reduced pressure and was in a vacuum pump for further 5 h to yield a brown oil (860 mg, 99%).

^{1}H NMR(400 MHz, Cl$_3$CD-*d*) δ 6.27 (m, 2H), 3.47 (t, 2H), 3.26 (m, 2H), 3.01 (m, 2H), 2.66 (m, 2H), 2.57 (t, 2H), 1.50 (d, 1H), 1.34 (d, 1H), 0.97 (d, 12H). HRMS (ESI+, MeOH, *m/z*) calculated. for [M + H]$^+$, 291.2067; found, 291.2063 ([M + H]$^+$)
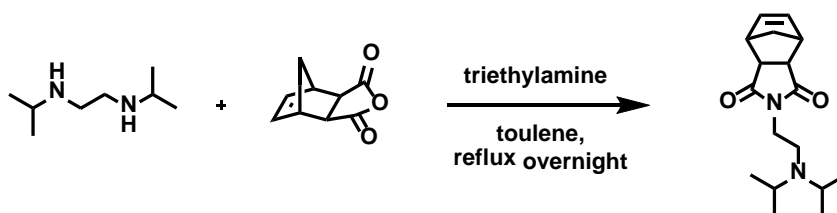
Scheme 10.3: schematic synthesis of the tertiary amine norbornene derivative (m2).

The hydrophilic monomer (**m3**) was chosen in the prospective of forming the nanoparticles shell, within the purpose of improving their colloidal stability and their ability to be up taken by cells. Consistently, it was chosen a PEG-norbornene derivative. In particular, accordingly with the consideration made before about the polymer aggregation angle, to obtain a spherical nanoparticles it was chosen a 4 units PEG chain. The synthesis is here described and schematized in scheme 10.4.
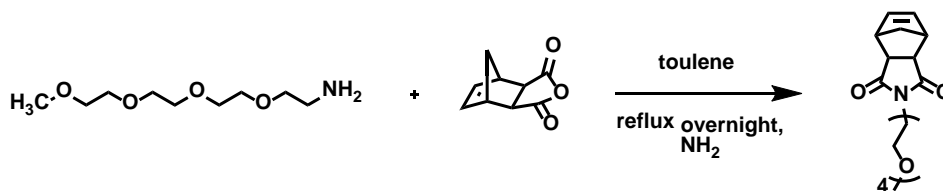
Scheme 10.4: Schematic synthesis of the hydrophilic monomer 2-(2,5,8,11-tetraoxatridecan-13-yl)- 3a,4,7,7a tetrahydro-1H-4,7-methanoisoindole-1,3(2H) - dione(m3).

For the synthesis of the hydrophilic monomer *2-(2,5,8,11-tetraoxatridecan-13-yl)- 3a,4,7,7atetrahydro-1H-4,7-methanoisoindole-1,3(2H)-dione* **(m3)** a solution of cis-5-norbornene-exo-2,3-dicarboxylic anhydride (1.5g, 9.1 mmols) and 2,5,8,11-tetraoxatridecan-13-amine (2.27g, 11.0 mmoles) in toluene (50 ml) was heated at

reflux overnight under a nitrogen atmosphere. The reaction mixture was cooled to room temperature, concentrated to dryness and purified by flash chromatography (2% MeOH in CH_2Cl_2) to give (**m3**) as a light yellow oil, 3.12g (97%).

^{1}H NMR, 400MHz, Cl$_3$CD-*d*, 1.35 (m, 1H), 1.47, (m, 1H), 2.66 (s, 2H), 3.24 (m, 2H), 3.36 (s, 3H), 3.5-3.7 (m, 16H), 6.26 (m, 2H).

^{13}C NMR, 100MHz, CDCl$_3$, 37.64, 42.63, 45.19, 47.73, 58.95, 66.78, 69.77, 70.50, 71.83, 137.73, 177.91. HRMS Calc M+Na = 376.1736, Obs. = 376.1730.[10]

10.2 Polymer (p4) synthesis and characterization.

Once synthesised monomer **m1** and **m2** their capability of polymerize had to be proven. It can, in fact, be limited or enabled by some parameters, such as the solubility in the reaction solvent or the steric hindrance reducing the double bond accessibility respect to the catalyst. To this end, the polymerization reaction was carried out in a tube and followed by ^{1}H NMR spectroscopy, evidencing the conversion of the norbornenyl olefinic protons to polynorbornenyl olefinic protons by tracking the disappearance of the norbornene peak at 6.25 ppm. (not reported) Same procedure for **m3** is reported in literature.[10]

Then, the polymerization of the three monomers **m1**, **m2** and **m3** have been carried out in order to obtain the desired amphiphilic co-block polymer **p4.**

Polymerization was carried out linking only an average number of 0.1 fluorescent monomers per polymer chain. Using such a small fraction of perylene diimide respect to the catalyst, the inclusion of more than one fluorescent units per polymeric chain is expected to be avoided as well as the dye quenching caused by the aromatic core vicinity in the same chain. In this way, π-π stacking can only be due to **m1** trapping into the nanoparticle core, allowing efficient chromophores disaggregation when the triggered nanoparticles disassembly occurs, letting the compound completely recover the fluorogenic properties.

In chapter 2 it has been underlined that the use of functionalized initiator as a technique to introduce functionality in the backbone is underutilized, since changes to the initiator structure can result in variation of the initiation and propagation rates. Nevertheless, this strategy was adopted in this case, where monomer **m1** has been used as chain initiator. Despite ROMP guarantees a good product weight monodispersity, in fact, the used ruthenium catalyst is oxide and water sensitive, and some of it can be poisoned before the reaction termination. This means that, if the fluorescent monomer is added as a termination agent, the ratio of 0.1 to 1 monomer to chain ratio may be not respected and multiple dye units can be

introduced in the same polymer. This would strongly affect the photophysical nanoparticles behaviour, since the π-π stacking may occur in the same chain and be not influenced by the pH variation. Schematic representation of the desired product is reported in Fig. 10.6.
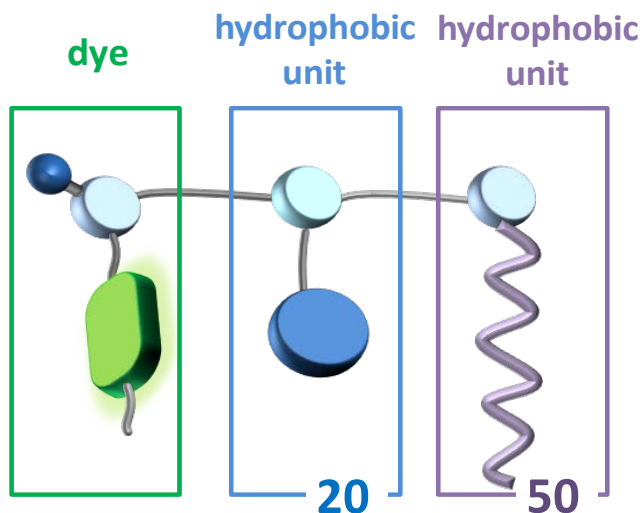
Figure 10.6: Schematic representation of the desired polymer p4. The fluorescent PDI unit is covalently linked to the hydrophobic, pH responsive block constituted of 20 units of monomer m2. The last hydrophilic block is composed of 50 units of monomer m3.

To the polymer (**p4**) synthesis, monomer **m1** (0.16 mg, 0.1:1 molar equivalent to the catalyst) was weighed out, dissolved in 400 μl of dry dichloromethane and added to a dry Schlenk flask with a stir bar charged with N_2. The catalyst solution (2.47 mg in 300 μl of dried DCM) was fast added to the monomer solution via syringe and allowed to polymerize at room temperature for ∼20 min under really slow stirring. Then monomer **m2** (11.6 mg in 400 μl, 20:1 molar equivalents to catalyst, where 20 is the degree of polymerization of monomer **m2**) was dissolved in dry DCM and added via syringe in the flask and allowed to polymerize for ∼30 min. A small aliquot of living solution (10% of the volume) was removed and terminated with excess ethyl vinyl ether (EVE) (10× molar excess with respect to the catalyst) for analysis. To the rest of the solution 33.5 mg in 363 μl (50:1 molar equivalents to catalyst) of the hydrophilic monomer **m3** were added and left under stirring for ∼20 min. Eventually an excess of ethyl vinyl ether (EVE) was added to

terminate the reaction and an aliquot (10% of the volume) was removed and used for analysis. The obtained polymer was purified crashing it out two times in a bad solvent (diethyl ether) after dissolution in DMF. The supernatant was then removed and the precipitated red solid dried under vacuum. Scheme of the reaction is reported below (Scheme 10.5).

0.1 eq.   20 eq.   50 eq.   1 eq.
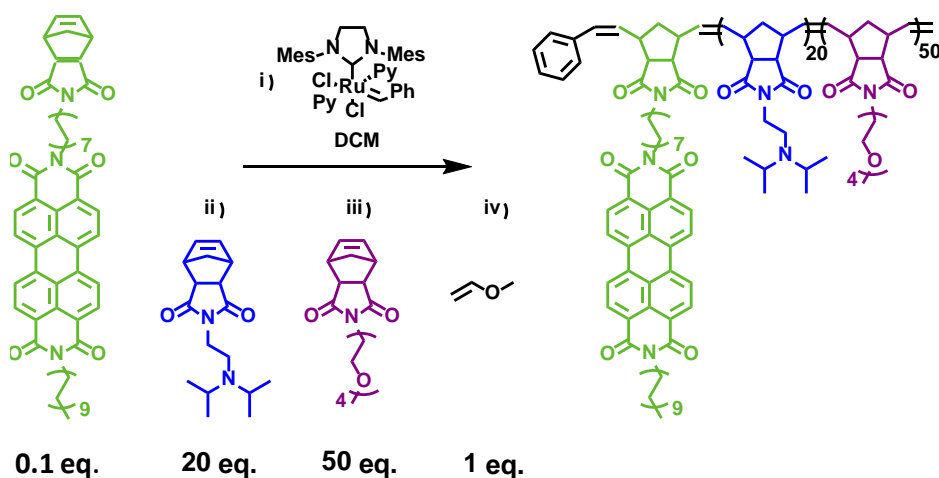
Scheme 10.5: Schematic polymerization reaction of monomer m1, m2 and m3 to obtain the amphiphilic block co-polymer p4.

Analysis of the fractions collected during the reaction were carried out by size exclusion chromatography with multiangle light scattering (SEC-MALS). Dispersing the samples in 40 µl of DMF, the relative size of the two blocks can be determined, proving the increasing of the molecular weight after the addiction of the second block constituted by **m3** (Fig.10.7, black curve), respect to the first one constituted by**m2**(Fig.10.7, red-curve), detecting the SLS scattered signal and the differential refractive index for each block.Since the *dn/dc* value is known only for **m3** in DMF (0.100) and it was not measured for **m1** and **m2**, absolute determination of molecular weight (MN) and dispersity (MW/MN) could not be performed. Accordingly, the value was calculated from the sum of the molecular weight of the single monomers as 2.3×10^4 g mol^{-1}. By this techniques it was proved the formation of the desired amphiphilic block co-polymer with a good polydispersive index.
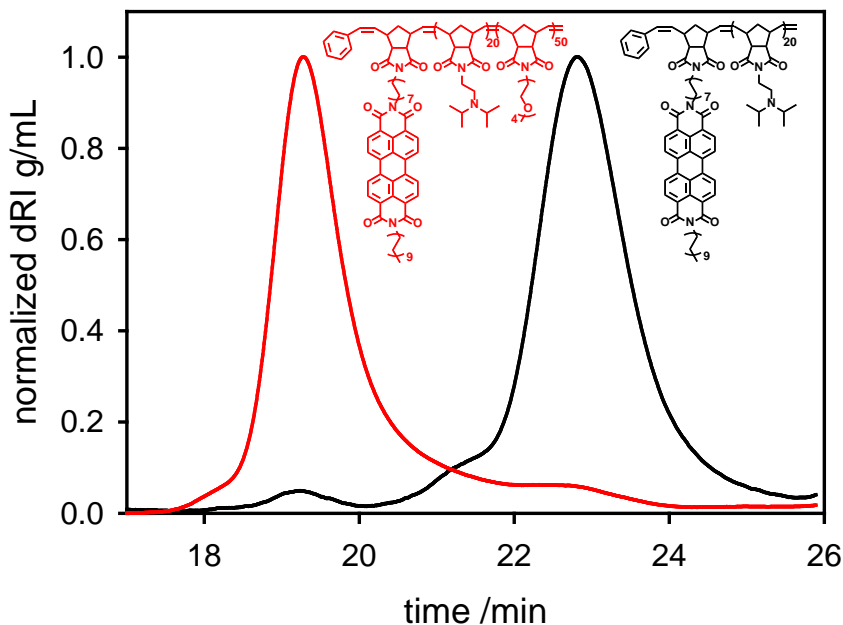
Figure 10.7: SLS scattered signal of the first and second fractions collected during the reaction by size exclusion chromatography with multiangle light scattering (SEC-MALS). Relative size of the two blocks can be determined, proving the increasing of the molecular weight after the addiction of the second block constituted by m3 (black curve), respect to the first one constituted by m2 (red-curve).

10.3 Nanoparticles (5NP) synthesis and characterization

In polar environment at neutral pH, the synthesised block co-polymer **p4** is expected to show an amphiphilic behaviour, being prone to self-assembly. In order to obtain spherical nanoparticles, conditions of aggregation have to be optimized varying different parameters. The solvent switch method[11] was adopted, choosing DMF as the good solvent, that well solubilised both the hydrophilic and the hydrophobic blocks. It is also mixable with the bad solvent, where the aggregation occurs. Then, the better initial polymer concentration in the good solvent and the speed of solvent switching was varied until the best self-assembly condition were achieved.

Polymer **p4** was hence dissolved in the co-solvent (DMF) at a concentration of 2 mg/ml (PDI-monomer concentration 4×10^{-4} M). Then, it was carefully dialysed in a dialysis tube under very gently magnetic stirring in PBS bath for 96h, slowly changing the bath after 24, 48 and 36 hours in order to complete remove any trace

of the organic solvent. This step of preparation is extremely critical, because every parameters can dramatically affect the final micellar morphology. When the volume ratio of the good respect to the bad solvent is less than 20%, micelles are kinetically very unstable and any variation in the solvent addition, stirring, temperature or other parameters affects the micellar morphology. Once the bad solvent percentage increases, the structure results frozen in the achieved morphology and environmental variations do not significantly affect the morphology. For this reason, a good control over the self-assembly conditions is required and the bad solvent, generally water, is slowly dropped on the dissolved polymer solution, carefully monitoring addiction speed, temperature and stirring conditions.

In the studied case, the switching was achieved by the uncommon strategy of the dialysis, which allows less control over the mentioned aspects. Nevertheless, the addiction of PBS could not be achieved otherwise, since dropping the buffer in the DMF solution causes the rapid formation of precipitate. Even if the precipitate tends to rapidly dissolve under stirring, it does not allow to maintain a good homogeneity of the polymer solution, required to the preparation of monodispersed self-assembled nanoparticles. The choice of switching the polymer from DMF to phosphate buffer solution, and not to water, was due to the observation that polymer could not aggregate in this last solvent. The reason was found in the MilliQ water pH which, at the work conditions, was too acidic to leave the tertiary amine of the **m2**monomer deprotonated, hence, hydrophobic.

Formed nanoparticles were morphologically studied by DLS without any dilution, proving the formation of a monodispersed population of spherical micelles with a 33 ± 1 nm hydrodynamic diameter and a good correlation curve was observed as reported in figure (Fig. 10.8). TEM images were collected for the sample stained with uranyl acetate and deposited on a copper grid cover by Formvar. The grid was previously treated by low energy plasma, in order to clean the surface from environmental contamination and increase the hydrophilicity.

TEM experiment proved the presence of a population of spherical nanoparticles, highly contrasted respect to the background. Although the images do not allow a proper statistic for the determination of the diameter (Fig. 10.9), it was measured in the range between 15 and 18 nm, which is in accord with the hypothesis that the uranyl acetate is included into the core, enhancing the contrast of this specific region respect to the shel,l which results almost completely undetectable. It has also to be considered that soft matter nanoparticles may tends to shrink when deposited on the grid and exposed to high vacuum.
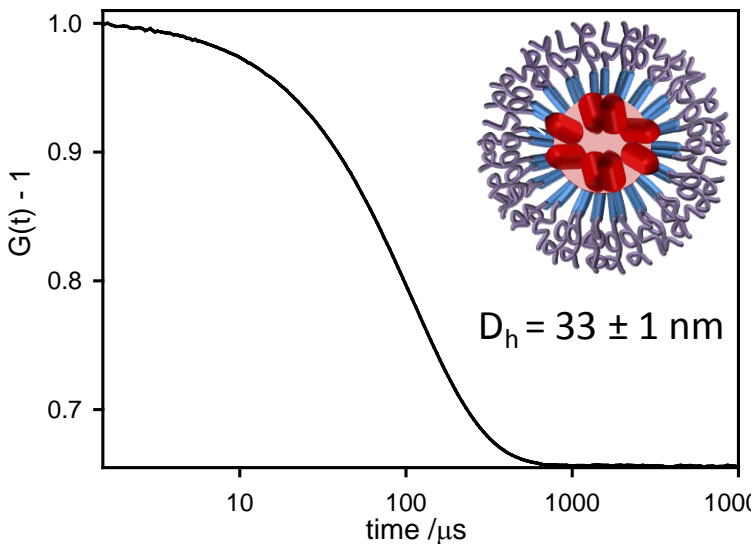
Figure 10.8: DLS measurement of the formed 5NP by solvent switching method from DMF to PBS (pH = 7.4). Good correlation curve proved the formation of monodispersed spherical nanoparticles, with a measured diameter of 33 ± 1 nm.
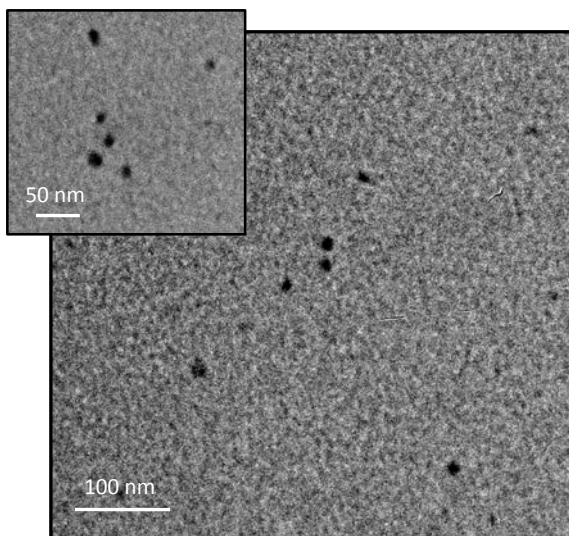
Figure 10.9: TEM images at different magnification of the nanoparticles 5NP stained with uranyl acetate, confirming the formation of spherical nanoparticles with a measured diameter ranging between 15 and 18 nm. These values are in accord with the hydrodynamic diameters measured by DLS.

It can hence be concluded that in this condition of pH polymer tends to aggregate, forming core-shell spherical micelles, where the shell is formed by the PEG-block and the core is formed by the amine-block terminated by the PDI unit. Self-assembly can occur in this situation since the amine are deprotonated at pH = 7.4 (free amine pKa=6.9)[12] and the block displays hydrophobic behaviour.

Considering the complete conversion of monomer **m1** in polymeric form and the volume variation caused by the dialysis treatment, **5NPs** nanoparticles have been obtained in with a concentration of the fluorescent unit equal to 4×10^{-5} M. In this condition, the fluorescence emission of the perylene derivative should be quenched as a consequence of the π-π stacking into the micelles core. To confirm this hypothesis, fluorescence spectrum collected for the sample in this condition proved that the perylene fluorescence emission is completely quenched (signal lower than the instrumental resolution limit).

Once proved the capability of polymer **p4** of self-assembly in monodispersed systems in neutral pH conditions, switching OFF the emissive signal of the perylene diimide, studies varying the pH conditions was carried on. Switching the environmental pH from neutral to acidic, it is expected the amines to get protonated, changing the solubility properties of the hydrophobic block. This should leads to the polymer **p4** solubilisation in polar environment and causes, as a consequence, the disaggregation of the self-assembled nanoparticles. A preliminary study was conducted adding to the **5NPs** sample small aliquots of HCl 1M, and measuring the resulting fluorescent signal.

To a 1 ml nanoparticle dispersion in PBS were added, under magnetic stirring, 5 aliquots of 100 µl of a 1 M HCl. Respective emission spectra were collected exciting at λ = 480 nm, where the monomer **m1** prove to absorb, and recorded in the range where perylene diimide derivative typically emits (500-750 nm). As it can be appreciate in figure 10.10, a clear increasing in the fluorescent intensity is observed with the increasing of the acid concentration. Considering that the emission intensity collected before the first acid addiction was not detectable by the instrument, being lower respect to the instrumental limit, an increasing of 25% on λ_{max} = 540 nm can be calculated. This qualitative behaviour is in accordance with the disaggregation of the self-assembled nanoparticles followed by the ON switching of the perylene diimide emission.

Further experiments have been conducted to prove NPs responsiveness in the pH range of interest, from 7.4 to 5. To this end, 0.5 ml of the 5NPs in PBS have been dialysed in a 0.5 ml dialysis cup for 48 in acetic acid buffer at pH = 5. The solution

was then studied by DLS and TEM in the same conditions as before the treatment. DLS measurement shows the disappearance of the monodispersed population observed at neutral pH (Fig. 10.11, gray-dotted curve) and the appearance of a poly-dispersed one (Fig. 10.11, red curve). Even if the hydrodynamic diameter value measured for this population is not significant, the result can be considered as a proof of the nanoparticles disaggregation.
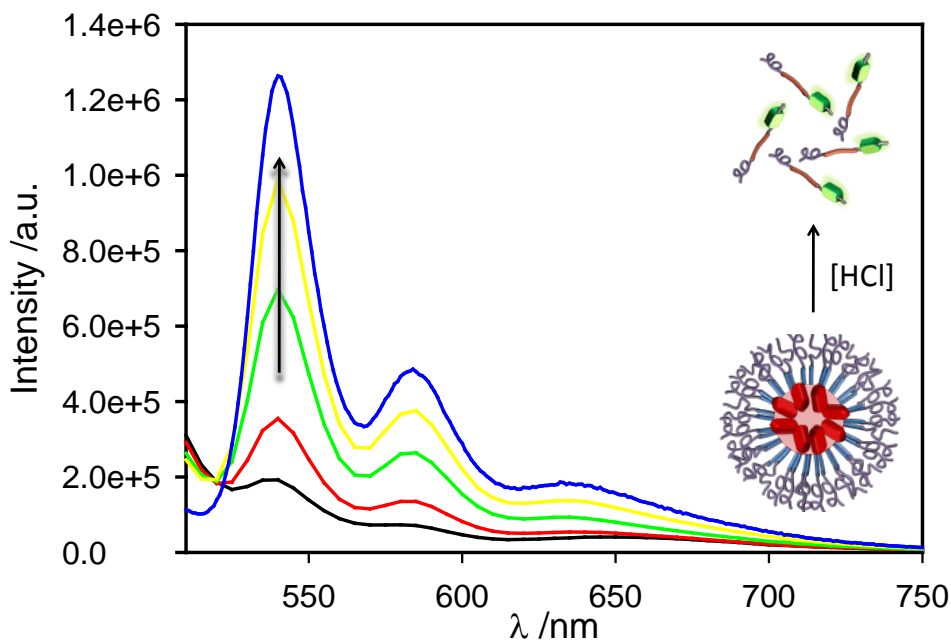
Figure 10.10: Emission titration of the 5NPs in PBS adding successive aliquots of HCl 1 M. A 25% emission intensity, collected on the maximum emission (λ_{max} = 540) increasing the acid concentration.

Results are confirmed by TEM images (Fig. 10.12) showing the formation of new bigger rod-shaped aggregates. These structures, which can get form either in solutions or during the drying of the copper grid, are the results of polymer disaggregation and re-aggregation in different morphologies. This results is not surprising, since previous studies showed how amphiphilic polymers can assembly in different geometries, if prepared by solvent or pH switching methods.[13] The clarification of the mechanism involved in this process, despite interesting to better understand some nano-aggregates behaviour, is behind the purpose of this thesis and not further experiments have been accomplished in this direction.

Nevertheless, these results allow to conclude that the acidification of the environment causes some structural changes in the components chemical properties, resulting in the nanoparticles disassembling.
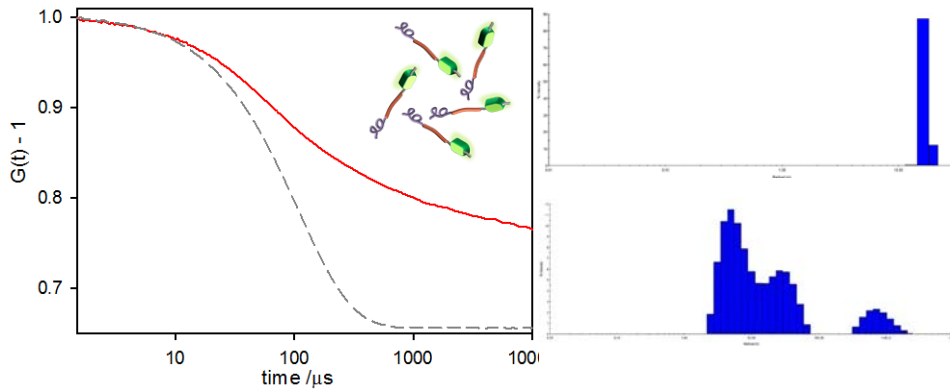
Figure 10.11: DLS measurement collected for 5NPs sample dialysed in acetic acid buffer at pH = 5. (dotted-gray curve) correlation curve of the not-dialysed NPs compared to the (red curve) dialysed NPs. (top-left) hydrodynamic radius of NPs before and (bottom-left) after dialysis.
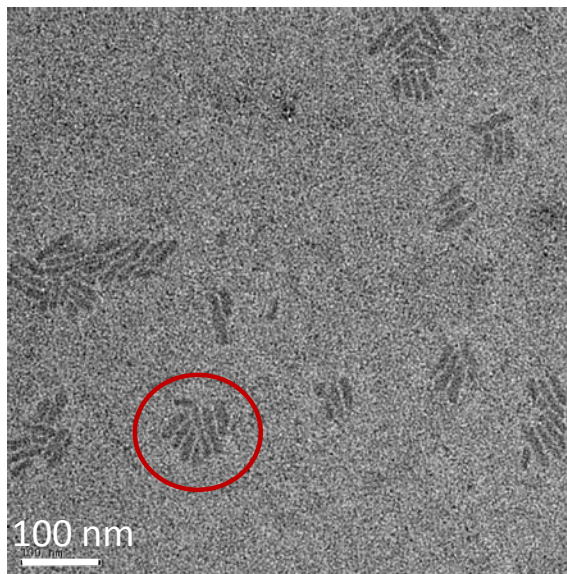
Figure 10.10: TEM images of the 5NPs after dialysis. It can be observed the formation of bigger rod-shaped aggregates and the disappearance of the spherical shaped nanoparticles.

Fluorescence quantum yield of the dialysed nanoparticles confirmed the previous results, since a value of 80% (measured using Fluorescein in NaOH 1M as a standard) was measured in this case.

Despite further experiments have still to be carried out, in order to better quantify the emission intensity increasing in acidic environment, it can be concluded that nanoparticles displayed the hypothesised result.

10.4 Conclusion

The synthesis of a monodispersed amphiphilic block co-polymer, constituted by a PEGylated hydrophilic block and a tertiary amine pH responsive hydrophobic block, efficiently functionalized by a fluorescent perylene derivative was achieved. The polymer intrinsic tendency to self-assembly was exploited to obtain spherical core-shell nanoparticles, where the dye emission is quenched in neutral pH environment, thanks to the π-π stacking occurring in the inner part of the structure.
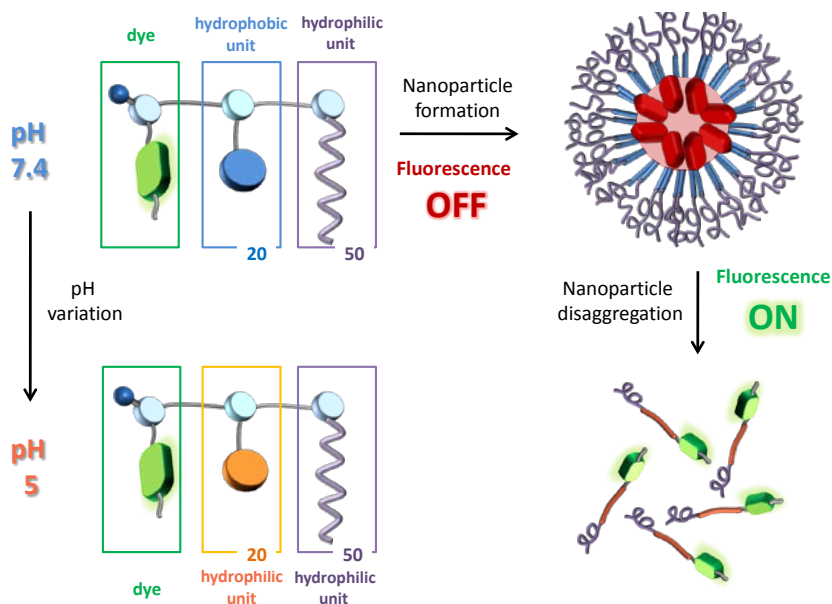
Figure 10.13: Schematic representation of the obtained system. The amphiphilic block co-polymer is functionalized by a perylene diimide derivative. At pH = 7.4 in water environment it tends to self-assemble in spherical micelles with the fluorescent unit aggregated and quenched into the core. The pH switching from 7.4 to 5 causes the protonation of the amine constituting the hydrophobic block. The polymer results water soluble, since formed from two hydrophilic blocks, and the micelles disassembly causing the DIE of the perylene diimide unit.

Thanks to the careful design, the variation of the pH from 7.4 to 5 leads to the amine of the hydrophobic block protonation, causing a structural change in the aggregation properties of the amphiphiles and the perylene diimide derivative. In last instance, it results in the ON-fluorescence switching of the emissive moiety. Despite *in-vitro* experiments have to be carried on in order to detect the same effect in cancer cells, nanoparticles internalization and disaggregation in biological environment are expected, as already observed in similar self-assembled structures.[3,14]

Interest in this structures is not only limited to the possibility of recognise cancer from normal tissues by bio-imaging techniques. The observed behaviour can be of scientific interest in the prospective of study aggregation and disaggregation mechanism of similar systems. The possibility of covalently functionalize other amphiphilic polymers with the same fluorescent monomer, without significantly affect the morphological behaviour and response to external changes, make this compound an interesting tool to explore their response by photophysical methods.

Bibliography

1   Champion, J. A. & Mitragotri, S. Role of target geometry in phagocytosis. *Proceedings of the National Academy of Sciences of the United States of America* **103**, 4930-4934 (2006).

2   Champion, J. A., Katare, Y. K. & Mitragotri, S. Particle shape: a new design parameter for micro-and nanoscale drug delivery carriers. *Journal of Controlled Release* **121**, 3-9 (2007).

3   Chien, M.-P., Rush, A. M., Thompson, M. P. & Gianneschi, N. C. Programmable Shape-Shifting Micelles. *Angewandte Chemie International Edition* **49**, 5076-5080, doi:10.1002/anie.201000265 (2010).

4   Yang, X., Xu, X. & Ji, H.-F. Solvent Effect on the Self-Assembled Structure of an Amphiphilic Perylene Diimide Derivative. *The Journal of Physical Chemistry B* **112**, 7196-7202, doi:10.1021/jp801413k (2008).

5   Tröster, H. Untersuchungen zur Protonierung von Perylen-3, 4, 9, 10-tetracarbonsäurealkalisalzen. *Dyes and Pigments* **4**, 171-177 (1983).

6   Nagao, Y. Synthesis and properties of perylene pigments. *Progress in organic coatings* **31**, 43-49 (1997).

7   Thompson, M. P. *et al.* Labelling polymers and micellar nanoparticles via initiation, propagation and termination with ROMP. *Polymer Chemistry* **5**, 1954-1964, doi:10.1039/C3PY01338C (2014).

8   Huang, C. *et al.* Photo-induced charge transfer and nonlinear absorption in dyads composed of a two-photon-absorbing donor and a perylene diimide acceptor. *Journal of Materials Chemistry* **21**, 16119-16128, doi:10.1039/C1JM12566D (2011).

9   Wurthner, F. Perylene bisimide dyes as versatile building blocks for functional supramolecular architectures. *Chemical Communications*, 1564-1579, doi:10.1039/B401630K (2004).

10   Hahn, M. E., Randolph, L. M., Adamiak, L., Thompson, M. P. & Gianneschi, N. C. Polymerization of a peptide-based enzyme substrate. *Chemical Communications* **49**, 2873-2875, doi:10.1039/C3CC40472B (2013).

11   Barnhill, S. A., Bell, N. C., Patterson, J. P., Olds, D. P. & Gianneschi, N. C. Phase Diagrams of Polynorbornene Amphiphilic Block Copolymers in Solution. *Macromolecules* **48**, 1152-1161, doi:10.1021/ma502163j (2015).

12   Wang, Y. *et al.* A nanoparticle-based strategy for the imaging of a broad range of tumours by nonlinear amplification of microenvironment signals. *Nat Mater* **13**, 204-212, doi:10.1038/nmat3819

http://www.nature.com/nmat/journal/v13/n2/abs/nmat3819.html#supplementary-information (2014).

13   Adams, D. J., Adams, S., Atkins, D., Butler, M. F. & Furzeland, S. Impact of mechanism of formation on encapsulation in block copolymer vesicles. *Journal of Controlled Release* **128**, 165-170 (2008).

14   Chien, M.-P., Thompson, M. P., Lin, E. C. & Gianneschi, N. C. Fluorogenic enzyme-responsive micellar nanoparticles. *Chemical Science* **3**, 2690-2694 (2012).

Conclusions

In conclusion, the preparation of a new perylene diimide derivative **(P)** by straightforward, reproducible and mild procedures, was achieved by microwave (MW) heating, using glycols as solvents. **P** solubility is strongly enhanced in polar environment by the substitution, in the amidic position, with a branched polypropylene oxide primary amine terminated. It was proved that aromatic core π-π stacking and inter-substituent interactions drove the self-assembly of strongly quenched nanoparticles, which can be efficiently internalized by yeast cells working as fluorogenic imaging agents. By controlling the dosage, they can also exploit either green or red fluorescence without affecting the background signal. Same nanoparticles can be used to achieve multicolour fluorescence imaging by photo-activation of the sample, under strong light irradiation. It is worthy underline that, in this system, the fluorogenic unit displays the dual role of emissive and structural component.

This first study on the new synthesised perylene derivative opened the door to the possibility of developing new covalently linked structures, where the self-assembled fluorescent building blocks are partially trapped by reticulation. The terminal amines of **P** PEGylated chains have been cross-linked by an epoxy monomer, letting the reaction occurs into Pluronic F-127 micelles formed in polar environment. This drives the formation of core-shell nanoparticles (**PNP**s), where the vicinity of the monomer aromatic regions caused a strong quenching of the emission signal. By light irradiation in proper conditions of concentration and/or polarity luminescence can be recovered, leaded by fluorophore disaggregation. The photo-activation was proved to occur also after nanoparticles internalization by tumour cell tissues, confirming the possibility of using **PNP**s as stimuli-responsive fluorogenic imaging agents in bio-applications.

Two examples of new fluorogenic light-responsive nanoparticles have been developed and studied, opening the way to a series of possible application of disaggregation induced emission (DIE) systems in bio-imaging and, potentially in drug delivery. These works suggested the possibility of further studies exploring new "smart" materials responsive to other stimuli. Considering that cells tissues and compartments are characterized by different pH, this parameter was chosen as environmental stimulus to trigger the emission signal.

To this purpose, a monodispersed amphiphilic block co-polymer, constituted by a PEGylated hydrophilic block and a tertiary amine pH responsive hydrophobic block, efficiently functionalized by a fluorescent perylene norbornene monomer have been synthesised by ring opening metathesis polymerization. The polymer intrinsic tendency to self-assembly was hence exploited to obtain spherical core-shell nanoparticles, strongly quenched in neutral pH, thanks to the π-π stacking occurring in the inner part of the structure. By switching the pH from 7.4 to 5, structural modification in the hydrophobic block are promoted, leading to the nanoparticles disassembly and to the recovery of the perylene fluorescence emission. New fluorogenic pH-responsive nanoparticles have been designed and developed, opening the way to potential application in bio-imaging and, considering the pH range of activation, in cancer and normal tissues differentiation.

In conclusion, three different examples of stimuli-responsive nanoparticles have been synthesised and studied, exploring the potentiality of self-assembly materials as efficient building blocks for the development of "smart" materials for bio-applications. In particular, perylene diimide derivative have been successfully used both as fluorogenic unit and structural components of the assembled structures. Photophysical and chemical properties of this class of compound proved to be extremely useful tools in the developing of high-brightness nanoparticles, where a strong fluorescent signal can be triggered by external (light) or internal (pH) stimuli by promoting disaggregation induced emission process (DIE).

The study of different nanostructures, obtained by quite similar building blocks, allowed to enhance the variability of morphologies and behaviours achievable by simply changing organization, reactivity or composition of the starting materials.

List of publications

(1) Montalti, M.; Battistelli, G.; Cantelli, A.; Genovese, D. *Chemical Communications* **2014**, *50*, 5326.

(2) Muniz-Miranda, F.; Pedone, A.; Battistelli, G.; Montalti, M.; Bloino, J.; Barone, V. *Journal of Chemical Theory and Computation* **2015**.

(3) Bell, N. C.; Doyle, S. J.; Battistelli, G.; LeGuyader, C. L. M.; Thompson, M. P.; Poe, A. M.; Rheingold, A.; Moore, C.; Montalti, M.; Thayumanavan, S.; Tauber, M. J.; Gianneschi, N. C. *Langmuir* **2015**, *31*, 9707.

(4) Montalti, M.; Cantelli, A.; Battistelli, G. *Chemical Society Reviews* **2015**, *44*, 4853.

(5) Tomasini, C.; Castellucci, N.; Caputo, V. C.; Milli, L.; Battistelli, G.; Fermani, S.; Falini, G. *CrystEngComm* **2015**, *17*, 116.

(6) Battistelli, G.; Cantelli, A.; Guidetti, G.; Manzi, J.; Montalti, M. *Wiley Interdisciplinary Reviews: Nanomedicine and Nanobiotechnology* **2015**, n/a.